
Experimental and Theoretical Analyses of Adiabatic Two-phase Flows in Horizontal Feed Pipes

A dissertation in partial fulfilment of the requirements for the degree of

Doktoringenieur (Dr.-Ing.)

presented to the

Faculty of Mechanical Science and Engineering

at the

Technische Universität Dresden

by

Dipl.-Ing. Alexander Döß

Born April, 16th 1991

22nd of September 2022
Dresden, Germany

Abstract

The majority of technical separation processes for fluid mixtures utilize the principle of rectification. If a two-phase mixture is fed into the column, possibly undesirable flow morphologies or severe droplet carry-over may occur, which detrimentally affect separation efficiency and equipment integrity. Currently, the two-phase flow behavior in feed pipes is hardly predicable and mostly based on empirical or heuristic methods, which do not properly account for a broad range of possible fluid properties and plant dimensions. As a consequence, costly safety margins are applied.

Feed pipes to separation columns are often characterized by horizontal inlet nozzles, small length-to-diameter ratios and complex routing, involving elbows or bends. The pipe lengths are too short to enable the two-phase flow to fully develop, which thus, enters the column with unknown flow morphology. Since developing flows have rarely been studied, today's engineering practice relies on existing predictive methods for fully developed two-phase flows. Graphical methods can hardly represent gradual transitions between flow regimes. Analytical models provide only simplified flow representations of the two-phase flow that have not yet been qualified for developing pipe flow.

In this work, a comprehensive experimental database of horizontal water-air flows in two test sections with nominal pipe diameters of $D = 50$ mm and $D = 200$ mm and feed pipe lengths in the range $10 < L/D < 75$ was established. This way, the data cover developing pipe flows with entrance lengths typical for two-phase feeds of separation columns and more developed flows that are comparable with the extensively studied reference system water-air. A particular focus was put on the effect of pipe bends on the flow morphology up- and downstream. The flow morphology was captured using imaging wire-mesh sensors. A 4D fuzzy algorithm was applied to objectively identify the flow two-phase morphologies. Based on their fuzzy representation, the flow morphologies were classified and a novel 2D visualization technique is proposed to discuss the flow development along the feed pipes.

Undesired flow morphologies (intermittent flow and entrainment) during the operation of two-phase feeds are hardly predictable by conventional design tools. The inception of intermittent flows was analyzed using the experimental data. Consequently, the inception criteria based on the required liquid levels for fully developed intermittent flows were adapted for short entrance lengths. The characteristic dynamics of flow morphologies that are known to cause the onset of entrainment were analyzed. Based on wave frequencies, a predictive criterion for the susceptibility of wavy flows for the onset of entrainment is introduced and applied to straight feed pipes and horizontal 90° bends.

Among the dozens available, 66 reduced-order models for the prediction of the void fraction were tested for straight feed pipes and horizontal 90° pipe bends. Thereof, the ones most suitable for variable operating conditions and pipe geometries were identified and adapted. Complementary 3D simulations were performed to verify the applicability of numerical codes (VoF, AIAD) for flows with free interfaces. The flow morphologies were successfully reproduced at macroscopic scale, however, the simulation results rank behind reduced-order models considering their quantitative predicting capabilities.

Kurzfassung

Die meisten technischen Verfahren zur Trennung von Flüssigkeitsgemischen beruhen auf dem Prinzip der Rektifikation. Wird ein Zweiphasengemisch in die Trennkolonne eingespeist, können unerwünschte Strömungsmorphologien oder ausgeprägte Tröpfchenverschleppung auftreten, welche sich nachteilig auf die Trennleistung und die Integrität einzelner Anlagenkomponenten auswirken. Derzeit lässt sich das Verhalten solcher Zweiphasenströmungen in Einspeiseleitungen kaum vorhersagen und basiert meist auf empirischen oder heuristischen Methoden, die ein breites Spektrum möglicher Stoffeigenschaften und Anlagendimensionen nicht angemessen berücksichtigen. Infolgedessen müssen kostspielige Sicherheitszuschläge angewendet werden.

Einspeiseleitungen von Trennkolonnen sind häufig durch horizontale Eintrittsstutzen, ein geringes Länge-zu-Durchmesser-Verhältnis und eine komplexe Leitungsführung mit Bögen und anderen Normteilen gekennzeichnet. Typische Rohrlängen sind zu kurz, um eine vollständig entwickelte Zweiphasenströmung auszubilden, welche daher mit unbekannter Strömungsmorphologie in die Trennkolonne eintritt. Da derartige Strömungen jedoch bisher nur selten untersucht wurden, verlässt man sich gegenwärtig in der technischen Praxis auf bestehende Vorhersagemethoden für voll entwickelte Zweiphasenströmungen. Grafische Methoden können jedoch die allmählichen Übergänge zwischen Strömungsformen kaum darstellen. Analytische Modelle liefern nur vereinfachte Näherungswerte der Zweiphasenströmung, die noch nicht für sich entwickelnde Rohrströmung qualifiziert wird.

In dieser Arbeit wurde eine umfangreiche experimentelle Datenbasis horizontaler Wasser-Luft-Strömungen in zwei Versuchsstrecken mit Rohrrinnendurchmessern von $D = 50$ mm und $D = 200$ mm und Einlauflängen im Bereich $10 < L/D < 75$ erstellt. Auf diese Weise decken die Daten sowohl sich entwickelnde Rohrströmungen mit typischen Einlauflängen für Einspeiseleitungen ab, als auch weiter (in axialer Richtung) entwickelte Strömungen, die mit dem umfangreich untersuchten Referenzsystem Wasser-Luft vergleichbar sind. Die Auswirkung von Rohrbögen auf die Strömungsmorphologie stromauf- und stromabwärts wurde gezielt

untersucht. Die Strömungsmorphologie wurde mit bildgebenden Gittersensoren erfasst. Ein 4D-Fuzzy-Algorithmus wurde zur objektiven Identifizierung der Strömungsmorphologien eingesetzt. Auf Grundlage dieser Fuzzy-Darstellung der Strömung wurden die Strömungsmorphologien klassifiziert, und es wurde eine neuartige 2D-Visualisierungstechnik entworfen, mit der die Strömungsentwicklung entlang der Einspeiseleitungen diskutiert wurde.

Unerwünschte Strömungsmorphologien (intermittierende Strömung und Tropfenmitriss) während des Betriebs zweiphasiger Einspeisungen sind mit herkömmlichen Auslegungswerkzeugen kaum vorherzusagen. Das Einsetzen intermittierender Strömungen wurde auf Grundlage der experimentellen Daten analysiert. Daraufhin wurden existierende Kriterien, basierend auf den notwendigen Mindestfüllständen, für das Einsetzen intermittierender Strömungen in Abhängigkeit von den untersuchten Einlaufängen angepasst. Die charakteristische Dynamik von Strömungsmorphologien, die Tropfenmitriss hervorrufen, wurde analysiert. Voraussagemethoden zur Vorhersage der Anfälligkeit welliger Strömungen für das Auftreten von Tropfenmitriss wurden auf der Grundlage von Wellenfrequenzen entwickelt und für gerade Einspeiserohre und horizontale 90°-Bögen angewandt.

Von den zahlreichen verfügbaren Modellen zur Vorhersage des Gasanteils wurden 66 Modelle reduzierter Ordnung für gerade Einspeiseleitungen und horizontale 90°-Rohrbögen getestet. Davon wurden die für variable Betriebsbedingungen und Rohrgeometrien am besten geeigneten Modelle ermittelt und angepasst. Komplementäre 3D-Simulationen wurden durchgeführt, um die Anwendbarkeit numerischer Codes (VoF, AIAD) für Strömungen mit freien Grenzflächen zu bestätigen. Die Strömungsmorphologien wurden im makroskopischen Maßstab erfolgreich reproduziert, die Simulationsergebnisse bleiben jedoch hinsichtlich ihrer quantitativen Vorhersagekraft hinter den Modellen reduzierter Ordnung zurück.

Acknowledgement

The scientific activities presented in this dissertation were carried out during my time as a research assistant at the Institute of Fluid Dynamics at the Helmholtz-Zentrum Dresden-Rossendorf (HZDR) and as a doctoral candidate at the Faculty of Mechanical Engineering at Technische Universität Dresden.

First of all, I would like to express my gratitude to Prof. Dr.-Ing. habil. Dr. h. c. Uwe Hampel for the honor of supervision and support during my time as a PhD student. Above all, his fundamental mechanistic understanding always brought new ideas and perspectives to the work. Especially, I would like to appreciate his quality as my Doktorvater, which he fulfills to an outstanding degree despite an enormous number of other obligations and responsibilities. The multitude of consultative exchanges, in which he regularly takes time to accompany discussions in a level-headed and goal-oriented manner in order to shape the structure and scope of scientific contributions is not to be taken for granted and serves as a great role model.

Secondly, I would like to thank Prof. Dr.-Ing. Markus Schubert for his scientific supervision and mentorship. Regardless of time, date or location, his creative and pragmatic attitude helped me to develop new perspectives, subtasks and structural aspects of the work. His ability to brainstorm creative ideas with hardly any preparation time to get to the core of the matter continues to impress me to the same degree that it challenged me, my creative abilities, and put a smile on my face.

Very special thanks go to my long-time comrade-in-arms and good friend Dr.-Ing. Sebastian Unger, whose constant urging and uncompromising determination contributed significantly to the completion of the work.

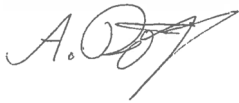
Furthermore, I would like to express my gratitude for being able to gain unique experience by working on the TERESA project (BMW, FKZ: 03ET1395) with a multifaceted project consortium and unique project content. In particular I thank my colleagues Dr.-Ing. Christian Geipel and

Dr.-Ing. Christian Mehringer from RVT Process Equipment GmbH, who made their pilot plant and their know-how accessible for a part of the experiments in this study.

Furthermore, my thanks go to Prof. Dr.-Ing. Marcus Grünewald and Prof. Dr.-Ing. Marco da Silva for accepting to review this thesis.

The number of colleagues and friends at the HZDR whom I would like to thank for shaping the working atmosphere and for their continuous motivation and willingness to discuss on a technical, scientific or social level is by far too numerous. However, I want to highlight those without whose contributions this work would not exist in this form: Ronny Berger, Matthias Beyer, André Flaisz, Ronald Franz, Thomas Geißler, Dr.-Ing. Thomas Höhne, Martin Löschau, Heiko Pietruske, Eckhard Schleicher, Christoph Schunk, Peter Schütz, Martin Tschofen, Dr.-Ing. Philipp Wiedemann, Michael Wiezorek as well as my former students: Patrick Junge and Abdulhadi Abdlgwad.

A final thank you goes out to my family and friends for their support, acceptance of the time and energy demands that a PhD entails, and providing adequate compensation in one way or another.



Alexander Döß

Nomenclature

Abbreviations

A	Annular
AW	Annular wavy
AIAD	Algebraic Interfacial Area Density
B	Bubbly
CAPEX	Capital expenditure
CCL	CFX Command Language
CFD	Computational Fluid Dynamics
CMFD	Computational Multiphase Fluid Dynamics
DFM	Drift-flux model
DFT	Discrete Fourier transform
EMP	Empirical model
FFPI	Fuzzy flow pattern identification
HFM	Homogenous flow model
HIDiC	Heat-integrated distillation column
I	Intermittent
IKH	Inviscid Kelvin-Helmholtz
ILG	Interfacial level gradient
INL	Inlet measurement position
LMP	Models based on the Lockhart-Martinelli parameter
LR	Low Reynolds regime
OE	Onset of entrainment
OUT	Outlet measurement position
PDF	Probability density function
PSD	Power spectral density
REF	Reference measurement position
RMS	Root mean square
RT	Rough turbulent

S	Stratified
SFM	Separated flow model
SST	Menter's Shear Stress Transport model
SW1, SW2	Stratified wavy
T	Transition
TE	Thermodynamic efficiency
TFM	Two-fluid model
TERESA	Tropfenentstehung und -reduzierung in Stoffaustauschapparaten (project name)
VoF	Volume of Fluid model
VKH	Viscous Kelvin-Helmholtz
VLE	Vapor-liquid equilibrium
WMS	Wire-mesh sensor

Latin symbols

A	Cross section, m^2
a	Weighting factor, -
C	Constant, misc.
C_0	Distribution parameter (DFM), -
C_D	Drag coefficient, -
C_S	Interfacial shape coefficient, -
C_r	Viscosity term, -
c_w	Wave celerity, $m\ s^{-1}$
D	Diameter, m
D_h	Hydraulic diameter, m
De	Dean number, -
E	Absolute uncertainty, -
$ENBW$	Effective noise bandwidth, Hz
e	Exponent, -
F	FFPI membership function, -
F_n, F_n^*, \tilde{F}_n	Degree of membership to main morphology n, -
F_1	Fluid property factor, -
Fr	Froude number, -
f	Frequency, Hz
f_w	Wave frequency, Hz
f_f	Friction factor, -
f_{res}	Grid points in the frequency domain, Hz
f_s	Sampling frequency or WMS frame rate, Hz
g	Gravity constant, $m\ s^{-2}$
H	Enthalpy, J

\bar{h}_L	Average liquid level, m
h_L	Dimensionless liquid level, -
$h_{L,W}$	Height of disturbance wave, m
I_r	Receiver current, A
K	Factor, -
K_l	Flow consistency index, $(Pa\ s)^{n'}$
K_{HFM}	Multiplier for homogenous flow models, -
Ku	Kutateladze number, -
k	Elevation parameter, -
L	Length, m
LMN	Lockhart-Martinelli number, -
\dot{M}	Mass flow rate, $kg\ s^{-1}$
$M_{G,L}$	Interphase momentum transfer, -
m	Ordinal number, -
\dot{m}	Mass flux, $kg\ m^{-2}\ s^{-1}$
N_{DFT}	DFT window length, -
N_η	Viscosity number, -
n_m	Measurement sample or time step, -
n_{DFT}	DFT window number, -
n'	Flow behavior index, -
PSD	PSD spectrum, -
p	Pressure, Pa
q	Thermal state of the feed mixture, -
R	(curvature) Radius, m
R^2	Coefficient of determination, -
R_n	Radial coordinate for FFPI visualization, -
Re	Reynolds number, -
R_r	Reflux ratio, -
R_s	Slip ratio, -
t	Time, s
S	Perimeter, m
$S_{DFT,1}, S_{DFT,1}$	DFT window sums, -
St	Strouhal number, -
U_G	Dimensionless gas velocity, -
U_r	Receiver voltage, V
U_t	Excitation voltage, V
u	Velocity, $m\ s^{-1}$
u_D	Drift velocity, $m\ s^{-1}$
u_h	Mixture volumetric flux, $m\ s^{-1}$
\mathbf{u}_k	Velocity field, -

u_D	Drift velocity, m s^{-1}
\dot{V}	Volumetric flow rate, - $\text{m}^3 \text{s}^{-1}$
VAR	Variance, -
$W(n_m)$	DFT window function, -
W	Weighting factor, -
We	Weber number, -
w	Mass fraction, -
X	Lockhart-Martinelli Parameter, -
x, y, z	Coordinates, misc.
x_{exp}	Measured quantity, -
y^+	Dimensionless distance from the wall, -

Greek symbols

α	Volumetric phase fraction, -
β	Angular coordinate for FFPI visualization, $^\circ$
γ	Kinetic energy correction term, -
$\dot{\gamma}$	Shear rate, s^{-1}
Δ	Difference, misc.
ε	Statistical uncertainty, misc.
η	Dynamic viscosity, Pa s
θ	Inclination angle, $^\circ$
λ_W	Unit length of an ellipsoid, -
μ	Kinematic viscosity, $\text{m}^2 \text{s}^{-1}$
ρ	Density, kg m^{-3}
σ	Surface tension, N m^{-1}
σ_{exp}	Standard deviation of a measurement, misc.
$\tau_{W,k}, \tau_{i,k}$	Wall and interfacial shear stresses, Pa
ϕ	Centroid angle, rad
χ_k	Mole fraction of the light boiling component in phase k , mol

Subscripts

A	Asymptote
ari	Arithmetic
Bend	Bend
Bot	Bottom
c	Critical
corr	Corre
DFM	Drift-flux model
Dis	Distillate

E	Entrainment
e	Equilibrium
exp	Experimental
F	Feed
f	Film
HFM	Homogenous flow model
h	(Homogenous) mixture
I, in	In
IKH	Inviscid Kelvin-Helmholtz
i	Interface
i ₁ , i ₂	Index of WMS electrodes
inl	Inlet
k	Phase indicator
L	Liquid
L _w	Wave length
LMP	Models based on the Lockhart-Martinelli parameter
log	Logarithmic
m	Mixture
n, n*	Flow morphology indicator (FFPI)
n _m	Time step or frame of WMS recording
max	Maximum
min	Minimum
mod	Modified
OE	Onset of entrainment
o	Out
opt	Optimum
ref	Reference
rel	Relative
SFM	Separated flow model
s	Superficial
sim	Simulation
stab	Stability
sat	Saturated
T	Temperature in °C
theo	Theoretical
tp	Two-phase
V	Vapor
VKH	Viscous Kelvin-Helmholtz
w	Wall

Table of Contents

Abstract	II
Kurzfassung	IV
Acknowledgement	VI
Nomenclature	VIII
Table of Contents	XIII
1 Introduction	1
1.1 Thermal separation in view of the 21st century	1
1.2 Engineering and design of rectification plants	2
1.3 Outline of the thesis	4
2 State of the art	5
2.1 Two-phase feeds in thermal separation	5
2.1.1 Feed condition as adjustable parameter	5
2.1.2 Thermohydraulic optimization	8
2.1.3 Hydrodynamic conditioning	9
2.2 Hydrodynamics of two-phase feeds	11
2.2.1 Flow morphologies in feed pipes	11
2.2.2 Droplet entrainment	14
2.2.3 Flow regime maps	17
2.2.4 Consequences for two-phase feeds	19
2.3 Modelling of two-phase feeds	23
2.3.1 Basic definitions	23
2.3.2 Fundamentals of the two-fluid model	25
2.3.3 The interfacial level gradient	29
2.3.4 Analytical models	32

2.3.5	CFD simulations for commercial feed pipes	34
2.4	Objectives of this thesis	36
3	Experimental method and algorithms for flow characterization	37
3.1	Experimental setups	37
3.2	Wire-mesh sensors	40
3.3	Experimental procedure	42
3.4	Data processing	44
3.4.1	Fuzzy flow morphology classification	45
3.4.2	Power spectral density	48
3.5	Measurement uncertainty	49
4	Flow morphologies in different feed pipe geometries	53
4.1	Developing two-phase flow in straight pipes	53
4.2	Effect of pipe curvatures on the flow morphology	55
4.3	Morphology recovery	57
4.4	Conclusions	60
5	Prediction of undesirable flow morphologies in feed pipes	61
5.1	Initiation of intermittent flows	61
5.2	Onset of droplet entrainment	62
5.2.1	Vulnerable flow morphologies	62
5.2.2	Derivation of a criterion for onset of entrainment	64
5.2.3	Adjustment of the criterion for the investigated pipe geometries	67
5.3	Conclusions	70
6	Reduced-order modelling of two-phase feeds	71
6.1	Prediction of void fraction	71
6.2	Liquid levels	75
6.3	Conclusions	78
7	CFD modelling of two-phase feeds	79
7.1	Simulation setup	79
7.2	Multiphase models	82
7.3	Comparison with experimental data	83
7.3.1	Straight pipes	83
7.3.2	Horizontal 90° bends	85
7.4	Conclusions	88

8 Summary and recommendations for future work	89
8.1 Summary	89
8.2 Recommendations for future work	91
References	94
List of figures	113
List of tables	118
Appendix	i
Scientific publications and contributions	xxxiii
Eidesstattliche Erklärung	xxxvii

1 Introduction

1.1 Thermal separation in view of the 21st century

Process intensification in the chemical industry is not only an economic issue, it also concerns reductions in primary energy consumption, storage and reuse of carbon dioxide. Re-designs towards climate-benign processes with reduced waste and circular economy are equally important aspects of international and national climate protection actions in separation technology and engineering (Riese et al., 2020). However, variable and thermally unstable raw materials and an increased demand for the separation of aqueous solutions, heavy hydrocarbons or gasses with elevated CO₂ content (Windmeier et al., 2021) require process designs that tolerate volatile process streams and variable operation modes (Knösche, 2020).

Thermal separation is integral part of commercial process engineering product chains and contribute to global industrial energy consumption in the order of 3 % (Liu et al., 2017) to 10 % (Sholl and Lively, 2016). Distillation units contribute to 30 - 80 % of the process' total energy consumption (Cussler and Dutta, 2012; Chavez Velasco et al., 2021). Yet, there is no alternative separation technology in sight, not to mention missing fundamental data for mass transfer (e.g. only 1.2 % of the vapor-liquid-equilibrium data of binary mixtures are available nowadays) and thus, technologies with high technical maturity are preferred (McBride et al., 2020).

However, most commercial distillation plants are still underdetermined with respect to the degrees of freedom of the design problem, and engineers therefore rely predominantly on heuristics (Degance and Atherton, 1970a; Doherty and Malone, 2001; Lee and Binkley, 2011). These, however, hardly cover typical operating conditions, material properties and undesired flow phenomena encountered in industry. The latter have to be compensated by means of tailored conditioning of e.g. interfaces between plant components or inlet/outlet flows. In particular, complex vapor-liquid phase interactions cannot be satisfactorily predicted with the current knowledge about hydrodynamics of two-phase flows.

1.2 Engineering and design of rectification plants

Thermal separation of multicomponent mixtures exploits their differences in the boiling points in order to enrich the low-boiling (light key) components in the vapor phase and the heavy-boiling (heavy key) components in the liquid phase. Essentially, this is a low efficiency Carnot heat engine where separation work is provided by degradation of heat from the mixture (Ognisty, 2000). Irreversible entropy production results from multiphase fluid mechanics and heat transfer phenomena and leads to process efficiency losses. Various thermodynamic optimization concepts (e.g. pinch analysis, exergy analysis, equipartition principle) of distillation processes (Demirel, 2004) have thus been introduced. Their common objective is the thermohydraulic conditioning of entering fluids in order to align with the distillation columns internal streams leveling out undesired enthalpy, concentration or momentum gradients.

Conditioning of the column feed mixture is one of the most promising approaches, since there is a high degree of freedom as explained by Couper et al. (2012) and the implementation is less costly than a full column revamp. However, proper feed conditioning is often overlooked during early design steps of the separation process and feasible methods to describe e.g. two-phase feeds do not yet exist (Lee and Binkley, 2011). Feed conditioning must also compensate possibly undesirable process conditions introduced by the streams entering from preceding process units as discussed by Agrawal and Herron (2001). As a result of process design or optimization measures, commercial feed pipes often transport multiphase (vapor-liquid) flows (Lee and Binkley, 2011), which require elaborated design concepts (Fleming et al., 1996).

For example, the stable operation of tray columns depends on the respective vapor and liquid loads (Figure 1.1) of the column that are determined by the reflux ratio (rectifying section), the vaporization ratio (stripping section) and the feed's composition and flow rate. The upper operation limit is defined by total blocking of the downcomer (downcomer flooding) and liquid carry over (entrainment flooding) at high liquid and gas loadings, respectively. These limits dictate the column diameter, that is typically designed at 60 % - 80 % of the flooding limits. Design calculations (Wankat, 2007) show that the column diameter can be reduced significantly, when two-phase feeds are used instead of vapor feeds, due to the lower vapor flow rate in the rectifying section. However, if the feed pipe is a two-phase mixture, turbulent interactions occur between the phases as well as with the surrounding pipe periphery. As a consequence, different flow morphologies can evolve in feed pipes that vary with pipe length and routing and may involve transient states.

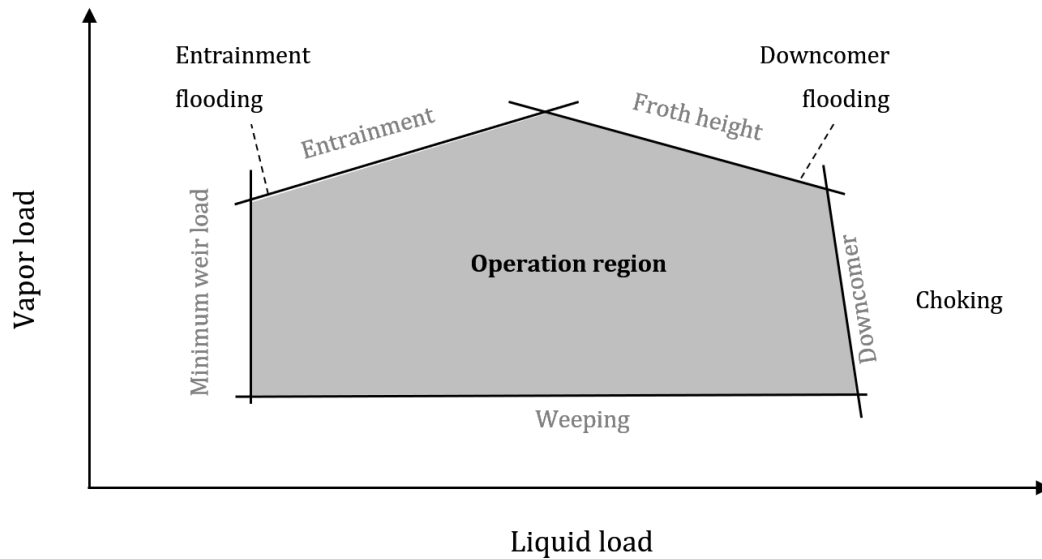


Figure 1.1: Operation region and operation limits of tray columns. Chart adapted from Mersmann et al. (2011).

According to Kister (1990), Pilling et al. (2010) and Lee and Binkley (2011) the occurrence of mist and intermittent flow as well as non-uniform momentum distribution at the inlet nozzle are the biggest concerns for the feed pipe design. Droplets that are carried over by the rising vapor in the column impair the mass transfer of theoretical stages in the rectifying section (reducing the separation efficiency) and may even cause product impurities or fouling in the head condenser. Intermittent flows enter the column with high momentum and uneven material distribution in the feed section, while simultaneously causing increased mechanical stresses to column, internals and supporting structures, which eventually increases maintenance costs. Improper handling of two-phase feeds can even cause equipment malfunctions or failure (see exemplary troubleshooting cases in Appendix A.1).

All these cause the engineering challenge: the feed pipe towards the columns inlet must be designed to counteract or eliminate detrimental flow condition or phase maldistribution (Kister, 1990; Wehrli et al., 2006; Aryan, 2022). However, Bothamley (2013a) stated that the performance of inlet devices and internals is scarcely tested and adequate information on evolving flow morphologies in feed pipes are hardly available. Same holds for experimental data considering pipe dimension and routing as well as fluids typically encountered in thermal separation. Currently, such data are only available from malfunction of real plants at narrow operation conditions and with limited diagnostic tools (Windmeier et al., 2021) or from research consortia with limited access to the public (Mersmann et al., 2011; Wankat, 2011), thus require research expenditure.

1.3 Outline of the thesis

Chapter 2 presents the fundamentals for the engineering of two-phase feeds for distillation columns. The state of the art regarding the occurrence and prediction of critical flow phenomena is discussed. Furthermore, available predictive methods and tools for void fraction and flow morphologies are revised and their weaknesses and strengths are discussed. Eventually, open questions for research and objectives are derived from the analysis of the state of the art.

Chapter 3 summarizes the applied setups, experimental procedures, specifications of applied measurement techniques as well as estimated measurement uncertainties. Furthermore, a novel fuzzy-based flow morphology classification and the derivation of wave properties from the power density spectrum are explained.

Chapter 4 presents the analysis of observed flow morphologies along horizontal straight and bent pipes. Based on the novel morphology classifier, required entrance and recovery lengths are discussed.

Chapter 5 introduces criteria for predicting the occurrence of undesired flow morphologies, i.e. intermittent flows and liquid entrainment. The latter is captured by a conceptual criterion based on characteristic dynamics of waves from which droplets are torn off.

Chapter 6 applies and assesses the predictive capability of reduced-order models and empirical correlations for the void fraction in straight and bent pipes. Recommendations are provided for the most versatile models, while comparing their predictions with the generated experimental database.

Chapter 7 presents complementary 3D numerical simulations for selected cases illustrate potential and shortcomings of Computational Multiphase Fluid Dynamics (CMFD) as design method.

Chapter 8 summarizes the most important findings of this thesis. The contribution of the work for the engineering of two-phase feeds is illustrated in a flow chart. Eventually, recommendations for future work arising from this thesis are formulated.

2 State of the art

This chapter explains the challenges during the design of two-phase feeds and the current state of the art in engineering and science to predict the flow morphologies. Further, the fundamental concepts to predict the void fraction, a key design parameter, are introduced.

Parts of this chapter have been published in:

Döß, A., Schubert, M., Wiezorek, M., Hampel, U., Flegiel, F., Windmeier, C., Schleicher, E. and Schunk, C. (2021). Morphology of Flashing Feeds at Critical Fluid Properties in Larger Pipes. *Chemie Ingenieur Technik* **93**, 1126–1133.

Döß, A., Schubert, M., Hampel, U., Mehringer, C., Geipel, C. and Schleicher, E. (2021). Two-Phase Flow Morphology and Phase Fractions in Larger Feed Line Sections. *Chemie Ingenieur Technik* **93**, 1134–1141.

Döß, A., Schubert, M., Wiedemann, P., Junge, P., Hampel, U., Schleicher, E., Mehringer, C. and Geipel, C. (2021). Flow Morphologies in Straight and Bent Horizontal Pipes. *ACS Engineering Au* **1**, 39–49.

2.1 Two-phase feeds in thermal separation

2.1.1 Feed condition as adjustable parameter

The thermal state q is the number of moles of saturated liquid formed at the feed stage of a separation column per mole feed mixture (Perry et al., 1997). It is commonly represented by the heat required to vaporize one mol of feed ($H_{\text{sat,V}} - H_{\text{F}}$) divided by the latent heat of vaporization ($H_{\text{sat,V}} - H_{\text{sat,L}}$) at feed conditions as

$$q = \frac{H_{\text{sat,V}} - H_{\text{F}}}{H_{\text{sat,V}} - H_{\text{sat,L}}}. \quad 2.1$$

Hanson et al. (1962) and Coker and Ludwig (2010) showed that the calculation of required number of equilibrium stages, reflux and energy demand of the separation depend on q . The following possible feed conditions exist:

- superheated vapor: $q < 0$,
- saturated vapor: $q = 0$,
- two-phase mixture: $0 \leq q \leq 1$,
- saturated liquid: $q = 1$,
- subcooled liquid: $q > 1$.

Accordingly, q also represents the vapor–liquid ratio of the feed mixture that must match the internal vapor and liquid flow rates at feed stage of the separation column.

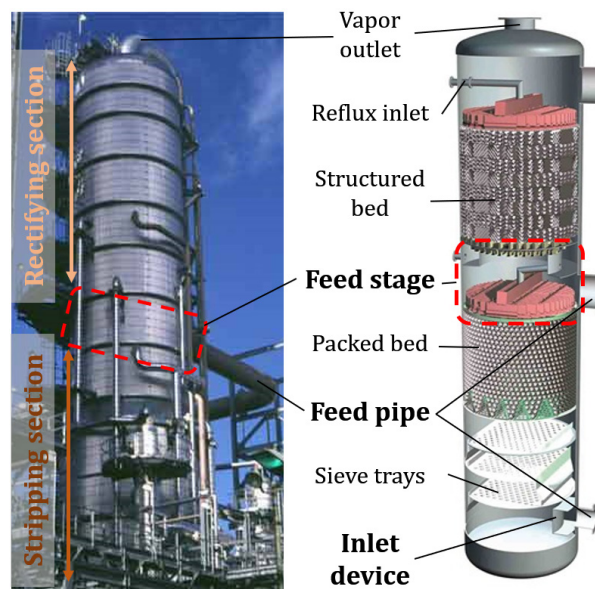


Figure 2.1: Photograph and schematic of a distillation column with exemplary internals (right). Image sources: Gálvez and Iglesias (2003); Sulzer (2019).

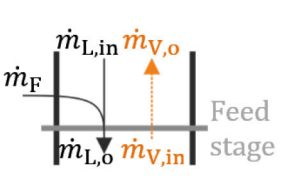
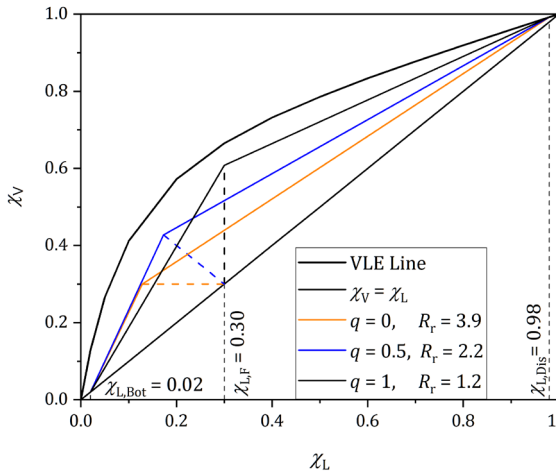
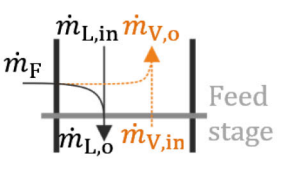
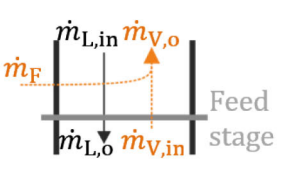
As a consequence of partial vapor condensation, subcooled liquid feed results in lower vapor flow in the rectifying section and increases the liquid flow rate in the stripping section (Figure 2.1). Superheated vapor feed promotes vaporization of liquid and increases the vapor flow in the rectifying section, while it reduces liquid flow in the stripping section. To avoid costly pretreatment or upstream conditioning, $0 \leq q \leq 1$ is commonly accepted (Agrawal and Herron, 1997; Seader and Henley, 2006; Jobson, 2014). Table 2.1 illustrates the three resulting feed conditions and the respective feed distribution in terms of liquid flow \dot{m}_L and vapor flow \dot{m}_V at the feed stage for the separation of the binary methanol/water mixture at various feed conditions.

The embedded McCabe-Thiele chart contains (dotted) “ q -lines”, which separate the (solid) operation lines of the rectifying and stripping sections. The intersection is defined by Hinrichsen (2007) as

$$\chi_V = \frac{q}{q-1} \chi_L + \frac{\chi_{L,F}}{q-1}. \quad 2.2$$

χ_V and χ_L in Equation 2.2 denote the mole fractions of the light key component in vapor and the liquid phase, respectively, and $\chi_{L,F}$ is the material composition of the feed (subscript F).

Table 2.1: Possible feed conditions for thermal separation.

Feed condition	Flow composition at feed stage	Example
Saturated liquid $q = 1$	 $\dot{m}_{L,o} = \dot{m}_{L,in} + \dot{m}_F$ $\dot{m}_{V,o} = \dot{m}_{V,i}$	 <p><i>McCabe-Thiele chart for separation of the binary methanol/water mixture (VLE data at ambient pressure, bottom composition $\chi_{L,Bot} = 0.02$, feed composition $\chi_{L,F} = 0.30$, distillate composition $\chi_{L,Dis} = 0.98$) at various feed conditions for the reflux $R_r = 1.4 \cdot R_{r,min}$.</i></p>
Two-phase mixture $0 < q < 1$	 $\dot{m}_{L,o} = \dot{m}_{L,in} + q \cdot \dot{m}_F$ $\dot{m}_{V,o} = \dot{m}_{V,in} + (1-q) \cdot \dot{m}_F$	
Saturated vapor $q = 0$	 $\dot{m}_{L,o} = \dot{m}_{L,in}$ $\dot{m}_{V,o} = \dot{m}_{V,in} + \dot{m}_F$	

In order to estimate the minimum reflux $R_{r,min}$ at column head, the intersection between q -line and operating lines is determined. The optimal reflux R_r (according to Hinrichsen (2007), R_r is commonly 10 % to 20 % higher than $R_{r,min}$) shifts the intersection away from the VLE-line (see Table 2.1). Subsequently, the number of required theoretical stages can be determined, which provides a first cost estimate. For example, high values for R_r result in high reboiler duties (Blahušiak et al., 2018).

Thus, the impact of q on the total capital expenditure (CAPEX) of distillation processes is evident as explained by Hinrichsen (2007): vapor feeds (high R_r) demand higher operating costs (high energy demand of head condenser and bottom reboiler) but lower investment costs (due to less theoretical stages), while it is vice versa for liquid feeds (low R_r). Accordingly, intermediate values

of q , i.e. two-phase feeds, are the key factor for thermohydraulic optimization in order to satisfy the desired separation efficiency at minimal total costs.

2.1.2 Thermohydraulic optimization

Additional economic considerations – beyond the thermal state of the feed q – define the feed conditions. For example, high steam costs for the reboiler often justifies feed pre-heating or (partial) vaporization as shown by Seader and Henley (2006). Additionally, excess heat recovery may reduce the primary energy consumption and increases the process efficiency (Riese et al., 2020). For example, internally heat-integrated distillation columns (HIDiC, Nakaiwa et al., 2003) rely on the thermal state of the feed as a major tuning parameter. Last but not least, it is simply more feasible to change q in order to account for different reflux, reboiler or condenser duties during column retrofit or revamp. The alternative, namely changing the internal installation arrangement of the columns, i.e. the number of trays or type of packings, is more complicated due to e.g. construction limits (Ghorbani et al., 2013).

Commonly, optimization concepts are assessed via thermodynamic efficiency (TE), i.e. energy consumption required for the desired separation efficiency or purity). TE is either defined as the heat added to the process (for isothermal systems) or in terms of total exergy losses (Carnot efficiency, Cussler and Dutta, 2012). It was shown by Agrawal and Herron (1997) and Bandyopadhyay (2002) that higher TE can be achieved with two-phase feeds for mixtures of high relative volatility (Figure 2.2).

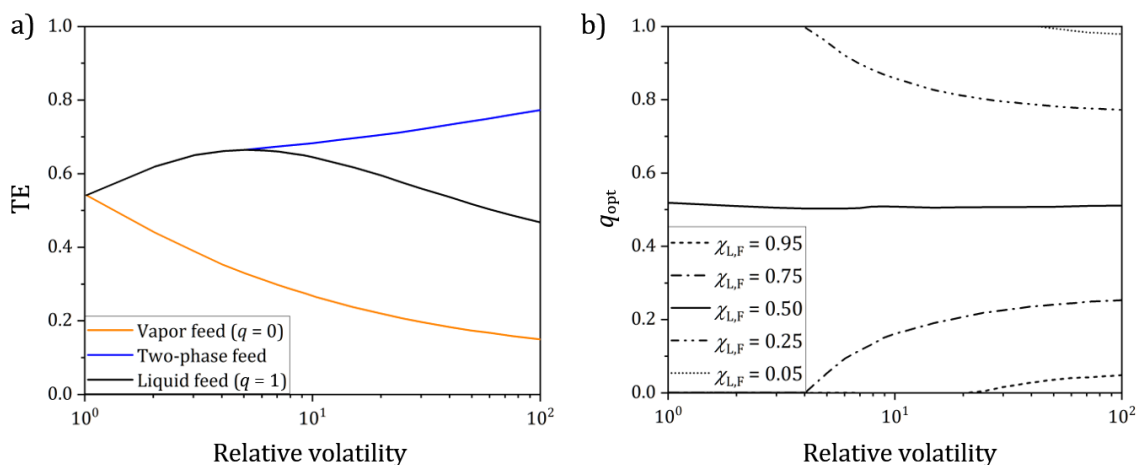


Figure 2.2: a) Thermodynamic efficiency (TE) for saturated feeds and two-phase feeds ($\chi_{L,F} = 0.25$), b) optimal feed condition q_{opt} for various feed compositions $\chi_{L,F}$, adapted from Bandyopadhyay (2002).

Figure 2.2a exemplarily shows that for high relative volatilities, two-phase feeds (blue line) with the optimal feed state q_{opt} can achieve higher TE than saturated feeds (vapor or liquid). However, the optimal thermal state of the feed approaches $q_{opt} = 0$ (saturated vapor) as the feed composition

$\chi_{L,F}$ increases (Figure 2.2b). Consequently, two-phase feeds are applied to satisfy maximum TE. Appendix A.2 lists further thermohydraulic optimization concepts, which utilize two-phase feeds.

2.1.3 Hydrodynamic conditioning

Optimal hydrodynamic conditioning of two-phase feeds targets operational conditions and constructive solutions that supply the feed mixture with minimal disturbances (Henry and Mujtaba, 1999) to the column inlet and that avoid mechanical instabilities (e.g. pipe vibrations, rupture of internals or column shell, additional loads for pipe connecting elements and support structures) and malfunction of sensors installed in the column (Kister, 1990). Disturbances can arise from carry-over of key components into the vapor phase. However, the major concern for feed pipes are undesired flow morphologies or phase interaction phenomena. Costly countermeasures are commonly applied, such as inlet devices, modifications in the pipe routing and additional equipment for droplet separation, as outlined below.

Column entrance: The column entrance connects feed line and feed stage of the column. Static inlet devices are often mounted at the column inside (Kister, 1992). Gas and liquid phases get separated as a result of momentum forces while impacting obstacles (baffles, vane-type inlet devices, flashing feed chambers) or due to centrifugal force introduced by cyclonic inlet devices (vapor horns, cyclones). The selection and sizing of inlet devices (e.g. in terms of phase separation efficiency, pressure loss and material consumption) mostly rely on proprietary experience of the respective vendors (Lee and Binkley, 2011; Koch-Glitsch, 2018) considering

- velocities of the involved phases (flow rates and nozzle diameter),
- degree of mixing of the phases (flow morphology),
- inner column diameter,
- column height required for proper disengagement of the separated phases,
- type of distributor in the column, below and above the feed stage.

In general, the performance of inlet devices depends on the inertia (momentum flux) of the feed (Bothamley, 2013a) as illustrated in Figure 2.3. The term ‘separation performance’ in Figure 2.3 refers to the gas-liquid separation of the inlet devices as well as to the droplet removal capability. It should be noted that the feed inertia is determined by the (averaged) mixture properties, but ignores actual two-phase morphologies and individual phase velocities. The respective operation ranges of the inlet devices in Figure 2.3 are allocated to regions of low to high forces of inertia (gray areas, values taken from AMACS Process Tower Internals, 2020). It is obvious that the selection of inlet devices based on the feed inertia only is very superficial. The development of more elaborated criteria requires performance tests for a wide range of flow morphologies that are encountered in feed pipes (Fair and Humphrey, 1984; Bothamley, 2013a).

Pipe routing: The external routing of the feed pipe strongly determines the two-phase flow morphology entering the column. A high degree of phase pre-separation in the feed line is beneficial (given that the column's feed entrance area can handle it). In particular, intermittent (slug) flow is detrimental (Bothamley, 2013b), since safety margins from 15 % to 40 % are applied during design.

Increasing feed pipe and nozzle diameter is the easiest solution to decrease interphase turbulence and droplet entrainment (Bothamley, 2013a). However, larger pipes increase the piping costs significantly (Nevers, 2005). Considering distillation columns of up to 10 m in diameter and 100 m in height (Mersmann et al., 2011) and feed pipes of 1.5 m diameter (Wehrli et al., 2006), the costs for vessels and piping can contribute up to 40 % of the total plant investment (Couper et al., 2012). Thus, feed pipe designs are an economic compromise considering achievable hydrodynamic conditions, piping costs and expenses for additional separation equipment. Moreover, space restrictions and high connectivity in chemical plants (Kiss, 2013) often require complex pipe routing or multiple feed lines (Lee and Binkley, 2011), where bends, junctions or pipe diameter cause changes in the flow morphology. Guidelines for best practice are provided for example by Moran (2017), where minimal spacing between columns should be 3 m and pipes connecting to elevated nozzles should rise close to the columns shell. Bothamley (2013a) recommends entrance lengths of $L/D \geq 10$.

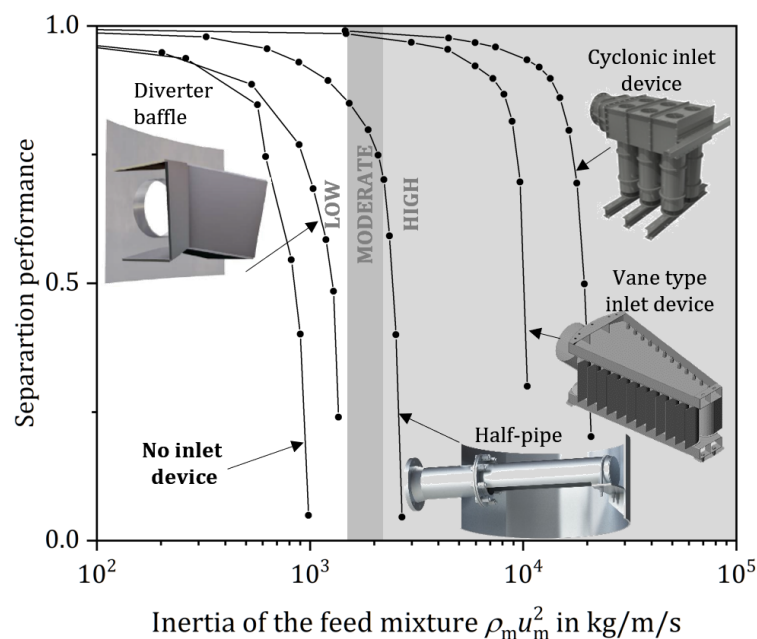


Figure 2.3: Separation performance of inlet devices adapted from Bothamley (2013a). Image sources: half pipe and vane type inlet device – RVT Process Equipment GmbH (2015), diverter baffle – Koch-Glitsch (2018), cyclonic inlet device – Sulzer Ltd (2018).

Droplet separation: Droplet formation and their carryover with the vapor phase limits the column operation. High vapor flow rates in the column of up to 80 % of the speed of sound (Wehrli et al., 2006) carry droplets into the rectifying section. This degrades the overall composition profile of the column and thus, virtually increases the number of required theoretical stages. Droplet carryover causes overhead product contamination, damaging of downstream rotating machinery (Kister, 1992), foaming (Shotton and Habeeb, 1954), deposition and fouling (Kister, 2006) as well as corrosion. Moreover, excessive entrainment limits the performance of tray columns (entrainment flooding) and causes undesired vapor or liquid redistribution in packed columns as discussed by McCabe et al. (1993) and Bennett and Kovak (2000). Droplet formation in two-phase feeds is initiated either by phase interactions due to shear forces (Bothamley, 2013a) or by phase transitions (Pilling et al., 2010; Lee and Binkley, 2011).

If properly designed, inlet devices can capture up to 99 % of the entrained liquid (Pilling et al., 2010). However, re-entrainment at the exit of inlet devices as well as shifts in the droplet size distribution have not yet been in the focus of research (Wehrli et al., 2006; Bothamley, 2013b). Only few inlet devices are capable to separate droplets below 10 μm to 20 μm diameter (Bothamley, 2013b; Sulzer Ltd, 2018), which are prone to carryover and encounter frequently in thermal separation processes (Doherty and Malone, 2001; Flegiel et al., 2021). On the other hand, total separation is often not required and droplet removal rates of 90 % are commonly tolerated (Goedecke, 2006; Mersmann et al., 2011).

2.2 Hydrodynamics of two-phase feeds

Two-phase feeds result either from mixing of gas and liquid single-phase streams or form due to phase change phenomena, such as flash evaporation (Seader and Henley, 2006). They involve complex morphologies of both the continuous phases and the disperse phases governed by pressure gradients as well as viscous and gravitational forces. With increasing distance from the origin (entrance length), the flow morphology becomes increasingly invariant and independent from the axial location. This is called fully developed flow. The performance of inlet devices depends on the momentum of the two-phase mixtures at a given entrance length. Undesired flow morphologies, such as e.g. droplet-laden feeds or slug flow, require specific treatment (Pilling et al., 2010) or should be avoided (Lee and Binkley, 2011), respectively.

2.2.1 Flow morphologies in feed pipes

The evolving flow morphology defines the hydrodynamic duty for the column inlet device. Further, it dictates the efficiency of fluid transport (Baker, 1958), heat transfer processes (Widell, 1949) and chemical reactions (Rouhani and Sohal, 1983) in the pipe. McMillan (1963) defined four categories of factors that determine the flow regime (see Table 2.2).

The allocation of two-phase flows to certain flow morphologies is subject to individual perceptions and depends on proposed criteria, handling of transitional morphologies as well as considered locations (i.e. state of flow development). Visual analysis of two-phase flows allows a qualitative classification of the morphology. Contrary, measurements (e.g. pressure recordings, local or averaged void fractions) provide characteristic signal features that can be directly linked to flow morphologies and allow quantitative allocation (Drahoš and Čermák, 1989). Commonly, probability density functions (PDFs) of measurement signals (pressure or phase fraction) and their statistical moments or transformed signals in the time or frequency domain are employed (Ohlmer, 1984; Franca et al., 1991; Hervieu and Seleglim, 1998; Seleglim et al., 1998; Klein et al., 2004; Mahvash and Ross, 2008; Nguyen et al., 2010; Elperin and Klochko, 2013; Jaiboon et al., 2013; Vieira et al., 2013). More advanced identification methods feature neural networks (Cai et al., 1994; Selli and Seleglim, 2007; Bai et al., 2008; Gao et al., 2013; Al-Naser et al., 2016; Ayegba et al., 2017) or Markov models (Mahvash and Ross, 2008) that are both trained with experimental datasets. Other identification methods rely on characteristic properties of the flow morphology (Ameel et al., 2012) or fuzzy-based methods (Canière et al., 2009; Kipping, 2014; Wiedemann et al., 2019).

Table 2.2: Relevant factors influencing the flow morphologies in horizontal pipes.

Fluid properties	Operational parameters	Piping	External factors
<ul style="list-style-type: none"> ▪ Densities: ρ_G, ρ_L ▪ Viscosities: η_G, η_L ▪ Surface tension: σ 	<ul style="list-style-type: none"> ▪ Flow rates: \dot{V}_G, \dot{V}_L ▪ Flow dynamics (stationary, transient) ▪ Interfacial friction 	<ul style="list-style-type: none"> ▪ Pipe diameter: D ▪ Pipe length: L ▪ Mixing device ▪ Inclination*: θ ▪ Piping elements (e.g. bends) ▪ Surface roughness 	<ul style="list-style-type: none"> ▪ Gravity: g ▪ Vibrations ▪ Heat transfer ▪ Phase change

*In this work, the inclination angle $\theta = 0^\circ$ refers to horizontal flow

Experimental studies of the past century resulted in extensive databases summarized in review articles (Lin, 1985; Drahoš and Čermák, 1989; Cheng et al., 2008; Amaya-Gómez et al., 2019; Hernandez et al., 2019) that are to a great extent limited to pipe diameters $D \leq 200$ mm and to fully developed water-air systems only. The two-phase morphologies result from the acting forces due to gravity (I), axial pressure gradient (II) and interfacial surface tension (III). Quandt (1965) proposed dimensionless numbers based on a balance of the governing forces. As a result, the main flow morphologies for the reference system water-air in horizontal pipes of $D = 200$ mm are classified as shown in Figure 2.4a.

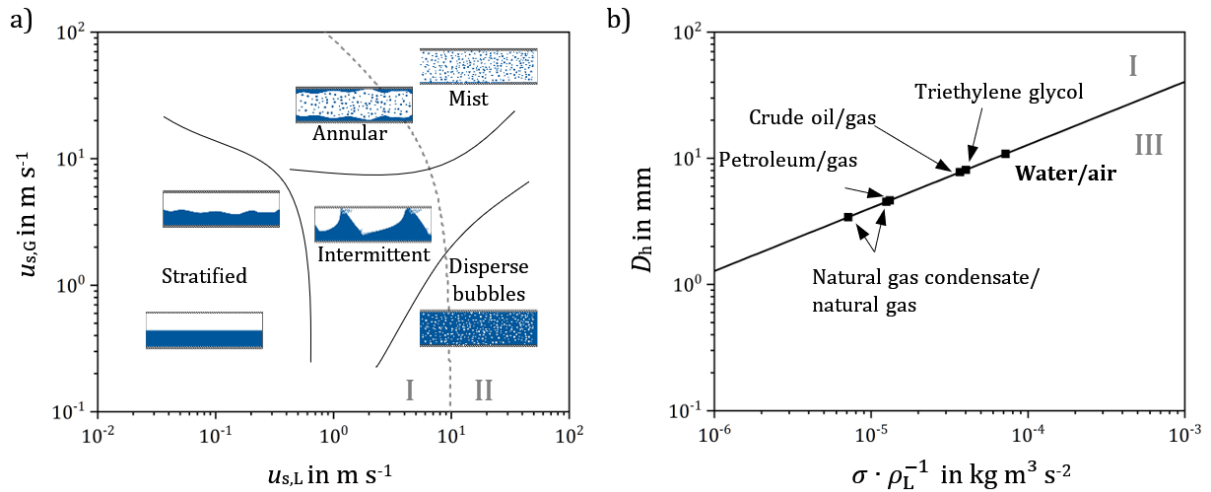


Figure 2.4: a) Ranges of superficial velocities $u_{s,k}$, based on dominant forces due to gravity (I) and pressure drop (II) and b) lower limit for the hydraulic diameters, D_h , below which surface tension (III) governs the flow morphology depending of the fluid properties.

At high superficial fluid velocities, the force due to the axial pressure drop fosters phase dispersion, which causes either bubbly or annular-mist flows. These morphologies are less sensitive to pipe orientation. At lower flow rates, gravity or surface tension forces dominate. Figure 2.4b illustrates that surface tension forces are only significant in small diameter pipes (e.g. $D_h = 11$ mm for water-air flow) and thus can be neglected for commercial feed pipes. Accordingly, gravity dominates the flow morphologies that encounter in larger industrial feed pipes at low flow rates. In particular, evolving intermittent (slug) flow poses a high risk for equipment damage and operation instabilities and should be prevented (Degance and Atherton, 1970b; Lee and Binkley, 2011; Dinaryanto et al., 2017). According to Woods and Hanratty (1999), transition from stratified to intermittent flow (or initiation of intermittent flow) occurs if the average liquid level \bar{h}_L

- (1) exceeds a threshold at which instabilities at the stratified interface can form and grow and
- (2) sustains the continuous liquid pick-up and shedding by front and tail of formed slugs.

While the first criterion describes the regime transition at low to moderate gas-liquid flow rates (see also Section 2.3.2), the second criterion dominates at higher flow rates.

Empirical values proposed in the literature range from $\bar{h}_L/D = 0.5$ (Taitel and Dukler, 1976a) to $0.2 \leq \bar{h}_L/D \leq 0.3$ (Woods and Hanratty, 1996). Woods and Hanratty (1999) studied the location of the slug formation in terms of the liquid phase Froude number

$$Fr_L = \frac{u_L}{\sqrt{g \bar{h}_L}}. \quad 2.3$$

According to their experimental results, intermittent flow will not form at entrance lengths $L/D < 40$ for subcritical flow ($Fr_L < 1$). At higher liquid flow rates, intermittent flow already evolves

for entrance lengths of $4 \leq L/D \leq 12$ (Woods and Hanratty, 1999; Ujang et al., 2006; Woods et al., 2006; Dinaryanto et al., 2017), thus, are crucial for feed pipes of distillation columns.

2.2.2 Droplet entrainment

Droplet entrainment refers to fragmented liquid (mainly in form of droplets) transitioning from the liquid bulk into the gas phase. The fraction of entrained droplets, their sizes and distribution influence the performance of inlet devices. The onset of entrainment (OE), i.e. conditions that feature droplet formation and carryover, is difficult to predict. Moreover, it can hardly be extrapolated from studies with more pronounced entrainment, where the entrained fraction increases nearly linear with the gas velocity (Ishii and Grolmes 1975).

As explained by Levy (1999) much effort has been spent studying heavy entrainment in annular flow. However, experimental data hardly confirmed derived inception criteria for droplet formation, entrainment and carry-over for different flow morphologies. The onset of entrainment occurs for wavy flow morphologies if interfacial shear forces exceed the stabilizing forces resulting from gravity and surface tension. The onset of entrainment depends on the wave characteristics of the bulk and its thickness (referred to as film thickness). Small amplitude ripple waves evolve at low gas velocities, while so called three-dimensional roll waves form at higher gas velocities. The latter are responsible for the onset of entrainment for fluids with low to medium viscosity (Ishii and Grolmes, 1975), however, for high viscosities ($\eta_L > 1.6 \cdot 10^{-2} \text{ Pa}\cdot\text{s}$) entrainment may occur despite the absence of roll waves. Possible mechanisms for droplet entrainment and the conditions, where entrainment happens, were proposed by Hewitt and Hall-Taylor (1970) and Ishii and Grolmes (1975) as shown in Figure 2.5.

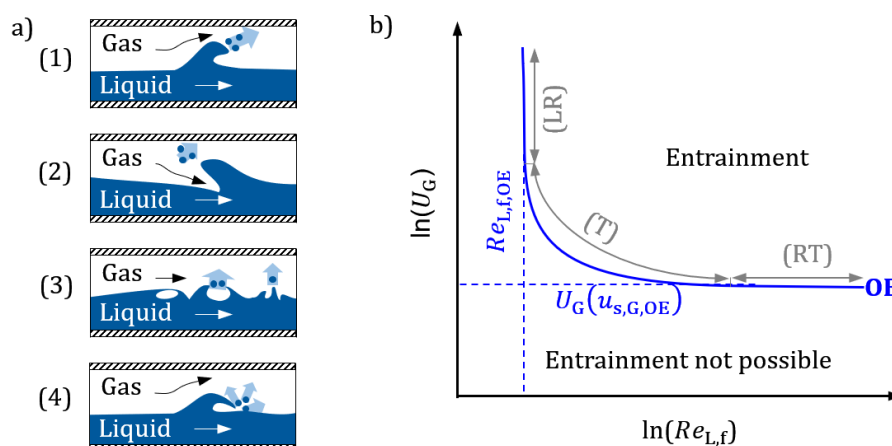


Figure 2.5: a) Mechanisms of droplet entrainment: (1) shear-off, (2) wave undercut, (3) bubble burst, (4) liquid impinging, b) conditions for the onset of entrainment (OE), classified into three entrainment regimes: low Reynolds regime (LR), transition regime (T) and rough turbulent regime (RT).

Figure 2.5a illustrates the four mechanisms of droplet entrainment caused by

- (1) shear-off of droplets from the crests of roll waves,
- (2) undercutting of liquid films by the gas,
- (3) bursting of entrained gas bubbles followed by rupturing of bridging liquid,
- (4) impinging of larger droplets or fragmented liquid on the liquid bulk surface.

These basic mechanisms for the onset of entrainment, however, do not answer the still unresolved question of how the detachment of droplets from the liquid bulk happens (Berna et al., 2014). Bothamley (2013a) concluded that the shear-off of roll waves is the main mechanism in many separation applications. Figure 2.5b demarcates the region (conditions) of possible entrainment (OE, blue line), which basically depends on the dimensionless gas velocity U_G and on the liquid film Reynolds number $Re_{L,f}$.

According to Ishii and Grolmes (1975), the dimensionless gas velocity U_G is defined as

$$U_G = u_{s,G} \frac{\eta_L}{\sigma} \sqrt{\frac{\rho_G}{\rho_L}}. \quad 2.4$$

The film (index f) Reynolds number is characterized by the average liquid height \bar{h}_L according to

$$Re_{L,f} = \frac{4 u_{L,f} \rho_L \bar{h}_L}{\eta_L} = \frac{u_{s,L} \rho_L D_h}{\eta_L}. \quad 2.5$$

The corresponding average liquid film velocity $u_{L,f}$ can be expressed (Berna et al., 2014) as

$$u_{L,f} \approx \frac{D_h}{4\bar{h}_L} u_{s,L,f} = \frac{D_h}{4\bar{h}_L} (1 - w_E) u_{s,L}. \quad 2.6$$

For horizontal two-phase flow, the film thickness varies with the circumferential angle (Paras and Karabelas, 1991a), which reduces the available surface area for the origin of entrainment. The experimental study of Paras and Karabelas (1991b) confirmed that entrainment occurs in the lower pipe half only at low gas velocity, while at higher gas flow rate, the whole pipe circumference contributes to entrainment.

Ishii and Grolmes (1975) determined the physical limit (minimum film Reynolds number at the onset of entrainment $Re_{L,f,\min}$), for which liquid film and gas chore have full dynamic interactions, as

$$Re_{L,f,\min} = \left(\frac{y^+}{0.347} \right)^{1.50} \left(\frac{\rho_L}{\rho_G} \right)^{0.75} \left(\frac{\eta_G}{\eta_L} \right)^{1.50}. \quad 2.7$$

Here, y^+ is the dimensionless distance of the film surface from the wall. Reported values differ between $y^+ = 10$ (Ishii and Grolmes, 1975) and $y^+ = 30$ (Azzopardi, 1997).

Table 2.3: Predictive correlations for U_G and $Re_{L,f,OE}$ for varying entrainment regimes.

Regime	Range of $Re_{L,f}$	Predictive correlations	Equation	Comment	Reference	
LR	$Re_{L,f} = Re_{L,f,OE}$	$U_G \geq 1.5 Re_{L,f}^{-0.5}$	2.8	Corresponds to $17 < We < 22$, valid for entrainment caused by wave undercut.	Ishii and Grolmes (1975)	
		$Re_{L,f,OE} = 13N_\eta^{-0.5}$	2.9	Valid for entrainment caused by shear-off. For water-air mixtures (25°C, 1 bar(a)), $N_\eta = 2 \cdot 10^{-3}$ and Equation 2.9 yields $Re_{L,f,OE} = 291$.	Sawant et al. (2009)	
		with $N_\eta = \eta_L \left(\rho_L \sigma \sqrt{\frac{\sigma}{g(\rho_L - \rho_G)}} \right)^{-\frac{1}{2}}$	2.10	The viscosity number, N_η , compares the viscous force induced by the internal flow with the surface tension force Ishii and Grolmes (1975).		
TR	$160 < Re_{L,f} < 1635$	$U_G > \begin{cases} 11.78 N_\eta^{0.8} Re_{L,f}^{-1/3} & \text{for } N_\eta \leq 1/15 \\ 1.35 Re_{L,f}^{-1/3} & \text{for } N_\eta > 1/15 \end{cases}$	2.11		Ishii and Grolmes (1975)	
		$7.5 > Ku > 3.2$	$Ku = 7.97 - 0.00292 Re_{L,f}$	2.12	The Kutateladze number, Ku , approximates the minimum gas velocity at OE	Epstein, 1990; Berna et al., 2014
			with $Ku = \frac{\rho_L^{0.5}}{((\rho_L - \rho_G)g\sigma)^{0.25}} \cdot u_{s,G,OE}$	2.13		Oliemans and Pots (2005)
RT	$Re_{L,f} > 1635$	$U_G > \begin{cases} N_\eta^{0.8} & N_\eta \leq 1/15 \\ 0.1146 & N_\eta > 1/15 \end{cases}$	2.14		Ishii and Grolmes (1975)	
		$u_G - u_L = \frac{C_S \sigma}{C_D C_r \rho_G} + \sqrt{\left(\frac{C_S \sigma}{C_D C_r \rho_G} \right)^2 + \frac{\pi \lambda_W \rho_L \sin(\theta)}{4 C_D \rho_G}}$ with $C_D = 0.95$ and $C_S = 0.77$	2.15	The viscosity term C_r depends on interfacial friction factor, film Reynolds number and N_η .	Mantilla, 2008; Mantilla et al., 2009a, 2009b	
Universal	-	$5.5 < We_c$	2.16	Requires knowledge of the height of the disturbance waves $h_{L,W}$ and relative superficial velocity, $u_{s,rel}$.	Paras and Karabelas (1991b)	
		with $We_c = \frac{\rho_G u_{s,rel} h_{L,W}}{\sigma}$	2.17			

For water-air mixtures, Equation 2.7 then yields $72 \leq Re_{L,f,\min} \leq 376$ for both values of y^+ , respectively. However, literature values for $Re_{L,f,\min}$ scatter significantly according to Azzopardi (1997) and Berna et al. (2014). For example, Andreussi et al. (1985) reported the formation of roll waves caused by the gas phase at low film Reynolds numbers $Re_{L,f,\min} = 95$.

The onset of entrainment is typically divided into three regimes (see gray labels in Figure 2.5b). In the low Reynolds regime (LR), roll waves (1) disappear and wave undercut (2) dominates until the liquid films break into the more stable configuration of multiple rivulets across the pipe circumference (Ishii and Grolmes, 1975). The rough turbulent regime (RT) describes the onset of entrainment at high film thickness and minimum gas velocity $U_{G,\min}$. In the transition region (TR), U_G is expressed as a function of the film Reynolds number. Table 2.3 presents numerical values for the boundaries between the entrainment regimes (taken from Ishii and Grolmes, 1975; Berna et al., 2014; Oliemans and Pots, 2005) and existing correlations for U_G and $Re_{L,f,OE}$.

For insufficient entrance length, the onset of entrainment is strongly dependent on the upstream pipe geometry, e.g. smoothness, abruptness and design of the mixing device that may induce additional entrainment. The expansion of the gas phase and the acceleration of the flow due to the pressure drop along the feed pipe also influences the interfacial shear, causing onset of entrainment (Ishii and Mishima, 1981). Accordingly, the passage of the respective phases and the film thickness vary along the pipe and stationary entrainment, where entrained and deposited liquid are equal, is reached at entrance lengths of $100 \leq L/D \leq 600$ (Dallman, 1978). Henry (2016) obtained the OE (in terms of U_G) by linear extrapolation from measurements at $3.8 \leq L/D \leq 11$ in a test section of 240 mm diameter. Contrary, Mantilla (2008) obtained lower gas velocities for the OE for developed flow at larger ratio of pipe length and diameter $L/D = 240$ in a pipe of 150 mm diameter. However, it is unclear whether these difference in $U_{G,OE}$ arise from the different measurement methods or from different pipe diameters and entrance lengths.

2.2.3 Flow regime maps

Flow regime maps define regions of similar flow features and demarcate those regions from each other with distinct transition lines or transition areas. Such maps are mostly derived from experimental studies, e.g. analyzing the flow morphologies for a large matrix of superficial gas and liquid flow rates (according to Hernandez et al. (2019), more than 27,670 experiments from 9,200 different studies are available). Reversely, flow regime maps are engineering tools used to anticipate the expectable flow morphology for a given set of superficial gas and liquid flow rates. Many adiabatic flow regime maps were proposed, whose respective peculiarities and pros and cons have been summarized in comprehensive reviews papers (e.g. Vohr, 1960; Nguyen, 1975; Rouhani and Sohal, 1983; Lin, 1985; Cheng et al., 2008; Corral, 2014). Additionally, online tools with graphical user interfaces have been provided for flow regime determination based on such

maps (<https://doi.org/10.14278/rodare.1531>, <http://two-phase-flow.ic.cz/>). The variety of flow regime maps ranges from maps limited to e.g. certain ranges of superficial velocities or volumetric flow rates to more versatile maps that feature

- scaling parameters for fluid properties (e.g. Baker, 1954; Mandhane et al., 1974),
- dimensionless numbers instead of net flow rates as axis designation (e.g. Oliemans and Pots, 2005; Spedding et al., 2008),
- scaling correlations for individual regime transitions (e.g. Weisman et al., 1979),
- fully mechanistic approaches (e.g. Taitel et al., 1978; Kind and Wetzel, 2018) in combination with the stability analysis as summarized in Section 2.3.2.

Flow regime maps were mainly derived for fully developed flows, and thus, have limited validity for complex pipe systems and short pipe length (Abdulkadir, 2011). Moreover, there is still no commonly accepted universal flow regime map that stands out from the rest. Considerable discrepancies exist for flow morphology predictions in larger pipes, as discussed by Weisman et al. (1979), Laurinat (1982), Ebner et al. (1987) and Kokal and Stanislav (1987), or for fluid properties deviating from air-water mixtures (Weisman et al., 1979). Despite plenty of research on flow morphologies and regime maps in the past century, there are no commonly accepted axes designations and no universal criteria to distinguish flow regimes, not to mention the variety and accuracy of underlying data, analyses and measurement methods. Same holds for the number of different morphologies. For example, Wong and Yau (1997) distinguished 45 different peculiarities, while more recent studies consider only the five main morphologies proposed by Alves (1954).

Figure 2.6 superimposes existing flow regime maps (Lin and Hanratty, 1987; Ghajar and Tang, 2007) and predictive criteria for the onset of entrainment (see Table 2.3) in order to emphasize the uncertainties that occur during the engineering of two-phase feeds. The axes designation follows Ghajar and Tang (2007), who assigned Reynolds numbers obtained from mass fluxes and all transitions are valid for a pipe diameter of $D = 25$ mm. Both maps predict the transition to annular flow with reasonable agreement. Due to the significantly longer inlet length ($L/D = 600$), Lin and Hanratty (1987) mapped intermittent flows even at lower gas-liquid flow rates, while stratified flows were observed by Ghajar and Tang (2007) at $L/D = 100$. Only very few flow regime maps account for additional phenomena such as e.g. droplet entrainment. Instead, the onset of entrainment from experimental studies and from the models presented in Table 2.3 are presented in Figure 2.6 by transition lines (blue). It is obvious that the predictive models cannot reproduce the experimentally determined values of Davis (1969) and Lin and Hanratty (1987). Since the onset of entrainment occurs in wavy flow, the assignment to the annular regime according to the flow maps indicates the predictive models (solid blue lines) overestimate the required gas

velocity. Consequently, the design of a commercial two-phase feeds (larger pipe diameter, different fluid properties) can hardly rely on such heuristic tools, which can – at best – be considered as a conservative estimate.

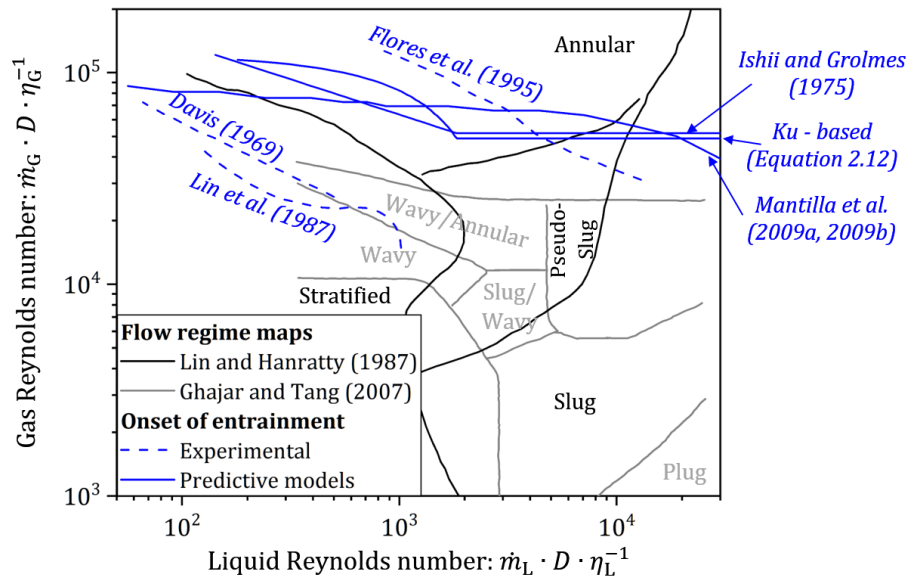


Figure 2.6: Superimposed flow regime maps from literature for water-air mixtures in pipes with $25 \leq D \leq 28$ mm and predictions for the onset of entrainment (blue dashed lines: based on experiments; blue solid lines: predictive criteria from Table 2.3).

2.2.4 Consequences for two-phase feeds

Short entrance lengths of commercial feed lines can cause ill-defined states of two-phase feeds entering the column. Hydrodynamics and flow inertia are governed by upstream feed pipe geometries and devices (mixing or inlet devices, curvatures, constrictions, junctions etc.) as well as thermodynamic effects (e.g. phase changes, depressurization, heat transfer).

Gas expansion due to pressure losses along the feed pipe continuously accelerates the mixture (Ishii and Mishima, 1981) and changes the hydraulic diameters of both phases, and thus, the dynamics and interactions between both phases. Moreover, even for a straight pipe, flow structures (e.g. interfacial area, dispersed fractions, length, amplitude and frequency of waves and characteristic features) and velocity profiles can continuously change (Kocamustafaogullari and Huang, 1994) along several hundreds of pipe diameters (Dallman, 1978; Nydal et al., 1992; Woods et al., 2006). In other words, the term ‘steady state’ for the flow in feed pipes of finite length is a precarious simplification as discussed by Sakaguchi et al. (1987) and Kocamustafaogullari and Huang (1994).

Available empirical studies (Butterworth, 1972; Kocamustafaogullari and Huang, 1994; Warren and Klausner, 1995; Sakamoto et al., 2004; Ujang et al., 2006; Tkaczyk and Morvan, 2011;

Bottin et al., 2014; Abdulkadir et al., 2016; Zhao et al., 2017; Kong et al., 2018b) for adiabatic systems have confirmed that the formation of characteristic features of the respective flow morphologies requires pipe lengths of at least $40 \leq L/D \leq 80$. Experimental studies with short entrance lengths addressed mainly small pipe diameters, e.g. $D = 25$ mm (Salcudean et al., 1983) or $D = 3$ mm (Zeguai et al., 2013). Studies in large diameter pipes (e.g. $D \approx 200$ mm by Simpson et al., 1981; Hori et al., 1985; Wu et al., 1987; Anoda et al., 1989; Koizumi et al., 1990) were obtained for entrance lengths $45 \leq L/D \leq 145$. However, such long feed pipes are hardly met in commercial practice.

Concerns during the design of two-phase feeds are the formation and entrainment of droplets and the appearance of intermittent flow (see above). Both can be prevented using tailored column entrance designs or specific inlet devices. However, the inception of intermittent flow depends not only on the superficial gas-liquid flow rates but also on the entrance length (Dinaryanto et al., 2017), i.e. in short feed pipes intermittent flows will occur only for increased flow rates. Thus, two-phase feeds may be operated at higher flow rates compared to longer pipes (more developed two-phase flows). Hitherto, the only available model that predicts flow morphology and void fraction for arbitrary entrance lengths, is based on a stability analysis of the two-fluid model (TFM). The governing equations and fundamentals of the model are summarized in Sections 2.3. and 2.3.3.

Subsequently, superpositioning the regime transitions predicted by the TFM with the predictive criteria for the onset of entrainment (see Table 2.3) and available theories for the inception of intermittent flow (see Section 2.2.1) results in the advanced flow map in Figure 2.7 that summarizes the main challenges during the design of two-phase feeds. Such combination of existing approaches has been illustrated for the first time.

Although all models for the onset of entrainment in Figure 2.7 are not validated for short entrance lengths, the model of Mantilla (2009b) was compared with data obtained for large pipe diameters, and thus, was used to identify regions where droplet separation will be required for the two-phase feed. The inception of intermittent flow at high gas velocities is linked to an average liquid level, however, since no experimental proof exists, $\bar{h}_L/D = 0.5$ can be considered as a sufficiently conservative criterion. The transitions obtained by the TFM for arbitrary entrance lengths agree reasonable well with the experimental data of Hori et al. (1985) that were obtained for a pipe with $D = 200$ mm at similar L/D . Note that for commercial entrance lengths ($L/D = 5$) the TFM yields a more conservative solution. To avoid extensive modelling required by the TFM, the Froude number criterion of Woods and Hanratty (1996) may be used as an approximation. As stated by the authors, their criterion overpredicts the inception of intermittent flows for fully developed flows in terms of liquid superficial velocities at lower gas velocities.

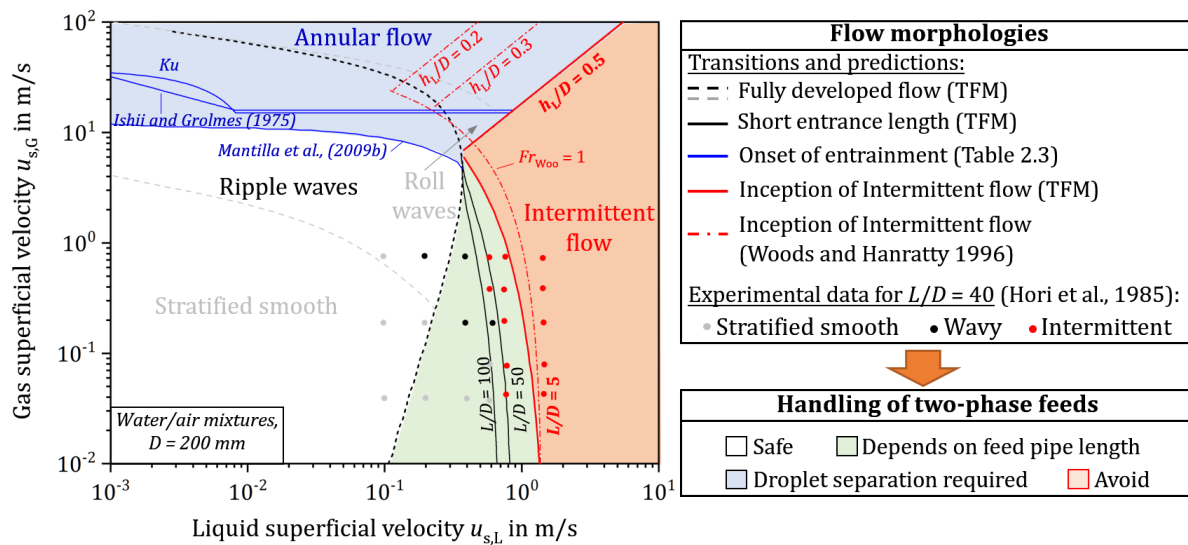


Figure 2.7: Handling of two-phase feeds (colored background) with short entrance lengths (typically $L/D = 5$, other lengths are shown as reference) as a consequence of flow morphology transitions (predicted with the TFM for $D = 200$ mm, water-air systems), onset of entrainment and inception of intermittent flows (Section 2.2.1).

CAPEX as well as space restrictions determine the pipe routing in chemical plants, which typically result in small pipe diameters and complex pipe arrangements upstream of feed inlet devices in distillation columns. Cost-optimized narrow feed pipes in turn, can lead to material stress, abrasion, unstable and pulsating flows as well as detrimental phase dispersions, caused by turbulent interactions between phases at high low rates. The influence of non-straight pipe configurations on the flow morphologies of two-phase feeds is yet hardly addressed in popular distillation design books of Kister (1990, 1992), Perry et al. (1997), Goedecke (2006), Speight (2011), Kiss (2013), Górak and Olujic (2014) and Górak and Schoenmakers (2014).

Experiments with various elements of commercial pipe routing were reviewed by Azzopardi and Sudlow (1993). Studies with various pipe geometries involving diameter expansions (Ahmed et al., 2008), contractions (Roul and Dash, 2011), junctions (Azzopardi, 1989, 1999; Azzopardi and Wren, 2004; Baker et al., 2007), helical coils (Banerjee et al., 1967; Naphon and Wongwiset, 2006; Vashisth and Nigam, 2008, 2009; Wang et al., 2016), S-shaped bends (Mazhar et al., 2014), mitre elbows (Al-Tameemi and Ricco, 2019) or pipes with internal structures (Benbella et al., 2009; Eyo and Lao, 2019) were performed in the past. The morphology changes (referred to as 'secondary flow') from inlet to outlet of curvatures is governed by centrifugal force, buoyancy and gravity. According to Hsu et al. (2015), the centrifugal force accelerates the mixture in the concave region of the curvature; at same time, the fluid decelerates in the convex region. The strength of the secondary flow in the bend, which determines the boundary layer thickness and the occurrence of vortices and swirly flows, is represented by the Dean number De (Azzi and Friedel,

2005; Tiwari et al., 2006; Motamedian et al., 2007; Saffari et al., 2014). The Dean number is the ratio of centrifugal and inertia forces to gravity expressed as

$$De_{\text{Bend}} = Re \sqrt{\left(\frac{D}{2R}\right)}. \quad 2.18$$

The ratio of centrifugal force to gravity is considered in the modified Froude number (Pietrzak and Witczak, 2013; Pietrzak, 2014) as

$$Fr_{\text{L,Bend}} = \frac{u_{\text{L}}^2}{gR}, \quad 2.19$$

where R is the bend radius. Higher numbers of vortices at high Dean numbers (Equation 2.18) increase the recovery length needed to retain the initial flow morphology (Saffari et al., 2014). Available empirical correlations properly predict the two-phase pressure drop (Mandal and Das, 2001; Sánchez Silva et al., 2010; Hsu et al., 2015) of straight pipe configurations. Contrary, no comprehensive study exists on the afore mentioned recovery length. $Fr_{\text{L,Bend}} > 1$ (Equation 2.19) indicates that liquid climbs at the outer wall of the bend, while the gas accumulates at the inner wall of the bend. Curvatures with small radius and high centrifugal forces have a strong influence on the flow morphology (Gardner and Neller, 1969). High void fractions, however, reduce centrifugal force and vorticity, while the turbulence increases (Saffari et al., 2014). De_{Bend} and $Fr_{\text{L,Bend}}$ were successful applied to up- or downward oriented curvatures. However, no comparable formulation is currently available for horizontal curvatures.

Available experimental data are limited to curvature radii $R/D > 1.3$ (Mandal and Das, 2001), pipe diameters in the range of $3 \text{ mm} \leq D \leq 76 \text{ mm}$ (Wang et al., 2004; Motamedian et al., 2007; Kesana et al., 2013) and curvature angles between 45° and 180° (Mandal and Das, 2001; Autee and Giri, 2016), however, flow morphologies were only analyzed at few flow rates. Details on the influence of horizontal curvatures on flow morphologies obtained from experiments are provided in Appendix A.3.

The effects of horizontal bends on the flow morphology, e.g. flow reversal (Hsu et al., 2015) are less compared with vertical bends. The use of curvatures as pre-separator was also discussed in the literature by James et al. (2000) and Pietrzak (2014), which would add a degree of freedom for the design of two-phase feed pipes for distillation columns. Moreover, larger entrained droplets were observed downstream horizontal bends (Ribeiro, 1993; Ribeiro et al., 1995, 2001), which increases the separation efficiency (Bothamley, 2013b) of inlet devices (see Section 2.1.3).

2.3 Modelling of two-phase feeds

In order to predict or simulate two-phase feeds properly, modeling of the governing two-phase flow phenomena is required. A fully three-dimensional modelling, which is possible through Computational Fluid Dynamics (CFD) approaches, would be desirable for tailored pipe routing and design of inlet devices. However, since CFD codes for transient two-phase flow are still not sufficiently developed, reduced-order models (1D or 2D approximations of the two-phase flow) are used instead. Two-fluid models feature more complex formulations and governing equations for each phase. Mechanistic models can predict flow morphology transitions, transient flows as well as developing flows. Single-phase or hybrid methods and approximations for the two-phase mixture and analytical models enable easy calculation of crucial design parameters, such as void fraction (Shoham 2006).

2.3.1 Basic definitions

Reduced-order models discretize and average three-dimensional flow morphologies and their steady state or transient properties in order to obtain 1D or 2D flow approximations. The thermodynamic state of the two-phase feed q (Equation 2.1) is equivalent to the liquid mass fraction w_L expressed by mass flow rate \dot{M}_k or mass flux $\dot{m}_k = \dot{M}_k/A$ of the respective phase (phase indicator k) as

$$q = w_L = \frac{\dot{M}_L}{\sum_k \dot{M}_k} = \frac{\dot{m}_L}{\sum_k \dot{m}_k}. \quad 2.20$$

Pressure and temperature variations (phase interactions, frictional pressure drop) along the feed pipe affect the gas and liquid densities for constant mass fractions and accelerate or decelerate the fluids (Ishii and Mishima, 1981; Kocamustafaogullari and Huang, 1994; Kong et al., 2018b). Thus, the volumetric gas fraction (further referred to as void fraction) α_G is preferably considered in predictive tools and design standards (e.g. VDI, 2013). α_G is defined as

$$\alpha_G = \left[1 + \left(\frac{1 - w_G}{w_G} \right) \left(\frac{\rho_G}{\rho_L} \right) \right]^{-1} = \frac{A_G}{A_G + A_L}, \quad 2.21$$

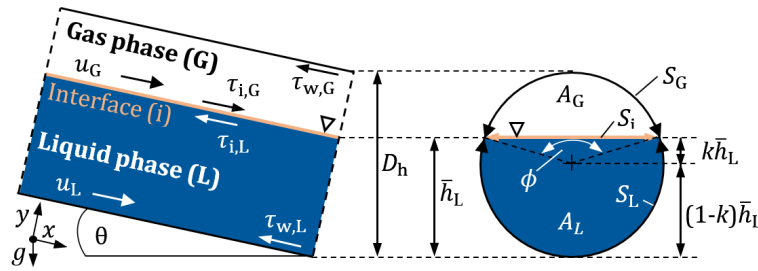
where A_G and A_L refer to the passage of the pipe cross-section occupied by the respective phase (Butterworth, 1975). Some flow morphologies correspond to certain characteristic void fraction ranges, e.g. $\alpha_G \rightarrow 0$ for bubbly flow and $\alpha_G \rightarrow 1$ for annular flow (Thome and Cioncolini, 2015).

For a flat interphase, void fraction and dimensionless liquid level $h_L = \bar{h}_L/D$ are linked (Kawaji, 2018) as

$$\alpha_G = \frac{1}{\pi} \left(\arccos(2h_L - 1) - (2h_L - 1) \sqrt{1 - (2h_L - 1)^2} \right). \quad 2.22$$

However, literature studies rarely specify whether measured void fraction data refer to local phase densities, values averaged along the pipe or to inlet conditions (assuming constant phase density). Thus, knowledge of void fraction or average liquid level \bar{h}_L in pipes is sufficient to derive the governing geometrical parameters for a circular conduit (Brauner and Maron, 1991, 1992; Sadatomi et al., 1993; Taitel and Dukler, 1976; Taitel et al., 1978) as shown in Table 2.4.

Table 2.4: Geometrical parameters and their relation to the liquid level \bar{h}_L for stratified flow with horizontal interface.



Parameter	Symbol	Relationship
Liquid level	\bar{h}_L	-
Centroid angle	ϕ	$2 \cos^{-1} \left(1 - 2 \frac{\bar{h}_L}{D} \right)$
Elevation parameter	k	$\frac{[\cos(\phi) \cdot (\pi - \phi) + \sin(\phi) - \sin^3(\phi/3)]}{[(1 + \cos(\phi))(\pi - \phi + \sin(\phi) \cdot \cos(\phi))]}$
Gas phase cross-section	A_G	$\frac{D^2}{4} \left(\cos^{-1} \left(2 \frac{\bar{h}_L}{D} - 1 \right) + \left(2 \frac{\bar{h}_L}{D} - 1 \right) \sqrt{1 - \left(2 \frac{\bar{h}_L}{D} - 1 \right)^2} \right)$
Liquid phase cross-section	A_L	$\frac{D^2}{4} \left(\pi - \cos^{-1} \left(2 \frac{\bar{h}_L}{D} - 1 \right) + \left(2 \frac{\bar{h}_L}{D} - 1 \right) \sqrt{1 - \left(2 \frac{\bar{h}_L}{D} - 1 \right)^2} \right)$
Gas phase perimeter	S_G	$D \left(\cos^{-1} \left(2 \frac{\bar{h}_L}{D} - 1 \right) \right)$
Liquid phase perimeter	S_L	$D \left(\pi - \cos^{-1} \left(2 \frac{\bar{h}_L}{D} - 1 \right) \right)$
Length of the interface	S_i	$D \left(\sqrt{1 - \left(2 \frac{\bar{h}_L}{D} - 1 \right)^2} \right)$
Gas phase hydraulic diameter	$D_{h,G}$	$\frac{4A_G}{S_G + S_i}$
Liquid phase hydraulic diameter	$D_{h,L}$	$\frac{4A_L}{S_L}$

Many phenomenological models rely on the geometrical relations given in Table 2.4 for model formulations and definitions of inception criteria for the most relevant flow morphologies. Other

geometries are proposed for specific stratified flow morphologies, such as the double-circle model for thin spreading liquid films and film wall climbing (Ahn et al., 2018; Chen et al., 1997) or models to account for the transition from flat to concave or convex bulk interphases (Deendarlianto et al., 2019; Ullmann and Brauner, 2006).

In reduced-order models, fictitious phase velocities (1D) are applied instead of the full 3D velocity field, thereby neglecting temporal fluctuations, transverse and rotational phase motion (i.e. constant pressure across each plane according to Sonnenburg (1991). Accordingly, the mass conservation for steady-state conditions at each cross-section of the pipe (Taitel and Dukler, 1987; Taitel et al., 1989) yields

$$\rho_k u_k A_k = \rho_k u_{s,k} A = const, \quad 2.23$$

where u_k refers to the effective velocity, depending on the occupied cross-section A_k of each phase and the superficial velocity (index s) is the phase velocity when the whole pipe cross-section is occupied by one single phase.

2.3.2 Fundamentals of the two-fluid model

This section briefly introduces the fundamentals of the most popular 1D formulation of the two-fluid model (TFM) for horizontal pipe flows (Barnea and Taitel, 1994; Taitel and Dukler, 1976; Taitel et al., 1978). The extended formulation that considers axial flow development in terms of an interfacial level gradient is presented in Section 2.3.3.

In general, two-fluid models involve conservation equations separately for each phase and include mechanistic formulations for particular flow phenomena (Shoham, 2006). Due to their complex formulation, numerical solutions are often required to cope with the complex formulations. Such solvers can be found e.g. in system codes, such as RELAP-5, (Rouhani and Sohal, 1983; RELAP5 Development Team, 1995), OLGA (Bendiksen et al., 1988, 1991), CATHARE (Bestion, 1990), TRACE (2008), NEPTUNE (Morel et al., 2004; Bottin et al., 2014), WCOBRA/TRAC-TF2 (Liao et al., 2015) and ATHLET (Austregesilo et al., 2016).

The governing equations are the 1D conservation of mass

$$\frac{\partial(\rho_k A_k)}{\partial t} + \frac{\partial(\rho_k u_k A_k)}{\partial z} = 0 \quad 2.24$$

and momentum

$$\begin{aligned} \frac{\partial(\rho_k A_k u_k)}{\partial t} + \frac{\gamma}{2} \frac{\partial(\rho_k A_k u_k^2)}{\partial z} + \rho_k A_k g \left(\cos \theta \frac{\partial \bar{h}_L}{\partial z} + \sin \theta \right) + A_k \left(\frac{\partial p}{\partial z} \right)_{tp,k} \\ + \tau_{w,k} S_{w,k} \pm \tau_{i,k} S_{i,k} = 0. \end{aligned} \quad 2.25$$

The right-hand-side of both equations indicates adiabatic flow condition with mass transfer terms equal to zero. The geometrical parameters are obtained according to Table 2.4.

$(\partial p/\partial z)_{tp,k}$ in Equation 2.25 is the two-phase (index tp) pressure gradient along the pipe. γ refers to the kinetic energy correction term introduced by Bishop and Deshande (1986) and Li et al. (2013) that accounts for the liquid phase rheology in a completely filled circular tube according to

$$\gamma = \frac{(2n' + 1)(5n' + 3)}{3(3n' - 1)^2}. \quad 2.26$$

Here, n' is the flow behavior index of a power law fluid ($\tau = K_1 \dot{\gamma}^{n'}$). For Newtonian fluids, $K_1 = \eta$ and $n' = 1$ apply, which leads to $\gamma = 2$. The kinetic energy correction term for the gas phase γ_G is negligible (Li et al., 2013).

Since A_k is a function of the liquid level h_L , combining Equations 2.24 and 2.25 yields a single equation (Taitel and Dukler, 1976) for a specified design point of the two-phase feed (input flow rates, fluid system and pipe geometry). Thereby, a constant liquid level along the pipe is assumed ($\partial \bar{h}_L/\partial z = 0$), which holds only for fully developed flows. For an incompressible steady-state flow ($\rho_k = const, \partial/\partial t = 0$) in a horizontal feed line, Equations 2.24 and 2.25 can be rearranged into

$$u_k \frac{\partial \bar{h}_L}{\partial z} + A_k \left(\frac{\partial A_k}{\partial h_L} \right)^{-1} \frac{\partial u_k}{\partial z} = 0 \quad 2.27$$

and

$$\frac{1}{A_k} \left(\gamma A_k u_k \frac{\partial (u_k)}{\partial z} + g A_k \frac{\partial \bar{h}_L}{\partial z} \right) = -\frac{1}{\rho_k} \left(\frac{\partial p}{\partial z} \right)_k - \frac{\tau_{w,k} S_{w,k}}{\rho_k A_k} \mp \frac{\tau_{i,k} S_{i,k}}{\rho_k A_k}. \quad 2.28$$

Taitel et al. (1978) showed that the derivative of A_k in Equation 2.27 is

$$\frac{\partial A_k}{\partial h_L} = A'_k = D \sqrt{1 - (2h_L - 1)^2}. \quad 2.29$$

The wall shear stresses $\tau_{w,k}$ is defined as

$$\tau_{w,k} = f_{f,k} \frac{\rho_k u_{s,k}^2}{2} \quad 2.30$$

with

$$f_{f,k} = 0.046 (Re_{s,k})^{-0.2} = 0.046 \left(\frac{D_{h,k} u_{s,k}}{\mu_k} \right)^{-0.2}, \quad 2.31$$

which is the friction factor of phase k. The constant values in Equation 2.31 were derived by Taitel and Dukler (1976a) for turbulent flows and are commonly accepted. Contrary, many empirical

correlations exist to determine the interfacial friction factor (Taitel et al., 1989; Essaied, 1992), whose predicted phase fractions scatter significantly as discussed by Omgba-Essama (2004). The most popular correlations are given in Table 2.5.

Table 2.5: Commonly applied terms for interfacial shear and interfacial friction factor in the TFM.

$\tau_{i,k} =$	$f_{f,i} =$	Comment	Reference
$f_{f,i} \frac{\rho_G(u_G - u_i)^2}{2}$	$f_{f,G}$	Assuming $u_G \gg u_i$	(Taitel and Dukler, 1976)
$f_{f,i} \frac{\rho_G(u_G - u_L) u_G - u_L }{2}$	$\max(f_{f,G}, 0.014)$	Accounts for the direction change of $\tau_{i,k}$ for $u_G < u_L$ (Barnea, 1991)	(Barnea and Taitel, 1994; Taitel and Barnea, 2018)
$f_{f,i} \frac{\rho_i(u_G - u_L) (u_G - u_L) }{2}$	$f_{f,G}$	$u_G > u_L, \rho_i = \rho_G$	(Brauner and Maron, 1992; Picchi et al., 2014;
	$f_{f,L}$	$u_G < u_L, \rho_i = \rho_L$	Picchi and Poesio, 2016a)

In order to apply mechanistic models, the momentum equations for liquid and gas phases (Equation 2.28) are combined by introducing an expression for the single-phase pressure gradients, $(\partial p / \partial z)_k$. Different definitions of the pressure gradient may be used as presented by Omgba-Essama (2004). In the past, the equal pressure formulation $(\partial p / \partial z)_G = (\partial p / \partial z)_L$ was used (Taitel and Dukler, 1976; Taitel et al., 1978), which results in the combined momentum equation

$$-\frac{\tau_L S_L}{A_L} + \frac{\tau_G S_G}{A_G} + \tau_i S_{i,k} \left(\frac{1}{A_L} + \frac{1}{A_G} \right) = -\rho_L \left(\frac{\gamma}{2} \frac{\partial u_L^2}{\partial z} + g \frac{\partial \bar{h}_L}{\partial z} \right) - \rho_G \left(\frac{\partial u_G^2}{\partial z} \right). \quad 2.32$$

Since the equal pressure formulation neglects the surface tension effects on the interphase (Omgba-Essama 2004), a formulation with unequal pressure gradients

$$\left(\frac{\partial p_i}{\partial z} \right)_G = \left(\frac{\partial p_i}{\partial z} \right)_L + \sigma \frac{\partial^3 h_L}{\partial z^3} \quad 2.33$$

was proposed by Barnea and Taitel (1993), which leads to a 4th order partial differential equation instead of Equation 2.32 (see Section 6.2). All terms in Equation 2.32 can be expressed by the operating conditions for the two-phase feed and an equilibrium liquid level $h_{L,e}$ that fulfills the equation. If $h_{L,e}$ exceeds the stability liquid level $h_{L,stab}$ or a specific flow morphology criterion obtained from a mechanistic model, a morphology transition is predicted.

As discussed in Section 2.2, the transition from stratified flows towards annular or intermittent flows is crucial for design and operation of two-phase feeds. This transition can be predicted via Kelvin-Helmholtz stability analysis for the growth of a small interface perturbation into a stable

wave. The basic mathematical derivations and formulations for this work were taken from the literature¹.

The resulting expression predicts stable stratified flow for

$$(u_G - u_L) < K \left[(\rho_L \alpha_G + \rho_G (1 - \alpha_G)) \frac{\rho_L - \rho_G}{\rho_L \rho_G} g \frac{A}{A'_L} \right]^{1/2}. \quad 2.34$$

Similar to $h_{L,e}$ that satisfies Equation 2.32, the stability liquid level $h_{L,stab}$ fulfills Equation 2.34 for a given set of operating conditions. If $h_{L,e}$ exceeds $h_{L,stab}$, transition mechanisms of mechanistic models are applied to predict the resulting flow morphology. For example, viscous forces were found to amplify the wave growth, which is referred to as the viscous Kelvin-Helmholtz stability (VKH, Barnea and Taitel, 1994a). The factor K in Equation 2.34 switches between the inviscid Kelvin-Helmholtz stability (IKH) $K = 1 = K_{IKH}$ and VKH for $K = K_{VKH}$ according to

$$K_{VKH} = \sqrt{1 - \frac{(c_W - c_{W,IKH})^2}{g \frac{\rho_L - \rho_G}{\rho_h} \frac{A}{A'_L}}}. \quad 2.35$$

Since Equation 2.35 depends on the wave's inception velocity c_W and the counterpart $c_{W,IKH}$ from the IKH analysis, a numerical solution is required for VKH (Picchi and Poesio, 2016a). However, for low viscosity fluids such as water-air, Taitel and Dukler (1976a) and Barnea and Taitel (1994a) successfully approximated Equation 2.35 with $K_{VKH} = 1 - h_L$. The resulting morphology transitions are shown in Section 2.3.3 (Figure 2.8).

The two-fluid model fundamentals and the stability analysis presented above briefly outline the underlying numerical calculation, where each operating condition is transferred into a liquid level, which is then further evaluated with mechanistic models. Although this approach is well applicable and quite universal (Issa and Kempf, 2003; Corral, 2014), the computational effort to obtain a solution often exceeds the available resources during the engineering of two-phase feed sections, in particular as no commercial software tool or system code is available. Moreover, the underlying mechanisms and flow regime transitions still deviate from experimental data (e.g. for the transition from stratified to intermittent flow as shown by Thaker and Banerjee (2015)) and are hardly applicable to larger pipe diameters (Wu et al., 1987; Kong et al., 2018a) or fluid properties different from air-water (Weisman et al., 1979; Simon, 1997).

¹ Referring to the work of, Taitel and Dukler (1976a), Taitel et al. (1978), Wu et al. (1987), Barnea (1991) and Barnea and Taitel (1993), 1994a; the treatment of numerical peculiarities and multiple solutions is based on the work of Barnea and Taitel (1989, 1992, 1994b, 1994c), Barnea (1991), Brauner and Maron (1991), Brauner and Maron (1992), Picchi and Poesio (2016b) and Dukler and Taitel (2018).

2.3.3 The interfacial level gradient

The aforementioned solution of the TFM considered an equilibrium liquid level $h_{L,e}$ for fully developed flow. In short feed pipes, however, this equilibrium level may not be reached. Instead the liquid level of the two-phase feed changes along the pipe, which is considered by the term $d\bar{h}_L/dz$ in Equation 2.28, referred to as interfacial level gradient (ILG).

Modelling the regime transitions by the two-fluid model with ILG extends the region of stratified flow morphologies to larger liquid superficial velocities (see Figure 2.7). According to Bishop and Deshpande (1986a), this delayed wave formation occurs when lower liquid levels (due to ILG) counteract the frictional resistance of the flow. The ILG is mostly driven by the liquid phase and occurs mainly for pipes with low L/D ratio and large diameter (Bishop and Deshpande, 1986b), for high-viscosity liquids (Li et al., 2013) and in pipe equipment such as tee joints (Koizumi et al., 1990). The characteristic liquid levels for ILG were defined by Taitel and Dukler (1987) as shown in Figure 2.8.

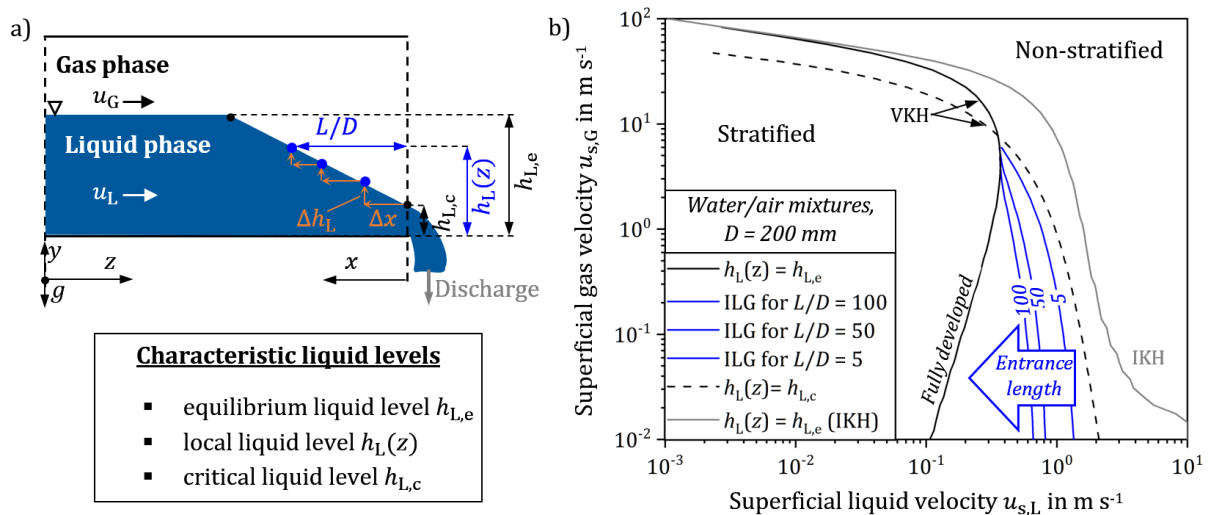


Figure 2.8: a) Characteristic liquid levels of the ILG, b) resulting transitions between stratified (smooth and wavy) and non-stratified (annular and intermittent) flow morphologies depending on the upstream distance L/D from discharge.

$h_{L,c}$ approximates the minimum liquid level for subcritical discharge (Taitel and Dukler, 1987) in close vicinity ($L/D = 2 \times h_{L,c}$) to the real pipe discharge location (Sadatomi et al., 1993). The local liquid level $h_L(z)$ refers to any entrance length of the feed pipe upstream of $h_{L,c}$. If $h_L(z)$ is used instead of $h_{L,e}$ in the two-fluid model, the range of stratified flows extends towards higher liquid velocities as the entrance length decreases (blue lines in Figure 2.8b). The black lines are shown as references, i.e. the viscous Kelvin-Helmholtz analysis (VKH) for fully developed flows and the theoretical limit ‘no entrance length’ ($h_L(z) = h_{L,c}$). The transition line of the simplified IKH theory (gray line) significantly overpredicts the occurrence of stratified flows (e.g. compare with data in

Figure 2.7) and was therefore not further considered. The orange arrows in Figure 2.8a illustrate the solution procedure that was applied by Bishop and Deshpande (1986a), Taitel and Dukler (1987) Sadatomi et al. (1993) and Li et al. (2013) to determine the local liquid level $h_L(z)$.

Rearranging Equation 2.32 yields the mathematical expression for the interfacial level gradient

$$ILG = \frac{d\bar{h}_L}{dz} = \frac{-\frac{\tau_{w,L}S_L}{A_L} + \tau_i S_i \left(\frac{1}{A_L} + \frac{1}{A_G} \right) + \frac{\tau_{w,G}S_G}{A_G}}{\rho_L g - \frac{A'_k \gamma}{2} \left(\rho_G u_{s,G}^2 \frac{A^2}{A_G^3} - \rho_L u_{s,L}^2 \frac{A^2}{A_L^3} \right)}. \quad 2.36$$

The limits of Equation 2.36 return the equilibrium liquid level, $h_{L,e}$, (for $ILG \rightarrow 0$) and the critical liquid level $h_{L,c}$ (for $ILG \rightarrow \infty$). The axial variation of the liquid level upstream the pipe exit (note that the coordinate x is against the flow direction) can be numerically derived from $h_{L,e}$ and $h_{L,c}$ using the method of small differences (indicated by the orange arrows in Figure 2.8a). Assuming $h_L(x=0) = h_{L,c}$ at the pipe exit and $h_L(x) \rightarrow h_{L,e}$, Equation 2.36 is solved for incremental Δx that satisfies an initial incremental Δh_L . Accordingly, the gradient can be approximated as

$$ILG = -\frac{\Delta h_L}{\Delta x}, \quad 2.37$$

while averaging the phasic velocities, area fractions and geometric parameters along Δx (Sadatomi et al., 1993). Depending on geometry, fluid system and operating conditions, Equation 2.36 does not necessarily return a single solution (Sadatomi et al., 1993), in particular for high liquid kinetic energy ($\rho_L u_{s,L}^2 A_L^{-1}$). Equation 2.36 may also result in multiple solutions for high gas velocities.

Figure 2.9 illustrates the behavior of Equation 2.36 for varying liquid levels. With increasing $u_{s,L}$, numerator and denominator have their zeros at larger values of $h_{L,e}$ and $h_{L,c}$. This reflects conditions with constricted gas phase cross-section and thus increased gas phase velocity. Moreover, both liquid levels share similar values and numerical instabilities (asymptotic blue curve in Figure 2.9, middle), multiple solutions occur and the ILG cannot be explicitly determined. For lower superficial velocities (black and red line in Figure 2.9), Equations 2.36 and 2.37 can be solved to determine $h_{L,c} < h_L(z) < h_{L,e}$. A slightly different derivation to calculate the ILG was obtained by Bishop and Deshande (1986) accounting for the unequal phase pressures applying

$$p_L = p_G + k\rho_L g h_L. \quad 2.38$$

Using the derivative of Equation 2.38

$$\left(\frac{\partial p}{\partial z} \right)_G = \left(\frac{\partial p}{\partial z} \right)_L - k\rho_L g \frac{\partial \bar{h}_L}{\partial z} \quad 2.39$$

shows that the resulting correlation coincides with Equation 2.36.

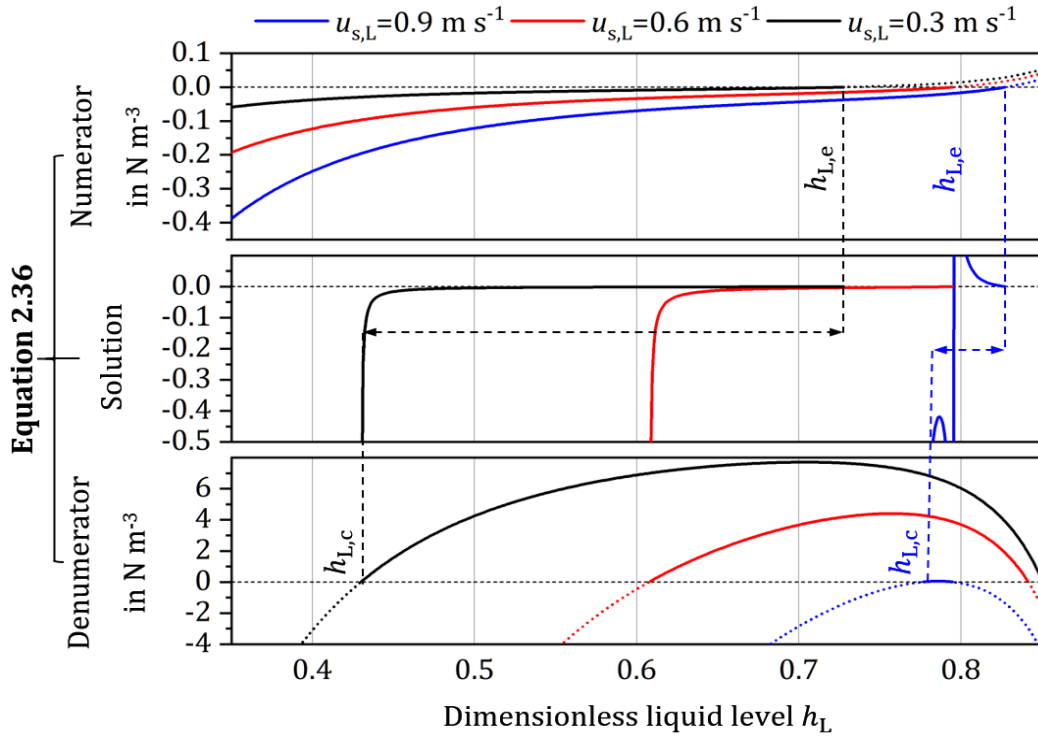


Figure 2.9: Solution of Equation 2.36 depending on the liquid level h_L : numerator (top), ILG (middle) and denominator (bottom) illustrated for different superficial liquid velocities.

Bishop and Deshande (1986) proposed a simplified explicit solution for the ILG assuming open channel flow and $\tau_i = \tau_{w,G}$ for non-Newtonian fluids and Newtonian fluids according to

$$\text{ILG} = \frac{\frac{2K}{\rho_L g (D_h/2)^{(n'+1)}} \left(\frac{3n'+1}{n'}\right)^{n'} u_L^{n'}}{1 - Fr_{\text{mod}}^2}, \quad Fr_{\text{mod}}^2 = \gamma \frac{u_L^2}{g A_L} A'_k \quad 2.40$$

and

$$\text{ILG} = \frac{\frac{32}{Re_L} \frac{u_L^2}{g D_h}}{1 - Fr_{\text{mod}}^2} = \frac{32 Fr_L^2}{Re_L (1 - Fr_{\text{mod}}^2)}, \quad 2.41$$

respectively. Contrary to the model of Sadatomi et al. (1993), their iterative solution depends on entrance and exit conditions and pipe geometry. However, no plausible values for the ILG were obtained with Equation 2.41. Recently, Li et al. (2013) derived a model based on Equations 2.32 and 2.39 accounting twice for the pressure term. Reasonable agreement was claimed with experimental data from Essaied (1992), however, a factor (0.5) was introduced to Equation 2.36 without further explanation.

It can be concluded, that although there is a basic concept that accounts for short entrance lengths in the TFM available, further analysis for a wider range of flow rates is required. So far, studies focused mostly on selected operating conditions without comprehensive experimental validation and estimation of the ILG.

2.3.4 Analytical models

Analytical models provide simplified correlations to determine key parameters of the two-phase flow (e.g. void fraction, drift velocity, Lockhart-Martinelli parameter). Based on the respective approximation of the two-phase flow, the models are classified into the following groups:

Homogenous flow models (HFM) consider a two-phase mixture without relative motion between the phases (no-slip condition). The void fraction is obtained from

$$\alpha_{G,HFM} = K_{HFM} \alpha_G, \quad 2.42$$

which 'scales' the void fraction from Equation 2.21 to account for fluid parameters and flow regimes (Bankoff, 1960; Woldesemayat and Ghajar, 2007). To account for the real phase properties, the scaling parameter K_{HFM} utilizes average fluid properties according to

$$\rho_h = \alpha_G \rho_G + (1 - \alpha_G) \rho_L. \quad 2.43$$

Other definitions for averaged fluid properties are provided by Omgba-Essama (2004).

Separated flow models (SFM) define the void fraction $\alpha_{G,SFM}$ as

$$\alpha_{G,SFM} = \left[1 + f(R_S) \left(\frac{1 - w_L}{w_L} \right)^{e_1} \cdot \left(\frac{\rho_G}{\rho_L} \right)^{e_2} \cdot \left(\frac{\mu_L}{\mu_G} \right)^{e_3} \right]^{-1}, \quad 2.44$$

where e_1 to e_3 are empirical fitting parameters. SFM consider both phases separately using a fitting correlation $f(R_S)$ for the slip ratio R_S , which is defined as

$$R_S = \frac{u_G}{u_L} = \left(\frac{w_L}{1 - w_L} \right) \left(\frac{1 - \alpha_G}{\alpha_G} \right) \left(\frac{\rho_L}{\rho_G} \right) = \frac{u_{s,G}(1 - \alpha_G)}{u_{s,L} \alpha_G}. \quad 2.45$$

Drift-flux models (DFM) consider the two-phase flow as a homogenous mixture and include additional terms for local variations of velocity or void fraction by

$$\langle\langle u_G \rangle\rangle = \frac{\langle u_{s,G} \rangle}{\langle \alpha_{DFM} \rangle} = C_0 \langle u_h \rangle + \langle\langle u_D \rangle\rangle. \quad 2.46$$

The averaging mechanisms $\langle \rangle$ and $\langle\langle \rangle\rangle$ refer to cross-sectional-weighted and void-fraction-weighted quantities, respectively, as introduced by Zuber and Findlay (1965). The distribution parameter, C_0 , accounts for the cross-sectional distribution of the phase fraction and links the DFM to the two-phase flow morphology. The two-phase flow can be described by volumetric flux $u_h = \sum_k u_k \alpha_k = \sum_k u_{s,k}$ and drift velocity $u_{D,k} = u_k - u_h$, where u_h is the mixture volumetric flux and u_k is the respective phase velocity. Empirical relations are proposed for C_0 and u_D , which allow the calculation of α_{DFM} from Equation 2.46.

Basically, the HFM is a special case of SFM or DFM, where $R_S = 1$ and $C_0 = 1$, respectively. This holds for dispersed flow morphologies, such as mist or bubbly flow (Thome and Cioncolini, 2015),

and flows with heavily mixed phases, for example encountered downstream of valves (VDI, 2013), in confined channels (Winkler et al., 2012) or near the critical point (Winkler et al., 2012; VDI, 2013). Contrary, separated flow morphologies, e.g. stratified smooth flow with $R_S \neq 1$, can hardly be predicted by the HFM (Schaffrath and Ringel, 2000).

Drift-flux models were originally proposed for vertical flows (Zuber and Findlay, 1965), where gravitational acceleration and drag governs the drift velocity u_D . Contrary, buoyancy has no effect on horizontal two-phase flows. Thus, for horizontal flows, $u_D = 0$ was assumed in the early works and still holds in current models of e.g. Winkler et al. (2012) and Rassame and Hibiki (2018). As emphasized by Bendiksen (1984), França and Lahey (1992) and Winkler et al. (2012), this assumption is controversial since a non-zero drift velocity exists in horizontal flows. This drift velocity originates from local phase distribution phenomena and slip as a consequence of lateral and axial pressure gradients (intermittent flows,) or structures of the phase interphase (separated flows). Correlations for u_D , however, are only valid for individual flow morphologies (i.e. França and Lahey, 1992 and Lamari, 2001), and thus, require a-priori knowledge of the flow.

Models based on the Lockhart-Martinelli parameter (LMP) estimate the void fraction of the two-phase flow via so-called two-phase multipliers as

$$\alpha_{G,LMP} = f(X). \quad 2.47$$

Here, X , is the Lockhart-Martinelli parameter (Lockhart and Martinelli, 1949; VDI, 2013), which refers to the single-phase pressure drops $dp/dz|_k$ of both phases according to

$$X = \sqrt{\frac{dp/dz|_G}{dp/dz|_L}} = \left(\frac{1 - w_G}{w_G}\right)^{0.875} \left(\frac{\rho_G}{\rho_L}\right)^{0.5} \left(\frac{\eta_L}{\eta_G}\right)^{0.125}. \quad 2.48$$

While the determination of X is always biunique for a certain pair of gas and liquid superficial velocities $[u_{s,G}, u_{s,L}]$, a recursive calculation requires specification of one superficial velocity.

The complexity and generalizability of the reduced-order models varies. Recent review articles (Coddington and Macian, 2002; Woldesemayat and Ghajar, 2007; Godbole et al., 2011; Pietrzak and Płaczek, 2019; Márquez-Torres et al., 2020) reported 66 available correlations for the prediction of the void fraction for horizontal two-phase flows. The agreement between predicted and experimental data for air-water systems is above 90 % (with error bands of ± 15 %), while it reduces below 80 % for other fluids mixtures. However, only few data are available for pipe diameters larger than 78 mm, short entrance lengths or curvatures, which has severe consequences for the design of two-phase feeds in distillation columns (e.g. the selection of inlet devices) based on uncertain void fractions as shown in Figure 2.10.

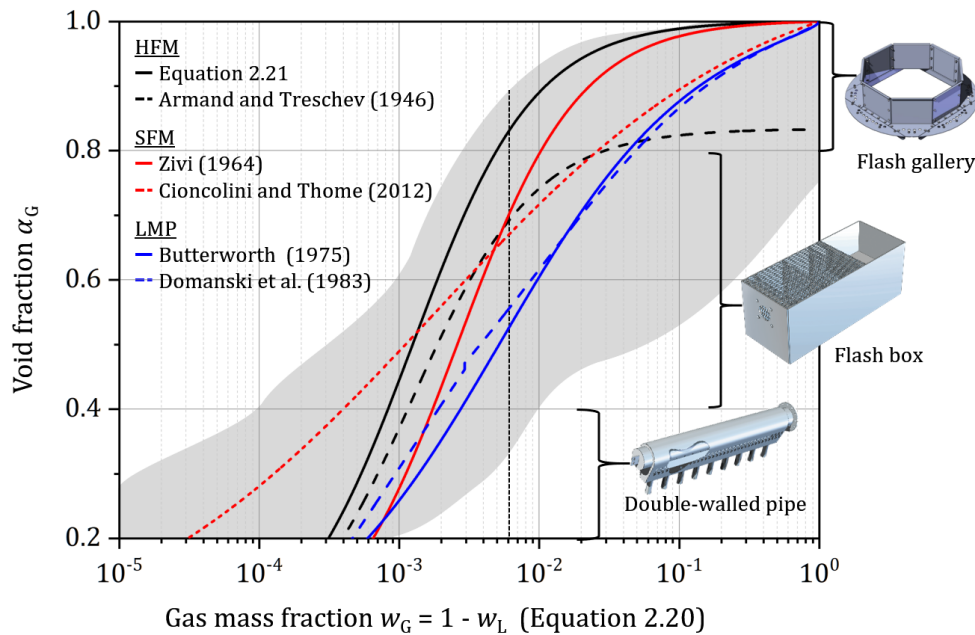


Figure 2.10: Engineering guidelines for the selection of two-phase feed inlet devices based on predicted void fractions α_G (the gray area indicate the scattering predictions of existing correlations). Source of embedded pictures of inlet devices: RVT Process Equipment GmbH (2015).

It should be mentioned that the selection and sizing of two-phase feed inlet devices depends also on many other parameters, such as column diameter, targeted separation performance, desired inlet phase separation. The vertical line in Figure 2.10 represents one exemplary two-phase feed design. While HFMs predict comparably high void fractions (Equation 2.21: $\alpha_G = 0.86$) suggesting the installation of a flash gallery, LMPs predict significantly lower values (Domanski et al., 1983): $\alpha_G = 0.53$) and a flash box would be used instead. Moreover, there are more general, **empirical models** (EMP) that determine the void fraction using e.g. dimensionless numbers to represent fluid dynamics. Their mathematical notations, however, have no common form and the ranges of applicability are hardly documented for most of them.

2.3.5 CFD simulations for commercial feed pipes

In the past two decades, Computational Fluid Dynamics (CFD) has gained increasing popularity for the prediction of single-phase and multiphase flow applications (Hewitt and Yadigaroglu, 2018). However, full-scale CFD-simulations of thermal separation columns and larger equipment such as feed pipes can hardly resolve scales that are relevant for flow dynamics. Instead, closure models for the conservation equations account for unresolvable phenomena (Lucas et al., 2016). Moreover, closure development is challenging and often bottlenecks reliable results. For instance, Xiao et al. (1990) reported that only few correlations exist to model entrainment in annular flow. According to Höhne et al. (2015), numerical modelling for the onset of entrainment requires additional effort to consider all capture mechanisms leading to droplet entrainment (see Figure 2.5). Their entrainment model accounts for fluid properties and considers the turbulent kinetic

energy and outward velocity gradient of the liquid phase as the most significant parameters. However, no experimental evidence is yet available.

So far, horizontal two-phase flows in feed pipes of commercial dimensions have not been studied numerically as described by Ali (2017). A number of studies (Meknassi et al., 2000; Ghorai and Nigam, 2006; Ali, 2017; Schmelter et al., 2020) refer to data of Strand (1993), who measured pressure drop, interfacial structures and velocity profiles of stratified flows in a pipe of $D = 100$ mm. However, these data are limited to fully developed flows at one liquid superficial velocity only. Other studies at larger scale, e.g. water-air flow in a rectangular channel (Vallée et al., 2008), are hardly comparable with flow conditions in feed pipes of thermal separation units.

Short entrance lengths have received little attention in numerical studies. Only Costa et al. (2018) investigated intermittent flows in a $D = 26$ mm pipe at $L/D = 10$. They reported satisfactory agreement (average deviation of $\pm 7\%$) of void fraction, phase velocity and characteristic frequencies for two flow conditions. Few simulation studies for gas-liquid flow in piping elements with inlet/outlet in vertical-to-horizontal (and vice versa) orientation were performed (see Table 2.6).

Table 2.6: Numerical studies in curved pipes (vertical to horizontal orientation).

Curvature type	D in mm	R/D	Reference
Helical coil	10 - 40	25 - 20	Saffari et al. (2014)
	1.6	6	Tiwari et al. (2006)
	5 - 15	8 - 20	Vashisth and Nigam (2008); Vashisth et al. (2008)
90° bend (vertical orientation)	140	1	Hu et al. (2017)
	100	6	Legius and Van den Akker (1997)
	36	3	Aung and Yuwono (2013)
	12	1.5	Mazumder and Siddique (2011)
90° bend (horizontal orientation)	63	6	James et al. (2000)
	40	not specified	Tang et al. (2020)

In contrast to two-phase flow in bends with vertical to horizontal orientation, bends with inlet/outlet in horizontal-horizontal orientation have hardly been considered. Simulations with dispersed droplet phase up- and downstream of a 90° bend by James et al. (2000) and in horizontal 90° bends in series by Tang et al. (2020) were performed with geometries that can hardly be upscaled to commercial pipe dimensions or geometries. Accordingly, the predictive capabilities of today's multiphase CFD is highly uncertain and deviations in the range of 5 - 30 %

(Ekambara et al., 2008; Pinilla et al., 2019) between experimental data and simulation results can be expected.

2.4 Objectives of this thesis

The following research objectives are derived from the state of the art:

- (I) **Establishment of a comprehensive database for developing two-phase flow:** Available engineering and design methods for two-phase feeds mostly rely on applied heuristics and further development demands experimental data for not fully developed two-phase flows in typical feed pipe dimensions. An objective classification of the flow morphologies is required, which can be achieved by means of fuzzy identification algorithms. Such algorithm shall realistically quantify and visualize gradual transitions between flow morphologies. Further, morphology transitions introduced by e.g. curvatures and the morphology recovery downstream should be quantified. The capabilities of such an approach shall be demonstrated in various straight and bent pipe geometries.
- (II) **Derivation of predictive criteria for undesirable flow morphologies:** In order to reliably operate two-phase feeds, there is a strong demand to predict the inception of intermittent flow and entrainment for developing two-phase flow. Available criteria for intermittent flow are based on sufficient liquid supply and wave formation, which require minimum entrance length. Thus, inception criteria for short feed pipes should be adapted to account for the lower liquid levels and the observed transitions. It is assumed that the onset of entrainment can be predicted for fully developed flows with acceptable agreement. The governing mechanisms are linked to interfacial shear, phase slip and the occurrence of wavy morphologies, which will be captured by characteristic temporal features. A criterion is then required to classify any wavy flow with respect to susceptibility for entrainment. This criterion shall be applied to different pipe geometries and entrance lengths to obtain predictive correlations.
- (III) **Assessment of suitable two-phase models and methods:** Engineering of two-phase feeds is increasingly forced to rely on either reduced-order models or CFD-aided methods to predict two-phase flow morphologies for arbitrary geometries or fluid systems. However, state of the art CFD codes have not been tested for typical feed pipe geometries. Thus, the codes will be assessed for exemplary operating conditions in various pipe geometries. Among other reduced-order models, the TFM is capable of modelling developing flows by determining the liquid level for any entrance length. The comprehensive data from this work (see Objective I) shall be used to obtain parameters and terms in the fundamental model. The wide variety of the remaining reduced-order models will be compared in order to identify the most versatile models. Adaptations shall be proposed to allow more accurate predictions of the phase fraction of developing flows.

3 Experimental method and algorithms for flow characterization

This chapter summarizes the design of the setups, the experimental procedures as well as applied measurement technique and corresponding data post-processing. An uncertainty analysis is performed to assess the reliability of the measurement data.

Parts of this chapter have been published in:

Döß, A., Schubert, M., Hampel, U., Mehringer, C., Geipel, C. and Schleicher, E. (2021). Two-Phase Flow Morphology and Phase Fractions in Larger Feed Line Sections. *Chemie Ingenieur Technik* **93**, 1134–1141.

Döß, A., Schubert, M., Wiedemann, P., Junge, P., Hampel, U., Schleicher, E., Mehringer, C. and Geipel, C. (2021). Flow Morphologies in Straight and Bent Horizontal Pipes. *ACS Engineering Au* **1**, 39–49.

3.1 Experimental setups

The experimental studies in this work were carried out in two different experimental facilities. In the DN50 feed pipe setup (installed at HZDR) test sections with inner diameter of $D = 50$ mm are investigated in the facility. This pipe diameter was chosen as a reference for later comparison with experimental studies and flow regime maps in the literature. The DN200 feed pipe setup contains test sections with inner diameter of $D = 200$ mm, which is comparable with commercial feed pipes. The DN200 setup is part of the experimental facility located at the pilot plant center of RVT Process Equipment GmbH, Steinwiesen. Both facilities have comparable piping and instrumentation diagrams including peripheral equipment, components and process instrumentation as illustrated in Figure 3.1.

Water and air are mixed at the inlet before entering the test sections. Phases are separated in the larger separator vessels at the outlet. The air outlet is open to the atmosphere, while water is cycled with axial pumps from the storage vessels. Technical specifications of both facilities are

summarized in Appendix A.4. Various straight and bent PMMA and PVC pipe modules, described below, are installed to study their impact on flow morphology, void fraction and entrainment.

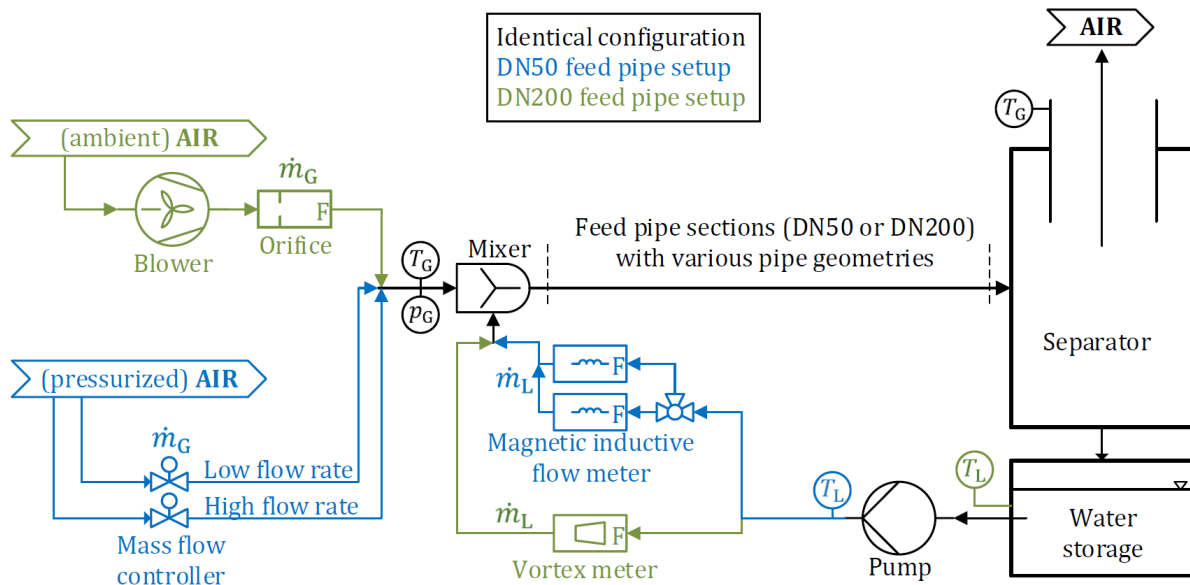


Figure 3.1: Schematic of the experimental setups (black: identical configuration, blue: DN50 feed pipe setup, green: DN200 feed pipe setup).

DN50 feed pipe setup (reference setup): The feed pipe section in the reference setup is mounted in a frame (Figure 3.2) and directly connected to the separator at elevated height (with respect to water supply) in order to avoid influence from piping upstream the test section. To cover the full range from low to high gas flows, different air supply lines and inlet mixers are used (concentric arrangement for $u_{s,G} < 11 \text{ m s}^{-1}$, T-junction arrangement for $u_{s,G} \geq 11 \text{ m s}^{-1}$) as illustrated in Figure 3.2c. Figure 3.2b shows the straight feed pipe section in horizontal orientation. The bent pipe configurations considered in this study are upright S-bend, horizontal S-bend and 90° horizontal bend as shown in Figure 3.3b. All bends are with inlet and outlet in horizontal orientation and $R/D = 1$ (dimensions of the bends are shown in Figure 3.3a). In order to minimize the distance between the end of the curvature and the outlet opening (connecting flanges) and to allow visual observation, the bends were fabricated by additive manufacturing (stereolithography, PTZ Prototypenzentrum GmbH, Dresden) using a transparent epoxy resin (P3005).

DN200 feed pipe setup: Figure 3.4 shows the DN200 feed pipe setup used for the flow analysis in a straight pipe. Gas and liquid of the DN200 feed pipe are mixed with a T-junction with concentric inlet, where liquid phase entered through a narrow annulus, while the gas was fed in the core region (Figure 3.4b). The two-phase mixture is then discharged into a DN1000 separator acting simultaneously as liquid storage tank (see Figure 3.4). Similar to the DN50 feed pipe setup,

a 90° horizontal bend ($R/D = 1, D = 200$ mm) is installed to analyze the downstream flow development.

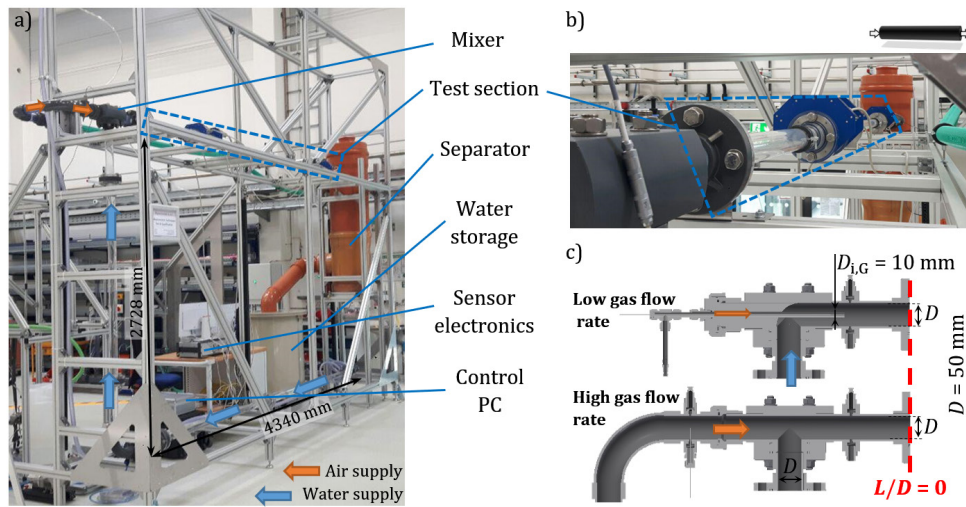


Figure 3.2: a) DN50 feed pipe setup (reference system), b) straight feed pipe section, c) CAD drawing of the gas-liquid mixers.

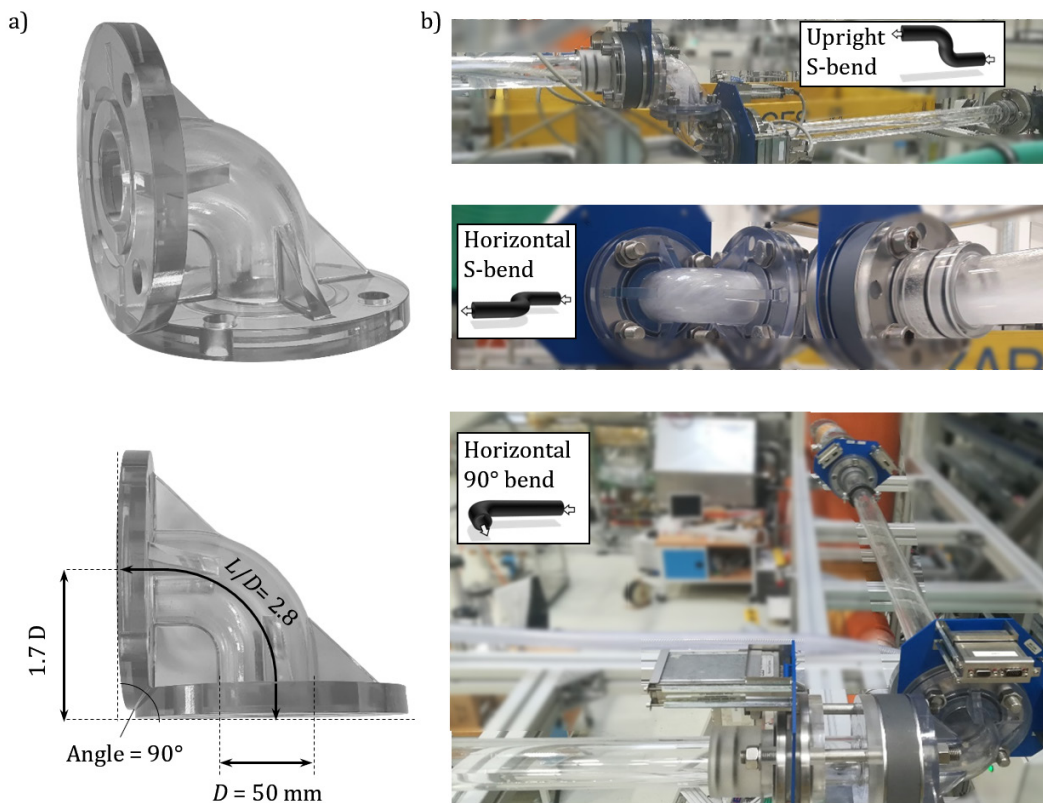


Figure 3.3: a) 90° bends used in the DN50 feed pipe setup, b) bent pipe arrangements with respective symbols used below (Table 3.2).

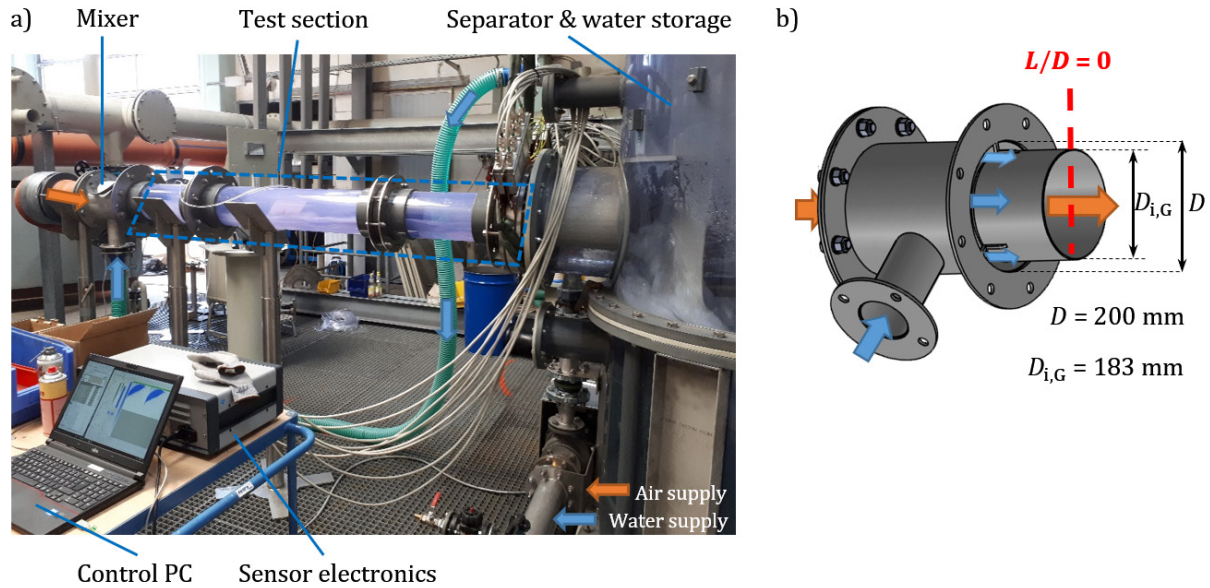


Figure 3.4: a) DN200 feed pipe setup with the straight test section, b) CAD drawing of the gas-liquid mixer.

3.2 Wire-mesh sensors

Wire-mesh sensors (WMSs) are well established (Prasser et al., 1998; da Silva, 2008; Velasco Peña and Rodriguez, 2015; Kipping et al., 2016) for multiphase flow imaging in vertical (Möller et al., 2019; H. M. Prasser et al., 2002; Sharaf et al., 2011) and horizontal (Da Silva et al., 2011; Vieira et al., 2014; Sahovic et al., 2020) pipes. They are low-intrusive, robust and provide high temporal resolution at less costs compared with radiation-based imaging techniques.

A WMS consists of two planes with parallel electrodes (wires) of perpendicular orientation. Measurements based on local conductivity differences in the two-phase flow were performed in this work. The measurement principle relates current signals, measured at each virtual WMS-crossing point between electrodes of respective orthogonal wires, to the phase fractions of water (conductive) or air (non-conductive). Figure 3.5 shows the sensor principle and exemplary illustrations of phase distribution images obtained after data post-processing.

The transmitter electrodes are consecutively excited (rectangular voltage excitation signal U_t) by corresponding switches, while the non-active electrodes are grounded. Current signals $I_r(t)$, measured at the receiver electrodes are converted into voltage signals U_r that refer to the instantaneous conductivity (i.e. volumetric phase fraction) in the virtual crossing point (fluid volume) between receiver and transmitter electrodes. The analogue signals are converted into digital data and stored. The maximum frame rate of a wire-mesh sensor is kHz. Ultimately, void fraction data are then obtained by normalizing the output voltage signals based on single-phase reference measurements. The latter are obtained at operation conditions to avoid temperature drift that affects electric conductivity of water (Wiedemann et al., 2020). Figure 3.5b shows one

single frame representing an instantaneous void fraction distribution within a sequence of a pseudo-slug flow. The visualization of flow morphologies is achieved plotting consecutive frames as a stack, which gives a pseudo-3D representation (see Figure 3.5c). It should be noted that x and y refer to the directions of the wires and t is the sampling time.

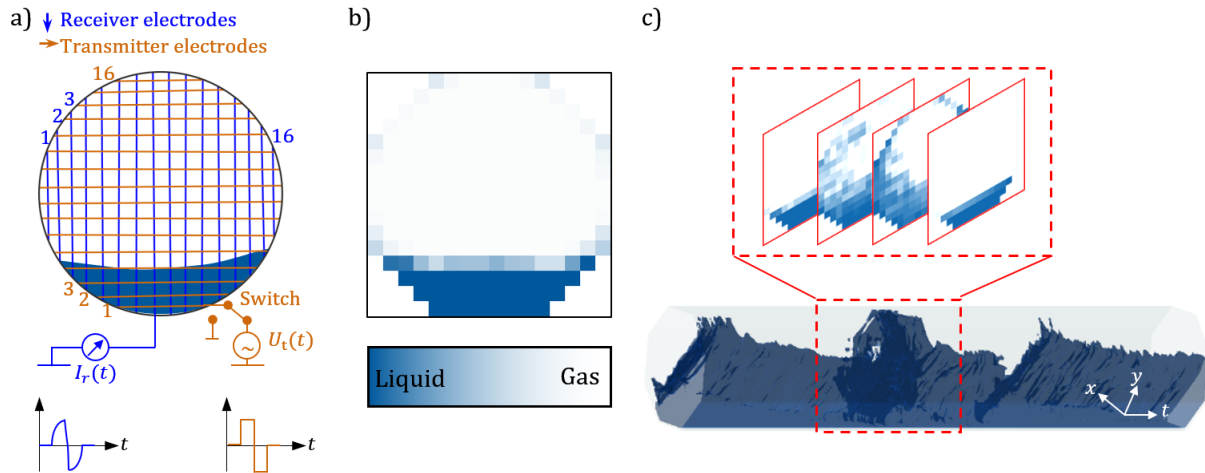


Figure 3.5: a) WMS measurement principle: b) post-processed data and c) visualization of flow morphologies.

Three WMSs with 16×16 virtual crossing points were installed in the DN50 feed pipe setup at different positions along the feed pipe. One WMS with 64×64 crossing points was installed in the DN200 feed pipe setup. The specifications of the installed WMSs are summarized in Table 3.1.

Table 3.1: Specifications of applied WMSs.

	DN200 WMS	DN50 WMS
Number of sensors	1	3
Opening diameter	200 mm	50 mm
Wire grid	64×64	16×16
Wire thickness	0.25 mm	0.25 mm
Spatial resolution	$3.05 \text{ mm} \times 3.05 \text{ mm}$	$3.13 \text{ mm} \times 3.13 \text{ mm}$
Frame rate, f_s	$2.5 \times 10^3 \text{ s}^{-1}$	$10 \times 10^3 \text{ s}^{-1}$

3.3 Experimental procedure

Experiments were carried out for flow rates based on the flow regime map of Mandhane et al. (1974), which is one of the most frequently used maps for small pipes and water-air two-phase flows. In order to capture the supposed transitions between flow morphologies, the experimental matrices were pre-defined on a log-log axes chart as shown in Figure 3.6.

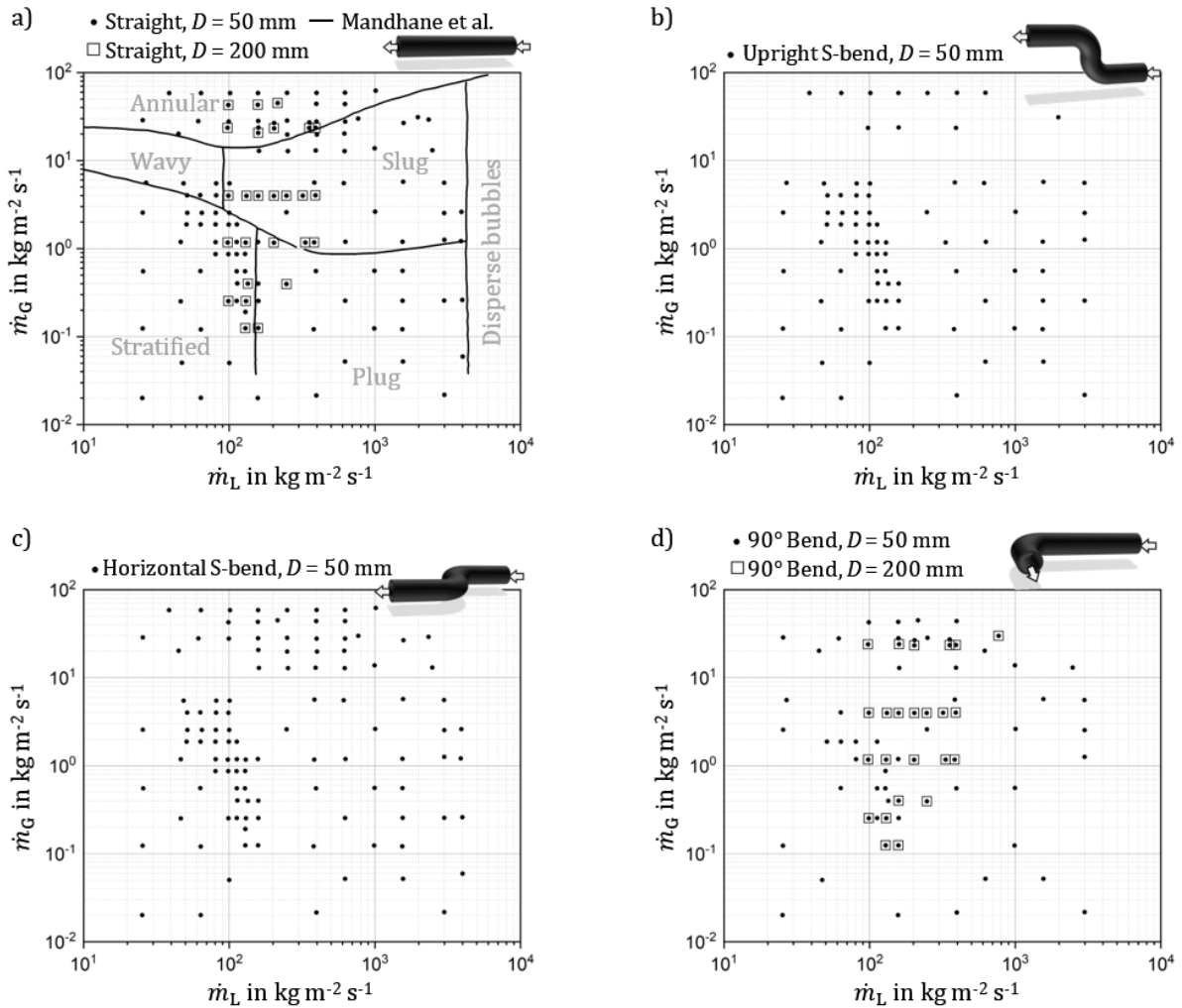


Figure 3.6: Experimental matrices for configurations with a) straight pipe, b) upright S-bend, c) horizontal S-bend and d) 90° horizontal bend.

Since two-phase feeds in separation columns are preferably operated with high gas flow rates, the experiments were designed to achieve high gas flow rates, while maximum liquid flow rates were limited by the pumps' maximum head. In order to enable easier comparison between both experiments, data are presented below in terms of mass fluxes (\dot{m}_k) according to

$$\dot{m}_k = \frac{\dot{M}_k}{D} = \rho_k u_{s,k} \cdot \quad 3.1$$

The operation and measurement procedures was identical for both setups. The liquid flow rates were adjusted via frequency inverters of the pumps and manual valve adjustments. The liquid flow rates were measured with flow meters for the ranges of flow rates below and above $6 \text{ m}^3\text{h}^{-1}$, installed in both branches of the DN50 feed pipe setup. Due to the lower range of liquid flow rates in the DN200 feed pipe setup, a single measurement in the main supply line was sufficient. The density of the incompressible liquid was calculated considering the measured liquid temperature.

The gas flow rates $\dot{V}_{G,\text{ref}}$ in the single-phase supply lines (reference value, index ref) of the DN50 feed pipe setup were determined with mass flow controllers based on differential pressures across a laminar flow element. Two devices were used for flow rates below and above 100 sl min^{-1} , respectively. In the DN200 feed pipe setup, $\dot{V}_{G,\text{ref}}$ was derived from the pressure drop across an orifice. Changes in the gas phase density due to pressure losses and temperature fluctuations were considered via local temperature and pressure measurements at the inlet (mixer). Accordingly, the gas flow rates were adjusted iteratively via mass flow controllers (reference setup) and blower rotational speed (DN200 feed pipe setup). The ideal gas equation was employed to obtain the gas flow rate at the inlet of the test sections (index inl) from the corresponding reference properties of the gas mass flow measurements:





$$\dot{V}_{G,\text{inl}} = \dot{V}_{G,\text{ref}} \frac{p_{G,\text{ref}} T_{G,\text{inl}}}{p_{G,\text{inl}} T_{G,\text{ref}}} \quad 3.2$$

The average inlet gas and liquid temperatures for the DN50 and DN200 feed pipe setup were $T_{G,\text{inl}} = 26.4 \pm 5.3 \text{ }^\circ\text{C}$, $T_{L,\text{inl}} = 24.4 \pm 1.6 \text{ }^\circ\text{C}$ and $T_{G,\text{inl}} = 19.3 \pm 2.7 \text{ }^\circ\text{C}$, $T_{L,\text{inl}} = 21.3 \pm 3.0 \text{ }^\circ\text{C}$, respectively. Eventually, the average temperature between water and air at inlet was used to calculate the fluid properties present in the test sections (assuming isothermal conditions) using the fluid property library 'CoolProp'. It should be noted that slightly higher water-air inlet temperature differences were obtained in the DN50 feed pipe setup resulting from the heat introduced by the pump (for high liquid flow rates) as well as from decreasing air temperature caused by the expansion of the supplied pressurized air (from 6 to 8 bar(a) to 1 to 2 bar(a) in the test section).

Pressure taps at the bottom of the test section were used to measure the operating pressure at test section inlets. In both test sections, the absolute pressure was measured by calibrated relative pressure transducers. Therefore, regular readings of the ambient pressure from online climate data (www.kachelmannwetter.com) were used to correct the measured pressure. The online data were corrected to account for the respective sea level of the installations according to Wagner and Kretzschmar (2008).

Once steady-state operation was achieved, WMS measurements were started. The default recording time of 60 s was extended up to 600 s when periodic structures with low frequency (e.g. slugs, long waves) were observed. The measurement positions of the WMSs are shown in Table 3.2.

Table 3.2: Investigated pipe configurations.

Geometry (↔ Flow direction)	Configuration	D in mm	Entrance lengths			Total number of measurements
			INL	OUT	REF	
	Straight pipe	50	L/D = 10	L/D = 25	L/D = 75	129
		200	L/D = 10	-	-	26
	Upright S-bend	50	L/D = 25	L/D = 30	L/D = 75	82
	Horizontal S-bend	50	L/D = 25	L/D = 30	L/D = 75	109
	Horizontal 90° bend	50	L/D = 75	L/D = 78	L/D = 108	72
		200	L/D = 7.5	L/D = 13	L/D = 23	24

The measurement positions in Table 3.2 refer to the entrance lengths upstream the recorded flow morphologies, i.e. the distance from $L/D = 0$ (the positions are highlighted in Figure 3.2 and Figure 3.4). The inlet (INL) and outlet (OUT) measurement locations were $L/D = 2.5$ apart from the investigated curvatures. The reference position (REF) was selected to analyze the recovery of the flow morphology downstream the bend. In the straight pipes, these positions revealed the developing flow morphology without impact of a bend. The maximum entrance length for each bent test section was used to compare the recovery of the flow morphology with respect to the straight reference pipe.

3.4 Data processing

The commercial WMS software framework (ver. 1.3.0, HZDR Innovation, M. Beyer et al., 2018) was used for data post-processing to determine the void fractions

$$\alpha_{G,i_1,i_2,n_m} = \frac{U_{r,W,i_1,i_2,n_m} - U_{r,tp,i_1,i_2,n_m}}{U_{r,W,i_1,i_2,n_m} - U_{r,G,i_1,i_2,n_m}}. \quad 3.3$$

The gas phase (air) is considered non-conductive (U_{r,G,i_1,i_2,n_m}). Thus, the instantaneous void fractions according to Equation 3.3 depend only on the measured voltage signals of the two-phase mixture (U_{r,tp,i_1,i_2,n_m}) and on the liquid phase reference (U_{r,L,i_1,i_2,n_m}). The indexes i_1 and i_2 in

Equation 3.3 refer to the electrodes, i.e. the virtual crossing points in the cross-section. Individual frames are labelled with index n_m and the time-averaged local void fraction α_{G,i_1,i_2} is

$$\alpha_{G,i_1,i_2} = \frac{1}{\max(n_m)} \sum_{n_m} \alpha_{G,i_1,i_2,n_m} \quad 3.4$$

Values outside the circular pipe cross-section were considered according to their area contribution by the weighting factor a_{i_1,i_2} to obtain the cross-sectional averaged void fraction according to

$$\alpha_G = \sum_{i_1=1}^{\max(i_1)} \sum_{i_2=1}^{\max(i_2)} \alpha_{G,i_1,i_2} \cdot a_{i_1,i_2} \quad 3.5$$

3.4.1 Fuzzy flow morphology classification

Recently, Wiedemann et al. (2019) introduced a novel fuzzy flow pattern identification (FFPI) method for fully developed horizontal two-phase flows. FFPI utilizes the fuzzy ‘c-means’ clustering of the following parameters of void fraction recordings (e.g. obtained from WMS):

- span of the void fraction time series of the upper pipe half,
- arithmetic mean of the void fraction time series of the lower pipe half,
- normalized standard deviation of the temporally averaged void fraction.

These parameters were analyzed and resulted in the definition of four cluster centers (index n), representing the main flow morphologies, i.e. annular (A), bubbly (B), intermittent (I) and stratified (S). The main advantage of the FFPI approach is the objective and rigorous representation of the flow morphology (Wiedemann et al., 2019). The FFPI represents any possible two-phase flow morphology via degrees of membership, F_n , (Euclidian distance from each of the four cluster centers) to the four main morphologies via the normalized (all F_n sum up to unity, the smallest F_n is set to zero) membership function F

$$F = [F_A, F_B, F_I, F_S]. \quad 3.6$$

Wiedemann et al. (2019) proposed a visualization that transforms the membership function into polar coordinates (β, R_n) . However, the full fuzzy representation in conventional flow regime maps (with Cartesian axes) is not possible assigning arbitrary symbols or colors. Thus, an advanced visualization approach is introduced that can be applied for transitional morphologies of evolving two-phase flows in short pipes or bends. The values of the 4D FFPI membership function are assigned to hue and intensity (lightness) of the HSL color model, which then can be transformed into the RGB color mode.

The procedure is exemplarily illustrated in Figure 3.7 for the beginning transition from intermittent (plug) towards bubbly flow and corresponding degrees of membership F_n . The degrees of membership, F_A, F_B and F_S are assigned to hue by the angular coordinate, β , and F_I is assigned to the intensity (lightness) by the radial coordinate, R_n , (Figure 3.7 b). Transformation from the HSL color model into the $RGB(\beta, R_n)$ color model yields the color-coded representation of the FFPI as shown in Figure 3.7c. The conversion from HSL to RGB is a common convention and not further specified here. Data processing using MATLAB R2015a featured the HSV color space and the conversion to RGB with the built-in function 'hsv2rgb'.

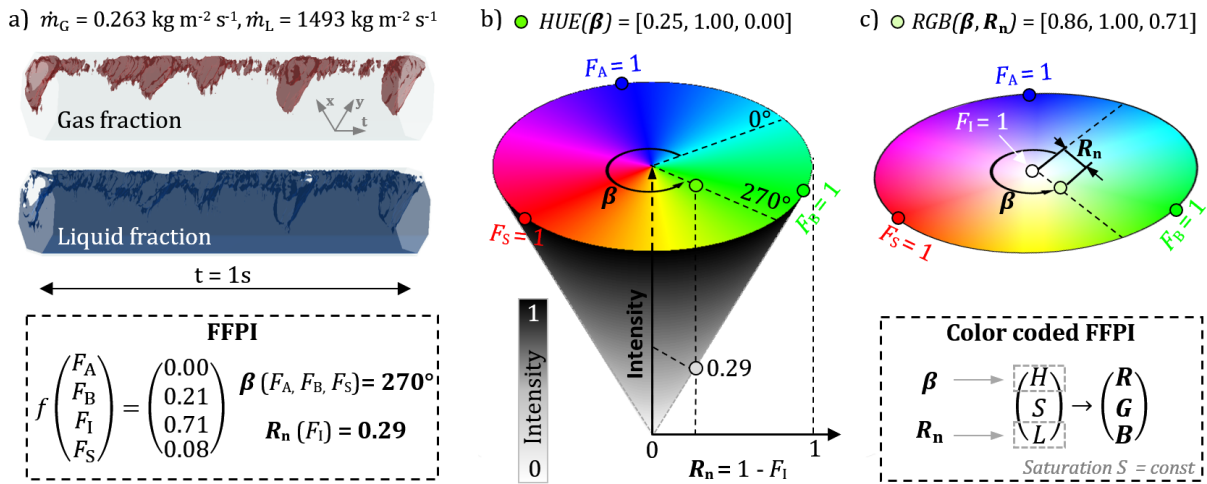


Figure 3.7: a) Pseudo-3D-visualization of the WMS recordings for a transitional morphology with FFPI membership function F and corresponding polar coordinates (β, R_n) , b) allocation of β in the hue map and R_n to the intensity of the HSL color model c) resulting color-coded representation in the $RGB(\beta, R_n)$ color model.

Figure 3.8 shows the resulting visualization in polar coordinates (according to the visualization approach introduced above) and in Cartesian coordinates (i.e. typical notion for traditional flow regime maps) for the experimental data obtained for the straight pipe configuration ($D = 50 \text{ mm}$). Color gradients between adjacent data points in Figure 3.8 represent the gradual transitions between flow morphologies that are disclosed by the fuzzy classification. To account for the irregularly and arbitrarily designed experimental matrices, the color-coded representation of the FFPI was interpolated using MATLAB R2015a's 'scattered interpolant' function (natural interpolation, nearest neighbor extrapolation) on a regular 500×500 grid in the axis limits of Figure 3.6.

Figure 3.8 (right) highlights the difference between a traditional flow regime map with rigorous boundaries from the areas occupied with points featuring similar flow morphologies (colors). For the sake of better interpretation of the results presented in this study, regions (ranges of mass flux) occupied by the four main morphologies, respectively, are distinguished. The main

morphologies are fairly well classified if the dominant degree of membership ($F_{n^*} = \max(F)$) exceeds the threshold $F_{n^*} > 0.8$ (black lines in Figure 3.8). The threshold value was obtained by analyzing the FFPI functions of known flow morphologies that occur in the reference geometry (straight pipe, both pipe diameters). Data points located outside the boundaries of the main regimes are considered as minor (transitional) regimes in the following.

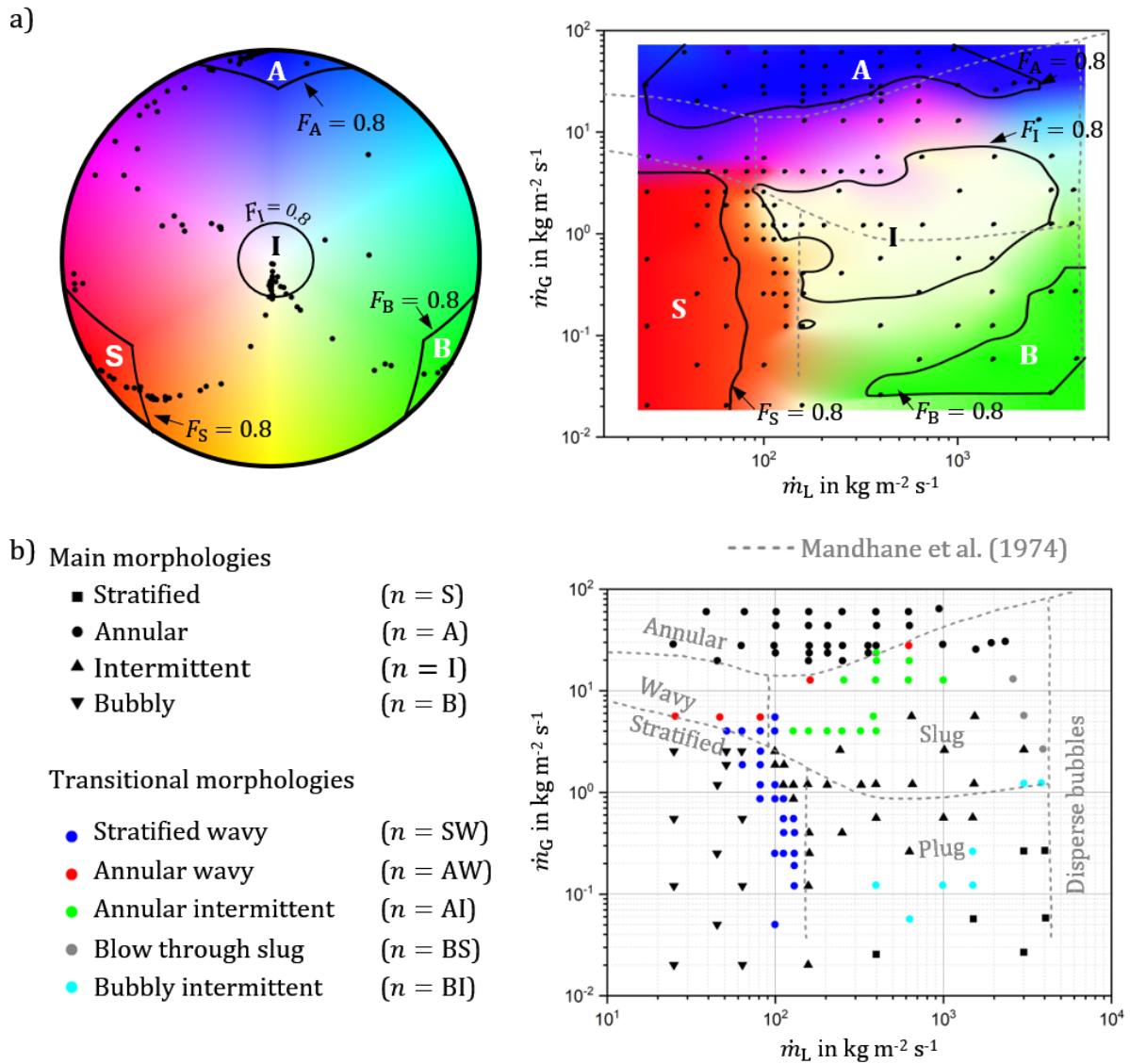


Figure 3.8: FFPI-based morphology classification (A - Annular, B - Bubbly, I - Intermittent, S - Stratified) of the measurements in the DN50 feed pipe at position REF in polar (left) and Cartesian coordinates (right). The flow regime map of Mandhane et al. (1974) is indicated by dotted lines and gray text labels.

Although this work focusses on the FFPI-based flow classification, further characterization of the transitional morphologies is possible, when considering more than one degree of membership at the same time. However, such method requires (semi-) empirical assumptions and leads to further

defuzzification. An example, which is similar to the constraint decision defuzzification (CDD) of Leekwijck and Kerre (1999), is provided in Appendix A.5.

3.4.2 Power spectral density

The onset of entrainment is linked to the presence of interfacial waves, which comprise characteristic fluid dynamics. Such characteristics can be revealed from dynamics in the void fraction data by means of analysis in the frequency domain (Jones and Zuber, 1975). Here, a signal is represented by its power spectral density function (PSD). Energy concentrates in frequency bands that refer to the characteristic frequencies f of the flow morphologies (Nguyen et al., 2010; Liu et al., 2012; Zhai et al., 2015).

According to ‘Welch’s overlapped segmented average spectral density estimate (Welch, 1967), consecutively overlapping segments (sliding windows) are averaged during the analysis to reduce the variance of the results (Heinzel et al., 2002). Each segment is obtained from the measured time series (void fraction signal) multiplied with a window function (W_{Hann}). The PSD of one segment is obtained by the discrete Fourier transformation (DFT) according to

$$PSD(m) = \frac{2}{f_s \cdot S_{\text{DFT},2}} \left| \sum_{n_m=0}^{n_{m,\text{max}}} \alpha_G(n_m) \cdot W_{\text{Hann}}(n_m) \cdot \exp\left(-i \frac{2\pi \cdot n_m \cdot m}{N_{\text{DFT}}}\right) \right|^2 \quad m = 0, 1, \dots, \frac{1}{2} N_{\text{DFT}} \quad 3.7$$

Here n_m denotes the discrete time step of the void fraction signal $\alpha_G(n_m)$ that is sampled with at frequency f_s . The PSD is obtained at discrete frequencies in the interval $[0; f_s/2]$ (the upper limit refers to the Nyquist-Shannon sampling theorem) that is resolved by equidistant grid points $f_{\text{res}} = m \cdot f_s / N_{\text{DFT}}$. Consequently, the DFT window length N_{DFT} affects the accuracy of the solution as follows:

For $N_{\text{DFT}} \rightarrow 2^{13}$ (equals 0.8 s and 3.3 s for the frame rates specified in Table 3.1):

- small frequencies in the signal $\alpha_G(n_m)$ cannot be resolved
- lower resolution of the frequency domain is obtained (less accurate determination of characteristic frequencies), the PSD shape is more steady

For $N_{\text{DFT}} \rightarrow 2^{17}$ (equals 13.1 s and 52.4 s for the frame rates specified in Table 3.1):

- small frequencies can be resolved
- the resolution of the frequency domain is increased, the PSD is more unsteady
- fewer windows n_{DFT} are taken from the signal $\alpha_G(n_m)$, increased deviation across all windows.

Since the characteristic frequency is unknown in advance, the DFT was performed for varying window lengths (in the range of $2^{13} < N_{\text{DFT}} < 2^{17}$) in order to obtain small and high frequency values. Details about the applied window function and the resulting accuracy of the determined

frequencies are provided in Appendix A.6. Figure 3.9 shows an example of the PSD obtained in the DN50 feed pipe setup with a straight pipe at $u_{s,G} = 4.50 \text{ m s}^{-1}$ and $u_{s,L} = 0.05 \text{ m s}^{-1}$.

Figure 3.9a illustrates different DFT window lengths in comparison to a full measurement signal (60 s acquisition time). The resulting PSDs obtained via DFT are shown in Figure 3.9b. Obviously, short window length (black lines) captures only higher frequencies and the PSD shows a slightly pronounced peak around 18.3 Hz. Contrary, longer window lengths (orange and blue lines) reveal peaks around 5.5 Hz and 0.5 Hz. The higher absolute values of the PSD account for higher signal energies at these frequencies, which can be considered the characteristic frequencies. However, the higher resolution of the frequency is accompanied by a more unsteady and less regular curve.

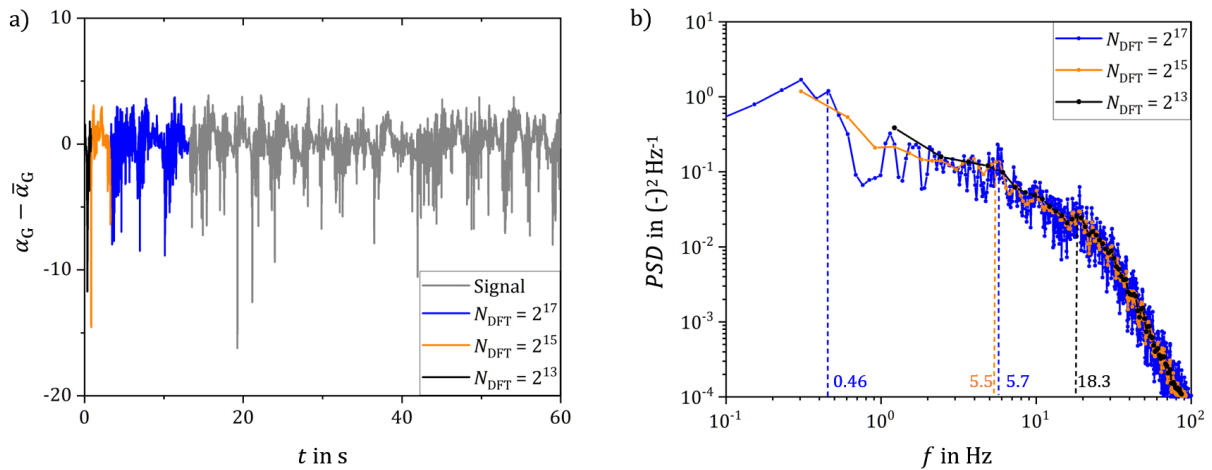


Figure 3.9: a) Visualization of the window length compared to the complete data set (normalized void fraction $\alpha_G - \bar{\alpha}_G$) and b) calculated PSD and obtained frequencies.

Consequently, the determination of the characteristic frequencies was performed iteratively for all window lengths. It should be mentioned that the selection of signal peaks is subjected to individual perception (e.g. for the peak at 0.46 Hz in Figure 3.9b). Note that not all data obtained in this work yielded reasonable frequencies from the respective PSDs and thus, were excluded from the analysis.

3.5 Measurement uncertainty

The data acquisition of the operating conditions differed between the DN200 feed pipe setup (manual read out of devices) and the DN50 feed pipe setup (automated system with a sampling rate of ca. 8 Hz for all sensors). The experiments in the DN200 feed pipe setup (Figure 3.6) resulted in flow morphologies with less pronounced fluctuations for which manual readings of the pressure and temperature sensors were sufficient.

Assuming isothermal flow, the average temperature between inlet and outlet of the test section could be calculated using the arithmetic mean (index ari) or logarithmic (index log) temperature difference. However, across all measurements this results in an average deviation of the gas density of $\Delta(|\rho_{G,inl} - \rho_{G,ari}|) = 8.6 \times 10^{-3} \pm 9.1 \times 10^{-3} \text{ kg m}^{-3}$ and $\Delta(|\rho_{G,inl} - \rho_{G,log}|) = 4.3 \times 10^{-3} \pm 4.6 \times 10^{-3} \text{ kg m}^{-3}$, which can be considered negligible.

Since the experiments were carried out for same volumetric flow rates (or superficial velocities), the uncertainty is determined by the measurements of temperature, pressure and flow rate of both phases, respectively. According to the error propagation law the uncertainty of the flow rate, $\Delta\dot{V}_k$, is determined from the uncertainty $E(x_{exp})$ of the measurand x_{exp} multiplied with the partial derivative of the correlation for $\dot{V}_{k,inl}(x_{exp})$ with respect to x_{exp} according to

$$\Delta\dot{V}_{k,inl} = \sqrt{\sum_{n_m=1}^{n_{m,max}} \left(\frac{\partial \dot{V}_{k,inl}(x_{exp})}{\partial x_{exp}} E(x_{exp}) \right)^2}. \quad 3.8$$

The mean uncertainty of the measurand was obtained from the statistical uncertainty of the recordings ε_1 and the uncertainty of the measurement device ε_2 according to

$$E(x_{exp}) = \sqrt{\varepsilon_1^2 + \varepsilon_2^2} = \sqrt{\left(\frac{\sigma_{exp}}{\sqrt{n_{m,max}}} \right)^2 + \varepsilon_2^2}. \quad 3.9$$

In Equation 3.9, σ_{exp} refers to the standard deviation of $n_{m,max}$ recordings and ε_2 is the uncertainty specified by the technical data sheet of the measurement device.

Appendix A.7 presents detailed information about the respective measurement uncertainty of the applied measurement techniques in this work. Table 3.3 shows the resulting measurement uncertainties applying Equations 3.8 and 3.9.

Table 3.3: Measurement uncertainty of the measured flow rates in both test sections.

Geometry	Phase k	$\Delta\dot{V}_k$ (average)		$\Delta\dot{V}_k$ (maximum)	
		l h ⁻¹	%	l h ⁻¹	%
DN200 feed pipe setup	G	46.2×10 ³	6	244×10 ³	6
	L	11.9 ×10 ¹	0.5	22.0 ×10 ¹	0.5
DN50 feed pipe setup	G	0.17×10 ⁻³	1.4×10 ⁻³	0.99×10 ⁻³	6.9×10 ⁻³
	L	0.15×10 ⁻³	5.3×10 ⁻³	0.69×10 ⁻³	22.9×10 ⁻³

According to Tompkins et al. (2018), the measurement uncertainty of the void fraction data obtained from the WMS measurements is dominated by

- current measurement (pre-amplification, uncertainty of the current measurements) and transformation of the digital signals into void fraction,
- physical dimensions of the sensor,
- intrusiveness of the sensor.

Previous validation studies (Sharaf et al., 2011; Velasco Peña and Rodriguez, 2015; Tompkins et al., 2018) compared the results obtained from WMS measurements with other state of the art measurement principles. Accordingly, average uncertainties of $\pm (2 - 5) \%$ to $\pm (10 - 11) \%$ (Tompkins et al., 2018) can be expected, depending on the flow morphology. While WMS were considered sufficiently accurate to capture characteristic features of the investigated flow morphologies, small-scale or local phenomena (e.g. droplet entrainment) cannot be captured (Theßeling and Grünewald, 2019).

The invasive nature of the measurement principle is known to influence the flow morphology downstream of the sensors by the reduced flow cross-section (Tompkins et al., 2018). Studies confirmed promoted bubble breakup and bubble acceleration (Tompkins et al., 2018) or increased pressure drop (Velasco Peña and Rodriguez, 2015), however, WMSs are still considered as accurate measurement technique. Preliminary tests revealed the small influence of the upstream WMSs on the recordings of the downstream WMS as illustrated in Figure 3.10.

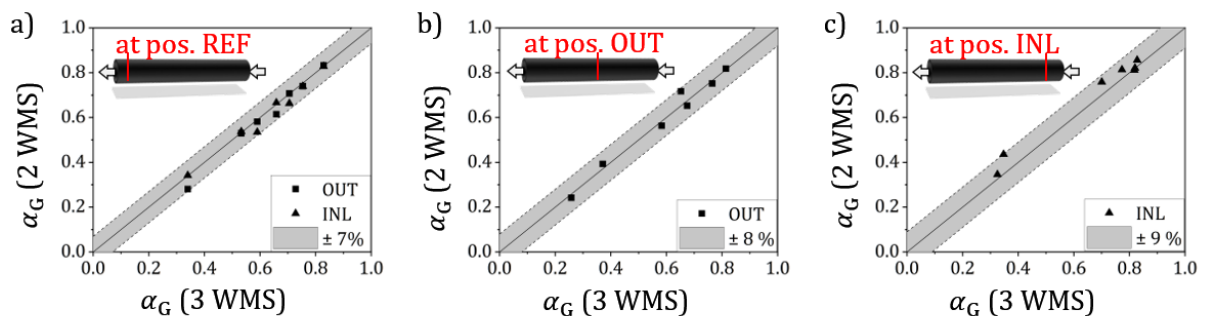


Figure 3.10: Recorded void fraction data at measurement position a) REF, b) OUT, c) INL, for two simultaneously installed WMS compared against the data for three installed WMS. Symbols indicate the installation position of the upstream WMS (INL or OUT) in the reference diameter test section (straight pipe configuration).

Figure 3.10 compares void fraction data obtained in the straight test section with three WMSs simultaneously installed (abscissa) against the data obtained when only two WMSs were installed (at position REF and at positions INL or OUT). The data are compared for each measurement position individually (Figure 3.10a to c) and the maximum relative deviation is highlighted by the

gray background. Note that the maximum deviation is attributed to single measurements that are shown for reference only. Fairly low average deviations of 3.5 % (REF), 2.1 % (OUT) and 3.1 % (INL) were obtained, which confirms that a negligible effect of the intrusive WMSs for the experimental method.

Wiedemann et al. (2020) demonstrated an influence of temperatures changes between reference measurement and two-phase measurement on the void fraction. In this work, the influence of the fluid temperature was compensated by repeating the reference measurements multiple times during the measurement campaigns. Additionally, repeated measurements revealed the statistical deviations of the captured void fraction data, i.e. $\pm 5.2 \times 10^{-3}$ absolute percentage points of the void fraction (± 0.7 % relative deviation) and $\pm 7.3 \times 10^{-3}$ absolute percentage points of the void fraction (± 4.7 % relative deviation) in the DN200 and DN50 feed pipe setups, respectively.

4 Flow morphologies in different feed pipe geometries

This chapter presents developing two-phase flows in the vicinity of different pipe curvatures. The flow morphologies are classified by the advanced FFPI classification introduced in Section 3.4.1.

Parts of this chapter have been published in:

Döß, A., Schubert, M., Hampel, U., Mehringer, C., Geipel, C. and Schleicher, E. (2021). Two-Phase Flow Morphology and Phase Fractions in Larger Feed Line Sections. *Chemie Ingenieur Technik* **93**, 1134–1141.

Döß, A., Schubert, M., Wiedemann, P., Junge, P., Hampel, U., Schleicher, E., Mehringer, C. and Geipel, C. (2021). Flow Morphologies in Straight and Bent Horizontal Pipes. *ACS Engineering Au* **1**, 39–49.

4.1 Developing two-phase flow in straight pipes

The two-phase flow in the straight pipe (DN50 feed pipe setup) was analyzed at positions INL, OUT and REF. Figure 4.1 allocates the identified main morphologies via FFPI (Section 3.4.1). Figure 4.1a to Figure 4.1c reveal the different entrance lengths required for the development of the respective morphologies in the DN50 feed pipe setup. Large regions of annular (A) and bubbly (B) flow at the inlet illustrate the influence of the mixing geometry causing pronounced liquid dispersion and bubble generation at position INL, respectively. Downstream the inlet, the areas occupied by both morphologies clearly shrink. Hence, this represents an increasing degree of membership to the intermittent morphology, i.e. the flow fluctuates (higher waves amplitudes and frequencies or even pseudo-slugs) and destabilize. The annular morphologies are fully developed at $L/D = 30$ (OUT). Along the pipe, the region of the intermittent morphology (I) spreads towards lower liquid mass fluxes as a result of growing waves (transition region between stratified and intermittent).

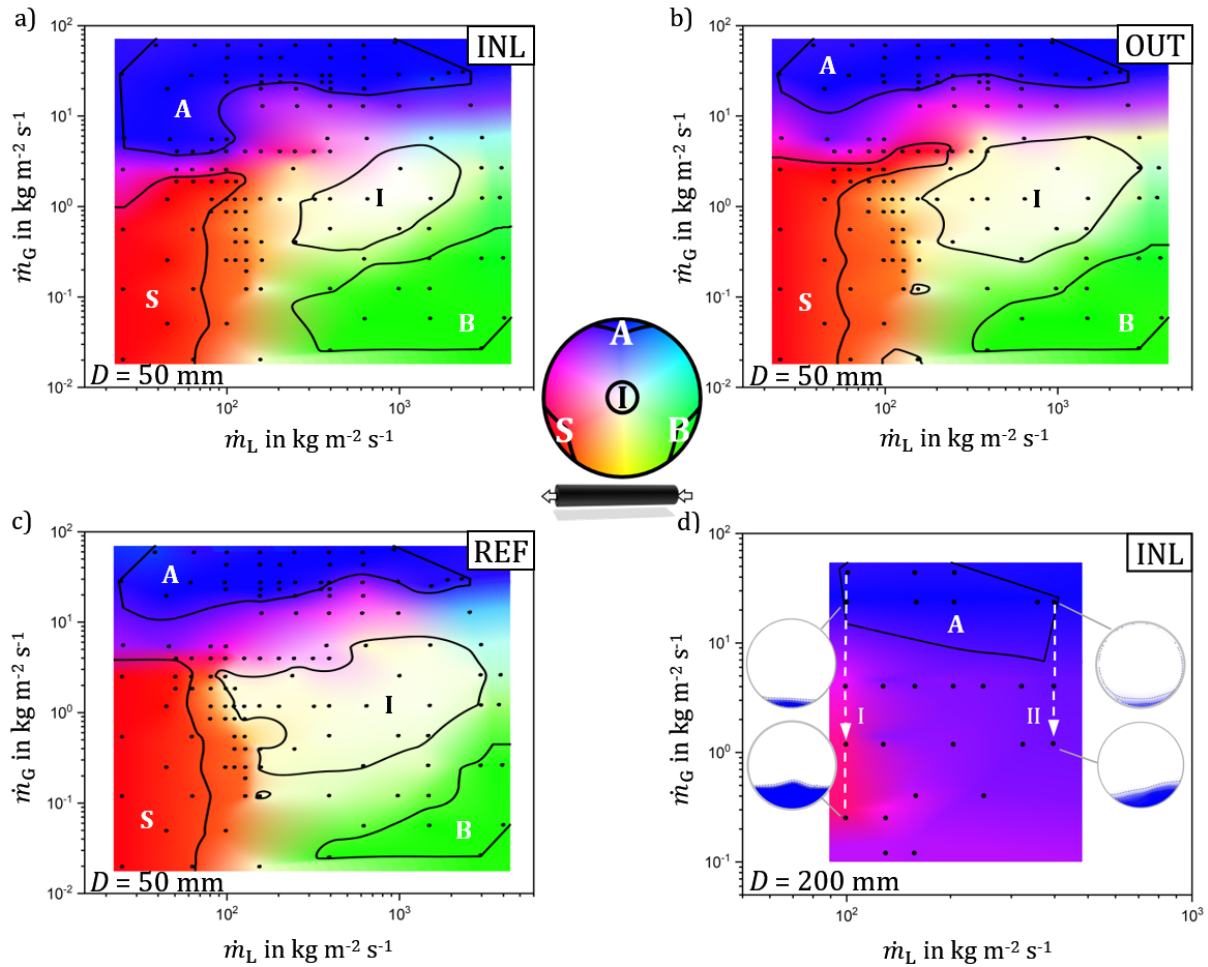


Figure 4.1: FFPI-based morphology classification of the developing two-phase flow in the DN50 feed pipe setup at positions a) INL, b) OUT, c) REF and d) in the DN200 feed pipe setup at position INL (with examples of time-averaged void fraction images).

Complementary measurements at same gas and liquid mass fluxes ($\dot{m}_{G/L}$) were performed in the DN200 feed pipe setup. The corresponding flow morphologies obtained via FFPI at $L/D = 10$ are shown in Figure 4.1d. The flow morphologies encountered in the DN200 pipe are FFPI-classified as either annular ($\dot{m}_G > 10 \text{ kg m}^{-2} \text{s}^{-1}$) or transitional stratified-wavy ($\dot{m}_G < 10 \text{ kg m}^{-2} \text{s}^{-1}$). However, the expansion of the annular region in Figure 4.1d reveals a more pronounced degree of membership towards annular flow at higher \dot{m}_L , which is also illustrated by the dispersion at the gas-liquid interphase and the circumferential liquid spreading. Compared with the $D = 50 \text{ mm}$ annular flow counterpart, however, the gas-liquid interphase is less distinctive (emphasized by the iso-lines in the embedded cross-sectional images in Figure 4.1d). Moreover, the void fraction in the large diameter test section is significantly higher at identical mass fluxes and the resulting morphologies feature low degrees of membership to the intermittent morphology. This is exemplarily shown in Figure 4.2 via ‘paths’ (I, II) along constant liquid mass fluxes \dot{m}_L . It is obvious that, for the same range of mass fluxes, the flow in the DN50 feed pipe setup experiences more

pronounced morphology changes. However, the overlap of the paths in the annular region of Figure 4.2 (represented by blue color) indicate similar flow features in both test sections.

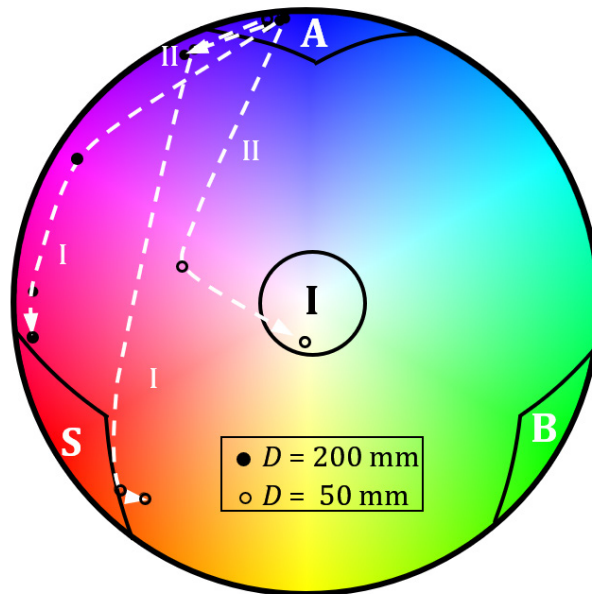


Figure 4.2: Effect of \dot{m}_G on the flow morphology for both feed pipe setups at (I) $\dot{m}_L = 100 \text{ kg m}^{-2} \text{ s}^{-1}$ and (II) $\dot{m}_L = 400 \text{ kg m}^{-2} \text{ s}^{-1}$.

4.2 Effect of pipe curvatures on the flow morphology

Bends are essential parts of commercial piping between process components. Their effects on the flow morphology upstream (position INL) and downstream (position OUT) the bent configurations (Table 3.2) are discussed here.

Figure 4.3 illustrates the two-phase morphologies featuring the FFPI-based morphology classification for both S-bend configurations. At low gas fluxes ($\dot{m}_G < 1 \text{ kg m}^{-2} \text{ s}^{-1}$), the upright S-bend causes intermittent flow as a result of the temporary blocking of the vertical pipe cross-section with accumulated liquid (Figure 4.3a). Stratified morphologies occur for high gas mass flux at low liquid mass flux and most of the neighboring transitional morphologies involve fluctuations and instabilities (higher degrees of membership to intermittent flow), as indicated by lower color intensity. The mixing induced by the twofold re-orientation of the flow shifts most of the intermittent morphologies towards the transition between annular (blue) and bubbly (green) morphologies for high and low gas mass flux, respectively (Figure 4.3b).

The horizontal S-bend has less influence on the flow morphology at inlet and outlet than the vertical S-bend (compare Figure 4.3a and b with Figure 4.3c and d). For high liquid mass flux, the horizontal S-bend promotes bubble coalescence (the bubbly regime disappears comparing Figure 4.3c and d) and more fluctuating morphologies at low and high gas mass flux, respectively. The transition region between stratified and intermittent patterns reveal less dynamics (lower

degrees of membership to the intermittent morphology) than in the straight pipe configuration (compare Figure 4.3d with Figure 4.3c and Figure 4.1b). This indicates an overall tendency of the S-bend to silence entering wavy morphologies, thus, suspending wave growing along the pipe.

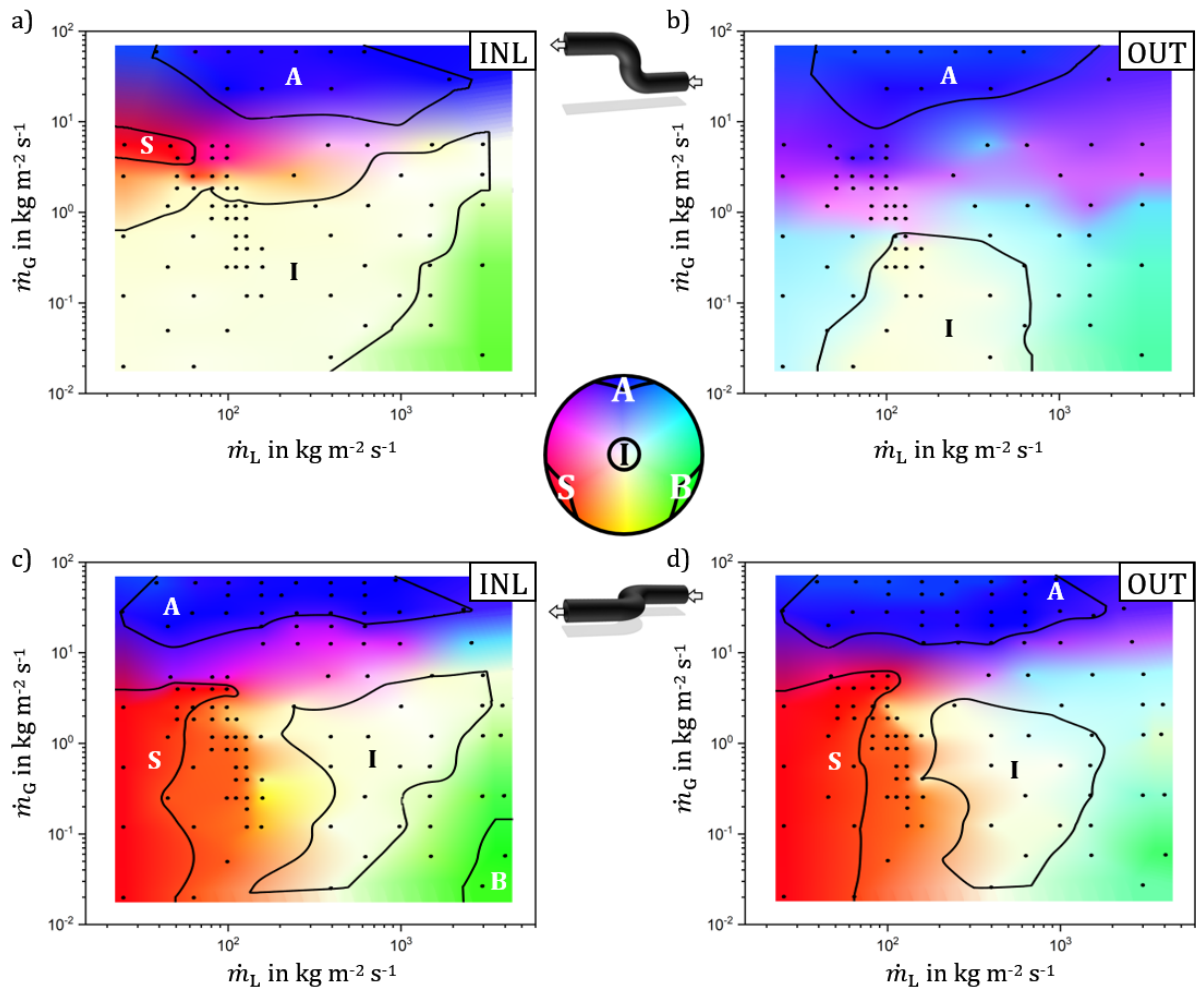


Figure 4.3: FFPI-based morphology classification of the developing two-phase flow in the DN50 feed pipe setup with upright S-bend at positions a) INL and b) OUT and with horizontal S-bend at position c) INL and d) OUT.

Figure 4.4 summarizes the identified two-phase morphologies for the horizontal 90° bend in both feed pipe sections. The encountered morphologies in the DN50 feed pipe section fairly coincide with those of the straight pipe (compare Figure 4.1c and Figure 4.4a). For low liquid mass flux, the bend fosters circumferential liquid spreading and dispersion (promoting annular morphologies) at the outlet (extension of the annular region in Figure 4.4b).

For higher liquid mass flux, the transitional morphologies shift from irregularly shaped, large amplitude waves towards more violently pseudo-slug flow, i.e. the degree of membership to stratified flow decreases and the degree of membership to bubbly increases. Similar to the horizontal S-bend (Figure 4.3b), the transition region between stratified and intermittent flow is

more distinct because only few slugs survive the sudden re-orientation. Moreover, pronounced coalescence at inlet and outlet (bubbly morphology was not observed) indicate the upstream effects of both bends.

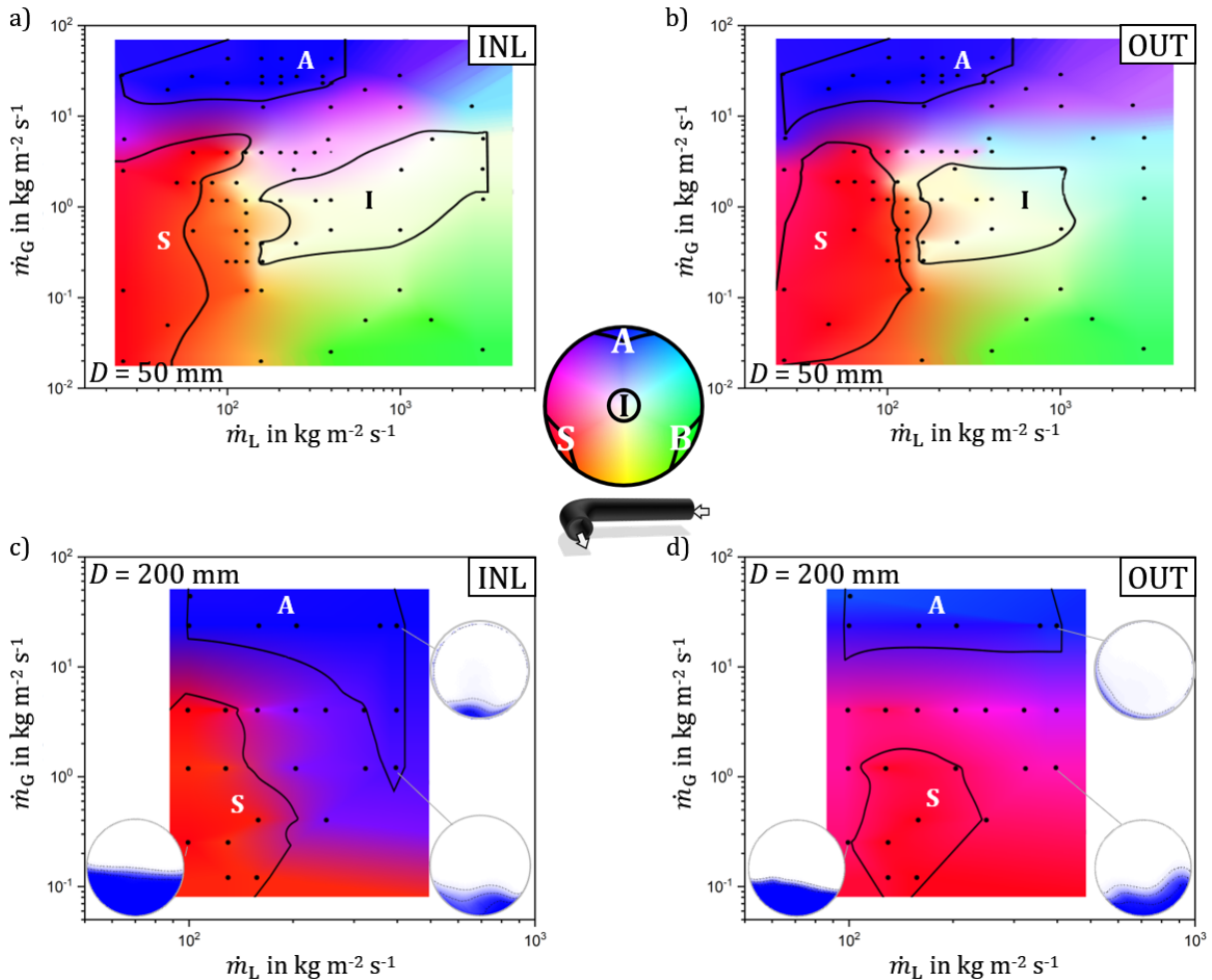


Figure 4.4: FFPI-based morphology classification of the developing two-phase flow in the horizontal 90° bend in the DN50 feed pipe setup at positions a) INL and b) OUT and in the DN200 feed pipe setup at positions c) INL and d) OUT. The flow direction is towards the image plane.

The horizontal 90° bend in the DN200 feed pipe section shifts stratified and annular morphologies (Figure 4.4a) towards transitional morphologies with irregular interface with a high degree of membership of the stratified morphology (Figure 4.4 b). At low mass flux, liquid accumulates upstream the bend and higher liquid levels are obtained at the inlet compared with the outlet or the straight pipe (see Figure 4.1a). The comparison of the degrees of membership at positions INL and OUT is provided in Appendix A.8

4.3 Morphology recovery

Preferably, pipe routing and plant design consider sufficient calming lengths downstream pipe curvatures to avoid or at least to minimize the occurrence of undesired flow morphologies (see

Section 4.2). The flow morphologies obtained far downstream the bends (position REF) are analyzed and compared with the morphologies at the inlet (referred to as ‘relative recovery’) and with the reference morphologies in straight pipes (referred to as ‘absolute recovery’). The FFPI method is applied again to assess the two-phase flow morphology recovery, i.e. whether the calming lengths were sufficient or not.

Figure 4.5 exemplarily shows the FFPI-based morphology classification and the (relative) morphology recovery for the upright S-bend at the reference position.

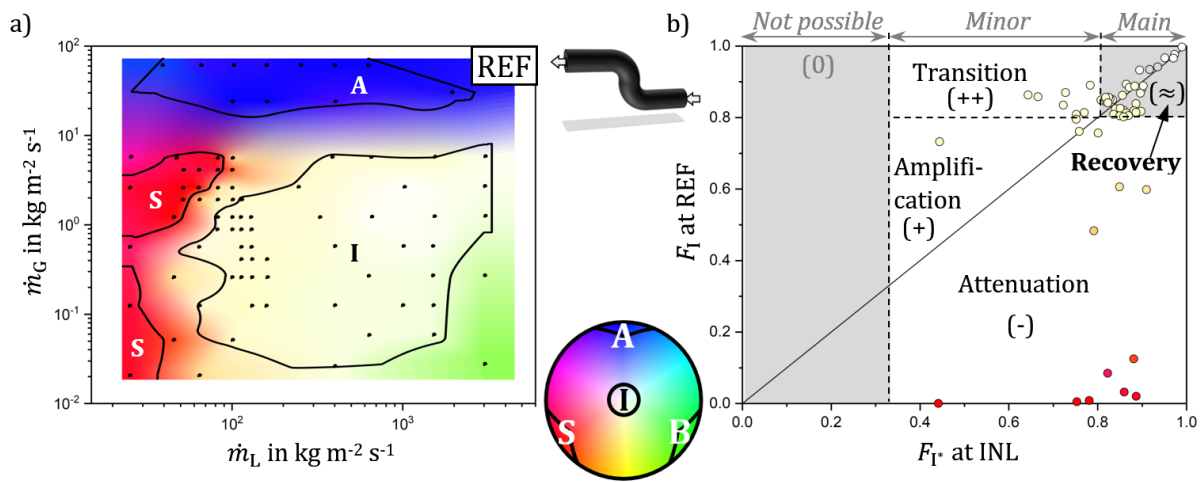


Figure 4.5: FFPI-based morphology classification for the developing two-phase flow in the upright S-bend (DN50 feed pipe setup) at position REF, b) parity plot of the morphology recovery exemplarily shown for F_I with colors referring to the morphology at the reference position (REF).

Figure 4.5a reveals that most of the transitional morphologies induced by the upright S-bend (compare with Figure 4.3b) change towards intermittent (I) flow similar to the bend inlet (Figure 4.3a). Furthermore, an additional stratified flow region is now established at low \dot{m}_L . In order to assess the morphology recovery, Figure 4.5b shows the parity plot of the degrees of membership to the intermittent regime F_I at positions INL (F_{I*}) and REF (F_I). For visual aid, only the dominant degrees of membership (indicated by the *, see Section 3.4.1) are shown on the abscissa of Figure 4.5b. Points located near the diagonal parity line ($F_{I*} = F_I$) for high values of $F_{I*} \geq 0.8$ indicate that the axial pipe length was sufficiently long to fully recover (or remain) the main inlet morphology, i.e. $L >$ entrance length. Based on the threshold between main and minor morphologies (Section 3.4.1), the parity plot can be subdivided into five characteristic regions (see Figure 4.5b):

- (\approx) Recovery: respective main morphology fully recovers,
- (++) Transition: initial morphologies change to different main morphologies,
- (+) Amplification: degree of membership of the initial morphologies increase,
- (-) Attenuation: degree of membership of the initial morphologies decrease,
- (0) Not possible: the normalized membership function f implies $1/3 < F_{n*} < 1$

Obviously, the majority of the main intermittent morphologies fully recover (\approx) or evolve as a result of a transition ($++$). Flow morphologies of the attenuation ($-$) or amplification ($+$) regions change towards other morphologies depending on the remaining three degrees of membership (note that F_A , F_B and F_S are not specified in Figure 4.5b). Detailed information about the morphology recovery for all degrees of membership (in terms of parity plots similar to Figure 4.5b) is provided in Appendix A.9.

The analysis in Section 4.2 revealed various upstream effects on the morphology, which superimposed the morphologies at outlet and reference locations of the bent pipes. In order to assess whether the two-phase flow morphology downstream bends recovers being comparable to that of the straight pipe at the reference position, the 'absolute recovery' is presented. Figure 4.6 shows parity plots (bent vs. straight pipe) at the reference position (REF) for representative degrees of membership F_h .

Figure 4.6 exemplarily shows the degrees of membership of intermittent (Figure 4.6 a-c) and annular (Figure 4.6d) morphologies. Note that Figure 4.6 and similar plots in Appendix A.10 visualize the absolute morphology recovery, i.e. the abscissa are not limited to the dominant degree of membership. Detailed information about the absolute morphology recovery for all degrees of membership (in terms of parity plots similar to Figure 4.6) is provided in Appendix A.10.

The upright S-bend (Figure 4.6a) induces sustainable morphology changes towards intermittent flow ($F_I > 0.8$) at the reference position compared with transitional morphologies in the straight pipe ($F_I < 0.8$). Contrary, the horizontal bends (Figure 4.6b and c) cause less pronounced formation of intermittent morphologies. Moreover, instead of intermittent morphologies encountered in straight pipes, stratified flow (red color) evolves. Similar behavior is observed for the horizontal 90° bend (DN200 feed pipe setup, Figure 4.6d), which fosters changes from annular to stratified morphologies as a result of the sudden re-orientation.

For all investigated curvatures, comprehensive look-up tables for the morphology recovery are provided in Appendix A.11. It can be concluded that the proposed calming lengths are not sufficient to counteract the effects of pipe curvatures (except for the main annular morphologies that remain mostly the same), which is significantly different from the conclusions derived from Table A.4 for the relative morphology recovery. This further emphasizes that design guidelines for straight pipes, such as conventional flow regime maps, are not applicable in the vicinity of curvatures.

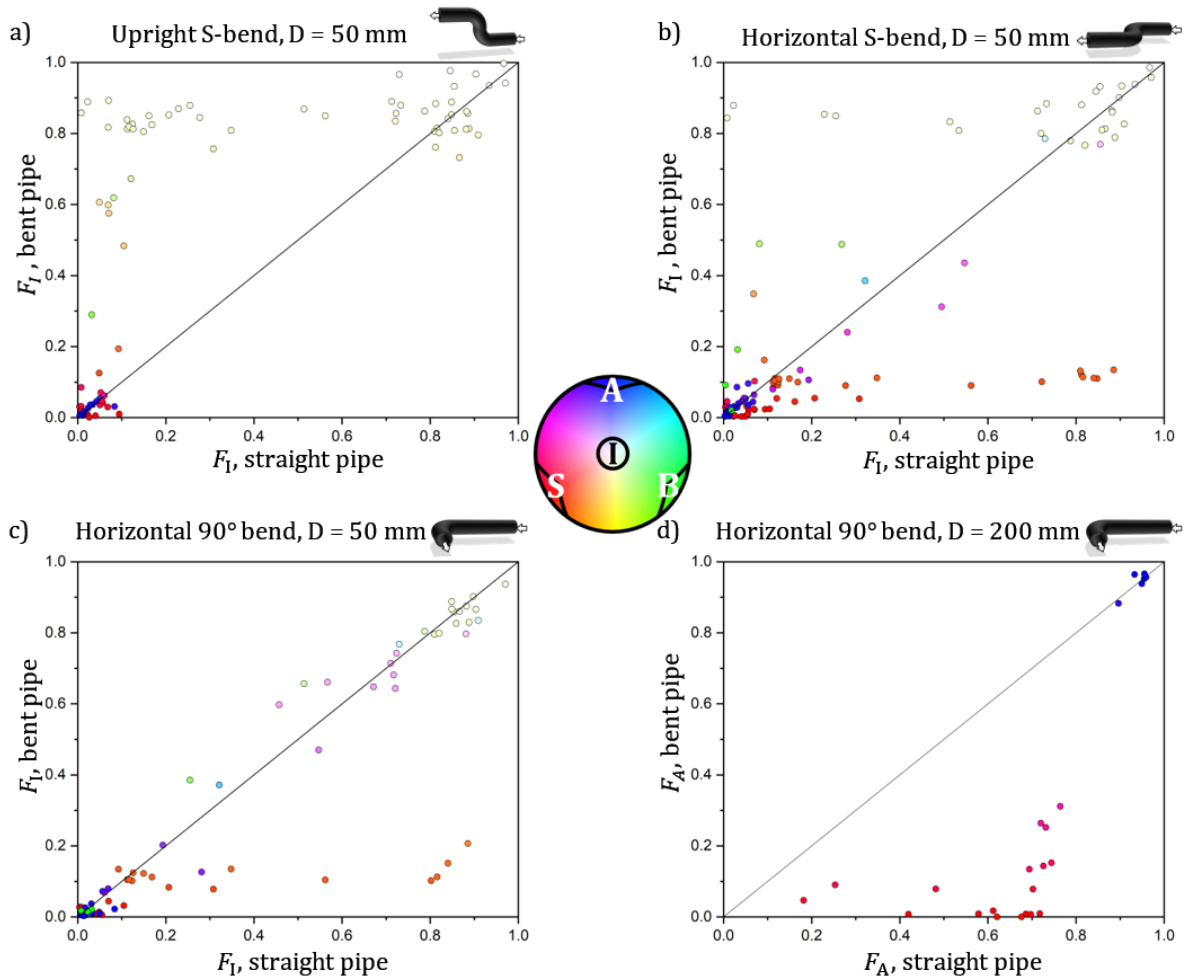


Figure 4.6: Parity plots of the absolute morphology recovery (at position REF) with colors referring to the morphologies of the bent pipes.

4.4 Conclusions

The comprehensive database generated in this work illustrates the axially developing two-phase flows for the first time and reveals the influence of pipe curvatures on upstream and downstream flow morphologies. An advanced fuzzy-based classification method was developed and utilized to characterize the flow behavior in an objective manner. The main findings are:

- Larger pipe diameter show less pronounced morphology changes for equal mass fluxes.
- Phase maldistributions introduced by the curvatures at high flow rates can survive along feed pipes of industrial distillation columns.
- For short entrance lengths, the main morphologies recover from the influence of curvatures, while transitional morphologies require longer entrance lengths.
- Full recovery of the flow morphologies is achieved only for pressure-driven morphologies, while the recovery of gravity-driven flow morphologies further depends on the entrance length.
- 90°-horizontal bends provide beneficial stratification of the flow morphology.

5 Prediction of undesirable flow morphologies in feed pipes

This chapter presents methods and criteria to predict undesirably flow morphologies for feed pipes. These include intermittent flows, which are difficult-to-handle and for which initiation with respect to the entrance length should be predicted. Flow morphologies that involve the onset of entrainment are particularly important during the feed pipe design as additional droplet separation equipment must be provided. The onset is linked to wavy morphologies where the bulk phase is expected to carry characteristic properties. Such characteristics can be tracked to obtain a predictive criterion for the onset of entrainment.

5.1 Initiation of intermittent flows

Based on the FFPI morphology classification introduced in Section 3.4.1, the entrance lengths in the DN50 pipe were determined, where intermittent flow was initiated. Figure 5.1 shows the experiments with observed intermittent flows (position REF).

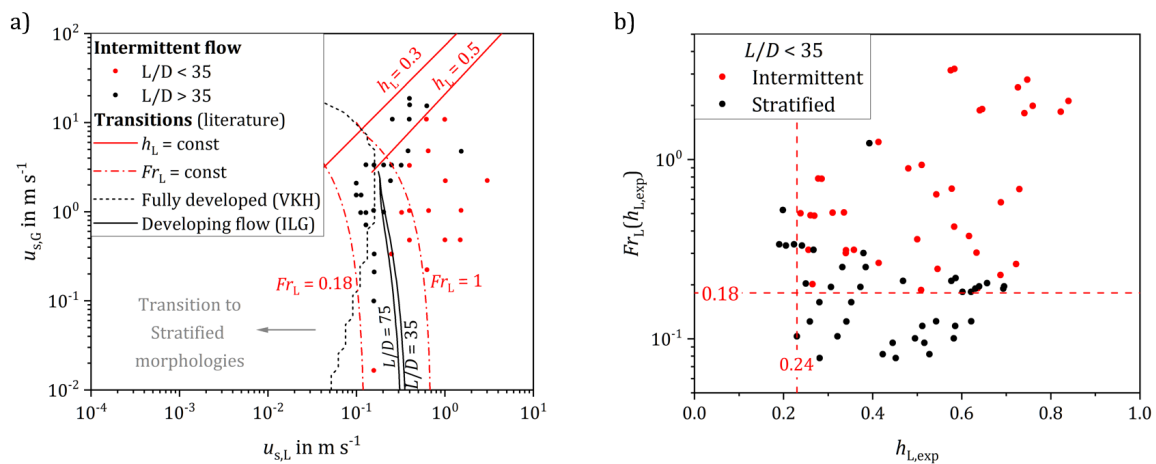


Figure 5.1: a) Experimentally observed intermittent flow for short (red symbols) and long entrance lengths (black symbols) compared with model predictions shown as transition lines, b) clustering of intermittent flows based on liquid Froude number Fr_L (calculated via measured liquid level $h_{L,exp}$).

Intermittent flow at higher water-air superficial velocities evolve regardless of the entrance lengths (red symbols in Figure 5.1a). At moderate superficial velocities, the onset depends on the entrance length (black symbols in Figure 5.1a), i.e. stratified morphologies were observed at sensor positions INL or OUT. The transition criteria $Fr_L = 1$ (see Section 2.2.1) proposed by Woods and Hanratty (1999) for $L/D = 40$ does not properly distinguish between both datasets. Improved classification is achieved by reduced-order models (black lines) with assumed ILG (solid lines). The dashed line resembles VKH and is shown as reference only. However, the transition lines based on ILG are less sensitive to the axial position. $L/D = 75$ is the entrance length for measurement position REF, where intermittent flow was observed at lower superficial liquid velocities than assumed by the ILG transition line. At higher gas superficial velocities, $h_L = 0.5$ also underpredicts the initiation of intermittent flow.

Figure 5.1b clusters the data for stratified and intermittent flow morphologies in terms of liquid level and Froude number, which are commonly used to describe the transition between both morphologies (see Section 2.2.1). The values for Fr_L (Equation 2.3) were calculated from the time-averaged liquid level (obtained experimentally according to Equation 2.22) for the experiments in Figure 5.1a at small entrance lengths (locations INL and OUT). The lower limit, i.e. the minimum amount of liquid that must be supplied at higher gas flow rates (see Section 2.2.2) is resembled by $h_{L,exp} = 0.24$, which is within the interval $0.2 \leq h_L \leq 0.3$ proposed by Woods and Hanratty (1999). At higher liquid levels, $Fr_L = 0.18$ is proposed to predict the onset of intermittent flow as a conservative limit as shown in Figure 5.1a.

5.2 Onset of droplet entrainment

In the following section, an empirical approach is developed that identifies conditions for separated flows that are prone to droplet entrainment. This holds in particular for annular and stratified wavy flow morphologies.

5.2.1 Vulnerable flow morphologies

Figure 5.2 shows available literature data for detected entrainment and onset of entrainment for gas-liquid flows studied in horizontal pipes with hydraulic diameter $D_h = 50$ mm. It should be noted that the data were predominantly gathered from fully developed flows.

Data (blue symbols) and correlations (blue lines) reveal the onset of entrainment at superficial gas velocities $u_{s,G} > 10$ m s⁻¹. According to the flow regimes observed in this work (see gray lines for demarcation of respective flow regimes), the considered literature studies mostly addressed annular flows with pronounced liquid entrainment for fully developed flows (large entrance lengths). In other words, entrainment was only reported, when a significant number of droplets was impinged at the pipe walls or withdrawn from the bulk gas. Thus, it is a reasonable conclusion that annular flows can be generally considered to entrain droplets. Only Mantilla (2008) studied

the onset of entrainment for wavy flow morphologies below $u_{s,G} < 10 \text{ m s}^{-1}$, and stated that onset of entrainment occurred already at gas flow rates lower than reported.

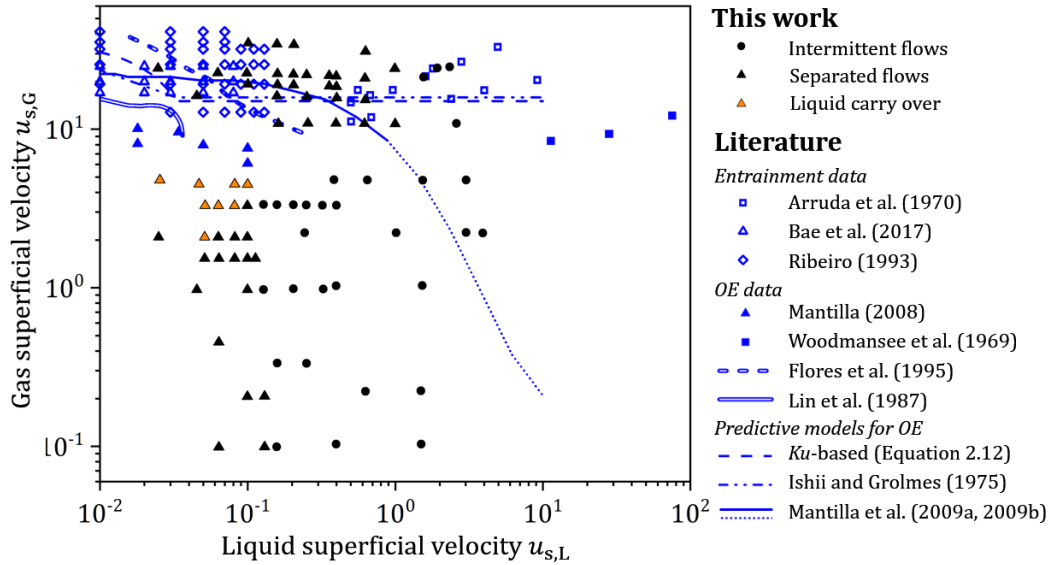


Figure 5.2: Flow regime map obtained from own data and literature data as well as predictive models for the onset of entrainment (OE). The blue shaded area indicates conditions requiring droplet separation from bulk gas.

The orange symbols in Figure 5.2 refer to flow morphologies that change from annular flow at the inlet ($L/D = 10$) towards wavy flow observed at $L/D = 75$. Here, the annular film gets fragmented along the test section. Liquid agglomerates and droplets are then carried with the bulk gas flow.

Figure 5.3 shows the axial transition of the flow morphologies visualized with the WMSs. It should be noted that some of the liquid agglomerates and droplets deposited on the sensor wires and remained there temporarily.

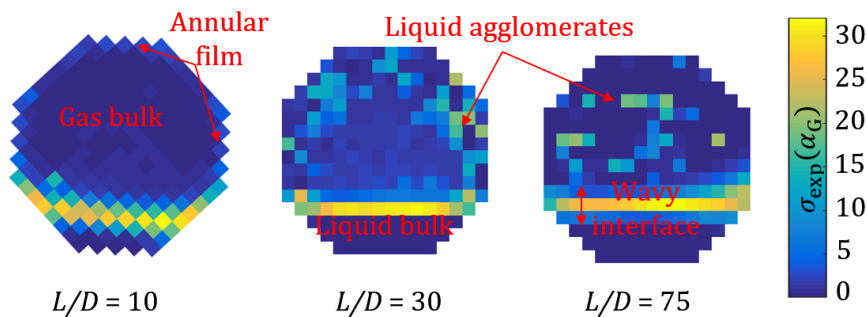


Figure 5.3: Standard deviation σ_{exp} of the void fraction data $\alpha_G(t)$ per sensor crossing point ($u_{s,G} = 3.29 \text{ m s}^{-1}$, $u_{s,L} = 0.08 \text{ m s}^{-1}$, straight pipe, DN50 feed pipe setup) at three axial locations. High values for σ_{exp} in the gas bulk region account for entrained liquid agglomerates and droplets.

The conductivity-based WMSs can only detect larger liquid agglomerates that occupy a significant amount of the volume within a virtual crossing point. Nonetheless, it is obvious that small droplets get entrained, too, and accompany liquid agglomerates detected in Figure 5.3. Hence, the shaded area in Figure 5.2 covers all flow conditions prone to entrainment, where liquid separation from the bulk gas is required.

5.2.2 Derivation of a criterion for onset of entrainment

Currently, there is no general agreement on the governing mechanism responsible for the onset of entrainment. It is assumed that either small amplitude ripple waves (Ishii and Grolmes, 1975) or shear-off from larger amplitude ripple waves (Bothamley, 2013a) eventually cause entrainment (see Section 2.2.2). However, the relation between wave dynamics (frequency, amplitude, wavelength, celerity) and onset of entrainment is an open question. Thus, dominant frequencies from the WMS time series data for experiments within and outside the dashed area (Figure 5.2) were determined from the PSDs via discrete Fourier transformation (see Section 3.4.2). The dominant wave frequency f_W can be expressed with the dimensionless Strouhal number as

$$St_{s,L} = f_W \frac{D}{u_{s,L}} \quad 5.1$$

using the pipe diameter D and superficial liquid velocity $u_{s,L}$ (Alamu and Azzopardi, 2011). Al-Sarkhi and Sarica (2010) introduced the Lockhart-Martinelli number

$$LMN = \frac{Fr_{s,L}}{Fr_{s,G}} = \frac{u_{s,L}}{u_{s,G}}, \quad 5.2$$

to correlate $St_{s,L}$ according to

$$St_{s,L} = C_1 \cdot LMN^{e_1}, \quad 5.3$$

where C_1 and e_1 are empirically parameters. Figure 5.4 visualizes the relation between $St_{s,L}$ and LMN for literature data and own experiments (based on the DFT analysis) as well as empirical models. The models are valid for $10^{-2} \leq LMN \leq 10^0$ based on the available experimental data (see Appendix A.12). The Strouhal numbers obtained via DFT from the experiments of this work are in good agreement with the literature. Symbols with colored inserts in Figure 5.4 indicate entrainment in form of droplets (blue, annular flow morphologies) or liquid carry-over (orange, wavy flow morphologies). The data reveal a slope change at the transition from separated flow (triangles) to intermittent flow (circles) as well as a kind of bifurcation for the separated flow (gray areas).

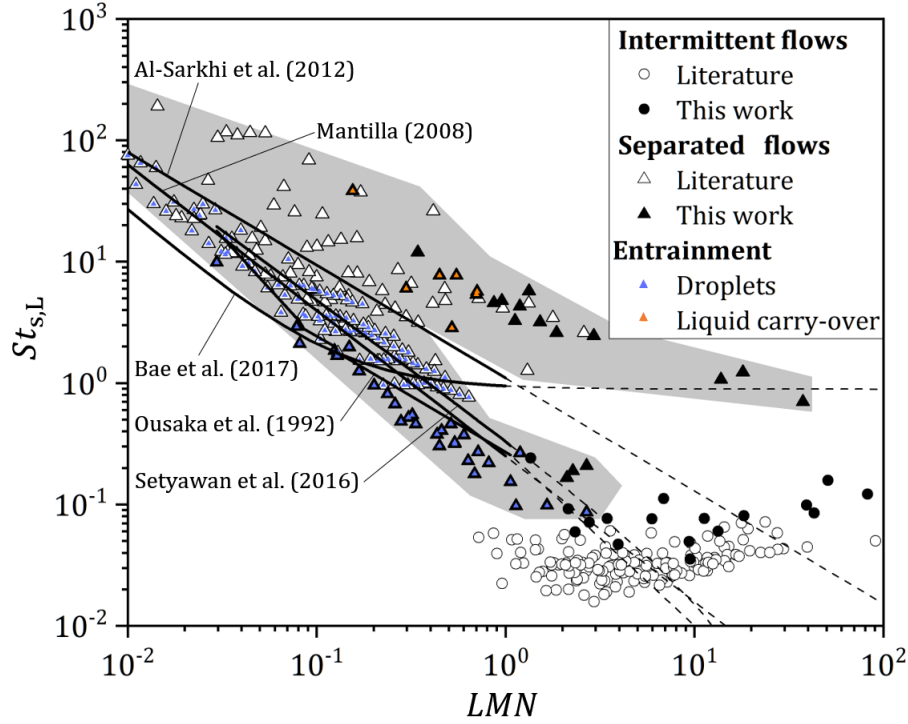


Figure 5.4: Relation of $St_{s,L}$ and LMN for separated and intermittent flow data with and without entrainment and liquid carry-over (lines represent literature correlations for $St_{s,L}$).

Thus, criteria to identify flow morphologies that are prone to liquid entrainment based on $St_{s,L}$ and LMN have the following weaknesses²:

1. Separated and intermittent morphologies can hardly be distinguished
2. $St_{s,L}$ and LMN based on superficial velocities ignore the impact of the pipe geometry³ and require additional geometry constraints.

Thus, a notation inspired by Setyawan et al. (2016) according to

$$St_{s,L} = C_2 F_1 \cdot \left(\frac{Re_{s,L}}{Re_{s,G,mod}} \right)^{e_2} \quad 5.4$$

is further used, where F_1 is a function of the fluid properties according to

$$F_1 = \left(\frac{\rho_L}{\rho_G} \right)^{0.574} \left(\frac{\eta_L}{\eta_G} \right)^{-1.148} \left(\frac{\sigma_L}{\sigma_{Water}} \right)^{0.11} \quad 5.5$$

$Re_{s,G,mod}$ is the modified superficial gas Reynolds number

² A similar behavior is obtained using $St_{s,G}$ instead of $St_{s,L}$, which is more commonly used for intermittent morphologies as proposed by Arabi et al. (2020), Fossa et al. (2003) and Wang et al. (2007).

³ According to Azzopardi et al. (2014), frequencies persist throughout pipe geometry changes (also termed to as 'flow memory').

$$Re_{s,G,mod} = \frac{D_h \rho_G}{\eta_G} (u_{s,G} - u_{s,L}). \quad 5.6$$

and $C_2 = 0.258$ and $e_2 = -1.148$ are empirical constants.

To consider changes in phase velocities and morphology resulting from pressure losses, changes in the cross-section or re-orientation due to bends, real phase velocities are applied for Re_L and $Re_{G,mod}$ according to

$$Re_L = \frac{D_h \rho_L}{\eta_L} u_L = \frac{D_h \rho_L}{\eta_L} \left(\frac{u_{s,L}}{(1 - \alpha_G)} \right) \quad 5.7$$

and

$$Re_{G,mod} = \frac{D_h \rho_G}{\eta_G} (u_G - u_L) = \frac{D_h \rho_G}{\eta_G} \left(\frac{u_{s,G}}{\alpha_G} - \frac{u_{s,L}}{(1 - \alpha_G)} \right). \quad 5.8$$

The void fraction α_G can be obtained directly from experimental or numerical data (if available), or from generalized models developed for particular pipe geometries. Consequently, Equation 5.4 becomes

$$St_{s,L} = C_3 \cdot \left(F_1 \cdot \frac{Re_L}{Re_{G,mod}} \right)^{-e_3} = C_3 \cdot \left(F_1 \cdot \frac{\rho_L \eta_G}{\rho_G \eta_L} \cdot (1 - R_S^{-1}) \right)^{-e_3}. \quad 5.9$$

Instead of using the *LMN*, the ratio $Re_L/Re_{G,mod}$ in Equation 5.9 can be expressed via slip ratio R_S (Equation 2.45) with C_3 and e_3 as empirical constants. For all calculations in this work, the impact of the two-phase pressure drop on fluid properties was considered via F_1 . Ultimately, a conceptual criterion for the onset of entrainment can be derived graphically as presented in Figure 5.5.

Here, Figure 5.5a visualizes the allocation of regions of separated flows without entrainment (black triangle), separated flows with entrainment or liquid carry-over (blue and orange triangles) and intermittent flows (black spheres). With the help of the empirical constants C_3 and e_3 (numerical values are provided in Table 5.1) and Equation 5.9 the limiting Strouhal number $St_{s,L,crit}$ (red line in Figure 5.5a) and a regression for the experimental data for each pipe geometry (black line in Figure 5.5a) is obtained.

The conceptual criterion for the onset of entrainment then becomes

$$St_{s,L} > St_{s,L,crit}. \quad 5.10$$

An alternative interpretation of the transition criterion is obtained when the relative velocity u_{rel} (interfacial shear) and the slip ratio (see Equation 5.9) are plotted in Figure 5.5b. The data refer to Figure 5.5a along three iso-lines of the Strouhal number $\bar{St}_{s,L} = \{9.3, 1.0, 0.1\}$. Increasing values $F_1 \cdot Re_L/Re_{G,mod}$ from right to left (shown by the gray arrow) indicate slip approaching

unity, i.e. more homogenous phase distribution. The onset of entrainment occurred for slip ratios $R_S > 7$, i.e. separated flows. For a fixed slip ratio, morphologies with liquid carry-over (roughly referring to $\bar{St}_{s,L} = 9.3$) shear-off at lower relative velocity, while droplet dispersion (referring to $\bar{St}_{s,L} = 1.0$ and $\bar{St}_{s,L} = 0.1$) requires higher values for u_{rel} .

It should be noted that few data (black triangles in the red shaded area) in Figure 5.5a fulfill Equation 5.10, although they were initially assigned as ‘no entrainment’ (outside of the dashed area in Figure 5.2). However, recalling that the wire-mesh sensor can hardly resolve small fractions of dispersed liquids, the presence of entrained droplets is not unlikely.

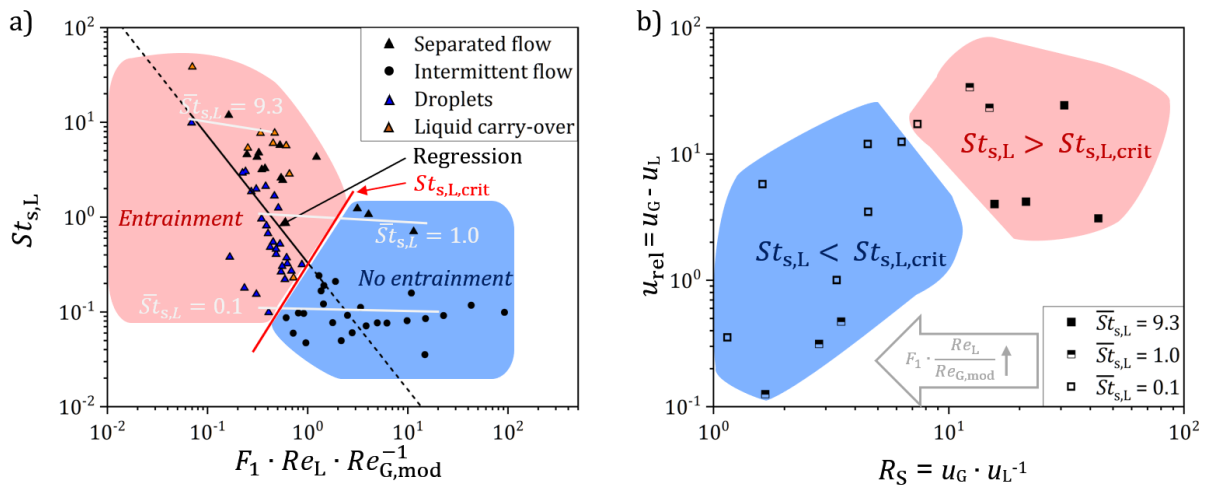


Figure 5.5: a) Graphical illustration of the conceptual criterion to predict the onset of entrainment (experimental data from this work: straight pipe, DN50 feed pipe setup), b) u_{rel} vs. R_S coordinates along iso-lines of average Strouhal numbers $\bar{St}_{s,L}$.

5.2.3 Adjustment of the criterion for the investigated pipe geometries

The new criterion (Equation 5.10) was developed based on literature data and own experimental data taken at entrance lengths $L/D \sim 75$, which represents nearly developed flow. Below, the criterion is also assessed for both test sections considering experimental data for entrance lengths of $L/D = 10$ in straight pipes (Figure 5.6) and horizontal 90° bends.

Figure 5.6a shows the entrainment classification for the reference feed pipe (DN50) based on the new Strouhal number criterion. In comparison to the more developed flow (red dotted line, $L/D = 75$), entrainment near the inlet (red solid line, entrance length of $L/D = 10$) occurs at lower shear force (represented by u_{rel}). In DN50 feed pipe section, only separated flows with a smaller range of Strouhal numbers were observed (Figure 5.6b). Using Equation 5.9 with the same empirical constants obtained for the reference feed pipe (DN50, red solid line in Figure 5.6a) predicts the presence of entrainment (red dotted line in Figure 5.6b) for all data, which was not confirmed visually during the experiments.

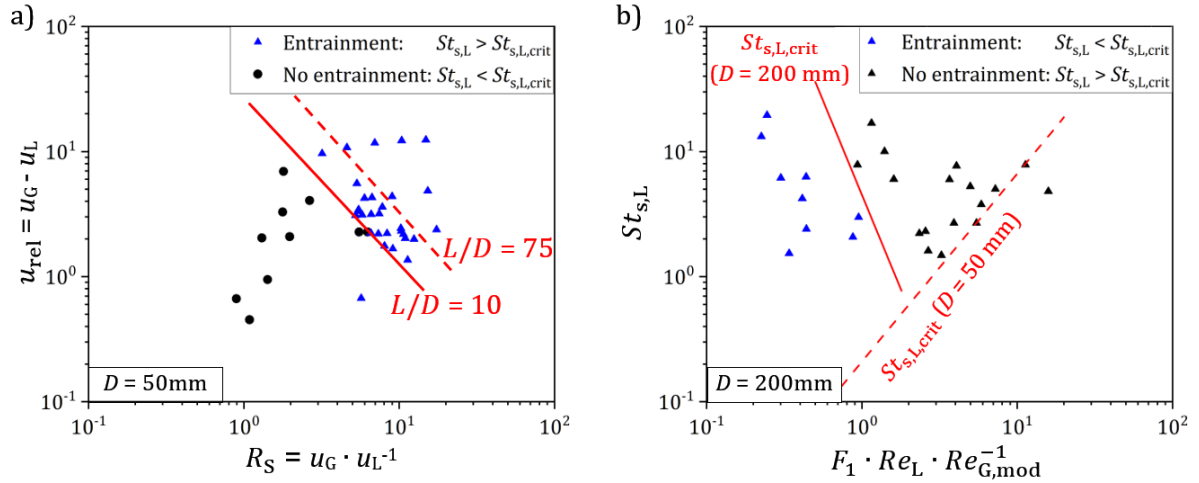


Figure 5.6: Entrainment prediction in straight pipes obtained at $L/D = 10$ for a) DN50 feed pipe setup, b) DN200 feed pipe setup.

Instead, it was assumed that similar interfacial shear (relative velocity) and slip are required for the onset of entrainment in both test sections. Hence, the transition for $L/D = 10$ in Figure 5.6a can be applied to classify the morphologies in the DN200 feed pipe setup (colored symbols in Figure 5.6b). Consequently, the parameters in Equation 5.9 were modified to obtain the $St_{s,L,crit}$ that classifies the morphologies as shown by the red solid line in Figure 5.6b. Contrary to $St_{s,L,crit}$ in the DN50 feed pipe (red dotted line in Figure 5.6b), $St_{s,L,crit}$ decreases with $F_1 \cdot Re_L / Re_{G,mod}$ and thus the comparative operator in Equation 5.10 inverts.

Ultimately, Equation 5.9 provides the basic formulation to obtain the critical Strouhal numbers ($St_{s,L,crit}$) for both pipe diameters as well as predictive correlations for the Strouhal number ($St_{s,L}$) in straight pipes and horizontal 90° bends. The latter can be used when no information about the characteristic wave frequencies of the desired morphologies are available. The empirical coefficients of Equation 5.9 are summarized in Table 5.1.

Table 5.1: Coefficients⁴ and validity for Equation 5.9.

Symbol	Description	D in mm	L/D	C_3	e_3	Range of $\frac{Re_L}{Re_{G,mod}}$
$St_{s,L,crit}$	Onset of entrainment	50	10 - 75	0.21	1.78	0.7 - 19
		200	10	4.50	-3.0	0.5 - 3.3
$St_{s,L}$	Straight pipe	50	75	0.33	-1.34	0.2 - 3.0
		50	10	1.53	-0.04	0.4 - 5.6
	200	10	4.80	-0.11	0.4 - 1.7	
	90° horizontal bend	50	10	0.26	-2.66	0.4 - 2.3
		200	10	2.75	-0.01	0.2 - 2.2

⁴ The coefficients were obtained via regression using OriginPro 2020. For simplicity, Strouhal numbers obtained for intermittent morphologies were neglected.

The conceptual criterion (Equation 5.10) allows identifying areas of flow regime maps, whose morphologies are prone to liquid entrainment. Examples for straight pipe and horizontal bend (DN50 feed pipe setup) are shown in Figure 5.7.

Equation 5.10 distinguishes the separated annular and wavy flow regions into conditions with and without entrainment (indicated by the blue area in Figure 5.7). The method is successfully applied to straight pipes and 90° horizontal bends for the DN50 reference pipe, respectively (Figure 5.7a and Figure 5.7b). Compared to the visual observation, the predicted entrainment area also covers the transition between separated and intermittent flows. Investigations (similar to Figure 5.3) of the WMS recordings in that region revealed liquid carry-over in the developing section of the two-phase flow (upstream locations $L/D = 30$ or $L/D = 10$ in the test section) that did not persist downstream. It can be concluded that the proposed criterion can be used as a conservative estimation regardless of the entrance length with slightly overprediction of the required $u_{s,G}$ for the onset of entrainment at higher entrance lengths.

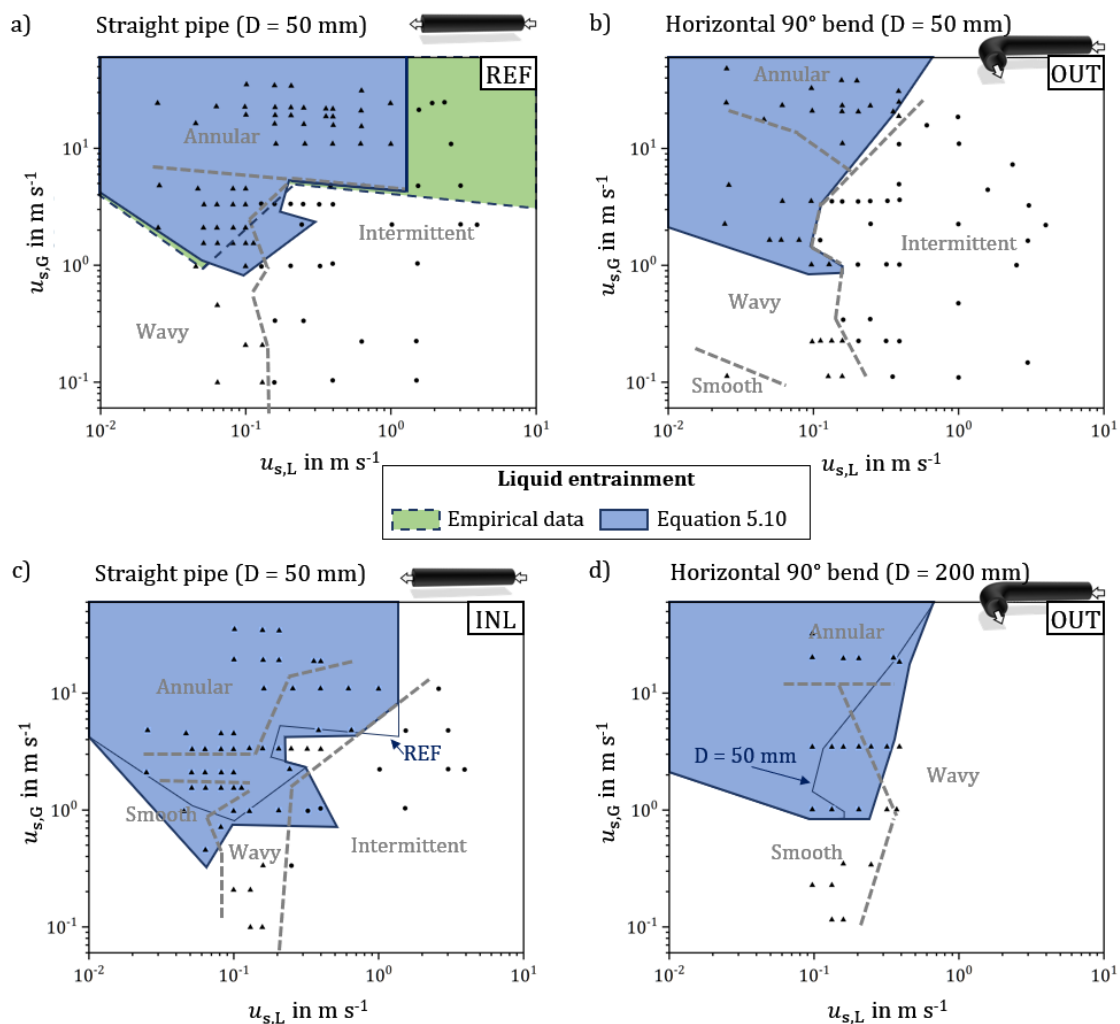


Figure 5.7: Identified flow morphologies (gray lines) with predicted areas (blue) prone to liquid entrainment: a) straight pipe (DN50) at position REF, b) 90°-horizontal bend pipe (DN50) at position OUT, c) straight pipe (DN200) at position REF, d) 90°-horizontal bend pipe (DN200) at position OUT.

5.3 Conclusions

The criteria derived in this chapter predict the occurrence of undesired flow morphologies (intermittent flows and entrainment) in two phase feeds. The experimentally observed inception of intermittent flows, were used to modify existing approaches. Wavy and annular morphologies involve characteristic flow dynamics that indicate the onset of entrainment. The predictive criteria derived from those dynamics provide a general understanding of the requirements for the onset of entrainment and can easily be applied to different flow scenario or pipe geometries if the phase fraction is known. The main findings are:

- Intermittent flows form above liquid levels $h_L = 0.2$ at high gas flow rates.
- For low gas flow rates and short entrance length, a two-fluid model that considered the interfacial level gradient (ILG) captured the transition from stratified to intermittent with acceptable agreement, but failed for larger entrance length.
- A more conservative approach for low gas flow rates is provided by the liquid phase Froude number, however, the values that represent the morphology transition depend on the entrance length.
- The onset of entrainment can be identified via frequencies obtained from void fractions signals of wire-mesh sensors.
- A conceptual criterium in terms of frequencies (Strouhal numbers) and Reynolds numbers describes the onset of entrainment, depending on interfacial shear (relative velocity) and phase separation (slip).
- Empirical factors for different pipe geometries were proposed that allow the classification of flow morphologies according to their susceptibility for entrainment by a universal correlation.

6 Reduced-order modelling of two-phase feeds

This chapter approaches ways to predict developing flows in straight pipes and horizontal 90° bends based on reduced-order models in order to predict relevant two-phase flow parameters such as void fraction or phase distribution, which are essential for a tailored design of two-phase feeds in separation columns. Reduced-order models are systematically analyzed and model parameters are adjusted to model developing two-phase flow in feed pipes. For stratified flows, the interfacial level gradient (ILG) and corresponding liquid levels are calculated based on a two-fluid model and assessed with regard to measured counterparts.

Parts of this chapter have been published in:

Döß, A., Schubert, M., Hampel, U., Mehringer, C., Geipel, C. and Schleicher, E. (2021). Two-Phase Flow Morphology and Phase Fractions in Larger Feed Line Sections. *Chemie Ingenieur Technik* **93**, 1134–1141.

6.1 Prediction of void fraction

Currently, 66 reduced-order models that provide an algebraic relation for the void fraction $\alpha_{G,corr}$ are in principle applicable to horizontal flows. However, unspecified validity ranges, unavailable primary sources and references as well as deficient descriptions in recent review articles (Coddington and Macian, 2002; Woldesemayat and Ghajar, 2007; Godbole et al., 2011; Pietrzak and Płaczek, 2019; Márquez-Torres et al., 2020) impose challenges for their application. Since the available models describe the two-phase flows quite differently (see Section 2.3), a statistical analysis was initially performed to identify models that are capable of describing undeveloped flows. All model predictions were compared against experimental data from both straight pipe configurations at reference measurement location (REF). The absolute deviation $\Delta\alpha_G$ from the void fraction data $\alpha_{G,exp}$ for each experiment is

$$\Delta\alpha_G = |\alpha_{G,corr} - \alpha_{G,exp}|. \quad 6.1$$

To assess the correlations for a wide range of operating conditions (flow morphologies), the variance between minimum, average and maximum of $\Delta\alpha_G$ was used for comparison according to

$$VAR(\alpha_{G,corr}) = \text{var}(|\min(\Delta\alpha_G)|, |\Delta\bar{\alpha}_G|, |\max(\Delta\alpha_G)|). \quad 6.2$$

The variance $VAR(\alpha_{G,corr})$ of the deviations were determined per model class (SLM, HFM, DFM, LMP and EMP, see Section 2.3.4) and summarized in the box plots in Figure 6.1a.

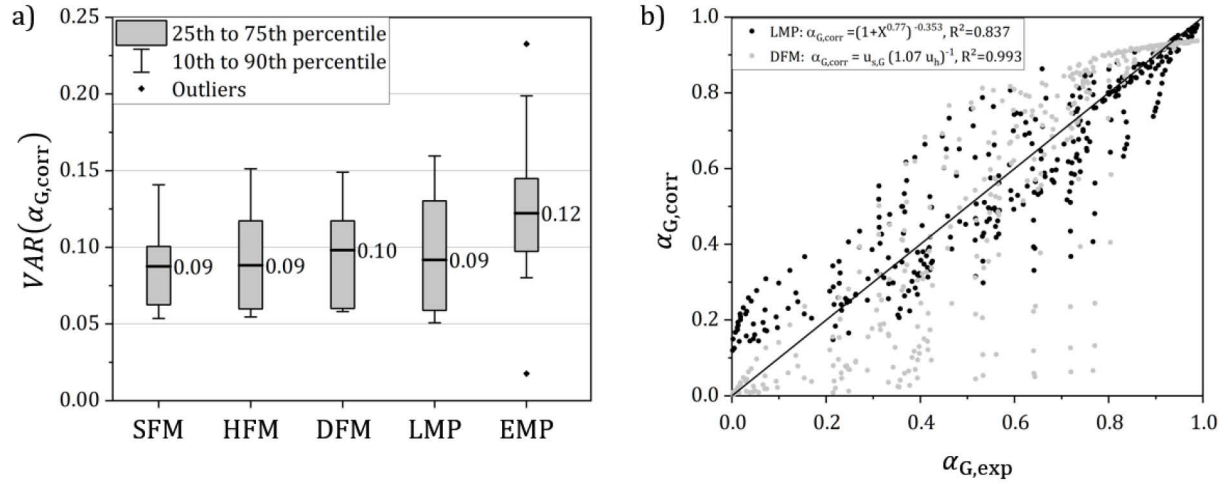


Figure 6.1: a) Variance of the void fraction predictions $\alpha_{G,corr}$ in straight pipes using reduced-order models (SLM - Separated flow models, HFM - Homogenous flow model, DFM - Drift Flux Model, LMP - Models based on the Lockhart-Martinelli parameter, EMP - Empirical models), b) fitted results of the two best performing correlations (LMP of Wallis (1969) and DFM of Gomez et al. (2000)) based on the experimental data in this work.

An overview of the models investigated in this work and the individual values $VAR(\alpha_{G,corr})$ are provided in Appendix A.12. Empirical models (EMP) show highest variance with outliers and can hardly be used to reliably predict developing flows. The other model types yield similar average variances (numbers in Figure 6.1a) with slightly different 25th and 75th percentiles. However, none of the available model types clearly outperforms the others for developing flows.

When fitting the models to the experimental data, best agreement (in terms of minimum absolute deviation $\Delta\alpha_G$) is obtained for LMP (correlation of Wallis (1969)) and for DFM (based on the correlation of Gomez et al. (2000)) for the DN50 feed pipe (see the parity plot in Figure 6.1b). Obviously, the LMP causes less scattering compared to the DFM, however, the correlation overpredicts the void fraction for $\alpha_{G,exp} < 0.2$. The DFM relies on a constant value for C_0 and $u_D = 0$ that significantly underpredict some experiments. Moreover, the DFM neglects the drift velocity, which causes $\alpha_{G,corr} \rightarrow C_0^{-1} \approx 0.94$ as $u_h \rightarrow 0$ (or $\alpha_{G,exp} \rightarrow 1$) and thus underpredicts void fractions close to unity. Other models (correlations and empirical functions) with acceptable deviations are summarized in Table 6.1.

Table 6.1: Performance assessment of empirical correlations for the prediction of α_G .

Model type	Literature			This work			
	Reference	R^2	$\Delta\alpha_G$	R^2	$\Delta\alpha_G$	$\max(\Delta\alpha_G)$	Modification
SFM	Madsen (1975)	8.3×10^{-1}	8.7×10^{-2}	8.1×10^{-1}	8.4×10^{-2}	3.4×10^{-1}	a_0 changed from 0.302 to 0.417
HEM	Chisholm (1983)	7.8×10^{-1}	9.6×10^{-2}	9.9×10^{-1}	9.2×10^{-2}	4.2×10^{-1}	$(1 - \alpha_G)^{0.5}$ changed to $(1 - \alpha_G)^{0.44}$
DFM	(Gomez et al., 2000)	9.9×10^{-1}	10.6×10^{-2}	9.9×10^{-1}	11.9×10^{-2}	4.4×10^{-1}	C_0 changed from 1.55 to 1.07
LMP	Wallis (1969)	8.3×10^{-1}	9.1×10^{-2}	8.4×10^{-1}	8.6×10^{-2}	3.6×10^{-1}	Exponents (Figure 6.1b) changed from 0.8 to 0.77 and 0.378 to 0.353

In addition to the absolute deviation $\Delta\alpha_G$ (accounts for the accuracy of the correlation), R^2 reveals how the respective model type captures the trend of $\alpha_{G,\text{exp}}$ in both pipe geometries. Modifying model parameters (right half of Table 6.1) does not significantly improve the accuracy. However, it should be noted that experimental data (in terms of mass fluxes) are not necessarily evenly distributed within the validity range of the respective models. Furthermore, SFM and HEM failed to predict $\alpha_{G,\text{exp}}$ measured at position INL for both pipe geometries. Contrary, DFM and LMP give reasonable predictions. However, none of the correlations given in Table 6.1 is applicable for the whole range of void fractions, i.e. flow morphologies. Thus, a hybrid approach is proposed, where LMP and DFM with multiple parameters are used depending on the values of X and u_h , respectively (see Figure 6.2).

In Figure 6.2a, a LMP (III, blue line) is proposed, which blends between two sets of parameters (I and II, black dotted lines) following the notion of Wallis (1969). Small void fractions (mostly dispersed bubbly flow according to the FFPI-classification) occur at larger values of X ($X = X_2 > 10^2$, correlation II in Figure 6.2a), while correlation I (in Figure 6.2a) is derived for $X < X_1$. Combining both equations with a weighting function between the intersection⁵ X_1 and the empirical limit X_2 , the full range of void fractions can be predicted with acceptable agreement ($\Delta\alpha_{G,\text{corr}} = 8.9 \times 10^{-2}$, $\max(\Delta\alpha_{G,\text{corr}}) = 3.6 \times 10^{-1}$). Figure 6.2b shows the predictions using the DFM approach, where the data cluster along a line with constant slope C_0 (distribution parameter) and intersect with the ordinate at u_D (drift velocity). The red dotted line refers to $u_D = 0$ (see Section 2.3.4). Obviously, the scattering data can hardly be described by a single DFM (e.g. the black dotted line deviate from the data points below $u_h = 10 \text{ m s}^{-1}$). Kong and Kim (2017) explained that gas bubbles in horizontal two-phase flows move slower than the mixture (negative drift velocity), thus an individual correlation would be required for the clustered bubbly data in Figure 6.2b

⁵ For cases where the correlations (I) and (II) obtained from regression do not shared an intersection, an approximate value of $X_1 = 1$ is used instead.

(bottom). However, this would require a priori knowledge of flow morphology or void fraction (bubbly flows are commonly evolving at $\alpha_G < 0.2$), which is hardly available during design of two-phase feeds. Using individual DFM parameters in respective ranges of u_h (see the three regions displayed in Figure 6.2b), void fractions are well predicted with $\Delta\alpha_{G,\text{corr}} = 10.4 \times 10^{-2}$ and $\max(\Delta\alpha_{G,\text{corr}}) = 4.2 \times 10^{-1}$. It should be noted that by changing the ranges for u_h , a more accurate fit to the experimental data may be obtained, however, empirical boundaries would then be required to ensure $\alpha_{G,\text{corr}} \leq 1$.

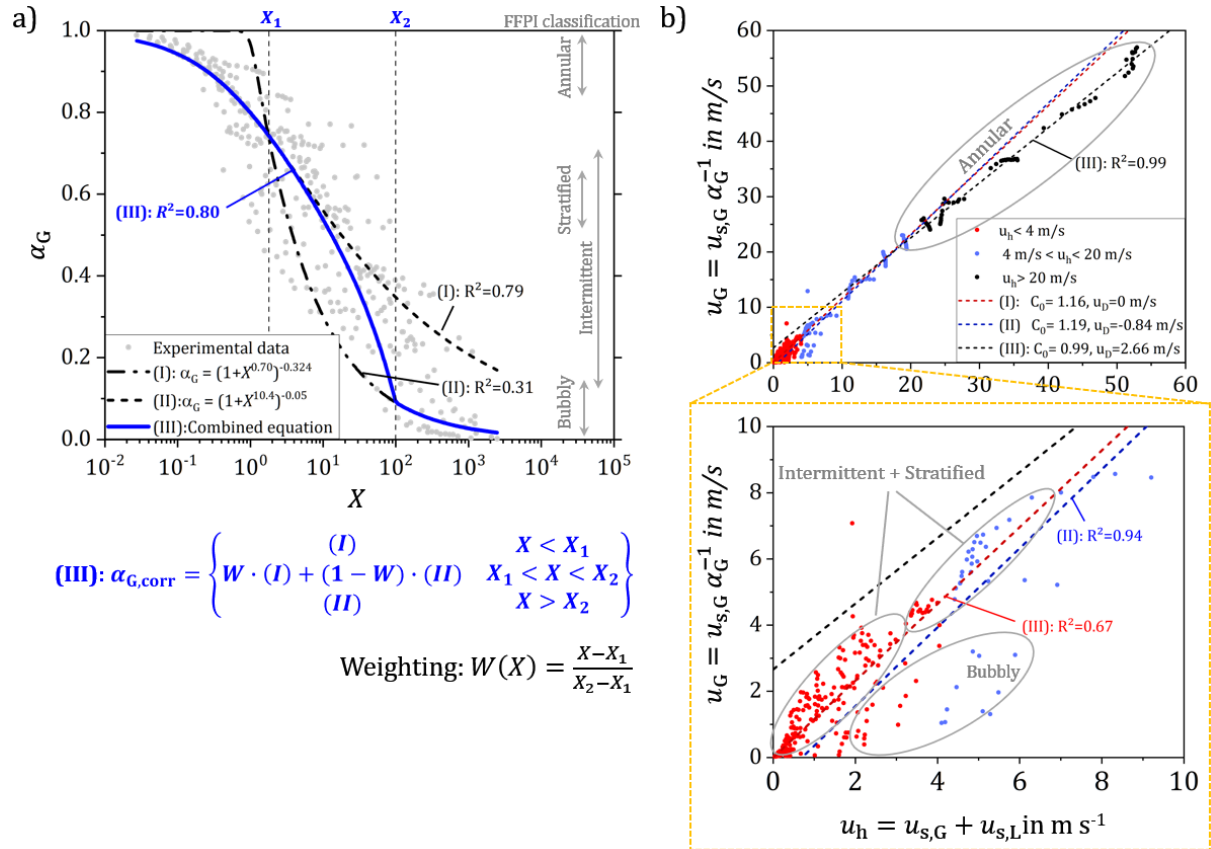


Figure 6.2: a) Morphology-adaptive prediction of the void fraction (position REF, DN50 feed pipe setup) combining a) LMP (III) and b) DFM's for annular flow at high u_h (I) and intermittent and stratified flows at lower u_h (II+III).

Both hybrid approaches for LMP and DFM in Figure 6.2 extend to the full range of void fractions (flow morphologies) for developing flow. Moreover, the blending introduced above provides a uniform methodology that can easily be applied to arbitrary pipe geometries. Eventually, the void fraction of horizontal two-phase flows with short entrance lengths or in bent pipes was determined for the first time. Table 6.2 summarizes the performance assessment of the resulting correlations (empirical parameters for each model are provided in Appendix A.14). Both, LMP and DFM perform equally well for the DN50 reference pipe. For the DN200 pipe, the experiments

cover a narrow range of $1 \times 10^{-1} \leq X \leq 3 \times 10^1$, thus blending between multiple LMPs was not required.

Table 6.2: Performance of LMP and DFM for the prediction of α_G in various pipe geometries.

Pipe geometry, location	LMP			DFM		
	R^2	$\Delta\alpha_{G,\text{corr}}$	$\max(\Delta\alpha_{G,\text{corr}})$	R^2	$\Delta\alpha_{G,\text{corr}}$	$\max(\Delta\alpha_{G,\text{corr}})$
Straight, $D = 50$, REF	8.0×10^{-1}	8.9×10^{-2}	3.6×10^{-1}	9.1×10^{-1}	10.4×10^{-2}	4.2×10^{-1}
Straight, $D = 50$, INL	8.4×10^{-1}	9.1×10^{-2}	4.0×10^{-1}	8.9×10^{-1}	10.6×10^{-2}	4.6×10^{-1}
Straight, $D = 200$, INL	5.1×10^{-1}	2.7×10^{-2}	1.2×10^{-1}	8.3×10^{-1}	16.7×10^{-2}	5.1×10^{-1}
Bend, $D = 50$, OUT + 10 L/D	8.4×10^{-1}	8.9×10^{-2}	5.0×10^{-1}	9.3×10^{-1}	8.2×10^{-2}	5.9×10^{-1}
Bend, $D = 200$, REF	5.0×10^{-1}	6.7×10^{-2}	1.8×10^{-1}	9.1×10^{-1}	10.1×10^{-2}	2.8×10^{-1}

The fairly small deviations $\Delta\alpha_{G,\text{corr}}$ are mostly attributed to the scattering of the data and low values R^2 indicate that LMPs insufficiently approximate the two-phase flow in larger pipe diameters. Instead, the DFM method was found to predict the void fraction in all investigated pipe geometries with acceptable accuracy.

6.2 Liquid levels

The determination of liquid levels is essential to predict flow morphology transitions with mechanistic models in the two-fluid model (see Section 2.3.2). Contrary to short pipes with small diameters, large feed pipes installed at separation columns will hardly reach the equilibrium liquid level. ILG calculations provide liquid levels along the pipe based on the critical liquid level $h_{L,C}$ at feed inlet (see Section 2.3.3). Thus, determination of the ILG is required before conventional mechanistic models can be applied for the prediction of flow morphologies.

The WMS data along the DN50 pipe that were FFPI-classified as stratified flows revealed interfacial level gradients, which are compared with the theoretical model for ILG (see Section 2.3.3). The liquid levels $h_{L,\text{REF}}$ and $h_{L,\text{OUT}}$ were obtained from the void fraction measurements at locations REF and OUT according to Equation 2.22 assuming a non-curved interface. Following Equation 2.37, the axial distance $L/D = 35$ between both sensors was used to obtain the experimental level gradients, ILG_{exp} which are compared with the theoretical values ILG_{theo} from Equation 2.36 (Figure 6.3).

Among the various terms (see Table 2.5) to calculate the interfacial shear, the method of Barnea (1991) (blue symbols in Figure 6.3) is the most accurate one. Even smaller deviations between experimental and theoretical ILG values were achieved for $f_{\text{fi}} = \max(0.027, f_{\text{f,G}})$. Changes in the sign of the ILG were observed, i.e. downwards oriented slopes (negative sign) and upwards oriented slopes (positive sign), in the experiments and predicted by Equation 2.36 regardless of the flow

morphology. This contradicts the assumption of Bishop and Deshpande (1986), where upwards oriented slopes occur for supercritical stratified flows ($Fr_{\text{mod}}^2 > 1$), while most experiments in this work refer to subcritical conditions.

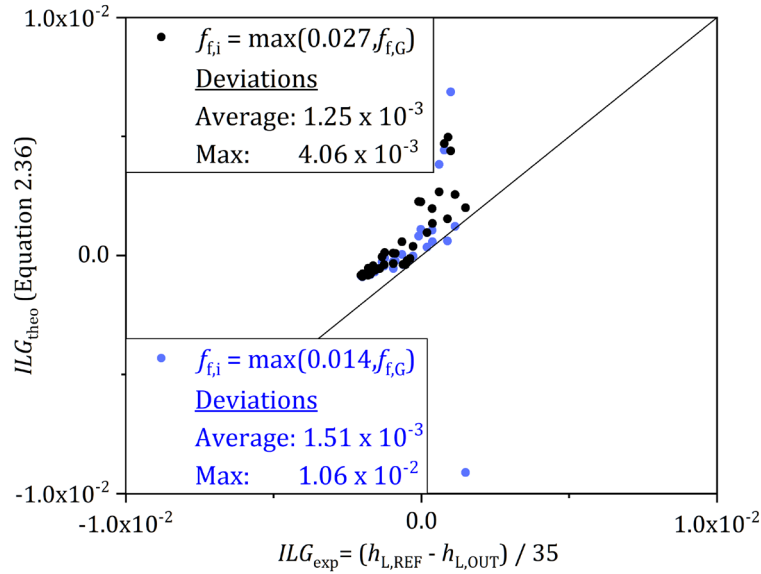


Figure 6.3: Parity plot of ILG values obtained from experiments (ILG_{exp}) and predicted values (ILG_{theo}) from Equation 2.36 using the interfacial friction factor proposed by Barnea (1991) (blue) and empirically fitted value obtained in this work (black).

The critical liquid levels $h_{L,c,\text{exp}}$ were located at the pipe's discharge $L/D = 8$ downstream the location REF, which was considered by Equation 2.37 and extrapolation of the ILG_{exp} . Figure 6.4 compares predicted and experimental critical liquid levels.

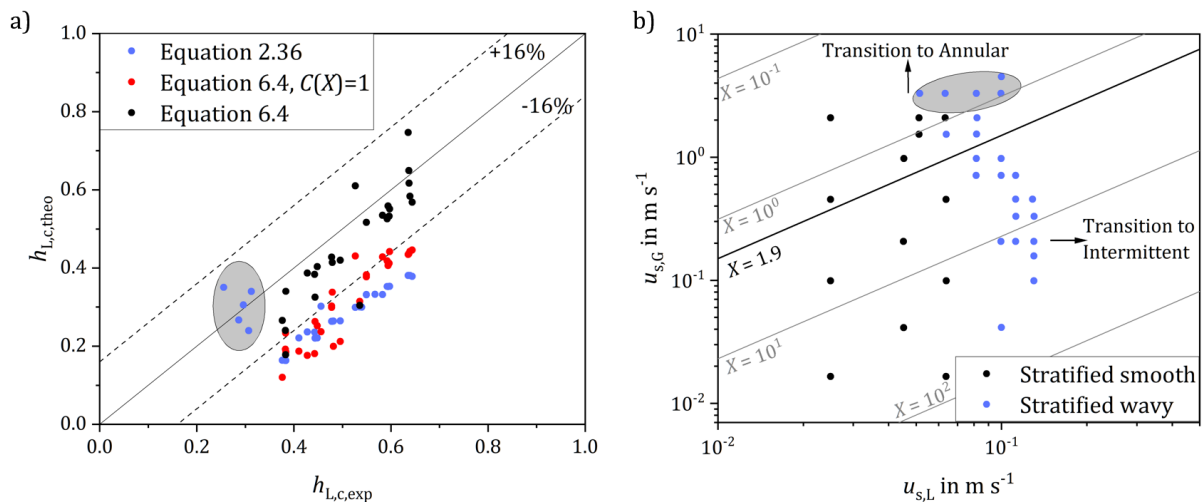


Figure 6.4: a) Parity plot of critical liquid levels obtained from experimental data and ILG models, b) flow regime map of the corresponding stratified flows (fuzzy classified, Section 3.4.1).

Equation 2.36 predicts $h_{L,c}$ fairly well for conditions with high gas momentum close to the transition to annular flows ($u_{s,G} > 3.2 \text{ m s}^{-1}$, encircled cluster in Figure 6.4a and b), while lower gas momentum causes systematic underprediction. Obviously, there is a consistent underprediction of the liquid levels (blue symbols in Figure 6.4a). This is attributed to the influence of surface tension forces on the developing liquid level, which is more pronounced for low inertia flows, which Equation 2.36 ignores.

Thus, the momentum balance equations were combined in this work using the formulation of the pressure terms introduced by Barnea and Taitel (1994) as

$$p_L = p_G - \sigma \frac{d\bar{h}_L}{dz}. \quad 6.3$$

Treating the balance equations in a similar way as described in Sections 2.3.2 and 2.3.3, a modified correlation for the ILG is derived (see Appendix A.15) as follows

$$ILG = \frac{d\bar{h}_L}{dz} = \frac{-\frac{\tau_L S_L}{A_L} + \tau_i S_i \left(\frac{1}{A_L} + \frac{1}{A_G} \right) + \frac{\tau_G S_G}{A_G}}{g(\rho_L - \rho_G) - \frac{A'_k \gamma}{2} \left(\rho_G u_{s,G}^2 \frac{A^2}{A_G^3} - \rho_L u_{s,L}^2 \frac{A^2}{A_L^3} \right) - \sigma \frac{d(ILG)}{dz} \cdot C(X)}. \quad 6.4$$

The surface tension term in Equation 6.4 depends on the first-order derivative of the ILG or the second-order derivative of the liquid level in axial direction ($d^2\bar{h}_L/dz^2$), i.e. the longitudinal curvature of the interface. $C(X)$ is an empirical scaling factor, described below.

In order to solve Equation 6.4 for the ILG, the experimental ILG-values were used to determine $d(ILG)/dz$ as shown in Figure 6.5. Note that small values $ILG_{\text{exp}} \leq 10^{-4}$ were excluded from the analysis, because of the high measurement uncertainty.

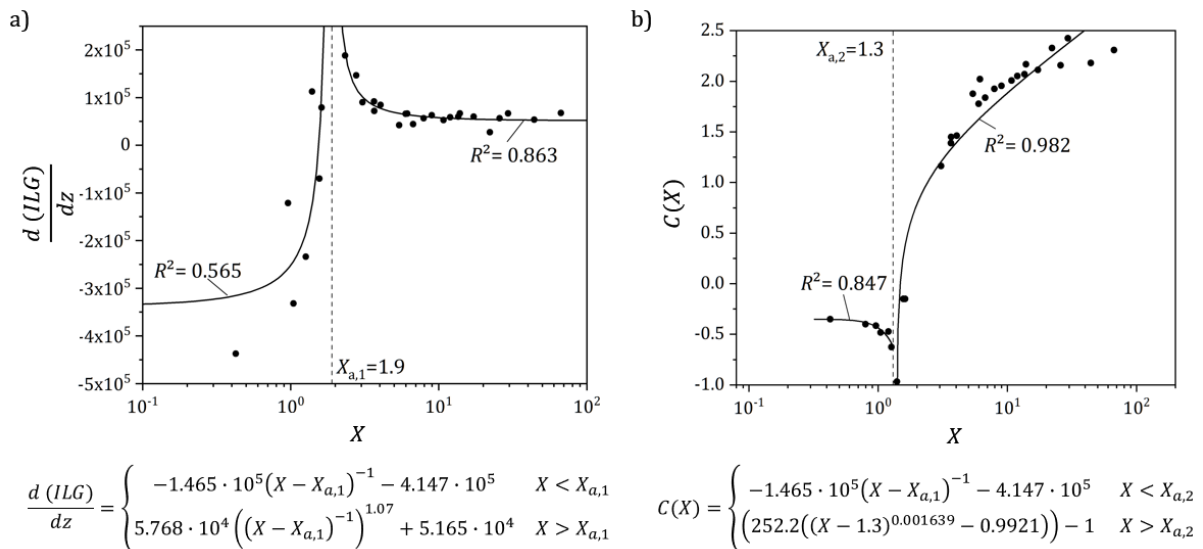


Figure 6.5: Experimental data (dots) and empirical correlations (lines) of a) longitudinal curvature of the interface ($d(ILG)/dz$) and b) scaling factor $C(X)$ with Lockhart-Martinelli parameter X (Equation 2.48).

Plotting $d(ILG)/dz$ versus X in Figure 6.5a reveals the asymptotic behavior at $X_{a,1} \approx 1.9$. Most data fulfill $d(ILG)/dz > 0$, i.e. convex longitudinal curvature. While Bishop and Deshpande (1986) define $X = 1$ as the lower limit for ILG or non-uniform flow, Figure 6.5a illustrates that ILG with concave curvature ($d(ILG)/dz < 0$) dominates at low X instead. The asymptote at $X_{a,1} \approx 1.9$ shows the transition from stratified-smooth to stratified-wavy flow morphologies at higher gas velocities (see Figure 6.4b), which obviously influences ILG .

The critical liquid levels derived from Equation 6.4 with the empirical fitting of $d(ILG)/dz$ are shown as red symbols in Figure 6.4a, however, only slightly better agreement could be achieved since Equation 6.3 is an approximate relation only. Thus, the experimental $h_{L,c}$ values, ILG and the empirical function for $d(ILG)/dz$ were used to derive a relation for the scaling factor $C(X)$ (see Figure 6.5b). Eventually, the critical liquid levels were determined (black symbols in Figure 6.4a) with acceptable agreement ($\pm 16\%$). Earlier models for fully developed two-phase flow (Taitel and Dukler, 1976) predict the transition from stratified to intermittent flow or to annular flow using a constant value $X = 1.6$ ($h_L = 0.5$). This value is also a characteristic value for describing the behavior of the ILG for stratified flows (see asymptotic values $X_{a,1}$ and $X_{a,2}$ in Figure 6.5).

Eventually, the denominator of Equation 6.4 allows the determination of the discharge liquid level of short feed pipes into the distillation column, if the void fraction is known. While this provides a relevant design parameter for inlet devices, Equation 6.4 may be applied to calculate the liquid level upstream of the column inlet. Note that further modification of the numerator of Equation 6.4 may be required to fully capture the ILG , however, this requires more grid points in axial direction.

6.3 Conclusions

For the first time, the applicability of reduced-order models and numerical simulations for not fully developed flows in straight and bent pipe geometries was comprehensively analyzed. Systematical evaluation of available reduced-order models identified the most versatile representatives. Consideration of the flow morphologies provided more accurate prediction of the void fraction using blending functions between multiple correlations. The main findings are:

- The void fraction of evolving two-phase flow can be well correlated using the Lockhart-Martinelli parameter or the drift flow analysis. Both approaches are applicable to all investigated pipe geometries with acceptable accuracy.
- While LMPs are much simpler and easier to compute and therefore suitable for rough estimations, the DFM analysis allows a versatile parameterization and consideration of the flow morphologies if a priori knowledge is available.
- Unified models based on the two-fluid model should consider the influence of the critical discharge level and ILG to reliably determine the liquid levels.

7 CFD modelling of two-phase feeds

The main disadvantage of reduced-order models (Chapter 6) is their averaging nature in terms of cross-sectional data and dynamics. Contrary, CFD provides void fraction and momentum data in the full 3D domain and predicts the transient flow behavior. Numerical simulations were carried out in ANSYS CFX, v18.2 and v20.2 using the Eulerian-Eulerian multiphase modelling approach with fluid-dependent turbulence modelling (RANS). In order to test the capability of multiphase CFD models (VoF, AIAD) for developing two-phase flows, simulations were carried out for different pipe geometries and results were compared with experiments.

7.1 Simulation setup

Two sets of operating conditions were simulated for straight pipe geometries and for 90° horizontal bends, respectively for $D = 50$ mm and $D = 200$ mm. The selected mass fluxes refer to

- low flow rates: $\dot{m}_G = 1 \text{ kg m}^{-2} \text{ s}^{-1}$ and $\dot{m}_L = 97 \text{ kg m}^{-2} \text{ s}^{-1}$
- high flow rates: $\dot{m}_G = 24 \text{ kg m}^{-2} \text{ s}^{-1}$ and $\dot{m}_L = 160 \text{ kg m}^{-2} \text{ s}^{-1}$

and are classified as stratified or annular flow according to the flow map in Figure 3.6. However, it should be noted that the experiments revealed predominantly stratified flow.

The geometries for the numerical simulations were created using ICEM CFD 18.2. The meshes all satisfy the ICEM-quality criteria of ≥ 0.6 . The hexahedral cells were organized in structured meshes (O-grid or butterfly grid), regularly spaced in flow direction. The O-grids comprise a combination of nodes distributed along orthogonal coordinates (pipe center), surrounded by nodes distributed along cylindrical coordinates. Figure 7.1 shows the simulation domain for the DN200 feed pipe setup with horizontal bend.

Single-phase inlets for air (red cells) and water (blue cells) were used to resemble the concentric phase mixers of both experimental setups. Note that this is a simplification for the DN50 feed pipe at high gas flow rates, where an upstream T-junction was used for phase mixing. To compensate any possible effect by the domain outlets (green cells) on the numerical results upstream, the domains were extended by $L/D = 10$ in flow direction.

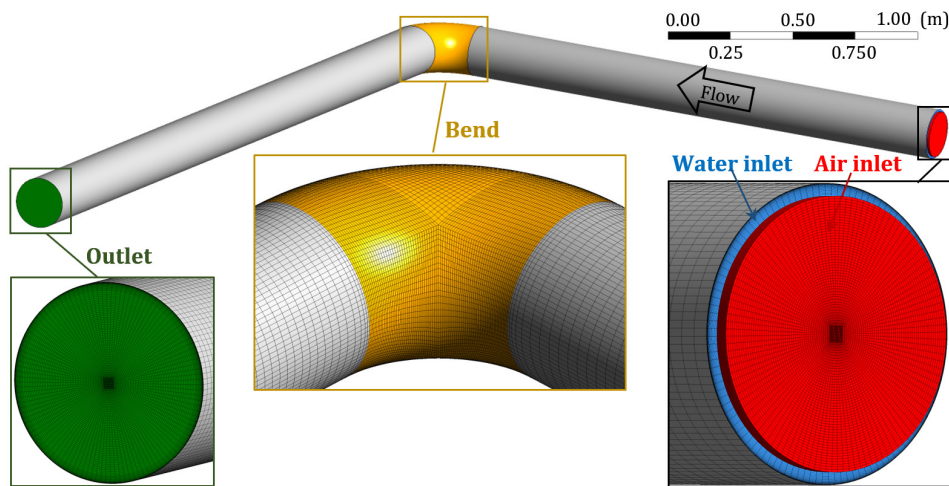


Figure 7.1: Simulation domain for the DN200 feed pipe section equipped with horizontal 90° bend in ANSYS CFX.

To achieve grid-independent results, simulations were repeated with different numbers of cells. During the mesh refinement the number of nodes per edge of the O-grid were scaled to the pipe diameter. Identical numbers of cells per cross-sectional area were used for both pipe diameters in order to resolve local phenomena at same scale. Figure 7.2 shows simulated void fractions for all geometries for the measurement location closest to the domain outlet at low flow rate for different mesh refinements. The mesh size in Figure 7.2 is shown in percent for easier comparison between the different geometries (100 % refers to the tabulated values in Figure 7.2), with coarser meshes ($< 100\%$) showing slight effects of the lower mesh refinement.

Identical boundary conditions were used for all geometries. Both phase inlets were bulk mass flow inlets (calculated from the superficial velocities during the experiments) with setting accounting for medium turbulence intensity. The outlet condition for average static pressure $p = 0$ Pa (ambient pressure) was chosen and pipe roughness and slip between water, air and inner pipe wall were neglected (smooth wall, no slip wall boundary conditions) due to the fairly smooth surface of the plastic pipes. The fluid properties for the both phases (adiabatic flow) were obtained from the ANSYS CFX material library. The gas density ($\rho_G = 1.20 \text{ kg m}^{-3}$) was selected as the buoyancy reference density and the simulations were initialized completely filled with water.

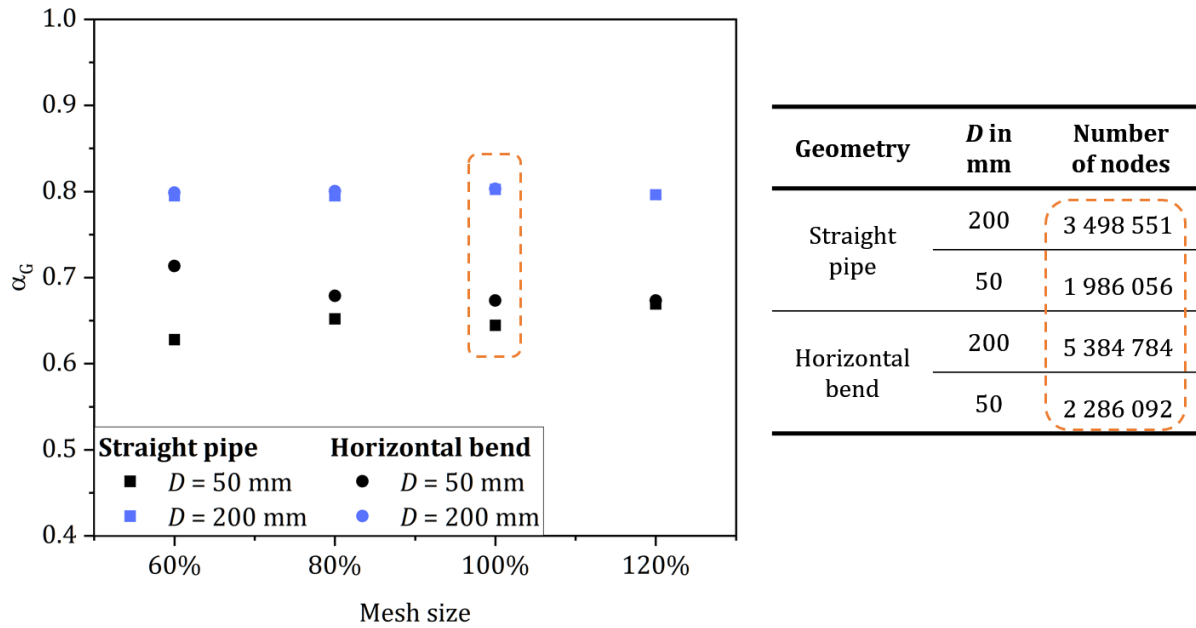


Figure 7.2: Effect of mesh size on void fractions for straight and bent pipes at low flow rates ($\dot{m}_G = 1 \text{ kg m}^{-2} \text{ s}^{-1}$ and $\dot{m}_L = 97 \text{ kg m}^{-2} \text{ s}^{-1}$).

The residual target of the convergence criteria was set as $\text{RMS} = 10^{-4}$. Since steady-state simulations did not reach convergence, quasi-steady-state simulations utilizing the transient analysis mode (first-order backward Euler scheme) were performed. The simulations were carried out for a maximum number of 30 coefficient loops between each timestep. This way, the simulations approximate the (quasi-)steady-state behavior after a sufficient amount of timesteps (simulation time) as illustrated in Figure 7.3.

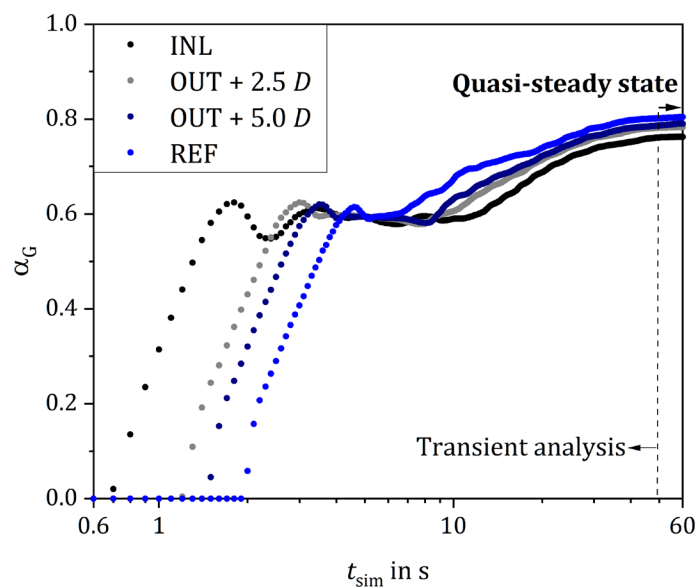


Figure 7.3: Average void fractions obtained using a transient analysis mode (90° horizontal bend, DN200 feed pipe setup, at low flow rates: $\dot{m}_G = 1 \text{ kg m}^{-2} \text{ s}^{-1}$ and $\dot{m}_L = 97 \text{ kg m}^{-2} \text{ s}^{-1}$).

The simulation time t_{sim} to reach quasi-steady-state behavior was between 50 s and 60 s with constant timesteps of 10^{-2} s for all cases.

7.2 Multiphase models

For the simulation of free surface flows in the Eulerian-Eulerian framework, the volume of fluid (VoF) model with built-in interface detection is widely accepted (Fan et al., 2019; Guerrero et al., 2017; Hirt and Nichols, 1981; Nasrfard et al., 2019). On the other hand, VoF involves a shared velocity field of the two-phase flow (treated as a homogenous mixture similar to HEM (Hirt and Nichols, 1981; Ali, 2017; Ban et al., 2018; Sadrehaghighi, 2018), which contradicts flows with disperse fractions.

Alternatively, the Algebraic Interfacial Area Density (AIAD) model can be applied, which accounts for local flow patterns and includes blending functions to consider correlations for interfacial area density, drag coefficient and local characteristic length scale, respectively. In the framework of VoF, the two-phase mixture is treated as a homogenous fluid (one-fluid approach with volume-averaged properties of both phases. AIAD is supposed to capture the morphology of the two-phase flow by providing laws for the interfacial area density and the drag coefficient at the interphase.

Volume of Fluid model: The adiabatic two-phase flow is governed by the balance equations for mass

$$\frac{\partial}{\partial t}(\alpha_k \rho_k) + \nabla(\alpha_k \rho_k \mathbf{u}_k) = 0 \quad 7.1$$

and momentum

$$\begin{aligned} \frac{\partial}{\partial t}(\alpha_k \rho_k \mathbf{u}_k) + \nabla(\alpha_k (\alpha_k \mathbf{u}_k \times \mathbf{u}_k)) \\ = -\alpha_k \nabla p_k + \nabla(\alpha_k \mu_k (\nabla \mathbf{u}_k + (\nabla \mathbf{u}_k)^T)) + \alpha_k \rho_k \mathbf{g} + \mathbf{M}_{G,L}. \end{aligned} \quad 7.2$$

\mathbf{u}_k refers to the velocity field of each phase. Forces acting on the interphase of each phase due to the presence of the second phase are described by the interphase momentum transfer $\mathbf{M}_{G,L}$. Turbulence was modelled using Menter's Shear Stress Transport model (SST, Menter, 1993; Menter, 1994) that was successfully applied in previous CMFD studies (Chinello et al., 2019; Menter, 2003; Höhne, 2016; Saffari et al., 2014; Tas-Koehler et al., 2021). SST is especially suited for separated morphologies such as stratified or annular flow as it blends between the $k - \varepsilon$ (free stream) and $k - \omega$ (near wall region) turbulence models.

AIAD model: The model involves a blending function to select correlations for interfacial area density, drag force and momentum transfer depending on the void fraction in order to account for different flow morphologies. Thus, improved detection and modelling of phase interface and flow morphology is achieved. In this work, the unified blending function proposed by Höhne et al.

(2020) was applied, while turbulence damping was enabled and subgrid turbulence model and drag law were disabled. After the VoF simulations reached quasi-steady state, the transient simulations were started using AIAD. The necessary code was implemented via CFX command language (CCL). The simulations were then continued in a similar manner as described in Section 7.1 until quasi-steady state was reached again.

7.3 Comparison with experimental data

The following section compares the two-phase flow morphologies and cross-sectional averaged void fractions obtained from numerical simulations and experiments in straight pipes and horizontal bends.

7.3.1 Straight pipes

The observed flow morphologies in the DN200 feed pipe setup are summarized in Figure 7.4. Figure 7.4a shows a 3D image of the liquid phase fraction obtained from AIAD simulation. The predicted flow is well developed for entrance lengths $L/D \geq 10$. Simulated and measured void fractions at $L/D = 10$ are inscribed in the cross-sections in Figure 7.4b, which reveal good quantitative and qualitative agreement for both modelling approaches. However, small amplitude waves in the experiments (reflected by the void fraction gradient near the interface) were not observed in the simulations.

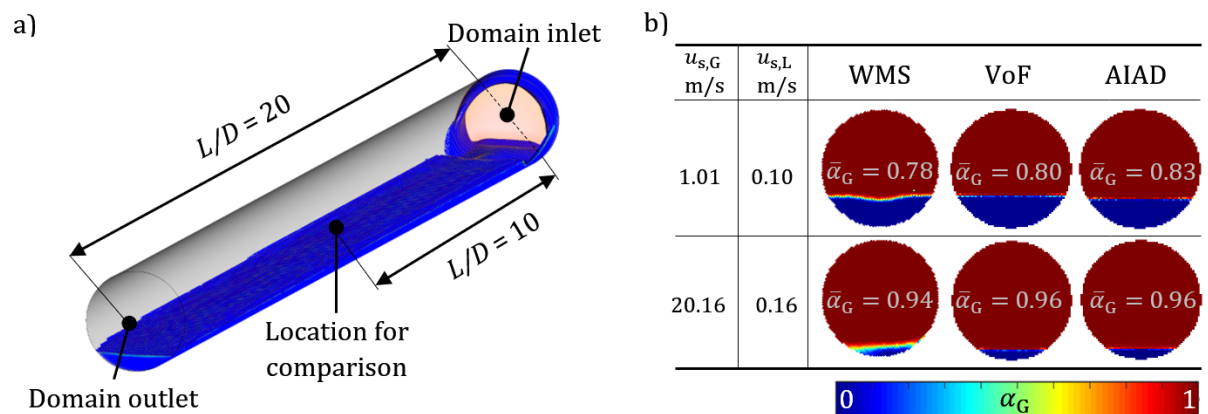


Figure 7.4: Two-phase flow in the straight DN200 feed pipe setup: a) rendered flow 3D morphology obtained from AIAD simulations at low flow rates, b) comparison of measured and simulated flow morphologies and average void fractions.

Figure 7.5 shows the phase distribution obtained from the simulations for the straight DN50 pipe at low flow rates. Both numerical models predict a developed flow with nearly constant liquid level along the pipe. Contrary, the hydraulic jump in the experiments causes higher liquid levels (at $L/D > 10$). Similar to the DN200 feed pipe setup (Figure 7.4a), the numerical models tend to predict this jump earlier (near the domain inlet) and thus, overpredict the void fraction beyond

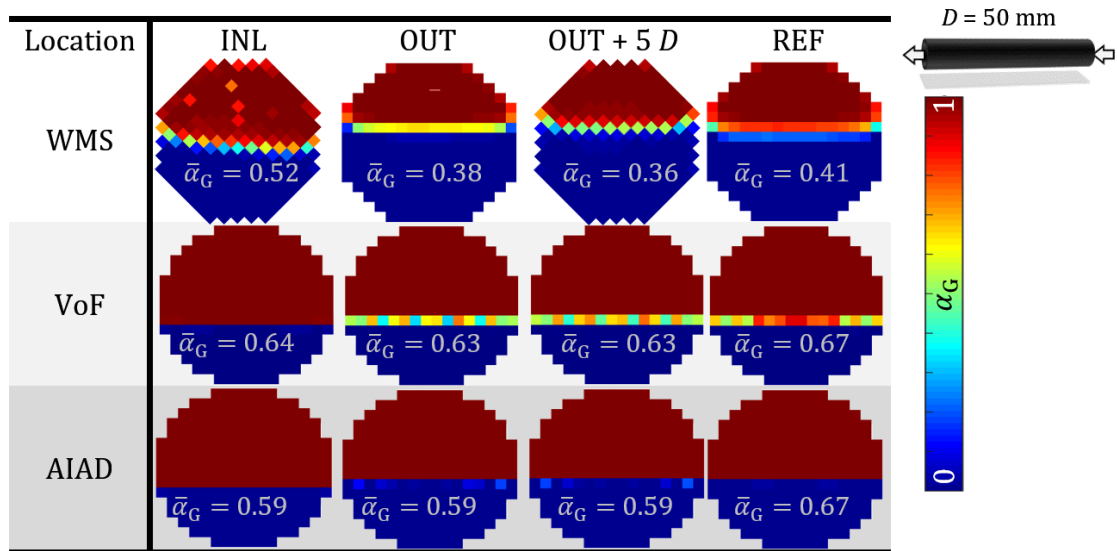


Figure 7.5: Void fractions and patterns of the phase distribution obtained from experiments and simulations (VoF, AIAD) for developing two-phase flow in the DN50 feed pipe setup at low flow rates.

Figure 7.6 shows the phase distribution obtained from the simulation for the straight DN50 pipe at higher flow rates, where annular flows exists for short entrance length (INL), but the flow develops towards a more stratified morphology (contrary to the flow map in Figure 3.6).

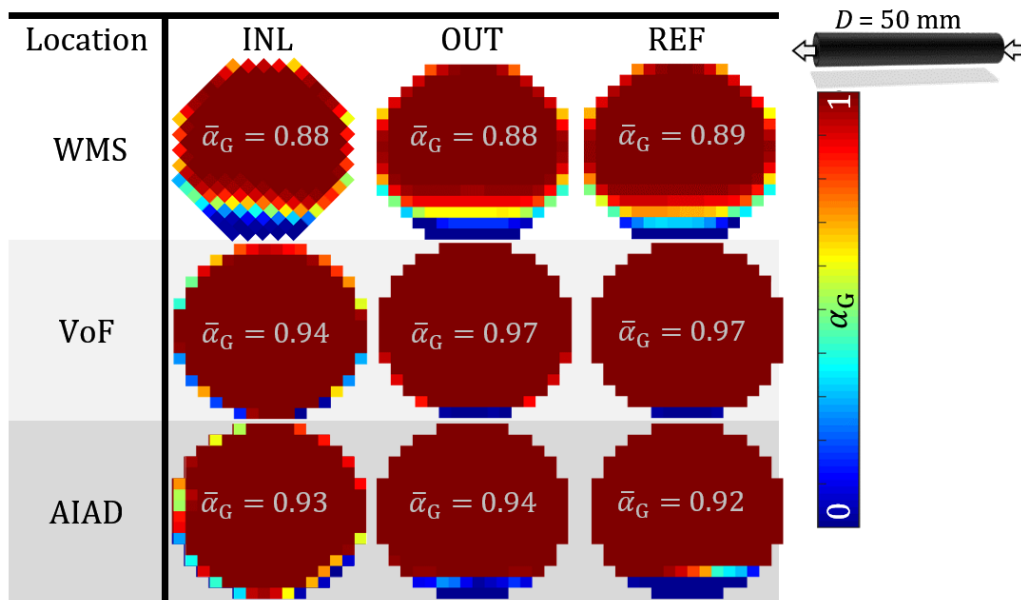


Figure 7.6: Void fractions and patterns of the phase distribution obtained from experiments and simulations (VoF, AIAD) for developing two-phase flow in the DN50 feed pipe setup at high flow rates. Both numerical models predict average void fraction with fair agreement. Flow patterns from the

AIAD simulations are more similar with the experiments (circumferential liquid spreading at $L/D = 10$), however, close to the inlet the simplified inlet geometry (see Section 7.1) causes the gas phase to enter the domain with very high momentum (velocity). Thus, the liquid film at pipe

bottom forms only in the downstream region of the straight pipe. On the other hand, both models fail to predict the circumferential wall wetting.

7.3.2 Horizontal 90° bends

The flow morphologies in the vicinity of the horizontal 90° bends are shown in Figure 7.7 for the higher flow rates, i.e. annular flow is predicted by the flow regime map. The re-orientation of the flow's momentum causes a zig-zag distribution of the liquid bulk with local inversion at the bend outlet in the DN50 geometry.

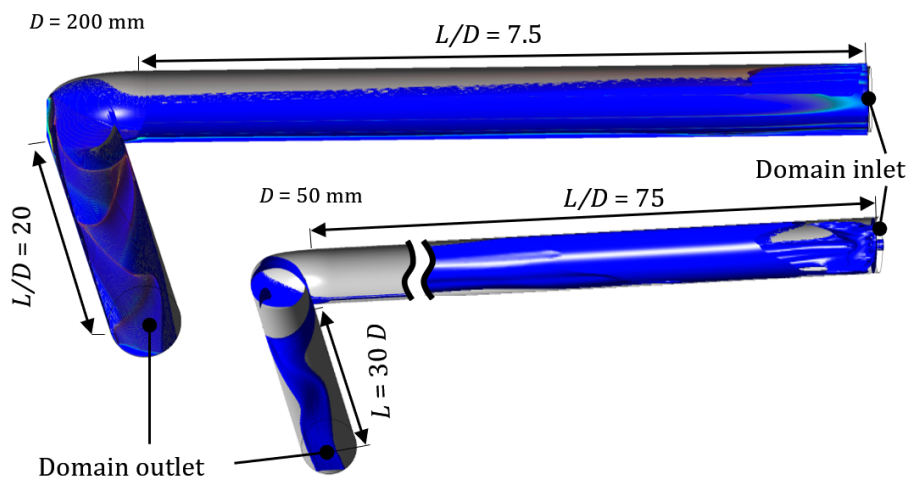


Figure 7.7: 3D-visualization of the liquid phase fraction (blue) of developing two-phase flow in the vicinity of horizontal 90° bends at high flow rates obtained from numerical simulations (VoF).

Figure 7.8 presents the phase distribution obtained from the simulation for the horizontal 90° bend with $D = 200$ mm at low flow rates. In contrast to inlet (INL) and recovery (REF) locations, the average void fraction downstream of the bend outlet (OUT) is well predicted by the numerical codes, with slightly more accurate results for VoF. The experiments revealed liquid accumulation at the bend inlet, which was not captured by the simulations. Moreover, the simulations failed to reproduce the slightly tilted interphase.

Figure 7.9 summarizes the phase distributions obtained from the simulation for the horizontal 90° bend with $D = 200$ mm at high flow rates. Both numerical models predict the average void fraction with similar deviation from the experimental values. However, the wavy morphology and disperse liquid fraction (not visible in WMS data but visually confirmed during the experiments) are not observed in the numerical results. The zig-zag motion of the liquid bulk along the pipe downstream of the bend agrees fairly well comparing WMS data and numerical simulation (VoF). The different phase distribution at $OUT + 2.5 D$ reveal a different propagation frequency of the

zig-zag motion of the liquid bulk in the numerical data. AIAD, however, fails to correctly predict the phase distribution close to the bend outlet.

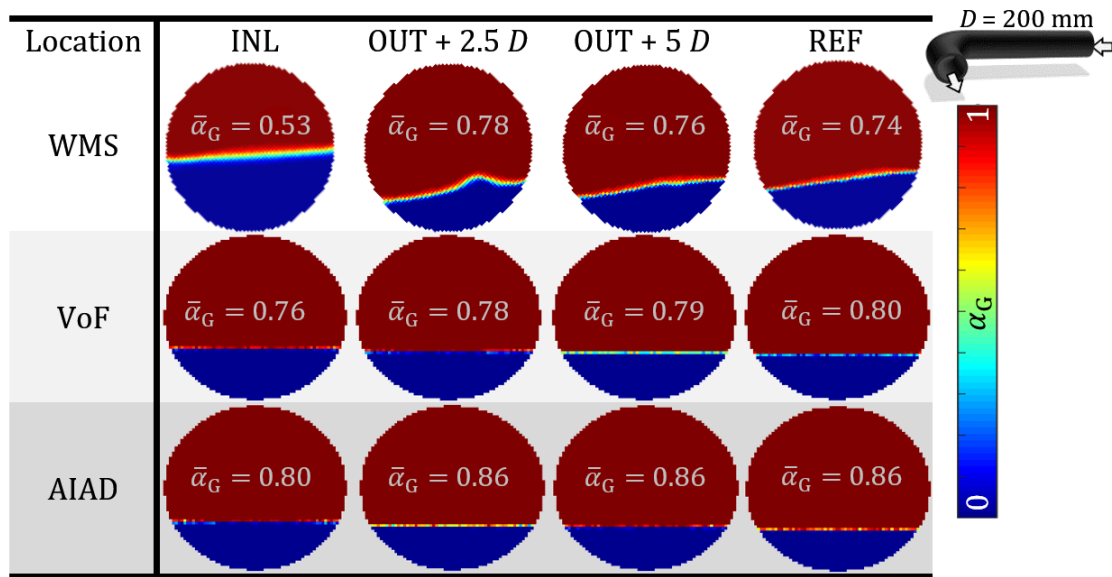


Figure 7.8: Void fractions and patterns of the phase distribution obtained from experiments and simulations (VoF, AIAD) for developing two-phase flow in the 90° horizontal bend (DN200 feed pipe setup) at low flow rates.

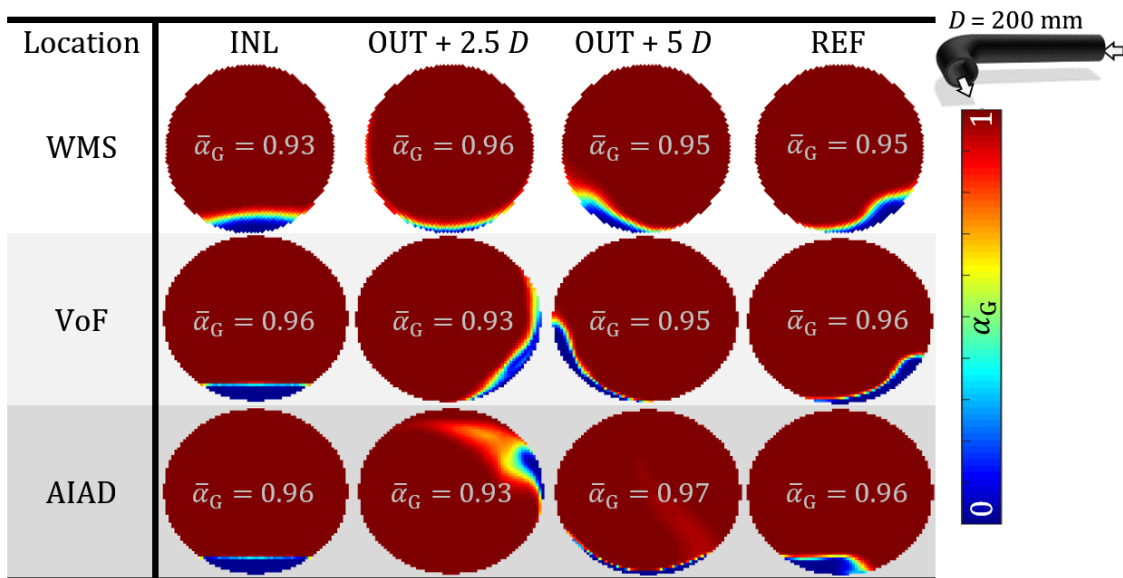


Figure 7.9: Void fractions and patterns of the phase distribution obtained from experiments and simulations (VoF, AIAD) for developing two-phase flow in the 90° horizontal bend (DN200 feed pipe setup) at low high flow rates.

Figure 7.10 summarizes the phase distributions obtained from the simulations for the horizontal 90° bend with $D = 50$ mm at low flow rates. Both numerical models slightly overpredict the average void fraction up- and downstream the horizontal bend ($D = 50$ mm). Small ripple waves,

that were present during the experiments were not observed in the simulation results. The overall phase distribution in the experiments was hardly affected by the horizontal bend, however, the simulations predict a slightly inclined interface at the bend outlet (OUT).

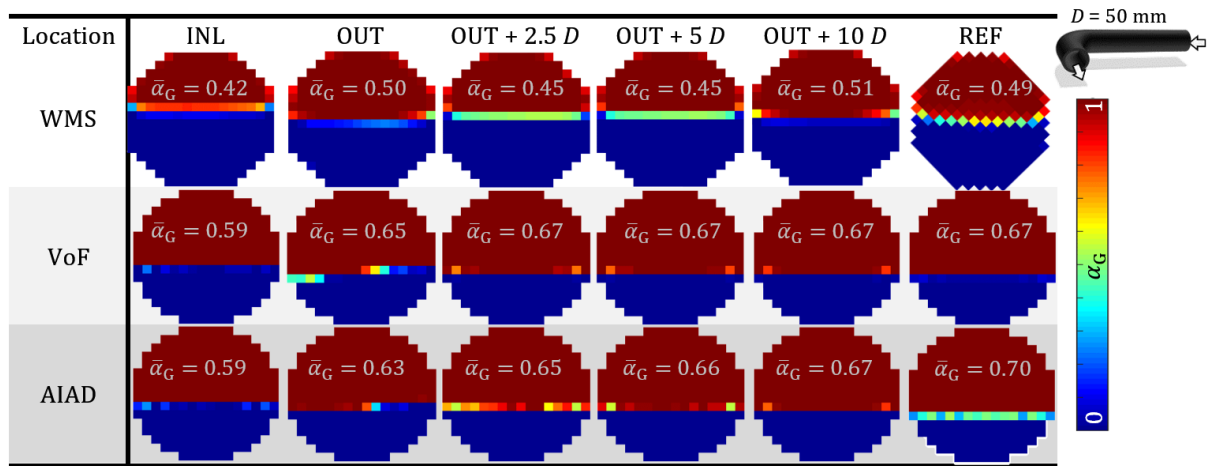


Figure 7.10: Void fractions and patterns of the phase distribution obtained from experiments and simulations (VoF, AIAD) for developing two-phase flow in the 90° horizontal bend (DN50 feed pipe setup) at low flow rates.

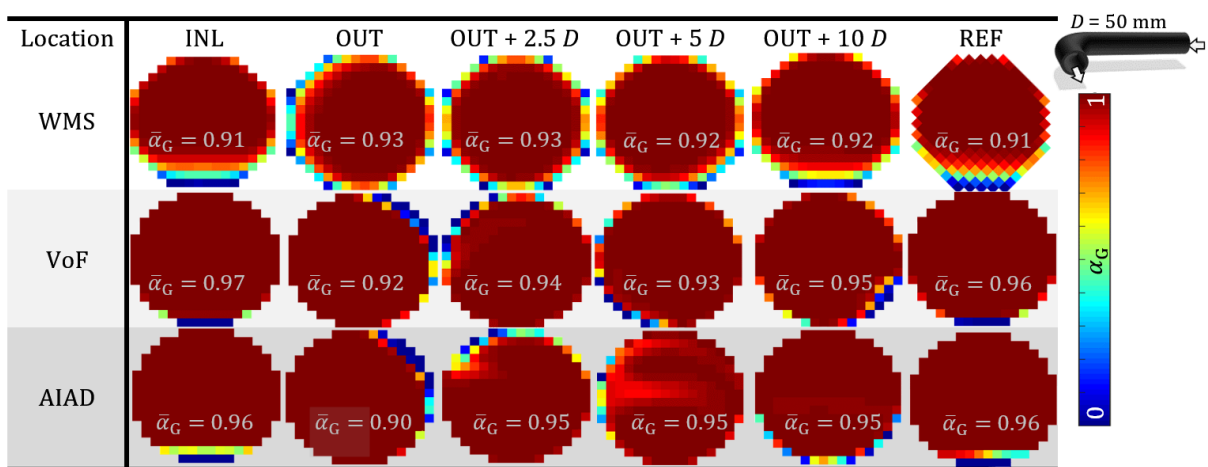


Figure 7.11: Void fractions and patterns of the phase distribution obtained from experiments and simulations (VoF, AIAD) for developing two-phase flow in the 90° horizontal bend (DN50 feed pipe setup) at high flow rates.

Figure 7.11 presents the phase distributions obtained from the simulations for the horizontal 90° bend with $D = 50$ mm at high flow rates. The averaged void fractions obtained by both numerical models downstream of the outlet of the horizontal bend agree fairly well with the experimental data. However, the deviation increases for large entrance lengths, i.e. more developed flows (INL and REF). Contrary to the experimental data, both numerical models predict flow inversion (the liquid bulk is located in the upper pipe half, see Figure 7.7) close to the bend outlet. As the flow develops, liquid accumulates at the pipe bottom for entrance lengths $5 \leq L/D \leq 10$ in the

experimental and numerical data. In the numerical simulations however, a zig-zag motion of the liquid bulk is predicted, which was not observed during the experiments. Instead a wavy interphase was observed, which was not predicted by the numerical models. Similar to the simulations in the larger pipe diameter at high flow rates (Figure 7.9), AIAD introduces unphysical liquid phase maldistribution.

7.4 Conclusions

In this chapter, the capabilities of VoF and AIAD models for predicting two exemplary flow morphologies in different pipe geometries were presented. The simulations performed well with respect to recovering some macroscopic two-phase flow features. However, the deviations obtained for the even rather stratified flow examples in this work demonstrate that the codes still require further development. The main findings are:

- Numerical simulations give an initial estimate of flow morphology, phase distribution and velocity, resolved in full 3D geometries
- The influence of curvatures on the two-phase flow in the downstream region was captured in the simulation results with good agreement.
- Phase dynamics, axial development of the flow morphology and void fraction can only be predicted with standard codes and are therefore highly uncertain for detailed engineering of two-phase feeds and require caution and safety margins.

8 Summary and recommendations for future work

8.1 Summary

For more than hundred years thermal separation processes in separation columns are an essential unit operation in chemical processing. Surprisingly, no universal approach for handling two-phase feeds has been proposed yet. This interdisciplinary field covering thermal separation and pipeline engineering commonly resorts to heuristic safety margins or individual experience of plant engineers, since data of two-phase flows in typical feed pipe dimensions are rarely available. As a consequence, the occurrence of detrimental flow phenomena remains often unnoticed and the flow development in early design phases can only be predicted with high uncertainty.

Today's design and engineering of two-phase feeds can only consult flow data classified as fully developed, since studies on entrance lengths, entrance behavior or flow morphologies in large diameter feed pipes are not available. Undesirable flow morphologies such as intermittent flows or entrainment are hardly be predictable, because either prediction criteria are missing or not yet qualified for two-phase feeds. Thus, the aim of this work was to create a comprehensive experimental database in order to derive criteria for the prediction of undesired flow morphologies and to systematically analyze the applicability of models for two-phase feeds.

Experiments were carried out in two feed pipe setups (DN50 and DN200). Measurements up- and downstream of pipe geometries (consisting of 90° pipe bends) revealed phase redistribution and entrance lengths. The developing two-phase flow morphologies were sampled along several axial positions by wire-mesh sensors with frame rates between 2.5 and 10 kHz and spatial resolution of 3 mm × 3mm. The comprehensive data base consisting of 1,274 measurements was made available online (via the research data repository 'RODARE').

An objective and reliable identification of flow morphologies was achieved by applying a fuzzy algorithm, which was extended by a new classification scheme. This method has been successfully tested and qualified for the investigated pipe geometries. By comparing the axial measurement points, entrance lengths and entrance behavior in terms of flow morphologies have been

determined. A comparison of pipe geometries indicated the different calming lengths required downstream of curvatures to recover from their influence on the flow morphology.

The occurrence of undesired flow morphologies for two-phase feeds was analyzed based on the experimental data. The inception of intermittent flows is characterized by average liquid level and liquid velocity. However, a conservative criterion requires knowledge of the void fraction. The onset of entrainment was identified from characteristic wave frequencies of the liquid bulk. A conceptual criterion was established to determine the susceptibility to entrainment based on dimensionless numbers that rely on the void fraction.

In addition, the applicability of 66 available reduced-order models was systematically assessed and LMPs and DFMs were identified as most versatile. Numerical simulations with VoF and AIAD were also performed considering exemplary morphologies and pipe geometries. While macroscopically approximated, phase dynamics could not be properly captured. Reduced-order models still outperform CFD simulations considering the deviations from the measured void fractions. The critical assessment of existing models and methods showed that reduced-order models can be used to predict two-phase flow in feed pipes with certain limitations. Reduced-order models are far more versatile and can be used for many geometrics and flow regimes and should still be used for design purposes.

For the first time, this thesis links the design of two-phase feeds in distillation columns with the multitude of methods and models, available to characterize the hydrodynamics. Since the thermal state of the feed mixture will continue as free design parameter, an estimation of the flow morphologies is still required. However, neither are empirical tools and models universally applicable, nor can all possible fluid combinations be experimentally studied. The flow chart in Figure 8.1 illustrates, how design and sizing of horizontal two-phase feed pipes for separation units benefit from the developed methods, models and correlations derived in this work. The diagram guides the designer based on different states (gray) and decisions (red) during the engineering of two-phase feeds and their consequences (blue). The applicable tools and contributions of this work and their parameters are shown in yellow and white, respectively.

The early design stages of the separation process will define the key constraints of the separation task, namely (1) the feasible operating range in terms of flow rates for the desired column type, and (2) the fluid properties and, based on equilibrium data, the thermal state of the feed. After the nominal feed pipe size is determined, potential undesirable flow conditions must be identified. If they cannot be avoided, tailored design of the two-phase feeds is required. Alternatively, the flow rates can be modified, which, however is often at the expense of a reduced separation performance or plant throughput. If fluid dynamic experience is available for the application, it may be necessary to adjust the pipe routing (increase pipe diameter or use/avoid curvatures).

Such tailored design of the two-phase feeds can be based on experience (e.g. from flow data before a column revamp or by suitable flow maps) and result in adjustments of pipe routing (increasing the pipe diameter or using/avoiding curvatures) in order to achieve the necessary flow stratification. Alternatively, CFD or reduced-order models can be consulted to determine the void fraction in order to select suitable inlet devices. Furthermore, the liquid level of the flow can be estimated and the occurrence of intermittent flows can be directly assessed. Moreover, after determination of ILG, a prediction of the occurring flow can be made with the TFM. Additionally, the void fraction ultimately allows determining the Strouhal number with the proposed empirical relations and thus, occurrence of entrainment can be verified.

Eventually, this procedure allows the design engineer to evaluate whether the two-phase feed will be operated with desired flow morphologies (i.e. no intermittent flow, no entrainment) or proper inlet devices, modified pipe routing or larger pipe diameter are required.

8.2 Recommendations for future work

In the future the experimental database may be consulted for design questions and engineering regarding the pipe routing of the feed section. This work has focused primarily on the bulk phases. Experimental work on local entrainment or droplet deposition phenomena along short pipes is still required. Furthermore, it would be advisable to contrast the beneficial flow influence of horizontal curvatures to common inlet devices to check for possible substitution. For example, the installation of a horizontal 90° bend upstream of the column inlet nozzle has been shown to have a beneficial effect on the flow by reducing the occurrence of droplet-laden annular flows and intermittent flows. The secondary flow introduced by the bend changes with the flow rates, i.e. optimal ranges of operation for bent feed pipes may be obtained. Moreover, the literature also indicates increasing droplet sizes at the outlet of horizontal bends, improving the separability of droplets. Here, the link between flow rate, bend geometry, possible re-entrainment by the bend and droplet size is still missing. As this work has focused on adiabatic two-phase flows and the hydrodynamic characterization of the entrance lengths, two-phase feeds with phase change, e.g. flashing feeds, require further investigation and characterization.

The criteria developed in this work to predict undesired flow morphologies – in principle – account for different fluid properties using dimensionless numbers. However, experimental validation is required, especially local onset and deposition phenomena of entrainment along the feed pipe have not yet been studied.

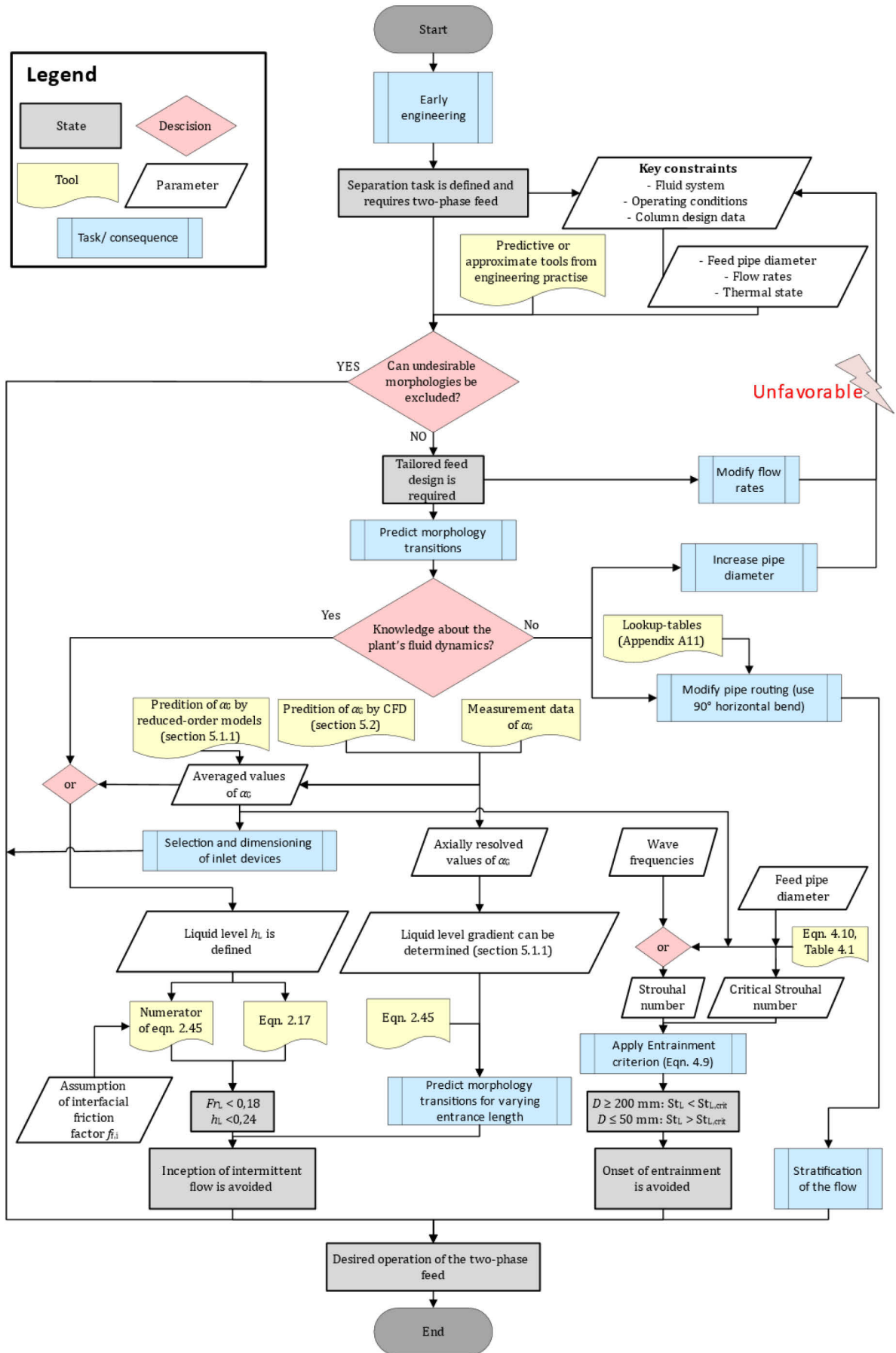


Figure 8.1: Advanced flow chart for design of horizontal two-phase feed pipes with particular contributions from this thesis.

The prediction of the void fraction as key parameter for the characterization of two-phase feeds and as model parameter for the prediction of flow morphologies in future should be based on reduced-order models. Thereof, drift-flux Models (Equation 2.46) are clearly more promising compared to empirical models, Homogenous flow models or separated flow models. Constant values for the distribution parameter can be provided by lookup tables for the respective flow morphologies, fluid properties and pipe geometries. However, the formulation of universal approaches are needed to determine the drift velocity for arbitrary flow morphologies and fluid properties without a priori knowledge. Models based on the Lockhart-Martinelli parameter are recommended for the practical use, since it also allows to determine the two-phase pressure drop in addition to void fraction. However, the definition according to Equation 2.48 neglects the influence of the surface tension on pressure drop and void fraction which should be experimentally verified for developing flows.

On the long term, numerical methods will advance the feed pipe design process. However, model development and validation for developing two-phase flow is still required. As shown in this work, the determination of the ILG can be used to describe the axial flow development. However, it assumes gradual progression from/towards an equilibrium liquid level, which hardly holds for short entrance lengths. Consequently, further work is needed to modify the numerator term in the ILG correlation (equilibrium liquid level) considering the equation for the denominator term (critical liquid level) formulated in this work by Equation 6.4.

The CFD simulations have shown, that experimental validation is still required, if accurate solutions are targeted. Different modelling approaches (e.g. large eddy simulations) or modification of model terms (e.g. for the onset of entrainment or growth of interfacial waves) in VoF or AIAD might result in simulation results closer to the experiments.

References

- Abdul-Majeed, G. H. (1996). Liquid holdup in horizontal two-phase gas-liquid flow. *Journal of Petroleum Science and Engineering* **15**, 271–280.
- Abdulkadir, M. (2011). Experimental and computational fluid dynamics (CFD) studies of gas-liquid flow in bends. PhD thesis, University of Nottingham. University of Nottingham.
- Abdulkadir, M., Hernandez-Perez, V., Lowndes, I. S., Azzopardi, B. J. and Sam-Mbomah, E. (2016). Experimental study of the hydrodynamic behaviour of slug flow in a horizontal pipe. *Chemical Engineering Science* **156**, 147–161.
- Agrawal, R. and Herron, D. M. (1997). Optimal thermodynamic feed conditions for distillation of ideal binary mixtures. *AIChE Journal* **43**, 2984–2996.
- Agrawal, R. and Herron, D. M. (2001). Feed pretreatment for binary distillation efficiency improvement. In: Gani, R. and Jørgensen, S. B. (eds) *Computer Aided Chemical Engineering*. Elsevier, 339–344.
- Ahmed, W. H., Ching, C. Y. and Shoukri, M. (2008). Development of two-phase flow downstream of a horizontal sudden expansion. *International Journal of Heat and Fluid Flow* **29**, 194–206.
- Ahn, T., Moon, J., Bae, B., Jeong, J., Bae, B. and Yun, B. (2018). An empirical model of the wetted wall fraction in separated flows of horizontal and inclined pipes. *Chemical Engineering Science* **178**, 260–272.
- Al-Naser, M., Elshafei, M. and Al-Sarkhi, A. (2016). Artificial neural network application for multiphase flow patterns detection: A new approach. *Journal of Petroleum Science and Engineering* **145**, 548–564.
- Al-Sarkhi, A. and Sarica, C. (2010). Power-Law correlation for two-phase pressure drop of gas/liquid flows in horizontal pipelines. *SPE Projects, Facilities and Construction* **5**, 176–182.
- Al-Sarkhi, A., Sarica, C. and Magrini, K. (2012). Inclination effects on wave characteristics in annular gas-liquid flows. *AIChE Journal* **58**, 1018–1029.
- Al-Tameemi, W. T. M. and Ricco, P. (2019). Water–air flow in straight pipes and across 90° sharp-angled mitre elbows. *International Journal of Multiphase Flow* **118**, 113–127.
- Alamu, M. B. and Azzopardi, B. J. (2011). Wave and drop periodicity in transient annular flow. *Nuclear Engineering and Design* **241**, 5079–5092.
- Ali, I. T. (2017). CFD Prediction of Stratified and Intermittent gas-liquid two-phase turbulent pipe flow using RANS models. University of Manchester.

- Alves, G. E. (1954). Co-current liquid-gas flow in a pipeline contractor. *Chemical Engineering Progress* **50**, 449–456.
- AMACS Process Tower Internals (2020). *Feed Inlet Devices*.
- Amaya-Gómez, R., López, J., Pineda, H., Urbano-Caguasango, D., Pinilla, J., Ratkovich, N. and Muñoz, F. (2019). Probabilistic approach of a flow pattern map for horizontal, vertical, and inclined pipes. *Oil and Gas Science and Technology – Revue d'IFP Energies nouvelles* **74**, 67.
- Ameel, B., De Kerpel, K., Canière, H., T'Joel, C., Huisseune, H. and De Paepe, M. (2012). Classification of two phase flows using linear discriminant analysis and expectation maximization clustering of video footage. *International Journal of Multiphase Flow* **40**, 106–112.
- Andreussi, P., Asali, J. C. and Hanratty, T. J. (1985). Initiation of roll waves in gas-liquid flows. *AIChE Journal* **31**, 119–126.
- Anoda, Y., Kukita, Y. and Nakamura, H. (1989). Flow regime transition in high-pressure large-diameter horizontal two-phase flow. *National Heat Transfer Conference / ANS proceedings*.
- Arabi, A., Salhi, Y., Zenati, Y., Si-Ahmed, E. K. and Legrand, J. (2020). On gas-liquid intermittent flow in a horizontal pipe: Influence of sub-regime on slug frequency. *Chemical Engineering Science* **211**, 115251.
- Armand, A. A. (1946). The resistance during the movement of a two-phase system in horizontal pipes. *Izvestia Vses. Teplotekh. Inst.* **1**, 16–23.
- Armand, A. A. and Treschev, G. G. (1946). Investigation of resistance during the movement of steam-water mixtures in heated boiler pipes at high pressures. *Izvestia Vses. Teplotekh. Inst.* **1**, 16–23.
- Aryan, A. F. (2022). Improving tray efficiency in the spray regime. *Hydrocarbon Engineering* 1–6.
- Asadollahi, M., Jalali Farahani, F. and Seader, J. D. (2017). Optimization of distillation separations using feed splitting by a homotopy continuation method. *Industrial and Engineering Chemistry Research* **56**, 4463–4476.
- Aung, N. Z. and Yuwono, T. (2013). Computational Fluid Dynamics simulations of gas-liquid two-phase flow characteristics through a vertical to horizontal right angled elbow. *ASEAN Journal on Science and Technology for Development* **30**, 1–16.
- Austregesilo, H., Bals, C., Hora, A., Lerchl, G., Romstedt, P., Schöffel, P., Cron, D. Von der and Weyermann, F. (2016). *ATHLET 3.1A Models and Methods*.
- Autee, A. T. and Giri, S. V. (2016). Experimental study on two-phase flow pressure drop in small diameter bends. *Perspectives in Science* **8**, 621–625.
- Ayegba, P. O., Abdulkadir, M., Hernandez-Perez, V., Lowndes, I. S. and Azzopardi, B. J. (2017). Applications of artificial neural network (ANN) method for performance prediction of the effect of a vertical 90° bend on an air-silicone oil flow. *Journal of the Taiwan Institute of Chemical Engineers* **74**, 59–64.
- Azzi, A. and Friedel, L. (2005). Two-phase upward flow 90° bend pressure loss model. *Forschung im Ingenieurwesen/Engineering Research* **69**, 120–130.
- Azzopardi, B. J. (ed.) (1989). The split of annular-mist flows at vertical and horizontal Ts. in: Proc 8th International Conference on Offshore Mechanics and Arctic Engineering. **V**, 389-395
- Azzopardi, B. J. (1997). Drops in annular two-phase flow. *International Journal of Multiphase Flow* **23**, 1–53.
- Azzopardi, B. J. (1999). Phase Separation at T-Junctions. *Multiphase Science and Technology* **11**, 223–329.
- Azzopardi, B. J., Ijioma, A., Yang, S., Abdulkareem, L. A., Azzi, A. and Abdulkadir, M. (2014). Persistence of frequency in gas-liquid flows across a change in pipe diameter or orientation. *International Journal of Multiphase Flow* **67**, 22–31.

- Azzopardi, B. J. and Sudlow, C. A. (1993). The effect of pipe fittings on the structure of two-phase flow. *Atti del XI Congresso Nazionale sulla Trasmissione del Calore*, 1–51.
- Azzopardi, B. J. and Wren, E. (2004). The phase separation capabilities of two T-junctions placed in series. *Chemical Engineering Research and Design* **82**, 364–371.
- Bae, B., Ahn, T., Jeong, J., Kim, K. and Yun, B. (2017). Characteristics of an interfacial wave in a horizontal air-water stratified flow. *International Journal of Multiphase Flow*. Pergamon **97**, 197–205.
- Bai, B., Zhang, S., Zhao, L., Zhang, X. and Guo, L. (2008). Online recognition of the multiphase flow regime. *Science in China Series E: Technological Sciences* **51**, 1186–1194.
- Baker, G., Clark, W. W., Azzopardi, B. J. and Wilson, J. A. (2007). Controlling the phase separation of gas-liquid flows at horizontal T-junctions. *AIChE Journal* **53**, 1908–1915.
- Baker, O. (1954). Designing for Simultaneous Flow of Oil and Gas. *The Oil and Gas Journal* **53**, 185–195.
- Baker, O. (1958). Progress Report - Multiphase Flow in Pipelines. *The Oil and Gas Journal*.
- Ban, S., Pao, W. and Nasif, M. S. (2018). Numerical simulation of two-phase flow regime in horizontal pipeline and its validation. *International Journal of Numerical Methods for Heat and Fluid Flow* **28**, 1279–1314.
- Bandyopadhyay, S. (2002). Effect of feed on optimal thermodynamic performance of a distillation column. *Chemical Engineering Journal* **88**, 175–186.
- Banerjee, S., Rhodes, E. and Scott, D. S. (1967). Film inversion of cocurrent two-phase flow in helical coils. *AIChE Journal* **13**, 189–191.
- Bankoff, S. G. (1960). A variable density single-fluid model for two-phase flow with particular reference to steam-water flow. *Journal of Heat Transfer* **82**, 265–272.
- Barnea, D. (1991). On the effect of viscosity on stability of stratified gas—liquid flow—application to flow pattern transition at various pipe inclinations. *Chemical Engineering Science* **46**, 2123–2131.
- Barnea, D. and Taitel, Y. (1989). Transient-formulation modes and stability of steady-state annular flow. *Chemical Engineering Science* **44**, 325–332.
- Barnea, D. and Taitel, Y. (1992). Structural and interfacial stability of multiple solutions for stratified flow. *International Journal of Multiphase Flow* **18**, 821–830.
- Barnea, D. and Taitel, Y. (1993). Kelvin-Helmholtz stability criteria for stratified flow: viscous versus non-viscous (inviscid) approaches. *International Journal of Multiphase Flow* **19**, 639–649.
- Barnea, D. and Taitel, Y. (1994a). Interfacial and structural stability of separated flow. *International Journal of Multiphase Flow* **20**, 387–414.
- Barnea, D. and Taitel, Y. (1994b). Structural stability of stratified flow—the two-fluid model approach. *Chemical Engineering Science*. Pergamon **49**, 3757–3764.
- Barnea, D. and Taitel, Y. (1994c). Non-linear interfacial instability of separated flow. *Chemical Engineering Science* **49**, 2341–2349.
- Baroczy, C. J. (1963). Correlation of Liquid Fraction in Two-phase Flow with Application to Liquid Metals. U.S. Atomic Energy Commission.
- Beggs, H. D. (1972). An experimental study of two-phase flow in inclined pipes. University of Tulsa.
- Benbella, S., Al-Shannag, M. and Al-Anber, Z. A. (2009). Gas-liquid pressure drop in vertical internally wavy 90° bend. *Experimental Thermal and Fluid Science* **33**, 340–347.
- Bendiksen, K., Espedal, M. and Malnes, D. (1988). Physical and numerical simulation of dynamic two-phase flow in pipe-lines with application to existing oil-gas field lines. *Conference on multiphase flow in industrial plants*.

- Bendiksen, K. H. (1984). An experimental investigation of the motion of long bubbles in inclined tubes. *International Journal of Multiphase Flow* **10**, 467–483.
- Bendiksen, K. H., Maines, D., Moe, R. and Nuland, S. (1991). The dynamic two-fluid model OLGA: Theory and application. *SPE Production Engineering* **6**, 171–180.
- Bennett, D. L. and Kovak, K. W. (2000). Optimize distillation columns. *Chemical Engineering Progress* **96**, 19–34.
- Berna, C., Escrivá, A., Muñoz-Cobo, J. L. and Herranz, L. E. (2014). Review of droplet entrainment in annular flow: Interfacial waves and onset of entrainment. *Progress in Nuclear Energy* **74**, 14–43.
- Bestion, D. (1990). The physical closure laws in the CATHARE code. *Nuclear Engineering and Design* **124**, 229–245.
- Bhagwat, S. M. and Ghajar, A. J. (2014). A flow pattern independent drift flux model based void fraction correlation for a wide range of gas-liquid two phase flow. *International Journal of Multiphase Flow* **59**, 186–205.
- Bishop, A. A. and Deshpande, S. D. (1986). Non-newtonian liquid-air stratified flow through horizontal tubes—ii. *International Journal of Multiphase Flow* **12**, 977–996.
- Bishop, A. A. and Deshpande, S. D. (1986a). Interfacial level gradient effects in horizontal newtonian liquid-gas stratified flow—i. *International Journal of Multiphase Flow* **12**, 957–975.
- Bishop, A. A. and Deshpande, S. D. (1986b). A criterion to determine uniform and non-uniform stratified liquid-gas flow through horizontal tubes. *International Communications in Heat and Mass Transfer* **13**, 209–217.
- Blahušiak, M., Kiss, A. A., Babic, K., Kersten, S. R. A., Bargeman, G. and Schuur, B. (2018). Insights into the selection and design of fluid separation processes. *Separation and Purification Technology* **194**, 301–318.
- Blahušiak, M., Kiss, A. A., Kersten, S. R. A. and Schuur, B. (2016). Quick assessment of binary distillation efficiency using a heat engine perspective. *Energy* **116**, 20–31.
- Bonnecaze, R. H., Erskine, W. and Greskovich, E. J. (1971). Holdup and pressure drop for two-phase slug flow in inclined pipelines. *AIChE Journal* **17**, 1109–1113.
- Bothamley, M. (2013a). Gas/Liquid Separators: Quantifying Separation Performance - Part 1. *Oil and Gas Facilities* **2**, 21–29.
- Bothamley, M. (2013b). Gas/Liquids Separators: Quantifying Separation Performance - Part 2. *Oil and Gas Facilities* **2**, 35–47.
- Bottin, M., Berlandis, J. P., Hervieu, E., Lance, M., Marchand, M., Öztürk, O. C. and Serre, G. (2014). Experimental investigation of a developing two-phase bubbly flow in horizontal pipe. *International Journal of Multiphase Flow*. Elsevier Ltd **60**, 161–179.
- Bowden, R. C., Lessard, É. and Yang, S.-K. (2018). Void fraction measurements of bubbly flow in a horizontal 90° bend using wire mesh sensors. *International Journal of Multiphase Flow* **99**, 30–47.
- Brauner, N. and Maron, D. M. (1991). Analysis of stratified/nonstratified transitional boundaries in horizontal gas—liquid flows. *Chemical Engineering Science* **46**, 1849–1859.
- Brauner, N. and Moalem Maron, D. (1992). Stability analysis of stratified liquid-liquid flow. *International Journal of Multiphase Flow* **18**, 103–121.
- Butterworth, D. (1972). Air-water annular flow in a horizontal tube. *Progr. Heat Mass Transfer* **6**, 235–251.
- Butterworth, D. (1975). A comparison of some void-fraction relationships for co-current gas-liquid flow. *International Journal of Multiphase Flow* **1**, 845–850.

- Cai, S., Toral, H., Qiu, J. and Archer, J. S. (1994). Neural network based objective flow regime identification in air-water two phase flow. *The Canadian Journal of Chemical Engineering* **72**, 440–445.
- Canière, H., Bauwens, B., T'Joel, C. and De Paepe, M. (2009). Probabilistic mapping of adiabatic horizontal two-phase flow by capacitance signal feature clustering. *International Journal of Multiphase Flow* **35**, 650–660.
- Chavez Velasco, J. A., Tawarmalani, M. and Agrawal, R. (2021). Systematic analysis reveals thermal separations are not necessarily most energy intensive. *Joule* **5**, 330–343.
- Chen, J. J. (1986). A further examination of void fraction in annular two-phase flow. *International Journal of Heat and Mass Transfer* **29**, 1760–1763.
- Chen, X. T., Cal, X. D. and Brill, J. P. (1997). Gas-liquid stratified-wavy flow in horizontal pipelines. *Journal of Energy Resources Technology* **119**, 209–216.
- Cheng, L., Ribatski, G. and Thome, J. R. (2008). Two-phase flow patterns and flow-pattern maps: Fundamentals and applications. *Applied Mechanics Reviews* **61**, 050802.
- Chexal, B., Lellouche, G., Horowitz, J. and Healzer, J. (1992). A void fraction correlation for generalized applications. *Progress in Nuclear Energy* **27**, 255–295.
- Chinello, G., Ayati, A. A., McGlinchey, D., Ooms, G. and Henkes, R. (2019). Comparison of Computational Fluid Dynamics simulations and experiments for stratified air-water flows in pipes. *Journal of Fluids Engineering* **141**.
- Chisholm, D., L. (1958). Two-phase flow in rough tubes. *Trans ASME*, **80**, 276–286.
- Chisholm, D. (1973). Void fraction during two-phase flow. *Journal of Mechanical Engineering Science* **15**, 235–236.
- Chisholm, D. (1983). 4 - Void fraction and mixture density. In: Godwin, G. (ed.) *Two-phase flow in pipelines and heat exchangers*. New York: Longman Inc., 35–62.
- Choi, J., Pereyra, E., Sarica, C., Park, C. and Kang, J. (2012). An efficient drift-flux closure relationship to estimate liquid holdups of gas-liquid two-phase flow in pipes. *Energies* **5**, 5294–5306.
- Cioncolini, A. and Thome, J. R. (2012). Void fraction prediction in annular two-phase flow. *International Journal of Multiphase Flow*. Elsevier Ltd **43**, 72–84.
- Coddington, P. and Macian, R. (2002). A study of the performance of void fraction correlations used in the context of drift-flux two-phase flow models. *Nuclear Engineering and Design* **215**, 199–216.
- Coker, A. K. and Ludwig, E. E. (2010). chap10 / feed. *Ludwig's applied process design for chemical and petrochemical plants. Volume 2*. Gulf Professional, 961.
- Corral, N. P. del (2014). *Analysis of Two-Phase Flow Pattern Maps*. .
- Costa, C. A. S., de Oliveira, P. M. and Barbosa, J. R. (2018). Intermittent flow initiation in a horizontal tube: quantitative visualization and CFD analysis. *Journal of the Brazilian Society of Mechanical Sciences and Engineering* **40**, 188.
- Couper, J. R., Penney, W. R., Fair, J. R. and Walas, S. M. (2012). Distillation and gas absorption. *Chemical Process Equipment: Selection and Design*. Butterworth-Heinemann, 399–486.
- Cussler, E. L. and Dutta, B. K. (2012). On separation efficiency. *AIChE Journal* **58**, 3825–3831.
- Czop, V., Barbier, D. and Dong, S. (1994). Pressure drop, void fraction and shear stress measurements in an adiabatic two-phase flow in a coiled tube. *Nuclear Engineering and Design* **149**, 323–333.
- da Silva, M. J. (2008). Impedance sensors for fast multiphase flow measurement and imaging impedance sensors for fast multiphase flow measurement and imaging. *Fakultät Elektrotechnik und Informationstechnik*. Technische Universität Dresden.

- da Silva, M. J., Hampel, U., Arruda, L. V. R., Do Amaral, C. E. F. and Morales, R. E. M. (2011). Experimental investigation of horizontal gas-liquid slug flow by means of wire-mesh sensor. *Journal of the Brazilian Society of Mechanical Sciences and Engineering* **33**, 237–242.
- Dallman, J. C. (1978). Investigation of separated flow model in annular gas-liquid two-phase. Illinois University, Urbana-Champaign.
- Davis, E. J. (1969). Interfacial shear measurement for two-phase gas-liquid flow by means of preston tubes. *Industrial and Engineering Chemistry Fundamentals* **8**, 153–159.
- Deendarlianto, Hudaya, A. Z., Indarto and Ozzilenda Soegiharto, K. D. (2019). Wetted wall fraction of gas-liquid stratified co-current two-phase flow in a horizontal pipe with low liquid loading. *Journal of Natural Gas Science and Engineering* **70**, 102967.
- Degance, A. E. and Atherton, R. W. (1970a). Chemical engineering aspects of two-phase flow part 2: Phase equilibria, Flow Regimes, Energy Loss. *Chemical Engineering*. **77**, 151–158.
- Degance, A. E. and Atherton, R. W. (1970b). Chemical engineering aspects of two-phase flow part 1, *Chemical Engineering*. **77**, 135–139.
- Demirel, Y. (2004). Thermodynamic analysis of separation systems. *Separation Science and Technology* **39**, 3897–3942.
- Dhole, V. R. and Linnhoff, B. (1993). Distillation column targets. *Computers and Chemical Engineering* **17**, 549–560.
- Dimentiev, B. A., Lepilin, R. S. and Loginov, A. A. (1959). An investigation of hydrodynamic process of bubbling through a vapor liquid mixture of considerable height. *Nauch Dokl Vish Shkol-Energy* **2**, 251–262.
- Dinaryanto, O., Prayitno, Y. A. K., Majid, A. I., Hudaya, A. Z., Nusirwan, Y. A., Widyaparaga, A., Indarto and Deendarlianto (2017). Experimental investigation on the initiation and flow development of gas-liquid slug two-phase flow in a horizontal pipe. *Experimental Thermal and Fluid Science* **81**, 93–108.
- Doherty, M. F. and Malone, M. F. (2001). Column design and economics. In: Munson, E. M. (ed.) *Conceptual Design of Distillation Systems*. Casson, Thomas, E., 257–287.
- Domanski, P., Vid Didion, D. and Ambler, E. (1983). Computer modeling of the vapor compression cycle with constant flow area expansion device. *NBS Building Science Series* **155**, 1-160.
- Drahoš, J. and Čermák, J. (1989). Diagnostics of gas—liquid flow patterns in chemical engineering systems. *Chemical Engineering and Processing: Process Intensification* **26**, 147–164.
- Dukler, A. E. and Taitel, Y. (2018). Measurement and modeling of flow pattern transitions in gas-liquid systems. *Multiphase Science and Technology*. Springer Nature , 182–275.
- Ebner, L., Drahoš, J., Ebner, G. and Čermák, J. (1987). Characterization of hydrodynamic regimes in horizontal two-phase flow Part I: Pressure drop measurements. *Chemical Engineering and Processing: Process Intensification*. Elsevier **22**, 39–43.
- Eghorieta, R. A., Afolabi, T. A. and Panacharoensawad, E. (2018). Drift-flux modeling of transient high-viscosity-liquid and gas two-phase flow in horizontal pipes. *Journal of Petroleum Science and Engineering* **171**, 605–617.
- Ekambara, K., Sanders, R. S., Nandakumar, K. and Masliyah, J. H. (2008). CFD simulation of bubbly two-phase flow in horizontal pipes. *Chemical Engineering Journal* **144**, 277–288.
- Elperin, T. and Klochko, M. (2013). Flow regime identification in a two-phase flow using wavelet transform. *Experiments in Fluids* **32**, 674–682.
- Epstein, M. (1990). Theory of scrubbing of a volatile fission product vapor-containing gas jet in a water pool. *Sixth proceedings of nuclear thermal hydraulics*. Washington, DC: Transactions of the American Nuclear Society, 217–224.

- Errico, M., Tola, G. and Mascia, M. (2009). Energy saving in a crude distillation unit by a preflash implementation. *Applied Thermal Engineering* **29**, 1642–1647.
- Essaied, M. A. (1992). A study of two-phase flow in a large diameter horizontal pipeline and the measurement of interfacial level gradient in smooth stratified flow conditions. University of Strathclyde, Glasgow, Scotland.
- Eyo, E. N. and Lao, L. (2019). Gas-liquid flow regimes in horizontal annulus. *Journal of Petroleum Science and Engineering* **175**, 573–586.
- F. R. Menter, M. K. and R. L. (2003). Ten years of industrial experience with the SST turbulence model. In: K. Hanjalic, Y. N. M. T. (ed.) *Turbulence, Heat and Mass Transfer 4*. Begell House, Inc., 625–632.
- Fair, J. R. and Humphrey, J. L. (1984). Distillation: Research needs. *Separation Science and Technology* **19**, 943–961.
- Fan, W., Li, H. and Anglart, H. (2019). Numerical investigation of spatial and temporal structure of annular flow with disturbance waves. *International Journal of Multiphase Flow* **110**, 256–272.
- Filimonov, A.I., Przhizhalovski, M.M., Dik, E.P., Petrova, J. N. (1957). The diving head in pipes with a free interface in the pressure range from 17 to 180 atm. *Teploenergetika* **4**, 22–26.
- Flanigan, O. (1958). Two-phase gathering systems. *The Oil and Gas Journal* **56**.
- Flegiel, F., Windmeier, C., Wiezorek, M., Döß, A., Schubert, M., Hampel, U. and Schleicher, E. (2021). Capacity and sizing of wire mesh mist eliminators at critical fluid properties. *Chemie Ingenieur Technik* **93**, 1166–1177.
- Fleming, B., Martin, G. R. and Hartman, E. L. (1996). Pay attention to reflux/feed entry design. *Chemical Engineering Progress*. United States **92**, 56–64.
- Fossa, M., Guglielmini, G. and Marchitto, A. (2003). Intermittent flow parameters from void fraction analysis. *Flow Measurement and Instrumentation* **14**, 161–168.
- Franca, F., Acikgoz, M., Lahey, R. T. and Clausse, A. (1991). The use of fractal techniques for flow regime identification. *International Journal of Multiphase Flow* **17**, 545–552.
- França, F. and Lahey, R. T. (1992). The use of drift-flux techniques for the analysis of horizontal two-phase flows. *International Journal of Multiphase Flow* **18**, 787–801.
- Fujie, H. (1964). A relation between steam quality and void fraction in two-phase flow. *AIChE Journal* **10**, 227–232.
- Gálvez, A. and Iglesias, A. (2003). Binary distillation column design using mathematica. *Computational Science — ICCS 2003*, 848–857.
- Gao, Z.-K., Zhang, X.-W., Du, M. and Jin, N.-D. (2013). Recurrence network analysis of experimental signals from bubbly oil-in-water flows. *Physics Letters A* **377**, 457–462.
- Gardner, G. C. and Neller, P. H. (1969). Phase distributions in flow of an air-water mixture round bends and past obstructions at the wall of a 76-mm bore tube. *Proceedings of the Institution of Mechanical Engineers, Conference Proceedings* **184**, 93–101.
- Ghajar, A. J. and Tang, C. C. (2007). Heat transfer measurements, flow pattern maps, and flow visualization for non-boiling two-phase flow in horizontal and slightly inclined pipe. *Heat Transfer Engineering*. Taylor and Francis Group **28**, 525–540.
- Ghorai, S. and Nigam, K. D. P. (2006). CFD modeling of flow profiles and interfacial phenomena in two-phase flow in pipes. *Chemical Engineering and Processing: Process Intensification* **45**, 55–65.
- Ghorbani, B., Maleki, M., Salehi, A., Salehi, G. R. and Amidpour, M. (2013). Optimization of distillation column operation by simulated annealing. *Gas Processing*. University of Isfahan **1**, 49–63.

- Godbole, P. V., Tang, C. C. and Ghajar, A. J. (2011). Comparison of void fraction correlations for different flow patterns in upward vertical two-phase flow. *Heat Transfer Engineering* **32**, 843–860.
- Goedecke, R. (ed.) (2006). *Fluidverfahrenstechnik*. Wiley.
- Gomez, L. ., Shoham, O. and Taitel, Y. (2000a). Prediction of slug liquid holdup: horizontal to upward vertical flow. *International Journal of Multiphase Flow* **26**, 517–521.
- Gomez, L. E., Shoham, O., Schmidt, Z., Chokshi, R. N. and Northug, T. (2000b). Unified mechanistic model for steady-state two-phase flow: horizontal to vertical upward flow. *SPE Journal* **5**, 339–350.
- Górak, A. and Olujic, Z. (2014). *Distillation: Equipment and Processes*. .
- Górak, A. and Schoenmakers, H. (2014). *Distillation: Operation and Applications*. Elsevier.
- Guerrero, E., Muñoz, F. and Ratkovich, N. (2017). Comparison between eulerian and vof models for two-phase flow assessment in vertical pipes. *CTandF - Ciencia, Tecnología y Futuro* **7**, 73–84.
- Guzhov, A.L., Mamayev, V.A., Odishariya, G. E. (1967). A study of transportation in gas-liquid systems. *10th International Gas Union Conference, Hamburg, Germany, June 6–10*.
- Hanson, D. N., Duffin, J. H. and Sommerville, G. F. (1962). *Computation of Multistage Separation Processes*. New York: Reinhold.
- Harbert, W. D. (1978). Preflash saves heat in crude unit. *Hydrocarbon Processing* **57**, 123–125.
- Hart, J., Hamersma, P. J. and Fortuin, J. M. H. (1989). Correlations predicting frictional pressure drop and liquid holdup during horizontal gas-liquid pipe flow with a small liquid holdup. *International Journal of Multiphase Flow* **15**, 947–964.
- Heinzel, G., Rüdiger, A. and Schilling, R. (2002). Spectrum and spectral density estimation by the Discrete Fourier transform (DFT), including a comprehensive list of window functions and some new flat-top windows. Max-Planck-Institut für Gravitationsphysik (Albert-Einstein-Institut), Teilinstitut Hannover. 1–84.
- Henry, F. (2016). Experimental and modeling investigations on droplet entrainment in a PWR hot leg under stratified flow conditions. Université catholique de Louvain.
- Henry, R. and Mujtaba, I. (1999). Distillation column control: The use of feed temperature to respond to modest variations in feed composition. *Computers and Chemical Engineering* **23**, S265–S268.
- Hernandez, J. S., Valencia, C., Ratkovich, N., Torres, C. F. and Muñoz, F. (2019). Data driven methodology for model selection in flow pattern prediction. *Heliyon* **5**, 1–9.
- Hervieu, E. and Selegim, P. (1998). An objective indicator for two-phase flow pattern transition. *Nuclear Engineering and Design* **184**, 421–435.
- Hewitt, G. F. and Yadigaroglu, G. (2018). Modelling strategies and two-phase flow models. *Introduction to Multiphase Flow*. Cham: Springer International Publishing, 39–77.
- Hewitt, G. and Hall-Taylor, N. S. (1970). The creation and behavior of entrained droplets in annular flow. *Annular Two-Phase Flow*. Pergamon Press Ltd., 136–172.
- Hibiki, T. and Ishii, M. (2001). Distribution parameter and drift velocity of drift-flux model in bubbly flow. *International Journal of Heat and Mass Transfer* **45**, 707–721.
- Hinrichsen, O. (2007). Technische Chemie. *Angewandte Chemie* **119**, 3241–3241.
- Hirt, C. . and Nichols, B. . (1981). Volume of fluid (VOF) method for the dynamics of free boundaries. *Journal of Computational Physics* **39**, 201–225.

- Höhne, T. (2016). Euler-Euler modeling of segregated flows and flows with transitions between different flow morphologies. In: Yeoh, G. H. (ed.) *Handbook of Multiphase Flow Science and Technology*. Singapore: Springer Singapore, 1–33.
- Höhne, T., Geissler, T., Bieberle, A. and Hampel, U. (2015). Numerical modeling of a horizontal annular flow experiment using a droplet entrainment model. *Annals of Nuclear Energy* **77**, 351–360.
- Höhne, T., Porombka, P. and Moya Sáez, S. (2020). Validation of AIAD sub-models for advanced numerical modelling of horizontal two-phase flows. *Fluids* **5**, 102.
- Hoogendoorn, C. J. (1959). Gas-liquid flow in horizontal pipes. *Chemical Engineering Science* **9**, 205–217.
- Hori, K., Ueno, T. and Kawanishi, K. (1985). Gas-liquid two-phase flow in large diameter tube (II. Horizontal Cocurrent Flow). *Proceedings of 22nd Japan National Heat Transfer Symposium*, 356–358.
- Hsu, L. C., Chen, I. Y., Chyu, C. M. and Wang, C. C. (2015). Two-phase pressure drops and flow pattern observations in 90° bends subject to upward, downward and horizontal arrangements. *Experimental Thermal and Fluid Science* **68**, 484–492.
- Hu, D., Huang, Z., Sun, J., Wang, J., Liao, Z., Jiang, B., Yang, J. and Yang, Y. (2017). Numerical simulation of gas-liquid flow through a 90° duct bend with a gradual contraction pipe. *Journal of Zhejiang University-Science A* **18**, 212–224.
- Hughmark, G. A. (1962). Holdup in gas liquid flow. *Chemical engineering progress* **58**, 62–65.
- Huq, R. and Loth, J. L. (1992). Analytical two-phase flow void prediction method. *Journal of Thermophysics and Heat Transfer* **6**, 139–144.
- Isao, K. and Mamoru, I. (1987). Drift flux model for large diameter pipe and new correlation for pool void fraction. *International Journal of Heat and Mass Transfer* **30**, 1927–1939.
- Ishii, M. (1977). One-dimensional drift-flux model and constitutive equations for relative motion between phases in various two-phase flow regimes. Argonne, IL (United States).
- Ishii, M. and Grolmes, M. A. (1975). Inception criteria for droplet entrainment in two-phase concurrent film flow. *AIChE Journal* **21**, 308–318.
- Ishii, M. and Mishima, K. (1981). Correlation for liquid entrainment in annular two-phase flow of viscous fluid. Argonne, IL (United States).
- Issa, R. I. and Kempf, M. H. W. (2003). Simulation of slug flow in horizontal and nearly horizontal pipes with the two-fluid model. *International Journal of Multiphase Flow* **29**, 69–95.
- Jaiboon, O. A., Chalermisinsuwan, B., Mekasut, L. and Piumsomboon, P. (2013). Effect of flow pattern on power spectral density of pressure fluctuation in various fluidization regimes. *Powder Technology* **233**, 215–226.
- James, P. W., Azzopardi, B. J., Graham, D. I. and Sudlow, C. A. (2000). The effect of a bend on droplet distribution in two-phase flow. *International Conference on Multiphase Flow in Industrial Plants*.
- Jana, A. K. (2010). Heat integrated distillation operation. *Applied Energy* **87**, 1477–1494.
- Jobson, M. (2014). Energy considerations in distillation. *Distillation*. Elsevier, 225–270.
- Jones, O. C. and Zuber, N. (1975). The interrelation between void fraction fluctuations and flow patterns in two-phase flow. *International Journal of Multiphase Flow* **2**, 273–306.
- Kanizawa, F. T. and Ribatski, G. (2016). Void fraction predictive method based on the minimum kinetic energy. *Journal of the Brazilian Society of Mechanical Sciences and Engineering*. Springer Berlin Heidelberg **38**, 209–225.
- Kawaji, M. (2018). Fundamental equations for two-phase flow in tubes. *Handbook of Thermal Science and Engineering*. Cham: Springer International Publishing, 1849–1906.

- Kesana, N. R., Vieira, R., Schleicher, E., McLaury, B. S., Shirazi, S. A. and Hampel, U. (2013). Experimental investigation of slug characteristics through a standard pipe bend. *Volume 7A: Fluids Engineering Systems and Technologies*. American Society of Mechanical Engineers, V07AT08A040.
- Kim, S., Park, J. H., Kojasoy, G., Kelly, J. M. and Marshall, S. O. (2007). Geometric effects of 90-degree elbow in the development of interfacial structures in horizontal bubbly flow. *Nuclear Engineering and Design* **237**, 2105–2113.
- Kind, M. and Wetzel, T. (2018). Strömungssieden – strömungsformen in verdampferrohren. In: Stephan, P. (ed.) *Stephan P., Mewes D., Kabelac S., Kind M., Schaber K., Wetzel T. (eds) VDI-Wärmeatlas*. Berlin, Heidelberg: Springer Reference Technik. Springer Vieweg, 1–7.
- Kipping, R., Brito, R., Scheicher, E. and Hampel, U. (2016). Developments for the application of the Wire-Mesh Sensor in industries. *International Journal of Multiphase Flow*. Elsevier Ltd **85**, 86–95.
- Kiss, A. A. (2013). *Advanced distillation technologies*. Chichester, UK: John Wiley and Sons, Ltd.
- Kister, H. Z. (1990). *Distillation Operation*. Mc Graw-Hill.
- Kister, H. Z. (1992). *Distillation Design*. McGraw-Hill Education.
- Kister, H. Z. (2006). *Distillation Troubleshooting*. Wiley.
- Klein, F. L., Selegim Junior, P. and Hervieu, E. (2004). Time-frequency analysis of intermittent two-phase flows in horizontal piping. *Journal of the Brazilian Society of Mechanical Sciences and Engineering* **26**.
- Knösche, C. (2020). Trends in thermal separation technologies – An industrial perspective. *Chemie Ingenieur Technik* **92**, 813–817.
- Kocamustafaogullari, G. and Huang, W. D. (1994). Internal structure and interfacial velocity development for bubbly two-phase flow. *Nuclear Engineering and Design* **151**, 79–101.
- Koch-Glitsch (2018). *Packed Tower Internals*. USA, 1–32.
- Koizumi, Y., Yamamoto, N. and Tasaka, K. (1990). Air/water two-phase flow in a horizontal large-diameter pipe. 1st Report. Flow regime. *Transactions of the Japan Society of Mechanical Engineers Series B* **56**, 3745–3749.
- Kokal, S. L. and Stanislav, J. . (1989). An experimental study of two-phase flow in slightly inclined pipes—II. Liquid holdup and pressure drop. *Chemical Engineering Science* **44**, 681–693.
- Kokal, S. L. and Stanislav, J. F. (1987). An experimental study of two phase flow in inclined pipes. *Chemical Engineering*. The University of Calgary, Faculty of Graduate Studies.
- Kong, R. and Kim, S. (2017). Characterization of horizontal air–water two-phase flow. *Nuclear Engineering and Design* **312**, 266–276.
- Kong, R., Kim, S., Bajorek, S., Tien, K. and Hoxie, C. (2018a). Effects of pipe size on horizontal two-phase flow: Flow regimes, pressure drop, two-phase flow parameters, and drift-flux analysis. *Experimental Thermal and Fluid Science* **96**, 75–89.
- Kong, R., Rau, A., Lu, C., Gamber, J., Kim, S., Bajorek, S., Tien, K. and Hoxie, C. (2018b). Experimental study of interfacial structure of horizontal air-water two-phase flow in a 101.6 mm ID pipe. *Experimental Thermal and Fluid Science* **93**, 57–72.
- Lamari, M. L. (2001). *An experimental investigation of two-phase (air-water) flow regimes in a horizontal tube at near atmospheric conditions*. Carleton University.
- Laurinat, J. E. (1982). *Studies of the effects of pipe size on horizontal annular two-phase flows*. University of Illinois.
- Lee, S. H. and Binkley, M. J. (2011). Optimize design for distillation feed. *Hydrocarbon Processing* **90**, 101–105.

- Lee, S. H. and Min, K. G. (2013). improving the distillation energy network. *Revamps 2013* 3–13.
- Leekwijck, W. Van and Kerre, E. E. (1999). Defuzzification: criteria and classification. *Fuzzy Sets and Systems* **108**, 159–178.
- Legius, H. J. W. M. and Van den Akker, H. E. A. (1997). Numerical and experimental analysis of transitional gas-liquid pipe flow through a vertical bend. In: Burns, A. P. (ed.) *8Th International Conference on Multiphase '97*, pp.437-453.
- Levy, S. (1999). Two-phase flow in complex systems. John Wiley & Sons.
- Li, H., Neng Wong, T., Skote, M. and Duan, F. (2013). Non-newtonian liquid-gas non-uniform stratified flow with interfacial level gradient through horizontal tubes. *Journal of Fluids Engineering* **136**, 021303.
- Liao, J., Ohkawa, K. and Frepoli, C. (2015). A horizontal stratified gas-liquid two-phase flow model for the two-fluid model in the WCOBRA/TRAC-TF2 PWR safety analysis code. *Nuclear Engineering and Design* **295**, 239–250.
- Liebert, Corp., T. (Pritchard, Park, O. and States)), K. (United (1993). Distillation feed preheat--Is it energy efficient. *Hydrocarbon Processing; (United States)*. [Gulf Pub. Co.] **72**, 37–42.
- Lima, R. J. D. S. and Thome, J. R. (2012). Two-phase frictional pressure drops in U-bends and contiguous straight tubes for different refrigerants, orientations, tube, and bend diameters: Part 1. Experimental. *HVACandR Research* **18**, 1047–1071.
- Lin, P.-Y. (1985). Flow regime transitions in horizontal gas-liquid flow. University of Illinois at Urbana-Champaign.
- Lin, P. Y. and Hanratty, T. J. (1987). Effect of pipe diameter on flow patterns for air-water flow in horizontal pipes. *International Journal of Multiphase Flow* **13**, 549–563.
- Liu, X., Chen, Y. and Shi, M. (2012). Influence of gravity on gas-liquid two-phase flow in horizontal pipes. *International Journal of Multiphase Flow* **41**, 23–35.
- Liu, X. G., He, C., He, C. C., Zhang, B. J. and Chen, Q. L. (2017). Optimization of feed locations for double-feed columns based on the column grand composite curve. *Energy Procedia* **105**, 5172–5179.
- Lockhart, R. W. and Martinelli, R. C. (1949). Proposed correlation of data for isothermal 2-Phase, 2-component flow in pipes. *Chemical Engineering Progress*. **45**, 39–48.
- Löscher, K. (1973). Der Schlupf bei ausgebildeter adiabater Einkomponenten-Zweiphasenströmung dampfförmig-flüssig im horizontalen Rohr. *Wissenschaftliche Zeitschriften TU Dresden*.
- Lucas, D., Rzehak, R., Krepper, E., Ziegenhein, T., Liao, Y., Kriebitzsch, S. and Apanasevich, P. (2016). A strategy for the qualification of multi-fluid approaches for nuclear reactor safety. *Nuclear Engineering and Design* **299**, 2–11.
- M. Beyer, L. Szalinski, E. Schleicher and C. Schunk (2018). Wire-mesh sensor data processing software user manual and software description. Dresden, Germany: Institute of Fluid Dynamics Helmholtz-Zentrum Dresden-Rossendorf, 1–82.
- Madsen, N. (1975). A void-fraction correlation for vertical and horizontal bulk-boiling of water. *AIChE Journal* **21**, 607–608.
- Mahvash, A. and Ross, A. (2008). Two-phase flow pattern identification using continuous hidden Markov model. *International Journal of Multiphase Flow* **34**, 303–311.
- Mandal, S. N. and Das, S. K. (2001). Pressure losses in bends during two-phase gas-newtonian liquid flow. *Industrial and Engineering Chemistry Research* **40**, 2340–2351.
- Mandhane, J. M., Gregory, G. A. and Aziz, K. (1974). A flow pattern map for gas-liquid flow in horizontal pipes. *International Journal of Multiphase Flow* **1**, 537–553.

- Mantilla, I. (2008). Mechanistic modeling of liquid entrainment in gas in horizontal pipes. The University of Tulsa.
- Mantilla, I., Gomez, L., Mohan, R., Shoham, O., Kouba, G. and Roberts, R. (2009a). Experimental investigation of liquid entrainment in gas in horizontal pipes. *Volume 1: Symposia, Parts A, B and C*. ASME DC, 943–969.
- Mantilla, I., Gomez, L., Mohan, R., Shoham, O., Kouba, G. and Roberts, R. (2009b). Modeling of liquid entrainment in gas in horizontal pipes. *Volume 1: Symposia, Parts A, B and C*. ASME Digital Collection, 979–1007.
- Márquez-Torres, L., Ochoa-Pineda, J., Pico, P., Valdés, J. P., Becerra, D., Pinilla, A., Pereyra, E. and Ratkovich, N. (2020). Comparison of 63 different void fraction correlations for different flow patterns, pipe inclinations, and liquid viscosities. *SN Applied Sciences* **2**, 1695.
- Mazhar, H., Cotton, J. S., Ewing, D. and Ching, C. Y. (2014). Mass transfer in S-shape dual pipe bends under annular two phase flow conditions. *International Journal of Heat and Mass Transfer* **72**, 308–318.
- Mazumder, Q. H. and Siddique, S. A. (2011). CFD analysis of two-phase flow characteristics in a 90 Degree elbow. *The Journal of Computational Multiphase Flows* **3**, 165–175.
- McBride, K., Sanchez Medina, E. I. and Sundmacher, K. (2020). Hybrid semi-parametric modeling in separation processes: A Review. *Chemie Ingenieur Technik*. Wiley-VCH Verlag **92**, 842–855.
- McCabe, W. L., Smith, J. C. and Peter, H. (1993). Unit operations of chemical engineering. New York: McGraw-Hill.
- McMillan, H. K. (1963). A study of flow patterns and pressure drop in horizontal two-phase flow. Purdue University
- Meknassi, F., Benkirane, R., Liné, A. and Masbernat, L. (2000). Numerical modeling of wavy stratified two-phase flow in pipes. *Chemical Engineering Science* **55**, 4681–4697.
- Menter, F. (1993). Zonal two equation k-w turbulence models for aerodynamic flows. *23rd Fluid Dynamics, Plasmadynamics, and Lasers Conference*. Reston, Virginia: American Institute of Aeronautics and Astronautics.
- Menter, F. R. (1994). Two-equation eddy-viscosity turbulence models for engineering applications. *AIAA Journal* **32**, 1598–1605.
- Mersmann, A., Kind, M. and Stichlmair, J. (2011). *Thermal Separation Technology*. Berlin, Heidelberg: Springer Berlin Heidelberg.
- Minami, K. and Brill, J. P. (1987). Liquid Holdup in Wet-Gas Pipelines. *SPE Production Engineering* **2**, 36–44.
- Miyatake, O. (1994). Comparative study of flash evaporation rates. *Desalination* **96**, 163–171.
- Möller, F., Lavetty, C., Schleicher, E., Löschau, M., Hampel, U. and Schubert, M. (2019). Hydrodynamics, mixing and mass transfer in a pilot-scale bubble column with dense internals. *Chemical Engineering Science* **202**, 491–507.
- Moran, S. (2017). Distillation Columns and Towers. *Process Plant Layout*. Elsevier, 325–338.
- Morel, C., Pouvreau, J., Laviéville, J. and Boucker, M. (2004). Numerical simulations of a bubbly flow in a sudden-expansion with the NEPTUNE code. *3rd International Symposium on Two-Phase Flow Modelling and Experimentation (ISTPME '04)*, 22–24.
- Motamedian, E., Kasiri, N. and Ghaemi, A. (2007). Modeling two-phase flow in horizontal pipe bends. *Hydrocarbon Processing* **86**, 145–150.
- Mukherjee, H. and Brill, J. P. (1983). Liquid holdup correlations for inclined two-phase flow. *Journal of Petroleum Technology* **35**, 1003–1008.

- Nakaiwa, M., Huang, K., Endo, A., Ohmori, T., Akiya, T. and Takamatsu, T. (2003). Internally heat-integrated distillation columns: A review. *Chemical Engineering Research and Design* **81**, 162–177.
- Naphon, P. and Wongwises, S. (2006). A review of flow and heat transfer characteristics in curved tubes. *Renewable and Sustainable Energy Reviews* **10**, 463–490.
- Nasrfard, H., Rahimzadeh, H., Ahmadpour, A. and Amani, E. (2019). Simulation of intermittent flow development in a horizontal pipe. *Journal of Fluids Engineering* **141**.
- Nevers, N. De (2005). *Fluid Mechanics for Chemical Engineers*. McGraw-Hill Higher Education.
- Nguyen, V. T. (1975). Two-phase, gas-liquid concurrent flow: an investigation of holdup, pressure drop and flow pattern in a pipe at various inclinations. The University of Auckland.
- Nguyen, V. T., Euh, D. J. and Song, C.-H. (2010). An application of the wavelet analysis technique for the objective discrimination of two-phase flow patterns. *International Journal of Multiphase Flow* **36**, 755–768.
- Nino, V.G.; Hrnjak, P.S.; Newell, T. A. (2002). Characterization of two-phase flow in microchannels. Urbana, Illinois.
- Nydal, O. J., Pintus, S. and Andreussi, P. (1992). Statistical characterization of slug flow in horizontal pipes. *International Journal of Multiphase Flow* **18**, 439–453.
- Ognisty, T. P. (2000). Distillation - Energy management. *Encyclopedia of Separation Science*. Elsevier, 1005–1012.
- Ohlmer, E., Fortescue, T., Riebold, W., Bors, B., Immink, J. and Wesser, U. (1984). Two-phase flow identification by calibration with stochastic parameters. In: Delhaye, J. M. (ed.) *Measuring Techniques in Gas-Liquid Two-Phase Flows*. Springer Berlin Heidelberg, 563–585.
- Oliemans, R. V. A. and Pots, B. F. M. (2005). Gas-liquid transport in ducts. In: Crowe, C. T. (ed.) *Multiphase Flow Handbook*. CRC Press, 1–40.
- Ongba-Essama, C. (2004). Numerical modelling of transient gas-liquid flows (application to stratified and slug flow regimes). Cranfield University.
- Ousaka, A., Morioka, I. and Fukano, T. (1992). Air-water annular two-phase flow in horizontal and near horizontal tubes. *Japanese Journal of Multiphase Flow* **6**, 80–87.
- Paras, S. V. and Karabelas, A. J. (1991a). Properties of the liquid layer in horizontal annular flow. *International Journal of Multiphase Flow* **17**, 439–454.
- Paras, S. V. and Karabelas, A. J. (1991b). Droplet entrainment and deposition in horizontal annular flow. *International Journal of Multiphase Flow* **17**, 455–468.
- Perry, R. H., Green, D. W. and Maloney, J. O. (1997). Perry's chemical engineers' handbook. McGraw-Hill.
- Picchi, D., Correra, S. and Poesio, P. (2014). Flow pattern transition, pressure gradient, hold-up predictions in gas/non-Newtonian power-law fluid stratified flow. *International Journal of Multiphase Flow* **63**, 105–115.
- Picchi, D. and Poesio, P. (2016a). A unified model to predict flow pattern transitions in horizontal and slightly inclined two-phase gas/shear-thinning fluid pipe flows. *International Journal of Multiphase Flow* **84**, 279–291.
- Picchi, D. and Poesio, P. (2016b). Stability of multiple solutions in inclined gas/shear-thinning fluid stratified pipe flow. *International Journal of Multiphase Flow* **84**, 176–187.
- Pietrzak, M. (2014). Flow patterns and gas fractions of air–oil and air–water flow in pipe bends. *Chemical Engineering Research and Design*. Institution of Chemical Engineers **92**, 1647–1658.
- Pietrzak, M. and Płaczek, M. (2019). Void fraction predictive methods in two-phase flow across a small diameter channel. *International Journal of Multiphase Flow* **121**, 103115.

- Pietrzak, M. and Witczak, S. (2013). Flow patterns and void fractions of phases during gas–liquid two-phase and gas–liquid–liquid three-phase flow in U-bends. *International Journal of Heat and Fluid Flow* **44**, 700–710.
- Pilling, M., Roza, M. and Wong, S. M. (2010). Entrainment issues in vacuum column flash zones. *Petroleum technology quarterly* **15**, 57–65.
- Pinilla, J. A., Guerrero, E., Pineda, H., Posada, R., Pereyra, E. and Ratkovich, N. (2019). CFD modeling and validation for two-phase medium viscosity oil-air flow in horizontal pipes. *Chemical Engineering Communications* **206**, 654–671.
- Prasser, H.-M., Böttger, A. and Zschau, J. (1998). A new electrode-mesh tomograph for gas–liquid flows. *Flow Measurement and Instrumentation* **9**, 111–119.
- Prasser, H. M., Krepper, E. and Lucas, D. (2002). Evolution of the two-phase flow in a vertical tube - Decomposition of gas fraction profiles according to bubble size classes using wire-mesh sensors. *International Journal of Thermal Sciences* **41**, 17–28.
- Premoli, A., Francesco, D. and Prima, A. (1970). An empirical correlation for evaluating two-phase mixture density under adiabatic conditions. *European Two-Phase Flow Group Meeting, 1970*.
- Qi, C., Wang, X., Feng, H. and Lv, Q. (2017). Performance analysis of low-temperature multi-effect distillation system under different feeding modes. *Applied Thermal Engineering* **112**, 1452–1459.
- Quandt, E. (1965). Analysis of gas-liquid flow patterns. *Chemical engineering progress / Symposium series* **57**, 128–136.
- Rassame, S. and Hibiki, T. (2018). Drift-flux correlation for gas-liquid two-phase flow in a horizontal pipe. *International Journal of Heat and Fluid Flow* **69**, 33–42.
- Reinhard Billet (1983). Energieeinsparung bei thermischen Stofftrennverfahren. Anwendungen im technologischen Umweltschutz. Hüthig.
- Ribeiro, A. M., Bott, T. R. and Jepson, D. M. (1995). Drop size and entrainment measurements in horizontal flow. *1st International symposium; on Two-phase flow modelling and experimentation, Rome*.
- Ribeiro, A. M., Bott, T. R. and Jepson, D. M. (2001). The influence of a bend on drop sizes in horizontal annular two-phase flow. *International Journal of Multiphase Flow* **27**, 721–728.
- Ribeiro, A. M. D. S. (1993). Studies of gas-liquid flow in bends. University of Birmingham.
- Riese, J., Hoff, A., Stock, J., Górak, A. and Grünewald, M. (2020). Separation Units 4.0 – Trennapparate heute und morgen. *Chemie Ingenieur Technik*. Wiley-VCH Verlag **92**, 818–830.
- Rouhani, S. and Axelsson, E. (1970). Calculation of void volume fraction in the subcooled and quality boiling regions. *International Journal of Heat and Mass Transfer* **13**, 383–393.
- Rouhani, S. Z. and Sohal, M. S. (1983). Two-phase flow patterns: A review of research results. *Progress in Nuclear Energy* **11**, 219–259.
- Roul, M. K. and Dash, S. K. (2011). Two-phase pressure drop caused by sudden flow area contraction/expansion in small circular pipes. *International Journal for Numerical Methods in Fluids* **66**, 1420–1446.
- RVT Process Equipment GmbH (2015). *Column internals*. https://www.rvtpe.com/fileadmin/documents/print_and_publications/RVT_Column_internals_141124.pdf, 1–20.
- Sadatom, M., Kawaji, M., Lorencez, C. M. and Chang, T. (1993). Prediction of liquid level distribution in horizontal gas-liquid stratified flows with interfacial level gradient. *International Journal of Multiphase Flow* **19**, 987–997.
- Sadrehaghghi, I. (2018). Multiphase Flow. *CFD Open Series*.

- Saffari, H., Moosavi, R., Nouri, N. M. and Lin, C.-X. (2014). Prediction of hydrodynamic entrance length for single and two-phase flow in helical coils. *Chemical Engineering and Processing: Process Intensification*. Elsevier B.V. **86**, 9–21.
- Sahovic, B. *et al.* (2020). Controlled inline fluid separation based on smart process tomography sensors. *Chemie Ingenieur Technik* **92**, 554–563.
- Sakaguchi, T., Ozawa, M., Hamaguchi, H., Nishiwaki, F. and Fujii, E. (1987). Analysis of the impact force by a transient liquid slug flowing out of a horizontal pipe. *Nuclear Engineering and Design* **99**, 63–71.
- Sakamoto, G., Doi, T., Murakami, Y. and Usui, K. (2004). Profiles of liquid film thickness and drop flow rate in U-bend annular mist flow. Proceedings of the international conference on multiphase flow. Yokohama, Japan: ICMF, 380.
- Salcudean, M., Chun, J. H. and Groeneveld, D. C. (1983). Effect of flow obstructions on the flow pattern transitions in horizontal two-phase flow. *International Journal of Multiphase Flow* **9**, 87–90.
- Sánchez Silva, F., Luna Resendiz, J. C., Carvajal Mariscal, I., Tolentino Eslava, R., I. C. M. and R, T. E. (2010). pressure drop models evaluation for two-phase flow in 90 degree horizontal elbows. *Ing. mecánica, Tecnol. y Desarrollo*. **3**, 115–122.
- Sawant, P., Ishii, M. and Mori, M. (2009). Prediction of amount of entrained droplets in vertical annular two-phase flow. *International Journal of Heat and Fluid Flow* **30**, 715–728.
- Schaffrath, A. and Ringel, H. (2000). Modelle zur Bestimmung der Relativbewegung der Phasen in einer Zweiphasenströmung. Forschungszentrum Rossendorf.
- Schmelter, S., Olbrich, M., Schmeyer, E. and Bär, M. (2020). Numerical simulation, validation, and analysis of two-phase slug flow in large horizontal pipes. *Flow Measurement and Instrumentation*. Elsevier Ltd **73**, 101722.
- Seader, J. D. and Henley, E. J. (2006). *Separation process principles*. Wiley.
- Selegim, P. J., Hervieu, E. and Santos, A. M. (1998). Time frequency characterization of two-phase horizontal air-water flow regimes. *Revista brasileira de ciencias mecanicas* **XX**, 39–50.
- Selli, M. F. and Selegim, P. (2007). Online identification of horizontal two-phase flow regimes through gabor transform and neural network processing. *Heat Transfer Engineering* **28**, 541–548.
- Setyawan, A., Indarto and Deendarlianto (2016). The effect of the fluid properties on the wave velocity and wave frequency of gas-liquid annular two-phase flow in a horizontal pipe. *Experimental Thermal and Fluid Science* **71**, 25–41.
- Sharaf, S., Da Silva, M., Hampel, U., Zippe, C., Beyer, M. and Azzopardi, B. (2011). Comparison between wire mesh sensor and gamma densitometry void measurements in two-phase flows. *Measurement Science and Technology* **22**, 104019.
- Shoham, O. (2006). Mechanistic modeling of gas-liquid two-phase flow in pipes. *The Society of Petroleum Engineers (SPE)*.
- Sholl, D. S. and Lively, R. P. (2016). Seven chemical separations to change the world. *Nature* **532**, 435–437.
- Shotton, E. and Habeeb, A. F. S. A. (1954). The entrainment of liquid during distillation. *Journal of Pharmacy and Pharmacology* **6**, 1023–1036.
- Simon, M. (1997). Experimentelle Untersuchungen zu Strömungsformen in horizontalen und geneigten Verdampferrohren. Karlsruher Insitut für Technologie.
- Simpson, H. C., Rooney, D. H., Grattan, E. and Al-Samarrae, F. A. A. (1981). Two-phase flow studies in large diameter horizontal tubes. *NASA STI/Recon Technical Report N*. Glasgow.

- Sloley, A. W. and A. C. S. Fraser (2000). Consider modeling tools to revamp existing process units. *Hydrocarbon Processing* **79**, 57–63.
- Smith, S. L. (1969). Void fractions in two-phase flow: A correlation based upon an equal velocity head model. *Proceedings of the Institution of Mechanical Engineers* **184**, 647–664.
- Sonnenburg, H. G. (1989). Full-range drift-flux model based on the combination of drift-flux theory with envelope theory. *Fourth International Topical Meeting on Nuclear Reactor Thermal Hydraulics*. Karlsruhe: IAEA, 1003–1007.
- Sonnenburg, H. G. (1991). *Entwicklung eines umfassenden Drift-Flux-Modells zur Bestimmung der Relativgeschwindigkeit zwischen Wasser und Dampf*.
- Sowinski, J., Dziubinski, M. and Fidos, H. (2009). Velocity and gas-void fraction in two-phase liquid-gas flow in narrow mini-channels. *Archives of Mechanics* **61**, 29–40.
- Spedding, P. L. and Chen, J. J. (1984). Holdup in two phase flow. *International Journal of Multiphase Flow* **10**, 307–339.
- Spedding, P. L., Cooper, R. K. and McBride, W. J. (2008). A universal flow regime map for horizontal two-phase flow in pipes. *Developments in Chemical Engineering and Mineral Processing* **11**, 95–106.
- Spedding, P. L. and Spence, D. R. (1989). Prediction of holdup in two-phase flow. *International Journal of Engineering Fluid Mechanics* **2**, 109–118.
- Spedding, P. L., Spence, D. R. and Hands, N. P. (1990). Prediction of holdup in two-phase gas-liquid inclined flow. *The Chemical Engineering Journal* **45**, 55–74.
- Speight, J. G. (2011). Distillation. *The Refinery of the Future*. Elsevier, 117–145.
- Sterman, L. S. (1956). The generalization of experimental data concerning the bubbling of vapor through liquid. *Technical physics* **1**, 1479–1485.
- Stomma, Z. (1979). Two-phase flows-void fraction values determination. *INR--1818/9/R*. Warsaw.
- Strand, Ø. (1993). An experimental investigation of stratified two-phase flow in horizontal pipes. University of Oslo.
- Sulzer (2019). Distillation technology. <https://www.sulzer.com/en/shared/products/distillation>.
- Sulzer Ltd (2018). Gas/Liquid Separation Technology. 1–26.
- Sun, K.H., Duffey, R.B., Peng, C. M. (1980). A thermal-hydraulic analysis of core uncover. *Proceedings of the 19th National Heat Transfer Conference, Experimental and Analytical Modeling of LWR Safety Experiments*. Orlando, Florida, 1–10.
- Taitel, Y. and Barnea, D. (2018). Structural Stability and transient changes of the liquid level in stratified flow. *Multiphase Flow Phenomena and Applications*. World Scientific, 97–113.
- Taitel, Y. and Dukler, A. E. (1976a). A model for predicting flow regime transitions in horizontal and near horizontal gas-liquid flow. *AIChE Journal* **22**, 47–55.
- Taitel, Y. and Dukler, A. E. (1976b). A theoretical approach to the Lockhart-Martinelli correlation for stratified flow. *International Journal of Multiphase Flow* **2**, 591–595.
- Taitel, Y. and Dukler, A. E. (1987). Effect of pipe length on the transition boundaries for high-viscosity liquids. *International Journal of Multiphase Flow* **13**, 577–581.
- Taitel, Y., Lee, N. and Dukler, A. E. (1978). Transient gas-liquid flow in horizontal pipes: Modeling the flow pattern transitions. *AIChE Journal* **24**, 920–934.
- Taitel, Y., Shoham, O. and Brill, J. P. (1989). Simplified transient solution and simulation of two-phase flow in pipelines. *Chemical Engineering Science* **44**, 1353–1359.

- Talley, J. D., Kim, S., Guo, T. and Kojasoy, G. (2009). Geometric effects of 45-deg elbow in horizontal air-water bubbly flow. *Nuclear Technology* **167**, 2–12.
- Tandon, T. N., Varma, H. K. and Gupta, C. P. (1985). A void fraction model for annular two-phase flow. *International Journal of Heat and Mass Transfer* **28**, 191–198.
- Tang, Z., Wu, W., Han, X., Zhao, M., Luo, J., Fu, C. and Tao, R. (2020). Numerical modelling and simulation of two-phase flow flushing method for pipeline cleaning in water distribution systems. *Water* **12**, 2470.
- Tas-Koehler, S., Neumann-Kipping, M., Liao, Y., Krepper, E. and Hampel, U. (2021). CFD simulation of bubbly flow around an obstacle in a vertical pipe with a focus on breakup and coalescence modelling. *International Journal of Multiphase Flow* **135**, 103528.
- Thaker, J. and Banerjee, J. (2015). Characterization of two-phase slug flow sub-regimes using flow visualization. *Journal of Petroleum Science and Engineering* **135**, 561–576.
- The RELAP5 Development Team (1995). RELAP5/MOD3 Code Manual, *Vol. 4 Models and Correlations*. .
- Theßeling, C. and Grünewald, M. (2019). Genauigkeit der Bestimmung von Blasengrößen aus Messdaten eines Leitfähigkeits-Gittersensors. *Chemie Ingenieur Technik* **91**, 1696–1701.
- Thom, J. R. S. (1964). Prediction of pressure drop during forced circulation boiling of water. *International Journal of Heat and Mass Transfer* **7**, 709–724.
- Thome, J. R. and Cioncolini, A. (2015). Void Fraction. *Encyclopedia of Two-Phase Heat Transfer and Flow, Set 1: Fundamentals and Methods, Volume 3: Flow Boiling in Macro and Microchannels*. World Scientific Publishing, 85–112.
- Tiwari, P., Antal, S. P. and Podowski, M. Z. (2006). Three-dimensional fluid mechanics of particulate two-phase flows in U-bend and helical conduits. *Physics of Fluids* **18**, 043304.
- Tkaczyk, P. M. and Morvan, H. P. (2011). Film thickness prediction in an annular two-phase flow around C-shaped bend. *The Journal of Computational Multiphase Flows*. SAGE PublicationsSage UK: London, England **3**, 27–39.
- Tompkins, C., Prasser, H. M. and Corradini, M. (2018). Wire-mesh sensors: A review of methods and uncertainty in multiphase flows relative to other measurement techniques. *Nuclear Engineering and Design* **337**, 205–220.
- TRACE (2008). User's Manual Volume 2: *Modeling Guidelines*. .
- Turner, J. M. and Wallis, G. B. (1965). Two-phase flow and boiling heat transfer - The separate-cylinders model of two-phase flow. Thayer School of Engineering.
- Ujang, P. M., Lawrence, C. J., Hale, C. P. and Hewitt, G. F. (2006). Slug initiation and evolution in two-phase horizontal flow. *International Journal of Multiphase Flow* **32**, 527–552.
- Ullmann, A. and Brauner, N. (2006). Closure relations for two-fluid models for two-phase stratified smooth and stratified wavy flows. *International Journal of Multiphase Flow* **32**, 82–105.
- Vallée, C., Höhne, T., Prasser, H.-M. and Sühnel, T. (2008). Experimental investigation and CFD simulation of horizontal stratified two-phase flow phenomena. *Nuclear Engineering and Design* **238**, 637–646.
- Vashisth, S., Kumar, V. and Nigam, K. D. P. (2008). A review on the potential applications of curved geometries in process industry. *Ind. Eng. Chem. Res.* **47**, 3291–3337.
- Vashisth, S. and Nigam, K. D. P. (2008). Liquid-phase residence time distribution for two-phase flow in coiled flow inverter. *Industrial and Engineering Chemistry Research* **47**, 3630–3638.
- Vashisth, S. and Nigam, K. D. P. (2009). Chemical engineering and processing: process intensification prediction of flow profiles and interfacial phenomena for two-phase flow in coiled tubes. *Control* **48**, 452–463.

- VDI (2013). VDI-Wärmeatlas. Berlin, Heidelberg: Springer Berlin Heidelberg.
- Velasco Peña, H. F. and Rodriguez, O. M. H. (2015). Applications of wire-mesh sensors in multiphase flows. *Flow Measurement and Instrumentation* **45**, 255–273.
- Vieira, R. E., Kesana, N. R., McLaury, B. S., Shirazi, S. A., Torres, C. F., Schleicher, E. and Hampel, U. (2014). Experimental investigation of the effect of 90° standard elbow on horizontal gas-liquid stratified and annular flow characteristics using dual wire-mesh sensors. *Experimental Thermal and Fluid Science* **59**, 72–87.
- Vieira, R. E., Kesana, N. R., Torres, C. F., McLaury, B. S., Shirazi, S. A., Schleicher, E. and Hampel, U. (2013). Experimental investigation of horizontal gas-liquid stratified and annular flow using wire mesh sensor. *American Society of Mechanical Engineers, Fluids Engineering Division (Publication) FEDSM*. ASME, V01CT17A005.
- Vohr, J. H. (1960). *Flow patterns of two-phase flow - A survey of literature*. Engineering Research Laboratories, Columbia University.
- Wagner, W. and Kretzschmar, H.-J. (2008). *International Steam Tables*. Berlin, Heidelberg: Springer Berlin Heidelberg.
- Wallis, G. B. (1969). *One-dimensional Two-phase Flow*. McGraw-Hill .
- Wang, C.-C., Chen, I. Y. and Yang, Y.-W. (2002). Influence of horizontal return bend on the two-phase flow pattern in a 6.9 mm diameter tube. *The Canadian Journal of Chemical Engineering* **80**, 478–484.
- Wang, C.-C., Youn Chen, I., Yang, Y.-W. and Hu, R. (2004). Influence of horizontal return bend on the two-phase flow pattern in small diameter tubes. *Experimental Thermal and Fluid Science* **28**, 145–152.
- Wang, J., Wang, H., Azzopardi, B. J., Yang, L., Zhao, Z. and Xu, S. (2016). Phase separation of gas-liquid two-phase stratified and plug flows in multitube T-junction separators. *AIChE Journal* **63**, 2285–2292.
- Wang, X., Guo, L. and Zhang, X. (2007). An experimental study of the statistical parameters of gas-liquid two-phase slug flow in horizontal pipeline. *International Journal of Heat and Mass Transfer* **50**, 2439–2443.
- Wankat, P. C. (2007). Balancing diameters of distillation column with vapor feeds. *Industrial and Engineering Chemistry Research* **46**, 8813–8826.
- Wankat, P. C. (2011). *Separation process engineering*. 2012 Pearson Education, Inc.
- Warren, B. A. and Klausner, J. F. (1995). Developing lengths in horizontal two-phase bubbly flow. *Journal of Fluids Engineering* **117**, 512–518.
- Wehrli, M., Schaeffer, P., Marti, U., Muggli, F. and Kooijman, H. (2006). Mixed-phase feeds in mass transfer columns and liquid separation. *ICHEME Distillation and Absorption 2006*, 230–240.
- Weisman, J., Duncan, D., Gibson, J. and Crawford, T. (1979). Effects of fluid properties and pipe diameter on two-phase flow patterns in horizontal lines. *International Journal of Multiphase Flow* **5**, 437–462.
- Welch, P. (1967). The use of fast Fourier transform for the estimation of power spectra: A method based on time averaging over short, modified periodograms. *IEEE Transactions on Audio and Electroacoustics* **15**, 70–73.
- Widell, T. (1949). Pressure losses in the flow of gas and liquid mixture in horizontal pipes. *IVA*.
- Wiedemann, P., Dias, F. de A., Schleicher, E. and Hampel, U. (2020). Temperature compensation for conductivity-based phase fraction measurements with wire-mesh sensors in gas-liquid flows of dilute aqueous solutions. *Sensors* **20**, 7114.
- Wiedemann, P., Döß, A., Schleicher, E. and Hampel, U. (2019). Fuzzy flow pattern identification in horizontal air-water two-phase flow based on wire-mesh sensor data. *International Journal of Multiphase Flow*. Pergamon **117**, 153–162.

- Windmeier, C., Flegiel, F., Döß, A., Franz, R., Schleicher, E., Wiezorek, M., Schubert, M. and Hampel, U. (2021). A new research infrastructure for investigating flow hydraulics and process equipment at critical fluid properties. *Chemie Ingenieur Technik* **93**, 1119–1125.
- Winkler, J., Killion, J., Garimella, S. and Fronk, B. M. (2012). Void fractions for condensing refrigerant flow in small channels: Part I literature review. *International Journal of Refrigeration*. Elsevier Ltd and IIR **35**, 219–245.
- Woldesemayat, M. A. and Ghajar, A. J. (2007). Comparison of void fraction correlations for different flow patterns in horizontal and upward inclined pipes. *International Journal of Multiphase Flow* **33**, 347–370.
- Wong, T. N. and Yau, Y. K. (1997). Flow patterns in two-phase air-water flow. *International Communications in Heat and Mass Transfer* **24**, 111–118.
- Woods, B. D., Fan, Z. and Hanratty, T. J. (2006). Frequency and development of slugs in a horizontal pipe at large liquid flows. *International Journal of Multiphase Flow* **32**, 902–925.
- Woods, B. D. and Hanratty, T. J. (1996). Relation of slug stability to shedding rate. *International Journal of Multiphase Flow* **22**, 809–828.
- Woods, B. D. and Hanratty, T. J. (1999). Influence of Froude number on physical processes determining frequency of slugging in horizontal gas-liquid flows. *International Journal of Multiphase Flow* **25**, 1195–1223.
- Wu, H. L., Pots, B. F. . and Hollenberg, J. F. (1987). Flow pattern transitions in two-phase gas/condensate flow at high pressure in an 8-inch horizontal pipe line. *3rd International Conference on Multiphase Flow*, 13–21.
- Xiao, J. J., Shonham, O. and Brill, J. P. (1990). A comprehensive mechanistic model for two-phase flow in pipelines. *All Days*. SPE.
- Yadav, M. S., Kim, S., Tien, K. and Bajorek, S. M. (2014a). Experiments on geometric effects of 90-degree vertical-upward elbow in air water two-phase flow. *International Journal of Multiphase Flow* **65**, 98–107.
- Yadav, M. S., Worosz, T., Kim, S., Tien, K. and Bajorek, S. M. (2014b). Characterization of the dissipation of elbow effects in bubbly two-phase flows. *International Journal of Multiphase Flow*. Elsevier Ltd **66**, 101–109.
- Yashar, D. A., Wilson, M. J., Kopke, H. R., Graham, D. M., Chato, J. C. and Newell, T. A. (2001). An investigation of refrigerant void fraction in horizontal, microfin tubes. *HVACandR RESEARCH* **7**, 67–82.
- Zeguai, S., Chikh, S. and Tadrist, L. (2013). Experimental study of two-phase flow pattern evolution in a horizontal circular tube of small diameter in laminar flow conditions. *International Journal of Multiphase Flow* **55**, 99–110.
- Zhai, L. S., Jin, N. De, Zong, Y. B., Hao, Q. Y. and Gao, Z. K. (2015). Experimental flow pattern map, slippage and time-frequency representation of oil-water two-phase flow in horizontal small diameter pipes. *International Journal of Multiphase Flow* **76**, 168–186.
- Zhao, D., Omar, R., Abdulkadir, M., Abdulkareem, L. A., Azzi, A., Saidj, F., Hernandez Perez, V., Hewakandamby, B. N. and Azzopardi, B. J. (2017). The control and maintenance of desired flow patterns in bends of different orientations. *Flow Measurement and Instrumentation* **53**, 230–242.
- Zhao, H. D., Lee, K. C. and Freeston, D. H. (2000). Geothermal two-phase flow in horizontal pipes. *World Geothermal Congress 2000*, 3349–3353.
- Zivi, S. M. (1964). Estimation of steady-state steam void-fraction by means of the principle of minimum entropy production. *Journal of Heat Transfer* **86**, 247–251.
- Zuber, N. and Findlay, J. A. (1965). Average volumetric concentration in two-phase flow systems. *Journal of Heat Transfer* **87**, 453.

List of figures

Figure 1.1:	Operation region and operation limits of tray columns. Chart adapted from Mersmann et al. (2011).....	3
Figure 2.1:	Photograph and schematic of a distillation column with exemplary internals (right). Image sources: Gálvez and Iglesias (2003); Sulzer (2019).	6
Figure 2.2:	a) Thermodynamic efficiency (TE) for saturated feeds and two-phase feeds ($\chi_{L,F} = 0.25$), b) optimal feed condition q_{opt} for various feed compositions $\chi_{L,F}$, adapted from Bandyopadhyay (2002).....	8
Figure 2.3:	Separation performance of inlet devices adapted from Bothamley (2013a). Image sources: half pipe and vane type inlet device – RVT Process Equipment GmbH (2015), diverter baffle – Koch-Glitsch (2018), cyclonic inlet device – Sulzer Ltd (2018).....	10
Figure 2.4:	a) Ranges of superficial velocities $u_{s,k}$, based on dominant forces due to gravity (I) and pressure drop (II) and b) lower limit for the hydraulic diameters, D_h , below which surface tension (III) governs the flow morphology depending of the fluid properties.	13
Figure 2.5:	a) Mechanisms of droplet entrainment: (1) shear-off, (2) wave undercut, (3) bubble burst, (4) liquid impinging, b) conditions for the onset of entrainment (OE), classified into three entrainment regimes: low Reynolds regime (LR), transition regime (T) and rough turbulent regime (RT).	14
Figure 2.6:	Superimposed flow regime maps from literature for water-air mixtures in pipes with $25 \leq D \leq 28$ mm and predictions for the onset of entrainment (blue dashed lines: based on experiments; blue solid lines: predictive criteria from Table 2.3).	19
Figure 2.7:	Handling of two-phase feeds (colored background) with short entrance lengths (typically $L/D = 5$, other lengths are shown as reference) as a consequence of flow morphology transitions (predicted with the TFM for $D = 200$ mm, water-air systems), onset of entrainment and inception of intermittent flows (Section 2.2.1).....	21
Figure 2.8:	a) Characteristic liquid levels of the ILG, b) resulting transitions between stratified (smooth and wavy) and non-stratified (annular and intermittent) flow morphologies depending on the upstream distance L/D from discharge.	29
Figure 2.9:	Solution of Equation 2.36 depending on the liquid level h_L : numerator (top), ILG (middle) and denominator (bottom) illustrated for different superficial liquid velocities.	31
Figure 2.10:	Engineering guidelines for the selection of two-phase feed inlet devices based on predicted void fractions α_G (the gray area indicate the scattering predictions of existing correlations). Source of embedded pictures of inlet devices: RVT Process Equipment GmbH (2015).	34

Figure 3.1:	Schematic of the experimental setups (black: identical configuration, blue: DN50 feed pipe setup, green: DN200 feed pipe setup).....	38
Figure 3.2:	a) DN50 feed pipe setup (reference system), b) straight feed pipe section, c) CAD drawing of the gas-liquid-mixers.....	39
Figure 3.3:	a) 90° bends used in the DN50 feed pipe setup, b) bent pipe arrangements with respective symbols used below (Table 3.2).....	39
Figure 3.4:	a) DN200 feed pipe setup, b) CAD drawing of the gas-liquid mixer.....	40
Figure 3.5:	a) WMS measurement principle: b) post-processed data and c) visualization of flow morphologies.....	41
Figure 3.6:	Experimental matrices for configurations with a) straight pipe, b) upright S-bend, c) horizontal S-bend and d) 90° horizontal bend.....	42
Figure 3.7:	a) Pseudo-3D-visualization of the WMS recordings for a transitional morphology with FFPI membership function F and corresponding polar coordinates (β, R_n) , b) allocation of β in the hue map and R_n to the intensity of the HSL color model c) resulting color-coded representation in the RGB(β, R_n) color model.....	46
Figure 3.8:	FFPI-based morphology classification (A - Annular, B - Bubbly, I - Intermittent, S - Stratified) of the measurements in the DN50 feed pipe at position REF in polar (left) and Cartesian coordinates (right). The flow regime map of Mandhane et al. (1974) is indicated by dotted lines and gray text labels.....	47
Figure 3.9:	a) Visualization of the window length compared to the complete data set (normalized void fraction $\alpha_G - \bar{\alpha}_G$) and b) calculated PSD and obtained frequencies.....	49
Figure 3.10:	Recorded void fraction data at measurement position a) REF, b) OUT, c) INL, for two simultaneously installed WMS compared against the data for three installed WMS. Symbols indicate the installation position of the upstream WMS (INL or OUT) in the reference diameter test section (straight pipe configuration).....	51
Figure 4.1:	FFPI-based morphology classification of the developing two-phase flow in the DN50 feed pipe setup at positions a) INL, b) OUT, c) REF and d) in the DN200 feed pipe setup at position INL (with examples of time-averaged void fraction images).....	54
Figure 4.2:	Effect of \dot{m}_G on the flow morphology for both feed pipe setups at (I) $\dot{m}_L = 100 \text{ kg m}^{-2} \text{ s}^{-1}$ and (II) $\dot{m}_L = 400 \text{ kg m}^{-2} \text{ s}^{-1}$	55
Figure 4.3:	FFPI-based morphology classification of the developing two-phase flow in the DN50 feed pipe setup with upright S-bend at positions a) INL and b) OUT and with horizontal S-bend at position c) INL and d) OUT.....	56
Figure 4.4:	FFPI-based morphology classification of the developing two-phase flow in the horizontal 90° bend in the DN50 feed pipe setup at positions a) INL and b) OUT and in the DN200 feed pipe setup at positions c) INL and d) OUT. The flow direction is towards the image plane.....	57
Figure 4.5:	FFPI-based morphology classification for the developing two-phase flow in the upright S-bend (DN50 feed pipe setup) at position REF, b) parity plot of the morphology recovery exemplarily shown for F_I with colors referring to the morphology at the reference position (REF).....	58
Figure 4.6:	Parity plots of the absolute morphology recovery (at position REF) with colors referring to the morphologies of the bent pipes.....	60

Figure 5.1:	a) Experimentally observed intermittent flow for short (red symbols) and long entrance lengths (black symbols) compared with model predictions shown as transition lines, b) clustering of intermittent flows based on liquid Froude number Fr_L (calculated via measured liquid level $h_{L,exp}$).....	61
Figure 5.2:	Flow regime map obtained from own data and literature data as well as predictive models for the onset of entrainment (OE). The blue shaded area indicates conditions requiring droplet separation from bulk gas.....	63
Figure 5.3:	Standard deviation σ_{exp} of the void fraction data $\alpha_G(t)$ per sensor crossing point ($u_{s,G} = 3.29 \text{ m s}^{-1}$, $u_{s,L} = 0.08 \text{ m s}^{-1}$, straight pipe, DN50 feed pipe setup) at three axial locations. High values for σ_{exp} in the gas bulk region account for entrained liquid agglomerates and droplets.	63
Figure 5.4:	Relation of $St_{s,L}$ and LMN for separated and intermittent flow data with and without entrainment and liquid carry-over (lines represent literature correlations for $St_{s,L}$).....	65
Figure 5.5:	a) Graphical illustration of the conceptual criterion to predict the onset of entrainment (experimental data from this work: straight pipe, DN50 feed pipe setup), b) u_{rel} vs. R_S coordinates along iso-lines of average Strouhal numbers $\bar{St}_{s,L}$	67
Figure 5.6:	Entrainment prediction in straight pipes obtained at $L/D = 10$ for a) DN50 feed pipe setup, b) DN200 feed pipe setup.	68
Figure 5.7:	Identified flow morphologies (gray lines) with predicted areas (blue) prone to liquid entrainment: a) straight pipe (DN50) at position REF, b) 90°-horizontal bend pipe (DN50) at position OUT, c) straight pipe (DN200) at position REF, d) 90°-horizontal bend pipe (DN200) at position OUT.....	69
Figure 6.1:	a) Variance of the void fraction predictions $\alpha_{G,corr}$ in straight pipes using reduced-order models (SLM - Separated flow models, HFM - Homogenous flow model, DFM - Drift Flux Model, LMP - Models based on the Lockhart-Martinelli parameter, EMP - Empirical models), b) fitted results of the two best performing correlations (LMP of Wallis (1969) and DFM of Gomez et al. (2000)) based on the experimental data in this work.	72
Figure 6.2:	a) Morphology-adaptive prediction of the void fraction (position REF, DN50 feed pipe setup) combining a) LMP (III) and b) DFM's for annular flow at high u_h (I) and intermittent and stratified flows at lower u_h (II+III).	74
Figure 6.3:	Parity plot of ILG values obtained from experiments (ILG_{exp}) and predicted values (ILG_{theo}) from Equation 2.36 using the interfacial friction factor proposed by Barnea (1991) (blue) and empirically fitted value obtained in this work (black).....	76
Figure 6.4:	a) Parity plot of critical liquid levels obtained from experimental data and ILG models, b) flow regime map of the corresponding stratified flows (fuzzy classified, Section 3.4.1).	76
Figure 6.5:	Experimental data (dots) and empirical correlations (lines) of a) longitudinal curvature of the interface ($d(ILG)/dz$) and b) scaling factor $C(X)$ with Lockhart-Martinelli parameter X (Equation 2.48).....	77
Figure 7.1:	Simulation domain for the DN200 feed pipe section equipped with horizontal 90° bend in ANSYS CFX.....	80
Figure 7.2:	Effect of mesh size on void fractions for straight and bent pipes at low flow rates ($\dot{m}_G = 1 \text{ kg m}^{-2} \text{ s}^{-1}$ and $\dot{m}_L = 97 \text{ kg m}^{-2} \text{ s}^{-1}$).	81
Figure 7.3:	Average void fractions obtained using a transient analysis mode (90° horizontal bend, DN200 feed pipe setup, at low flow rates: $\dot{m}_G = 1 \text{ kg m}^{-2} \text{ s}^{-1}$ and $\dot{m}_L = 97 \text{ kg m}^{-2} \text{ s}^{-1}$).	81

Figure 7.4:	Two-phase flow in the straight DN200 feed pipe setup: a) rendered flow 3D morphology obtained from AIAD simulations at low flow rates, b) comparison of measured and simulated flow morphologies and average void fractions.....	83
Figure 7.5:	Void fractions and patterns of the phase distribution obtained from experiments and simulations (VoF, AIAD) for developing two-phase flow in the straight DN50 feed pipe setup at low flow rates.....	84
Figure 7.6:	Void fractions and patterns of the phase distribution obtained from experiments and simulations (VoF, AIAD) for developing two-phase flow in the straight DN50 feed pipe setup at high flow rates.	84
Figure 7.7:	3D-visualization of the liquid phase fraction (blue) of developing two-phase flow in the vicinity of horizontal 90° bends at high flow rates obtained from numerical simulations (VoF).....	85
Figure 7.8:	Void fractions and patterns of the phase distribution obtained from experiments and simulations (VoF, AIAD) for developing two-phase flow in the 90° horizontal bend (DN200 feed pipe setup) at low flow rates.....	86
Figure 7.9:	Void fractions and patterns of the phase distribution obtained from experiments and simulations (VoF, AIAD) for developing two-phase flow in the 90° horizontal bend (DN200 feed pipe setup) at low high flow rates.....	86
Figure 7.10:	Void fractions and patterns of the phase distribution obtained from experiments and simulations (VoF, AIAD) for developing two-phase flow in the 90° horizontal bend (DN50 feed pipe setup) at low flow rates.....	87
Figure 7.11:	Void fractions and patterns of the phase distribution obtained from experiments and simulations (VoF, AIAD) for developing two-phase flow in the 90° horizontal bend (DN50 feed pipe setup) at high flow rates.....	87
Figure 8.1:	Advanced flow chart for design of horizontal two-phase feed pipes with particular contributions from this thesis.	92
Figure A.1:	Plot of the dominant degrees of membership towards stratified morphologies F_n^* against the standard deviation of the WMS void fraction recordings $\sigma(\alpha_G)$ obtained in the straight DN50 feed pipe section at measurement location REF.....	vi
Figure A.2:	Main and transitional regimes according to the derived constraints: a) ranges (colors) of the membership function, b) allocation of experimental data of the reference configuration (DN50 feed pipe setup, $L/D = 50$).....	viii
Figure A.3:	Individual contributions from each of the four main regimes (annular, bubbly, intermittent, stratified) to the transitional morphologies with respective constraints given in the tables.	ix
Figure A.4:	Resolution of the frequency domain (f_{res}), effective noise bandwidth (ENBW) and total number of windows (n_{DFT}), depending on the DFT window length N_{DFT}	xi
Figure A.5:	Power spectral densities (PSD's) obtained for different areas of the pipe-cross in the DN50 feed pipe setup ($L/D = 75$) for experimental conditions a) to d).	xii
Figure A.6:	Change of the morphologies from inlet (INL) to outlet (OUT) observed in the DN50 feed pipe setup with upright S-bend.	xiv
Figure A.7:	Change of the morphologies from inlet (INL) to outlet (OUT) observed in the DN50 feed pipe setup with horizontal S-bend.	xv
Figure A.8:	Change of the morphologies from inlet (INL) to outlet (OUT) observed in the DN50 feed pipe setup with horizontal 90° bend.....	xvi

Figure A.9:	Change of the morphologies from inlet (INL) to outlet (OUT) observed in the DN200 feed pipe setup with horizontal 90° bend.....	xvi
Figure A.10:	Fuzzy morphology classification in the downstream region of the test sections with a) upright S-bend (DN50 feed pipe setup), b) horizontal S-bend (DN50 feed pipe setup), c) horizontal 90° bend (DN50 feed pipe setup) and d) horizontal 90° bend (DN200 feed pipe setup) at position REF with examples of the time-averaged liquid phase fraction images (black dotted lines indicate iso-lines of $\alpha_G = \{0.1, 0.50, 0.9\}$). The flow direction is towards the image pane	xvii
Figure A.11:	Recovery of the morphology in the downstream region of the DN50 feed pipe setup with upright S-bend.	xviii
Figure A.12:	Recovery of the morphology in the downstream region of the DN50 feed pipe setup with horizontal S-bend.	xix
Figure A.13:	Recovery of the morphology in the downstream region of the DN50 feed pipe setup with horizontal 90°-bend.	xx
Figure A.14:	Recovery of the morphology in the downstream region of the DN200 feed pipe setup with horizontal 90° bend.....	xx
Figure A.15:	Recovery of the morphology comparing the DN50 feed pipe setup with straight pipe to the DN50 feed pipe setup with upright S-bend.....	xxi
Figure A.16:	Recovery of the morphology comparing the r DN50 feed pipe setup with straight pipe to the DN50 feed pipe setup with horizontal S-bend.....	xxii
Figure A.17:	Recovery of the morphology comparing the DN50 feed pipe setup with straight pipe to the DN50 feed pipe setup with horizontal 90° bend.....	xxiii
Figure A.18:	Recovery of the morphology comparing the DN200 feed pipe setup with straight pipe to the DN200 feed pipe setup with horizontal 90° bend.....	xxiii

The following figures were copied from own open access publications that are free to use according to CC-BY licensing: Figure 3.1, Figure 3.6 to Figure 3.8, Figure 3.10, Figure 4.1 to Figure 4.6, Figure A., Figure A.2, Figure A.6 to Figure A.18.

List of tables

Table 2.1: Possible feed conditions for thermal separation.....	7
Table 2.2: Relevant factors influencing the flow morphologies in horizontal pipes.....	12
Table 2.3: Predictive correlations for U_G and $Re_{L,FOE}$ for varying entrainment regimes.....	16
Table 2.4: Geometrical parameters and their relation to the liquid level hL for stratified flow with horizontal interface.....	24
Table 2.5: Commonly applied terms for interfacial shear and interfacial friction factor in the TFM.....	27
Table 2.6: Numerical studies in curved pipes (vertical to horizontal orientation).....	35
Table 3.1: Specifications of applied WMSs.....	41
Table 3.2: Investigated pipe configurations.....	44
Table 3.3: Measurement uncertainty of the measured flow rates in both test sections.....	50
Table 5.1: Coefficients and validity for Equation 5.9.....	68
Table 6.1: Performance assessment of empirical correlations for the prediction of α_G	73
Table 6.2: Performance of LMP and DFM for the prediction of α_G in various pipe geometries.....	75
Table A.1: Main and transitional flow morphologies.....	vii
Table A.2: Average measurement uncertainty across all measurements (liquid flow rate).....	xiii
Table A.3: Average measurement uncertainties across all measurements (gas flow rate).....	xiii
Table A.4: Relative morphology recovery downstream the pipe bends (compared to inlet).....	xxiv
Table A.5: Absolute morphology recovery downstream bent pipes (compared with straight pipes).....	xxv

The following tables were copied from own open access publications that are free to use according to CC-BY licensing: Table 3.2, Table A.1, Table A.4, Table A.5.

Appendix

A.1	Consequences of inappropriate two-phase feeds (examples)	ii
A.2	Thermohydraulic optimization utilizing two-phase feeds	iii
A.3	Influence of horizontal curvatures on the flow morphologies	iv
A.4	Specifications of the experimental facilities	v
A.5	FFPI sub-classification	vi
A.6	Window function and uncertainty of the PSD	x
A.7	Measurement uncertainty	xiii
A.8	Quantitative presentation of the effect of pipe curvatures	xiv
A.9	Recovery of the flow morphology downstream of curvatures	xvii
A.10	Recovery of the flow morphology (absolute)	xxi
A.11	Recovery of the flow morphology (lookup tables)	xxiv
A.12	Wave frequency correlations (horizontal)	xxvi
A.13	Determination of the void fraction by reduced-order models	xxvii
A.14	Empirical void fraction correlations	xxxii
A.15	Derivation of the modified correlation for ILG	xxxii

A.1 Consequences of inappropriate two-phase feeds (examples)

Consequence	Problem description and solution	Case number Kister (2006)
Fouling or plugging in parts of the separation column	Problem: Heavy feed entrainment caused an undesired polymerization reaction; Polymers plugged tower internals; Solution: Vapor phase redistribution due to new feed inlet position and modified inlet design.	874
	Problem: Crude entrainment carried over with the vapor phase from a preflash drum; Tar-like fouling on trays below feed nozzle and metal constituent in the gas phase.	1270
Reduced separation performance	Problems: Wrong inlet device obstructed the entrance area from the downcomer above; Tray capacity 15% below the target value; Solution: Re-arrangement of feed piping, installation of a different feed tray type.	729
	Problems: Two-phase feed (95% vapor phase) fed to liquid-only feed distributor; Poor distributor performance caused reduced tray efficiency.	748
Separator malfunction	Problems: Downcomer choking by flashing feed (unnoticed bottleneck for 16 years); Failed resizing of the downcomer; Solution: New feed inlet stage, trays in the stripping section substituted by packings.	739
	Problem: Premature flooding due to high momentum (in downwards direction) of the flashing feed; Solution: Enlargement of the downcomers in the stripping section and modification of the trays.	777
Mechanical damage	Problem: Flashing feed originating from a tapered slot in the inlet device caused portions of the seal pan above sheared-off; Solution: Installation of a new, more stable seal pan.	778
	Problem: Heavy entrainment, loss of fluids and corrosion (destruction of columns shell) due to high velocities in the flash gallery; Solution: Re-design of the inlet device with tangential inlet and replacement of column internals as required.	890
	Problems: Poor feed line and support design; Failure of shrouds, insufficient column shell protection; Hole in the column shell cut from heavy entrainment from flashing feeds.	889
Key-component maldistribution	Problem: Heavy frothing caused by insufficient phase separation and incorrect tray design; Solution: Re-design of the flashing feed inlet device.	8110

A.2 Thermohydraulic optimization utilizing two-phase feeds

Concept	Applied method	References
Feed pre-heating	<p>Targets: Reduction of reboiler duty and recovery of excess heat; Increasing the feed temperature reduces the external heat duty. Heat degradation: Temperature recovered at the columns head condenser is below the columns desired feed temperature and is thus often added to subsequent separation stages or columns.</p> <p>Findings: When the same heat source is used for pre-heater and reboiler, the possible energy saving by pre-heating is low; Only pre-heating above the boiling point results in two-phase feeds.</p>	Dhole and Linnhoff (1993); Liebert et al. (1993); Demirel (2004); Errico et al. (2009); Mersmann et al. (2011); Couper et al. (2012); Kiss (2013); Lee and Min (2013); Jobson (2014); Blahušiak et al. (2016)
	<p>Finding: Heat pump assisted distillation or heat integrated distillation may utilize flash evaporation (two-phase feeds) while coupling the separated rectifying and stripping sections.</p>	
External reflux	<p>Target: Mixing of head product with feed to increase w_F; Reduced reflux and reboiler heat duty (beneficial for high volatile systems, e.g. vacuum distillation).</p> <p>Finding: Head product and feed mixture may involve different thermal states.</p>	Reinhard Billet (1983)
Feed split	<p>Targets: Reduction of the overall heat duty of the main column and improved hydraulic performance; Pre-separation of key-components upstream of the distillation column; Removal of impurities (e.g. in multi-stage flash evaporations, multi-effect distillations).</p>	Miyatake (1994); Errico et al. (2009); Asadollahi et al. (2017); Qi et al. (2017)
Seasonal flexibility	<p>Targets: Variation of the evaporation to account for annual changing temperatures of external flows (e.g. in crude unit preflash devices); Adapt the column vapor load by changing the distillation preflash rate.</p>	Harbert (1978); Soley and A. C. S. Fraser (2000)
Varying column vapor load	<p>Target: Reducing the amount of vapor after preflash (e.g. in vacuum column) can result in more moderate vapor loading in downstream columns.</p>	Soley and A. C. S. Fraser (2000)
Removal of impurities	<p>Target: Applied in desalination plants, multi-stage flash evaporators or multi-effect distillation.</p>	Miyatake (1994); Kiss (2013); Qi et al. (2017)

A.3 Influence of horizontal curvatures on the flow morphologies

Morphology	Influence	References
Stratified smooth	<ul style="list-style-type: none"> ▪ Upwards inclination of the interface towards the outer bend radius ▪ Slight increase of the void fraction ▪ Pronounced transition to annular flow in small channels at moderate to high void fractions and for small curvature radii 	Wang et al. (2002), (2004); Lima and Thome (2012); Vieira et al. (2014)
Stratified wavy	<ul style="list-style-type: none"> ▪ Dislocation of waves towards outer bend radius ▪ Pronounced circumferential liquid spread (similar to annular flow) ▪ Swirling flow in the main flow direction ▪ Swaying interphase inclination in radial direction ▪ Increasing wavy amplitude 	Abdulkadir (2011); Lima and Thome (2012)
Annular	<ul style="list-style-type: none"> ▪ Deposition (inertia separation) of liquid droplets in the gas chore ▪ Increase of wetted wall fraction and decrease of liquid level at pipe bottom ▪ Effect of secondary flow in the gas chore on circumferential liquid film thickness 	Sakamoto et al. (2004); Kim et al. (2007); Abdulkadir (2011); Kesana et al. (2013)
Intermittent	<ul style="list-style-type: none"> ▪ Accumulation of gas bubbles (plug flow) at inner bend radius and subsequent gravity-induced drive towards outer bend radius ▪ Turbulence-induced bubble breakup (plug flow) at inner curvature radius ▪ Slug flow transitions towards annular flow at outlet and wavy flow in the downstream region in small channels ▪ Pronounced dispersion of gas in the liquid bulk 	Abdulkadir (2011); Kesana et al. (2013); Vieira et al. (2014); Yadav et al. (2014a)
Bubbly	<ul style="list-style-type: none"> ▪ Gas bubble agglomeration at inner curvature radius and homogenous distribution downstream the bend ▪ Bubble coalescence and breakup for low and higher void fractions, respectively ▪ Lower bubble velocity for lower void fractions ▪ Bubbles generation at the pipe top ▪ Transition to intermittent flow at lower gas velocities compared to straight pipes 	Azzopardi and Sudlow (1993); Kim et al. (2007); Talley et al. (2009); Yadav et al. (2014b); Bowden et al. (2018)

A.4 Specifications of the experimental facilities

	DN50 feed pipe setup	DN200 feed pipe setup
Fluids		
Liquid	De-ionized water	Tap water
Gas	Pressurized air (supply line with 6 to 8 bar(a))	Ambient air
Components		
Pump	BADU Resort 110 axial pump	FLOWSERVE ZLKD 050125 radial pump
Separator	Hydro cyclone $D = 500$ mm	Column ($D = 1000$ mm) with integrated water storage at the bottom, V-baffle (inlet device) and demister packings
Temperature measurement		
Liquid	Pt 1000 digital thermometer (GTH175/Pt)	Bimetal thermometer: FA 2300-A2522
Gas	Pt 100 resistance thermometers (Type 16, tolerance class B)	Bimetal thermometer: FA 2300-A2522
Pressure measurement		
System pressure	OMEGA PR12SY-V-2-B	U-tube manometer
Differential pressure	OMEGA PD23-C-0.2, Honeywell FDW1JE,2Y,5R	U-tube manometer
Flow rate measurement		
Liquid	Magnetic inductive flowmeters: SIEMENS MAG 5000, SIEMENS MAG 6000	Rotameter: Endress+Hauser Flowtec AG PROMAG 30F (DN150)
Gas	Mass flow controller*: OMEGA FMA-2613A, OMEGA FMA-2010A, Bronkhorst F-106Cl	Orifice (DN400) according to DIN-EN-5167-2

* The mass flow controllers determine the volumetric flow rate for different standard conditions: $T_G = 298.15$ K and $p_G = 101320$ Pa (OMEGA) and $T_G = 273.15$ K and $p_G = 101325$ Pa (BRONKHORST)

A.5 FFPI sub-classification

The degrees of membership F_n in the FFPI membership function F inherently facilitate clustering and classification algorithms for different peculiarities of the flow morphologies. As discussed in Section 3.4.1, the benefits of an objective and automated flow morphology classification is at the expense of introduced empiricism and a loss of fuzzy character due to pronounced defuzzification. The inherent clustering obtained from FFPI is exemplarily shown in Figure A.1.

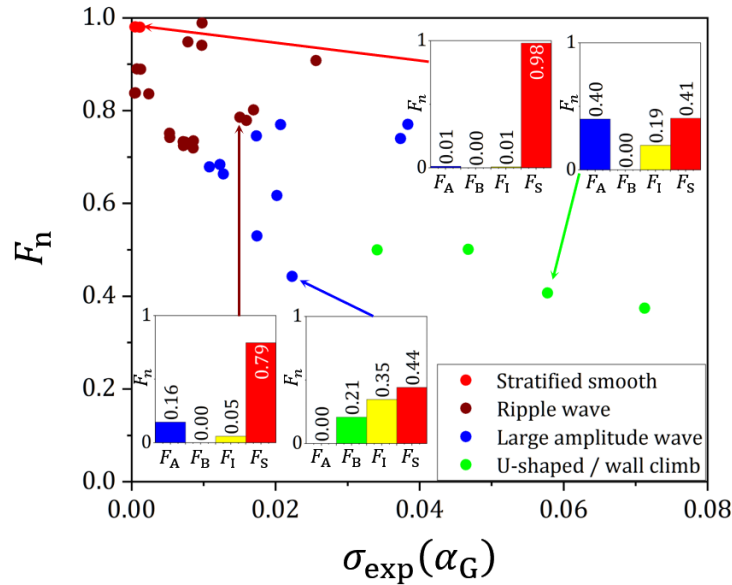


Figure A.1: Plot of the dominant degrees of membership towards stratified morphologies F_n^* against the standard deviation of the WMS void fraction recordings $\sigma(\alpha_G)$ obtained in the straight DN50 feed pipe section at measurement location REF.

Figure A.1 draws data that correspond to the dominant (maximum) degree of membership to stratified morphologies (ordinate) against the respective standard deviation of the WMS void fraction recordings. For stratified flows, the latter approximates the transition from stratified smooth morphologies towards wavy morphologies with higher standard deviation of the WMS recordings. From the visual interpretation of the WMS recordings, four types of flow morphologies were identified (colored dots in Figure A.1). With the given axis, the clustering into four groups along a line of decreasing F_S or $\sigma(\alpha_G)$ becomes obvious. The bar charts for selected experiments (indicated by arrows in Figure A.1) show all four degrees of membership. Note that the non-dominant degrees of membership are different for similar values of F_S (compare blue and green arrows). Contrary to $\sigma_{\text{exp}}(\alpha_G)$, which might not be equally sensitive to all flow morphologies, the non-dominant degrees of membership can be utilized to formulate empirical constraints for the classification of the flow morphologies. This is in line with the findings of Wiedemann et al. (2019),

who concluded that a single criteria applied to the FFPI membership function gives insufficient reclassification success.

In order to employ any classification on the FFPI membership function, the respective degrees of memberships are normalized according to

$$\tilde{F}_n = \frac{F_n}{F_{n^*} - F_n}. \quad \text{A.1}$$

Subsequently, constraints for the second-order degrees of membership \tilde{F}_n can be applied to all transitional morphologies, i.e. $F_n = F_{n^*} < 0.8$. Based on the reference morphologies obtained at measurement location REF in both straight test sections, phenomenological assignment to 9 different flow morphologies is possible.

Table A.1: Main and transitional flow morphologies.

	Morphology	n	Phenomenological description
<i>Main</i>	Annular	A	Annular flow and mist flow
	Bubble	B	Dispersed bubbles and bubble agglomerates
	Intermittent	I	Slug, plug and aerated slug flow (not explicitly distinguished) for low to intermediate \dot{m}_g, \dot{m}_l
	Stratified	S	Stratified smooth (also with low amplitude ripple waves)
<i>Transitional</i>	Stratified wavy	SW1	Roll waves (waves with higher amplitude than in S)
		SW2	Large amplitude waves with non-aerated bulk; cross-section not fully occupied by waves
	Annular wavy	AW	Wavy flow with pronounced U-shaped phase interface, partially occurring aerated slugs; inhomogeneous liquid films / rivulets
	Annular intermittent	AI	Intermittent structures with irregular shapes or highly aerated slug flow; high dispersion with irregular annulus
	Blow through slug	BS	Aerated slug flow with higher frequency than in AI at high \dot{m}_g, \dot{m}_l
	Bubbly intermittent	BI	Large gas agglomerates with extended dimensions; similar to plug flow

In the color-coded polar plots of the FFPI membership function, these flow morphologies can be represented by regions of classification as shown in Figure A.2.

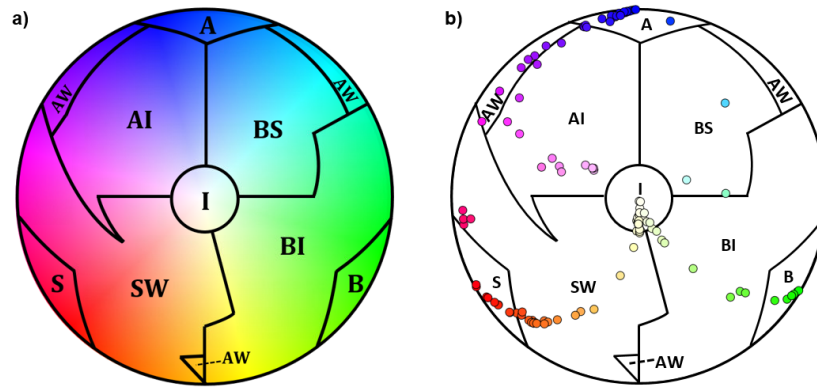


Figure A.2: Main and transitional regimes according to the derived constraints: a) ranges (colors) of the membership function, b) allocation of experimental data of the reference configuration (DN50 feed pipe setup, $L/D = 50$).

Note that the regions shown in Figure A.2. are the result of superposition as most transitional morphologies are distributed between multiple dominant degrees of membership. For example, wavy transitional morphologies are classified from dominant stratified ($F_{n^*} = F_S$) or intermittent ($F_{n^*} = F_I$) degrees of membership. The underlying constraints for the classification are presented in Figure A.2.

With the constraints proposed in Figure A.3, distinguishing rivulets on the pipe walls (AW), annular flows (A) and different amplitude waves (SW1, SW2) is achieved, which was not possible in the past (Wiedemann et al., 2019). In principle, the applied constraints are only valid for the range of the FFPI membership function covered by the experimental reference data. In order to assign all numerically possible values to one sub-regime, the constraints are extrapolated to the full range of the FFPI membership function (i.e. the whole chart area of Figure A.3). As a result, peculiar shapes of the transition lines (e.g. the triangular shaped annular-wavy region) occur. Since the reference dataset is considered to cover all existing flow morphologies that can be captured by WMSs, those regions in the polar plots are of no practical relevance and the extrapolation can be neglected.

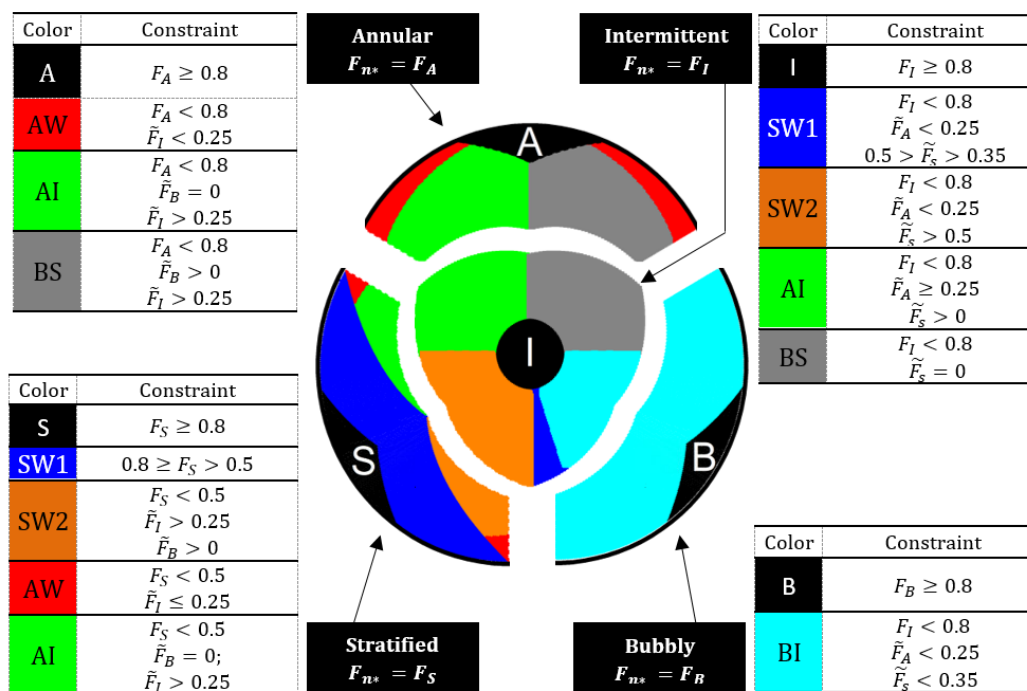


Figure A.3: Individual contributions from each of the four main regimes (annular, bubbly, intermittent, stratified) to the transitional morphologies with respective constraints given in the tables.

A.6 Window function and uncertainty of the PSD

The discrete Fourier transform (DFT) implicitly assumes a periodic signal that repeats infinitely (Heinzel et al., 2002). If the frequency of the signal does not match with one of the frequency axis grid points, a discontinuity occurs. The power is then spread into multiple frequency bins and the PSD is ‘smeared’ (so-called leakage effect). Window functions are multiplied to the time series before applying the DFT to compensate for the discontinuity.

The selection of appropriate window functions $W(n_m)$ always requires a compromise between accuracy of the determined frequency and the amplitude value of the PSD. In this work, the standard Hanning window function is used (as implemented in MATLAB R2015a), which yields low spectral leakage according to:

$$W_{\text{Hann}}(n_m) = \frac{1}{2} \left[1 - \cos \left(\frac{2\pi n_m}{N_{\text{DFT}}} \right) \right]. \quad \text{A.2}$$

The overlap between the windows was always set to 50 %. Full removal of the leakage effect is not possible using window functions. Despite removing the DC bias from the signal by normalizing with the signal average, leakage from the first bin may mask the lowest frequencies in the DFT.

While the leakage effect arises directly from the DFT, the determination of characteristic frequencies is also imposed with uncertainty, since any frequency obtained represents a whole bandwidth (i.e. the resolution of the frequency domain, see Section 3.4.2) instead of a discrete value. presented the ‘effective noise bandwidth’ ENBW

$$ENBW = \frac{f_s \cdot S_{\text{DFT},2}}{S_{\text{DFT},1}^2} \quad \text{A.3}$$

as a uncertainty indicator. The window sums $S_{\text{DFT},1}$ and $S_{\text{DFT},2}$ that are used for normalization are obtained from the window function by

$$S_{\text{DFT},1} = \sum_{n_m}^{n_{m,\text{max}}} W_{\text{Hann}}(n_m) \quad \text{A.4}$$

and

$$S_{\text{DFT},2} = \sum_{n_m}^{n_{m,\text{max}}} W_{\text{Hann}}(n_m)^2. \quad \text{A.5}$$

Moreover, any frequency obtained from measured signals should be supported by sufficient periods captured in the signal to ensure statistical accuracy. Hence, based on the experimental data obtained in this study, low frequencies < 0.5 Hz are imposed with a generally higher

uncertainty. Figure A.4 illustrates the relevant uncertainty measures for the DFT, depending on the length of the DFT window, N_{DFT} .

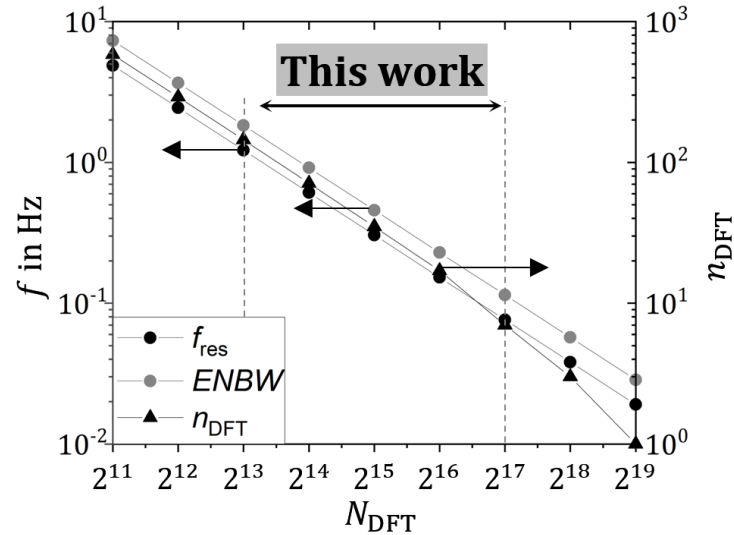


Figure A.4: Resolution of the frequency domain (f_{res}), effective noise bandwidth (ENBW) and total number of windows (n_{DFT}), depending on the DFT window length N_{DFT} .

Despite varying the DFT window length, not all experiments yielded PSDs that allowed determining characteristic frequencies. Thus, filtering (high-pass and low-pass) and binarization were performed for some data sets to determine the characteristic frequencies. Moreover, the method presented in Section 3.4.2 was applied to the area-averaged void fraction data α_G (Equation 3.5). It was assumed that the characteristic frequencies of the bulk are well represented in each recording and possible superposition of frequencies originating from non-bulk areas of the two-phase flow were neglectable.

Figure A.5 shows exemplarily PSDs for four separated flow morphologies, obtained with a DFT window length $N_{\text{DFT}} = 2^{15}$. The PSDs were obtained by masking regions of the pipe cross-section before applying cross-sectional averaging and DFT to the resulting signals. Here, liquid bulk region (blue), non-liquid bulk region (red) and central vertical chord (gray) are shown together with the PSD obtained for the full cross-section (black). Peaks of the PSD that occur in the non-bulk region either corresponds to the peaks observed in the liquid bulk and full pipe cross-section (Figure A.5b) or occur at significantly higher frequencies (Figure A.5a,c,d). However, less signal energy is concentrated in these high frequencies, thus their contribution vanishes, when the whole pipe-cross-section is considered.

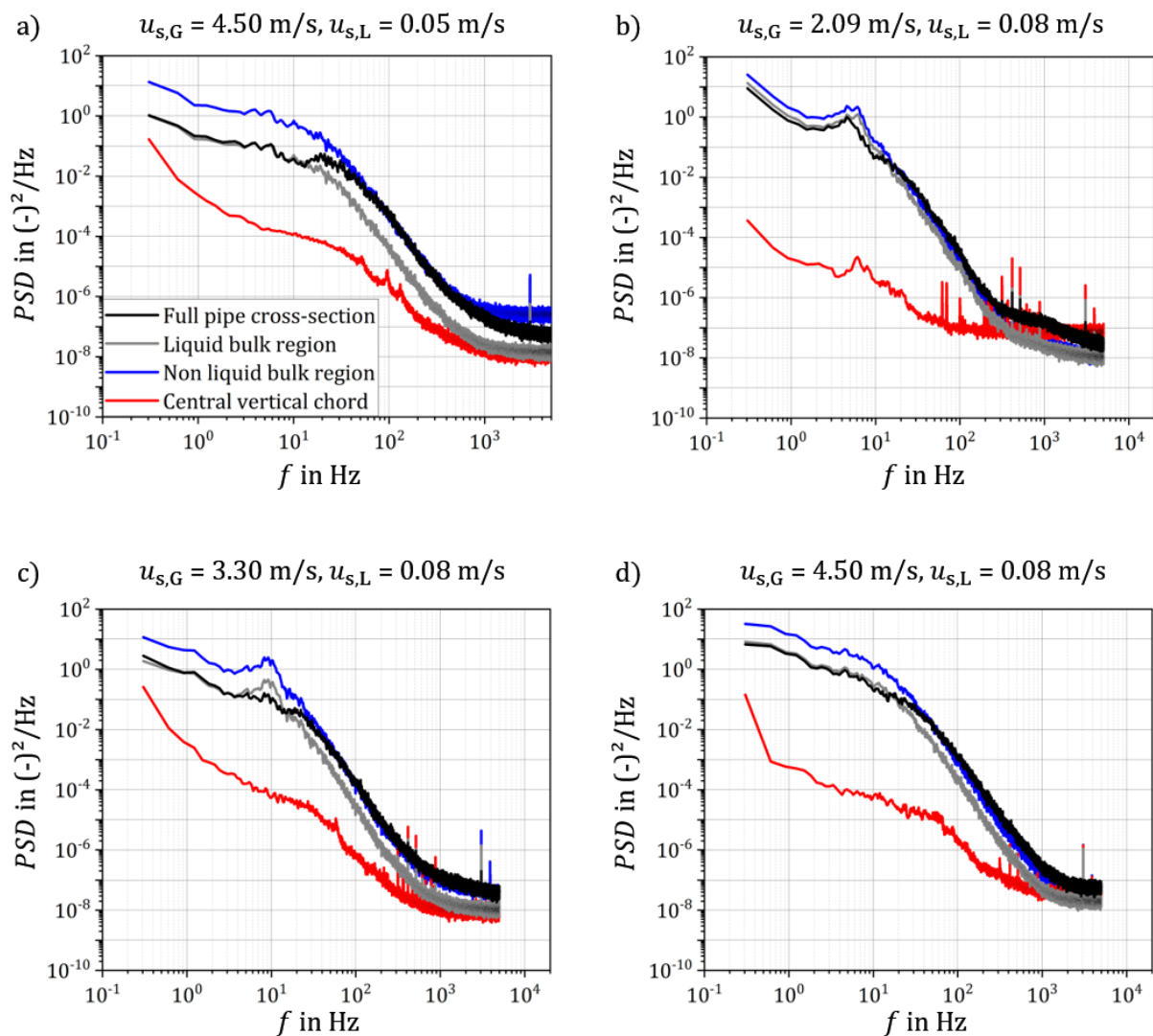


Figure A.5: Power spectral densities (PSD 's) obtained for different areas of the pipe-cross in the DN50 feed pipe setup ($L/D = 75$) for experimental conditions a) to d).

A.7 Measurement uncertainty

The **liquid flow rates** were directly obtained from the flow meters upstream the test sections. Consequently, the derivative in Equation 3.8 is equal to one and only the measurement uncertainty of the devices (Equation 3.9) contribute. Table A.2 gives the average measurement uncertainty E across all studied flow rates in both test sections.

Table A.2: Average measurement uncertainty across all measurements (liquid flow rate).

Test section	$\varepsilon_1 = \frac{\sigma_{\text{exp}}}{\sqrt{n_{\text{m,max}}}}$	ε_2	$E(\dot{V}_{\text{L,ref}})/\dot{V}_{\text{L,ref}}$
Reference diameter	$(1.2 \pm 1.1) \text{ l h}^{-1}$	$(15.8 \pm 17.0) \text{ l h}^{-1}$	$(0.61 \pm 0.34) \%$
Large diameter	-	$(120 \pm 56.5) \text{ l h}^{-1}$	$\pm 0,5\%$

Note that the data sheets of the respective flow meters define ε_2 as either a constant or a functional relation of the measured flow rate. The statistical uncertainty of the recordings ε_1 was determined individually for each measurement and yields the data presented in Table A.2.

The **gas flow rates** in the reference diameter test section were obtained by Equation 3.2. Applying the error propagation law, Equation 3.8, yields the partial derivatives:

$$\frac{\partial \dot{V}_{\text{G}}(\dot{V}_{\text{G,ref}})}{\partial \dot{V}_{\text{G,ref}}} = \frac{p_{\text{G,ref}} T_{\text{G,inl}}}{p_{\text{G,inl}} T_{\text{G,ref}}} \quad \text{A.6}$$

$$\frac{\partial \dot{V}_{\text{G}}(T_{\text{G,ref}})}{\partial T_{\text{G,ref}}} = \dot{V}_{\text{G,ref}} \frac{p_{\text{G,ref}}}{p_{\text{G,inl}}} \frac{1}{T_{\text{G,ref}}} \quad \text{A.7}$$

$$\frac{\partial \dot{V}_{\text{G}}(p_{\text{G,ref}})}{\partial p_{\text{G,ref}}} = -\dot{V}_{\text{G,ref}} \frac{p_{\text{G,ref}} T_{\text{G,inl}}}{p_{\text{G,inl}}^2 T_{\text{G,ref}}} \quad \text{A.8}$$

The device uncertainty and resulting average measurement uncertainties are shown in Table A.3.

Table A.3: Average measurement uncertainties across all measurements (gas flow rate).

x_{exp}	$\varepsilon_1 = \frac{\sigma_{\text{exp}}}{\sqrt{n_{\text{m,max}}}}$	ε_2	$E(x_{\text{exp}})/x_{\text{exp}}$
$\dot{V}_{\text{G,ref}}$	$(5.7 \pm 64.6) \times 10^{-3} \text{ sl min}^{-1}$	$(27.4 \pm 37.1) \text{ sl min}^{-1}$	$(7.4 \pm 10.0) \%$
$p_{\text{G,ref}}$	$(0.2 \pm 0.3) \times 10^{-3} \text{ bar(a)}$	10^{-3} bar(a)	$(16.6 \pm 13.8) \%^6$
$T_{\text{G,ref}}$	$(1.2 \pm 2.7) \times 10^{-3} \text{ K}$	0.5 K	$(2.6 \pm 0.3) \%$

The measurement uncertainty for the gas flow rate in the large diameter test section was provided by internal calculations provided by RVT Process Equipment GmbH.

⁶ Measured values smaller than $p_{\text{G,ref}} = 2 \times \varepsilon_2 \text{ bar(a)}$ were not considered for this calculation as they are below the device uncertainty.

A.8 Quantitative presentation of the effect of pipe curvatures

The following parity plots present the effect of pipe curvatures quantitatively. Figure A.6 to Figure A.9 compare the inlet (INL) and outlet (OUT) positions in terms of the degrees of membership (F_n) to the main morphologies (i.e. annular A, bubbly B, intermittent I, stratified S) for the investigated curvatures in both test sections. The symbols in the plot are colored based on the fuzzy morphology classification for the curvature outlet. Values of $F_n > 0.8$ are defined as main morphologies, while lower values represent transitional morphologies.

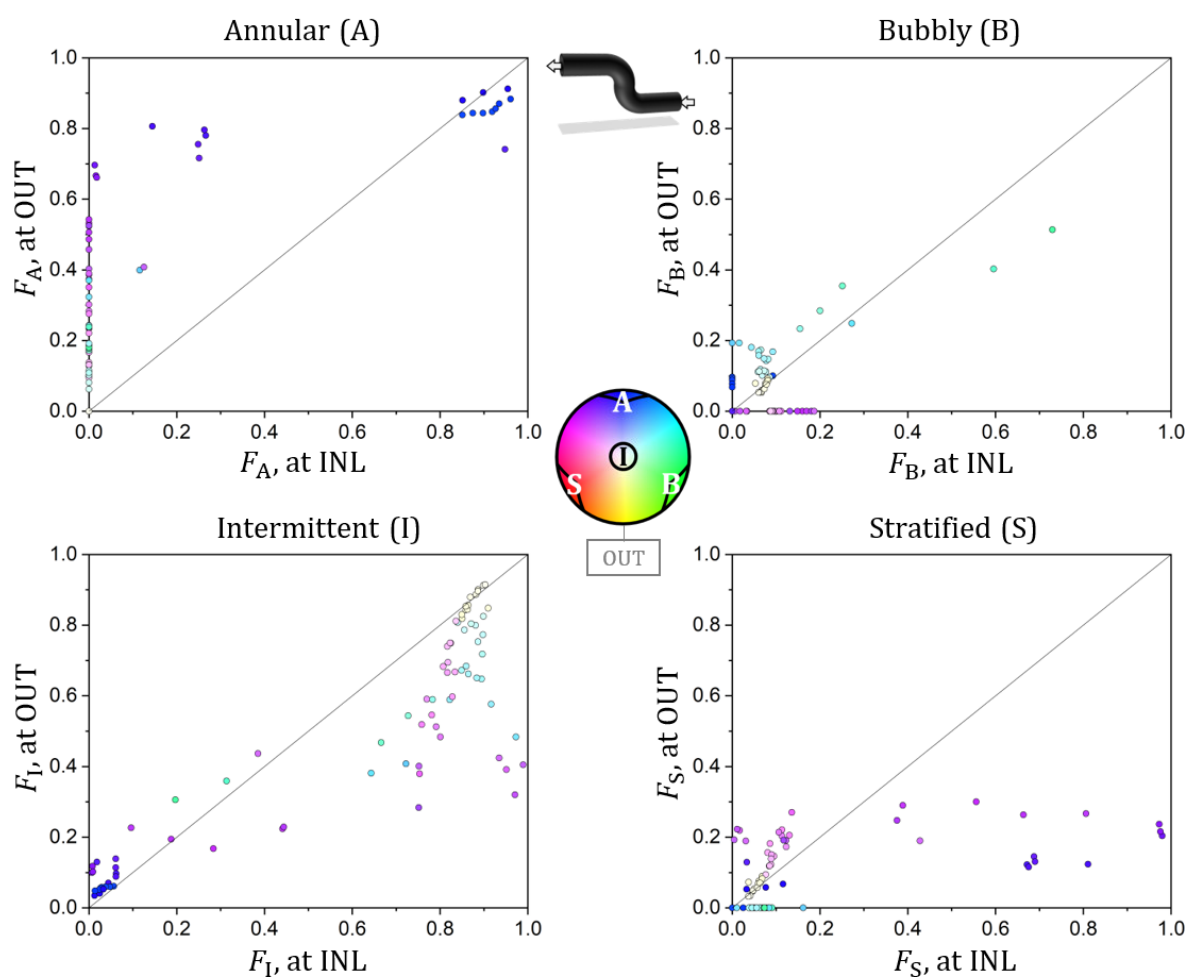


Figure A.6: Change of the morphologies from inlet (INL) to outlet (OUT) observed in the DN50 feed pipe setup with upright S-bend.

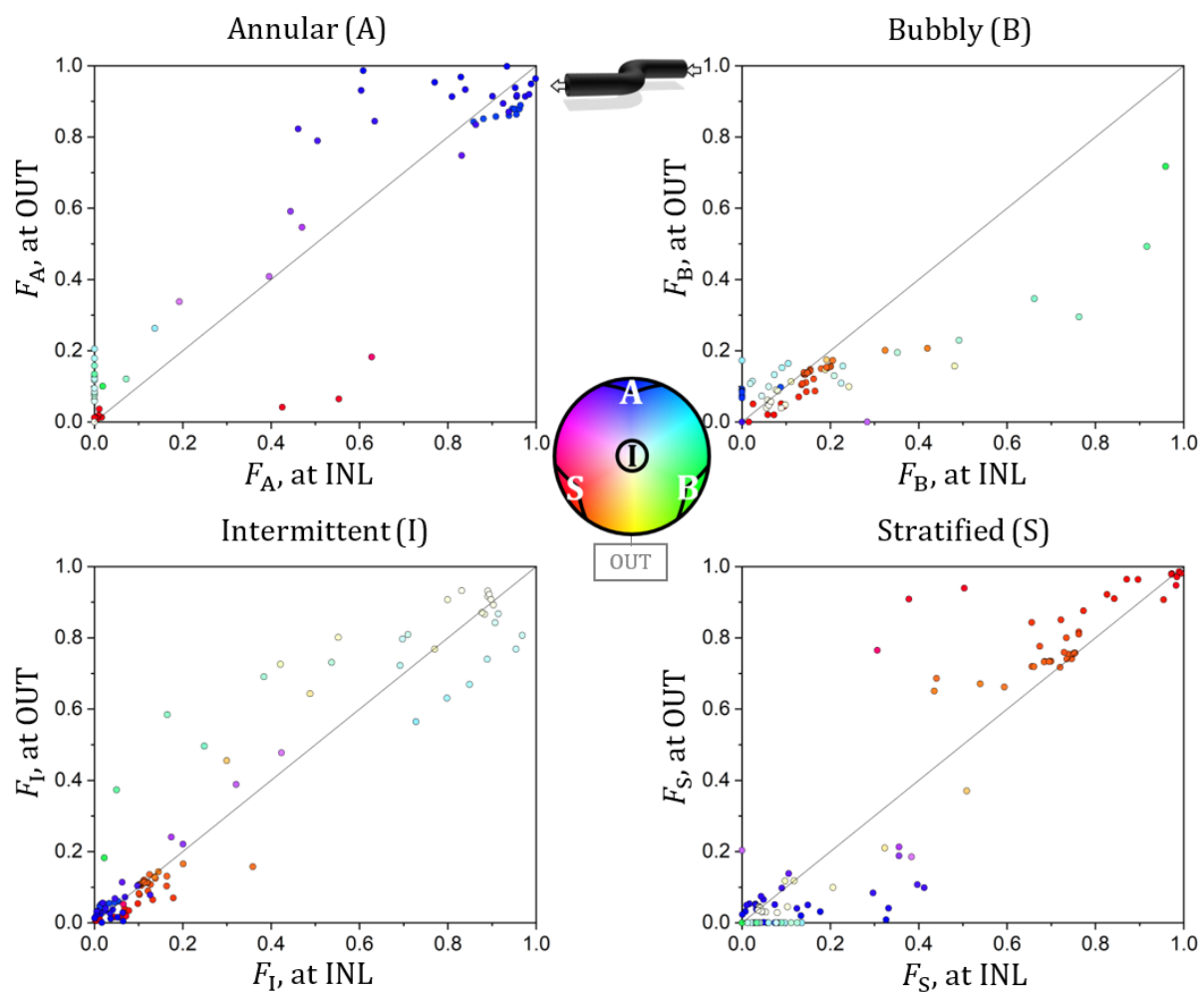


Figure A.7: Change of the morphologies from inlet (INL) to outlet (OUT) observed in the DN50 feed pipe setup with horizontal S-bend.

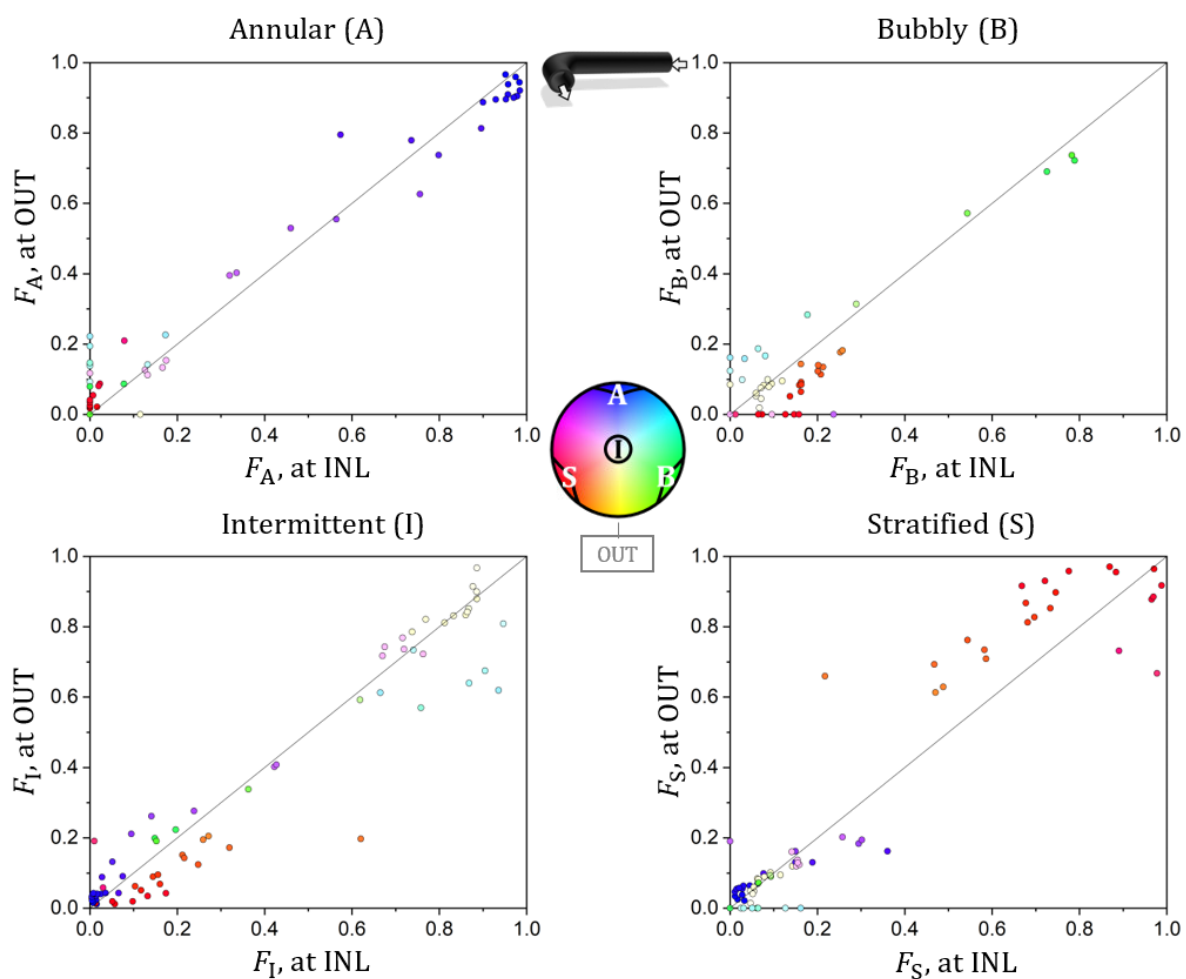


Figure A.8: Change of the morphologies from inlet (INL) to outlet (OUT) observed in the DN50 feed pipe setup with horizontal 90° bend.

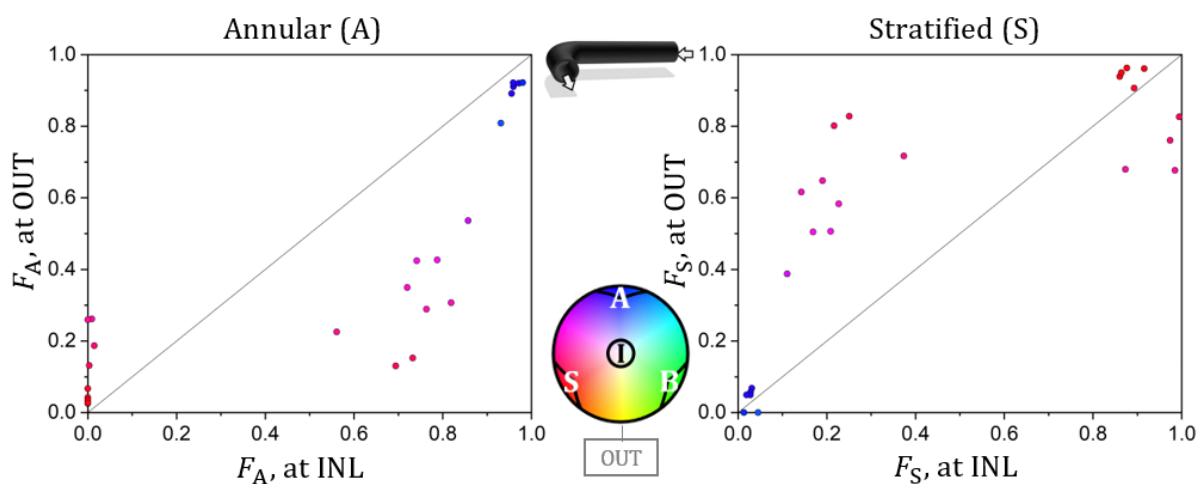


Figure A.9: Change of the morphologies from inlet (INL) to outlet (OUT) observed in the DN200 feed pipe setup with horizontal 90° bend.

A.9 Recovery of the flow morphology downstream of curvatures

The fuzzy morphology classification downstream of the curvatures at position REF is shown in Figure A.10.

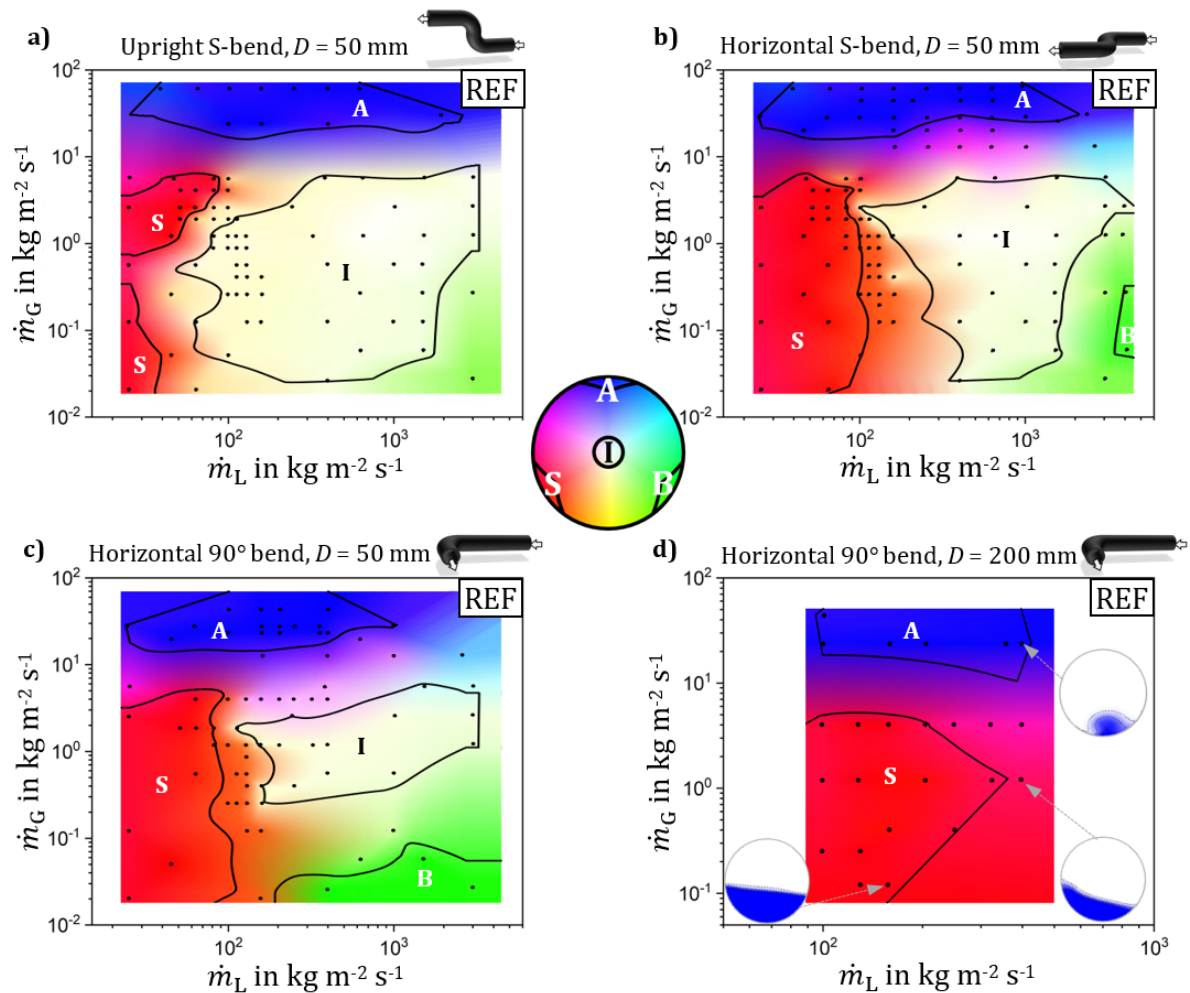


Figure A.10: Fuzzy morphology classification in the downstream region of the test sections with a) upright S-bend (DN50 feed pipe setup), b) horizontal S-bend (DN50 feed pipe setup), c) horizontal 90° bend (DN50 feed pipe setup and d) horizontal 90° bend (DN200 feed pipe setup) at position REF with examples of the time-averaged liquid phase fraction images (black dotted lines indicate iso-lines of $\alpha_G = \{0.1, 0.50, 0.9\}$). The flow direction is towards the image pane.

Downstream the curvatures the flow morphology recovers from the influence induced by the curvatures, given that sufficient calming length is provided. In this section, parity plots (Figure A.11 to Figure A.14) present the relative morphology recovery, comparing the inlet (INL) and reference (REF) positions in terms of the degrees of membership F_n for the investigated curvatures in both test sections. Displayed are the degrees of membership F_n of the respective main morphologies in the downstream region (position REF) of the test sections with curvatures, compared with the dominant morphology F_n^* at the curvature inlets. The symbol colors refer to

the fuzzy morphology classification at the inlet position (INL). The different regions of morphology recovery (see Section 4.3) are indicated by symbols: (\approx , ++, +, -, 0).

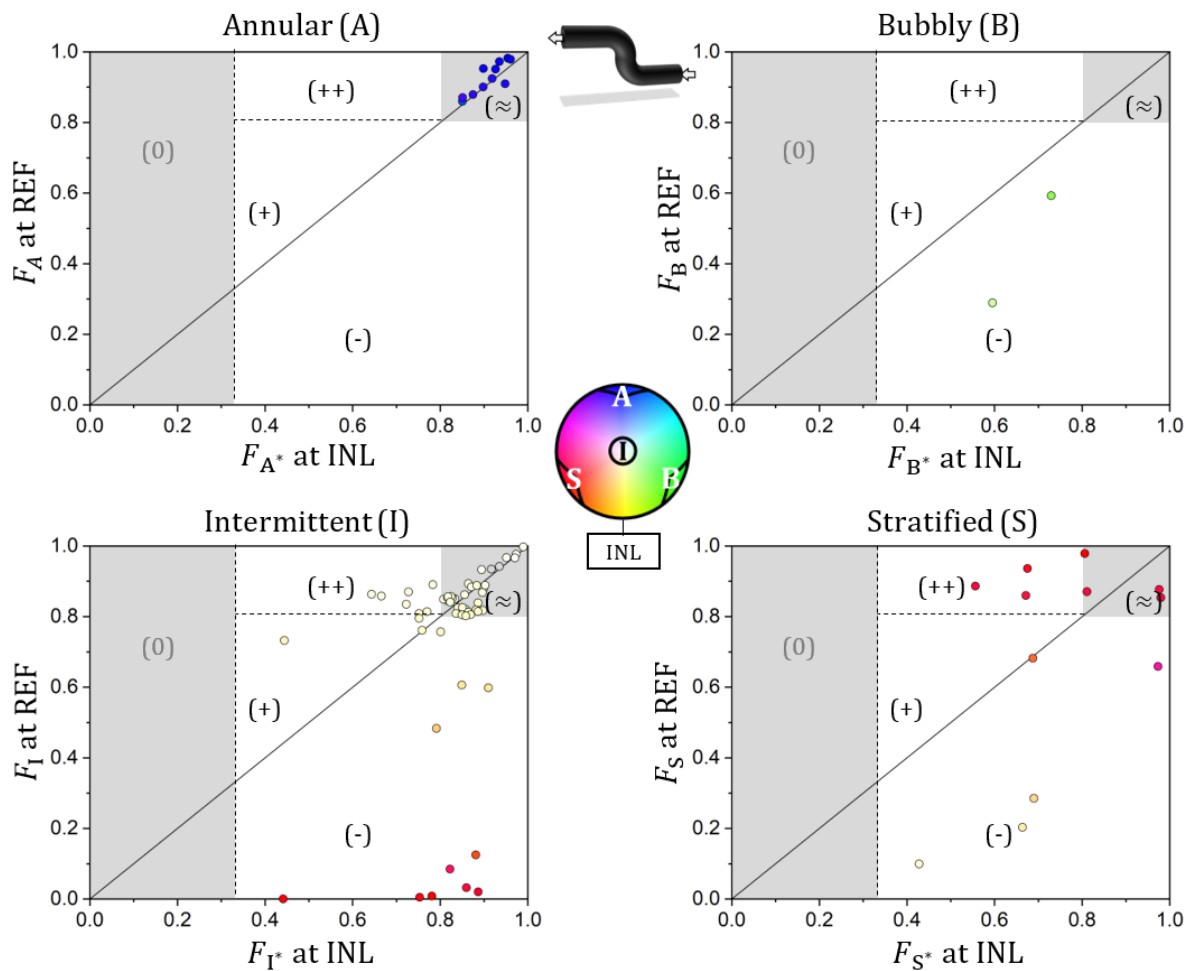


Figure A.11: Recovery of the morphology in the downstream region of the DN50 feed pipe setup with upright S-bend.

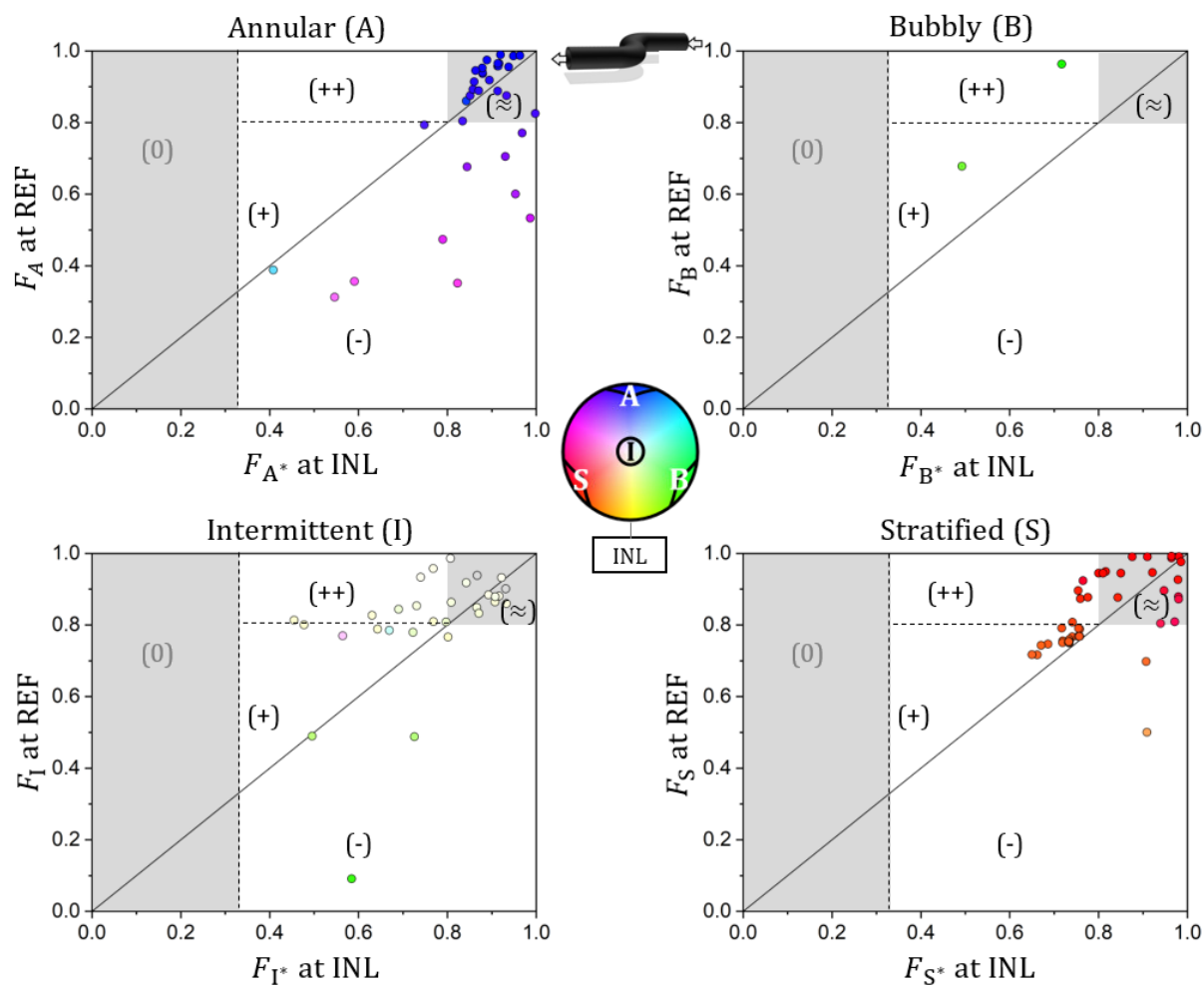


Figure A.12: Recovery of the morphology in the downstream region of the DN50 feed pipe setup with horizontal S-bend.

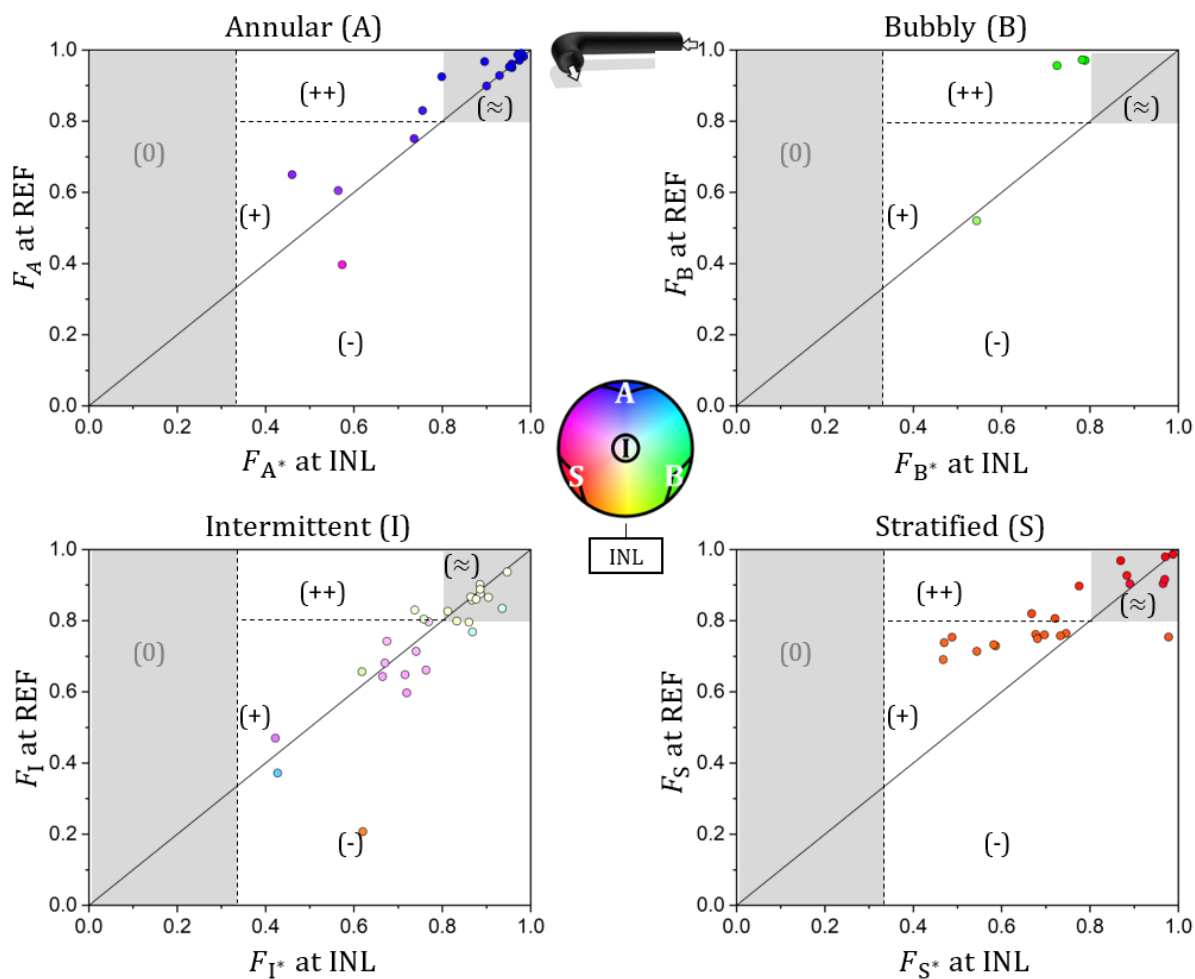


Figure A.13: Recovery of the morphology in the downstream region of the DN50 feed pipe setup with horizontal 90° bend.

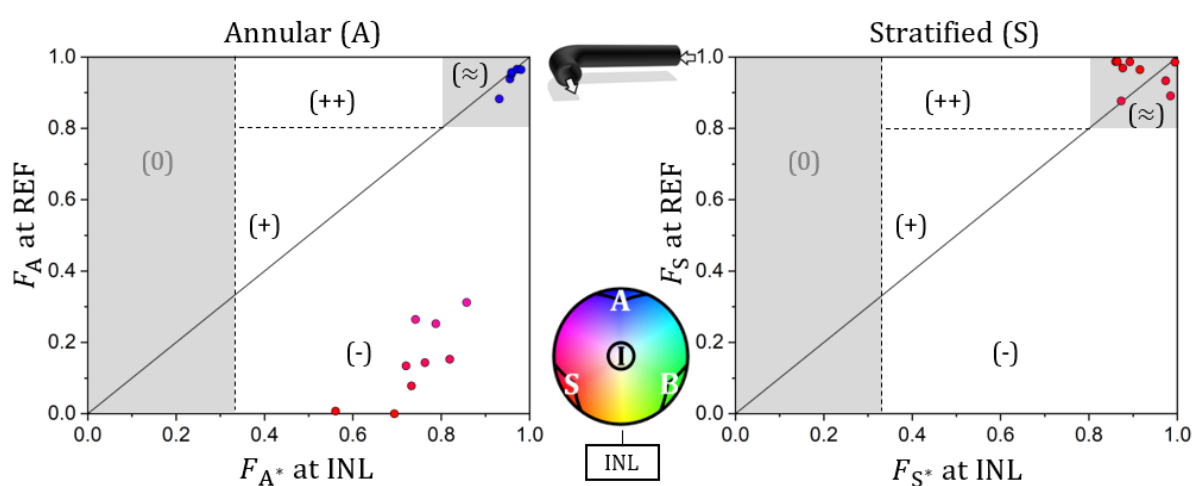


Figure A.14: Recovery of the morphology in the downstream region of the DN200 feed pipe setup with horizontal 90° bend.

A.10 Recovery of the flow morphology (absolute)

In the following, the morphology recovery in comparison to the DN50 feed pipe setup (straight pipe) is presented via parity plots (Figure A.15 to Figure A.18) for the investigated test sections with curvatures. Displayed are the degrees of membership F_n of the respective main morphologies at the reference position (REF), compared with the dominant morphology F_{n^*} at the curvature inlets. The symbol colors refer to the fuzzy morphology classification obtained from the experimental data in the test sections with curvatures. The different regions of morphology recovery (see Section 4.3) are indicated by symbols: (\approx , ++, +, -, 0).

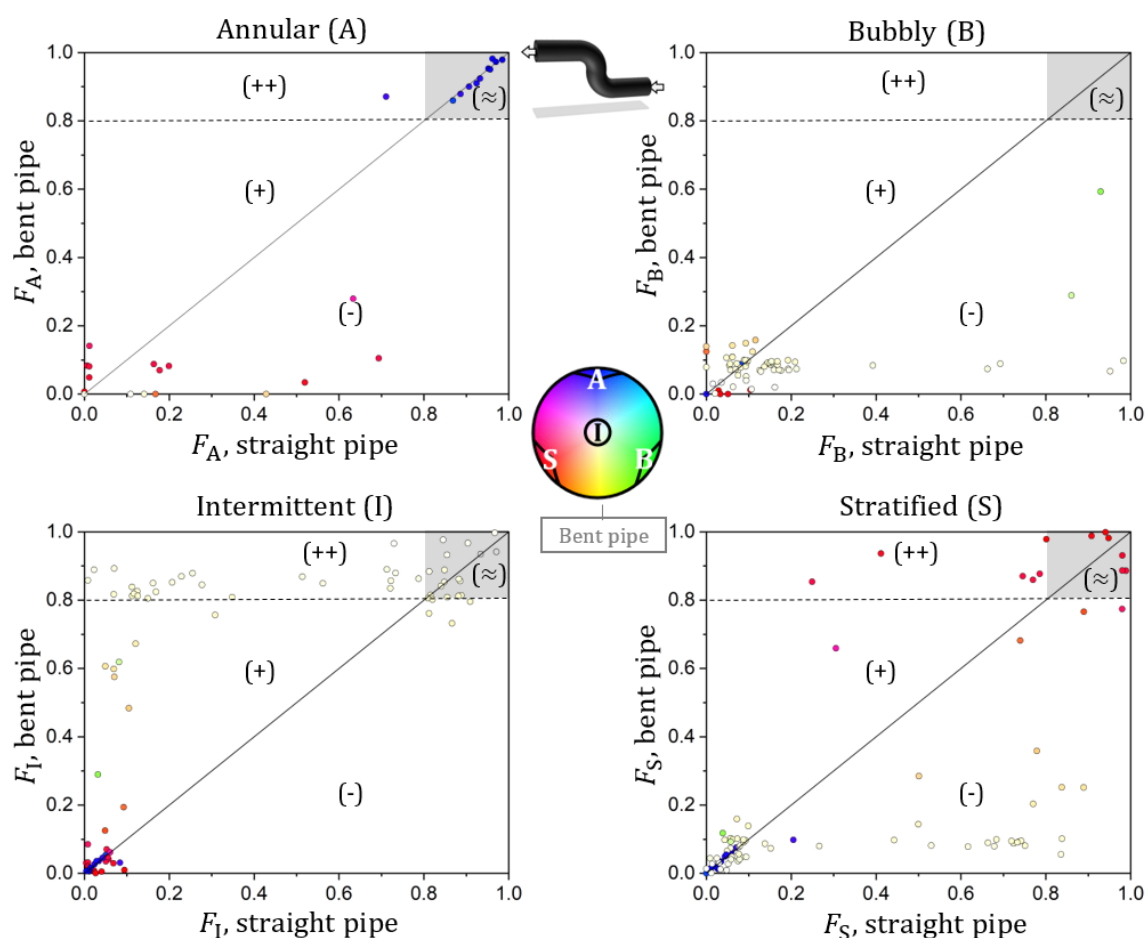


Figure A.15: Recovery of the morphology comparing the DN50 feed pipe setup with straight pipe to the DN50 feed pipe setup with upright S-bend.

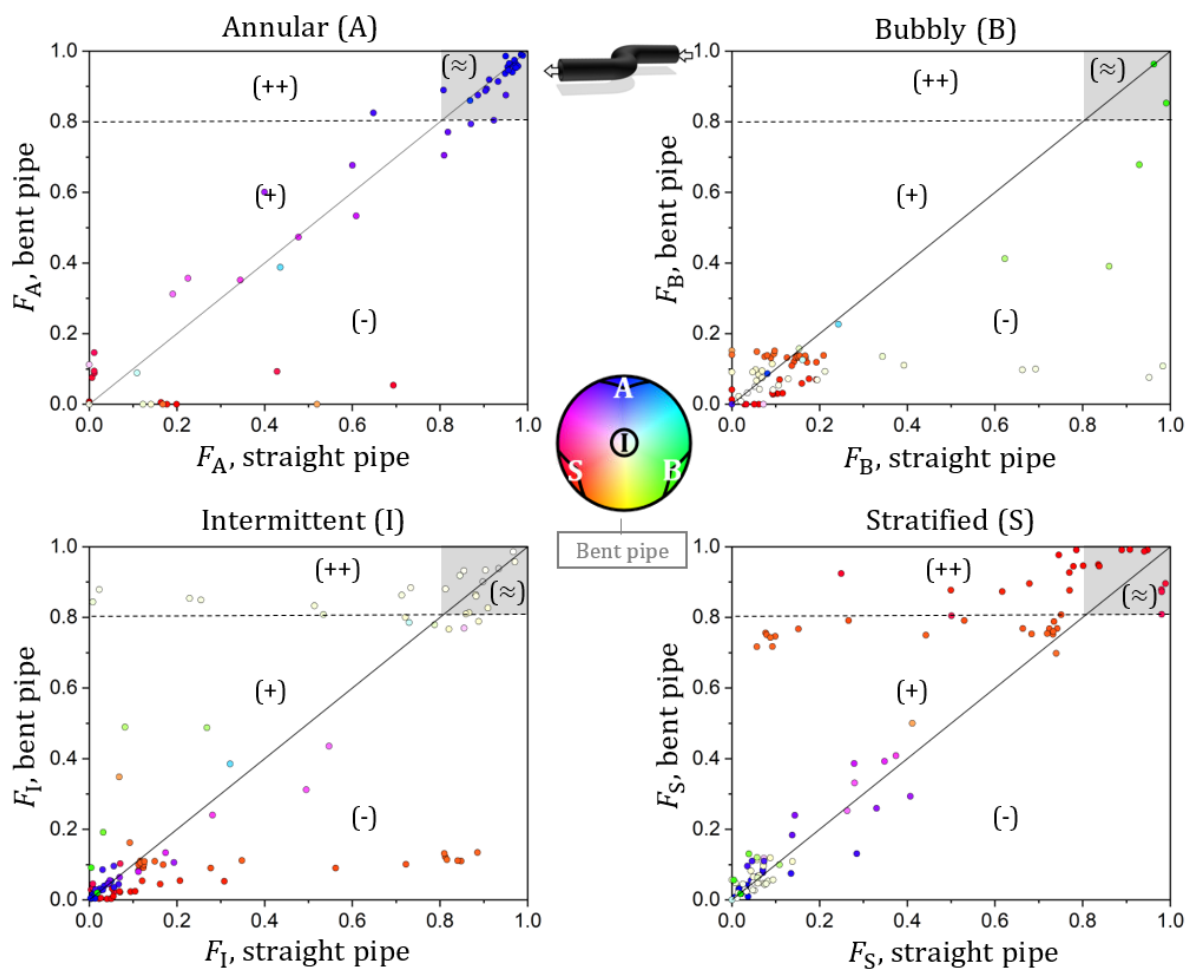


Figure A.16: Recovery of the morphology comparing the DN50 feed pipe setup with straight pipe to the DN50 feed pipe setup with horizontal S-bend.

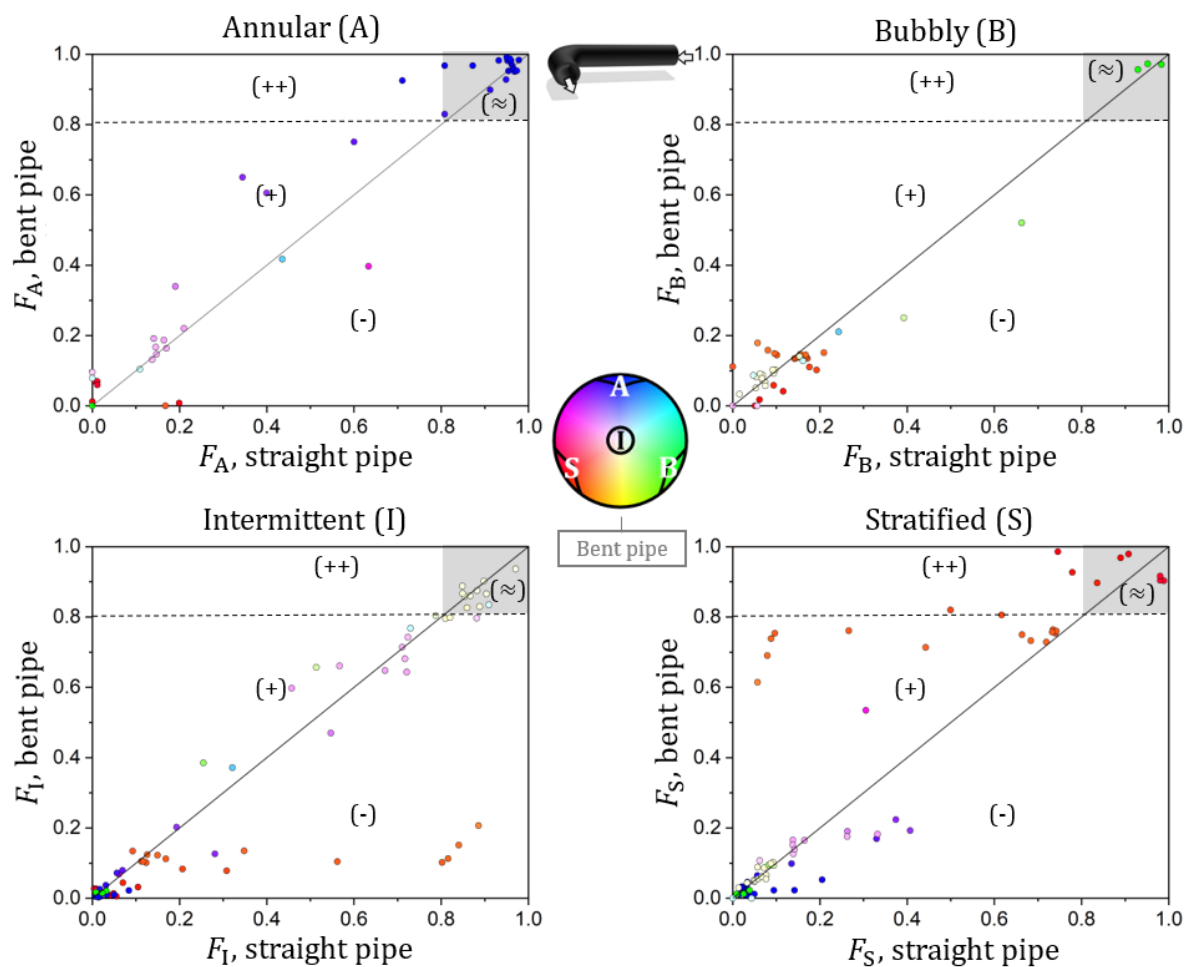


Figure A.17: Recovery of the morphology comparing the DN50 feed pipe setup with straight pipe to the DN50 feed pipe setup with horizontal 90° bend.

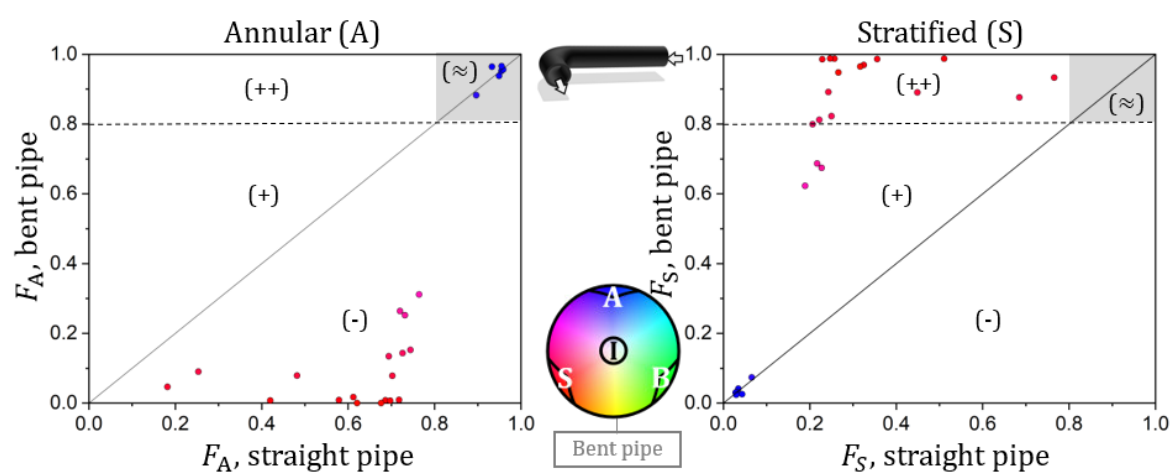





Figure A.18: Recovery of the morphology comparing the DN200 feed pipe setup with straight pipe to the DN200 feed pipe setup with horizontal 90° bend.

A.11 Recovery of the flow morphology (lookup tables)

Table A.4 provides a summary for all pipe configurations studied (morphologies that were not observed for the applied conditions are indicated by gray background).

Table A.4: Relative morphology recovery downstream the pipe bends (compared to inlet).




Geometry	Configuration	Morphology	Degree of membership				
			Annular	Bubbly	Intermittent	Stratified	
	Upright S-bend, $D = 50$ mm	Main	≈		≈ / -	≈	
		Minor		-	++	++ / -	
	Horizontal S-bend, $D = 50$ mm	Main	≈ / -		≈	≈	
		Minor	-	++ / +	++ / +	++ / +	
	Horizontal 90° bend, $D = 50$ mm	Main	≈		≈	≈	
		Minor	+	++	≈	+	
	Horizontal 90° bend, $D = 200$ mm	Main	≈ / -				≈
		Minor	-				

Full recovery (≈), transition (++), amplification (+) and attenuation (-), not observed at applied conditions

Table A.4 presents the relative morphology recovery of bent pipes at the reference position (REF) compared with the inlet position (INL). Main ($F_{n^*} \geq 0.8$) and minor ($1/3 \leq F_{n^*} < 0.8$) morphologies encountered at the inlet are considered separately. The latter represent degrees of membership that contribute to transitional morphologies. It is evident that main morphologies at the inlet recover more easily than transitional morphologies, which require longer entrance lengths than provided in this study to fully compensate the effect of bends. Both, horizontal and upright S-bends foster transitions towards stratified or intermittent flows, while the horizontal 90° bend ($D = 50$ mm) mostly amplifies annular and stratified features of the morphologies.

Table A.5 provides a summary about the absolute recovery of morphologies for all pipe curvatures studied.

Table A.5: Absolute morphology recovery downstream bent pipes (compared with straight pipes).

Geometry	Configuration	Morphology	Degree of membership			
			Annular	Bubbly	Intermittent	Stratified
			F_A	F_B	F_I	F_S
	Upright S-bend, $D = 50$ mm	Main	≈	-	≈	≈ / -
		Minor	-	-	+	+ / -
	Horizontal S-bend, $D = 50$ mm	Main	≈	-	≈ / -	≈
		Minor	≈	-	+ / -	≈ / +
	Horizontal 90° bend, $D = 50$ mm	Main	≈	≈	≈ / -	≈
		Minor	≈	≈	≈ / -	≈ / +
	Horizontal 90° bend, $D = 200$ mm	Main	≈			
		Minor	-			+

Full recovery (≈), transition (++) , amplification (+) and attenuation (-), not observed at applied conditions.

A.12 Wave frequency correlations (horizontal)

Correlation	Pipe configuration	Fluid combination	Operation conditions	Reference
$St_{s,L} = 1.1 \cdot LMN^{-0.93}$	$D = 76.2$ mm, $L/D = 229$	Air-water	$u_{s,L} = 0.004 - 0.04$ m s ⁻¹ $u_{s,G} = 40 - 80$ m s ⁻¹	Al-Sarkhi et al. (2012)
$f_W = 0.066 \frac{u_L}{D} \left(\frac{Re_G}{Re_L} \right)^{1.18}$	$D = 26.0$ mm, $L/D = 142$	Air-water	$u_{s,L} = 0.002 - 0.4$ m s ⁻¹ $u_{s,G} = 10 - 50$ m s ⁻¹	Ousaka et al. (1992)
$St_{s,L} = 0.25 \cdot LMN^{-1.2}$	$D = 48.6$ mm, $L/D = 245$ and $D = 153$ mm, $L/D = 53$	Air-water- butanol solutions, air-water- glycerine solutions	$u_{s,L} = 0.035 - 0.1$ m s ⁻¹ $u_{s,G} > 20$ m s ⁻¹ and $u_{s,L} = 0.035 - 0.1$ m s ⁻¹ $u_{s,G} > 10$ m s ⁻¹	Mantilla (2008)
$St_{s,L} = 0.258 \left(\frac{\rho_L}{\rho_G} \right)^{0.574} \cdot \left(\frac{\eta_L}{\eta_G} \right)^{-1.148} \cdot \left(\frac{Re_L}{Re_{G,mod}} \right)^{-1.148} \cdot \left(\frac{\sigma_L}{\sigma_{Water}} \right)^{-0.11}$	$D = \{16, 26\}$ mm, $L/D = 200$	Air-water- glycerol solutions	$u_{s,L} = 0.05 - 0.2$ m s ⁻¹ $u_{s,G} = 12 - 40$ m s ⁻¹	Setyawan et al. (2016)
$St_{s,L} = 0.057 \cdot LMN^{-1.33} + 0.89$	rectangular channel, 40 x 50 mm, $L = 4200$ mm	Air-water	$u_{s,L} = 0.01 - 0.08$ m s ⁻¹ $u_{s,G} > 5$ m s ⁻¹	Bae et al. (2017)

A.13 Determination of the void fraction by reduced-order models

Model type	Reference	Comment	Notation taken from	$VAR(\alpha_{G,corr})$
Separated flow models (SFM or slip ratio models, Equation 2.44) - 18 correlations	Butterworth (1975)	Homogenous equilibrium model (HEM, Equation 2.21)	Butterworth (1975)	0.06
	Lockhart and Martinelli (1949)	-	Lockhart and Martinelli (1949)	0.10
	Fujie (1964)	Iterative solution required	Fujie (1964)	0.07
	Thom (1964)	-	Thom (1964)	0.12
	Zivi (1964)	-	Butterworth (1975)	0.14
	Turner and Wallis (1965)	-	Butterworth (1975)	0.12
	Baroczy (1963)	-	Butterworth (1975)	0.10
	Smith (1969)	-	Smith (1969)	0.06
	Premoli et al. (1970)	Values $\alpha_G > 1$ possible	Woldesemayat and Ghajar (2007)	0.06
	Chisholm (1973)	-	Woldesemayat and Ghajar (2007)	0.06
	Madsen (1975)	Reasonable results are obtained only when inverting the sign of the proposed exponent e_1 (Equation 2.44).	Madsen (1975)	0.05
	Spedding and Chen (1984)	-	Woldesemayat and Ghajar (2007)	0.06
	Chen (1986)	-	Woldesemayat and Ghajar (2007)	0.09
	Hart et al. (1989)	-	Woldesemayat and Ghajar (2007)	0.10
	Petalas and Aziz	The correlation as specified in Woldesemayat and Ghajar (2007) gives the liquid fraction $\alpha_{L,Pet}$ instead of the gas fraction α_G (calculate $\alpha_{G,Pet} = 1 - \alpha_{L,Pet}$)	Woldesemayat and Ghajar (2007)	0.10
	Huq and Loth (1992)	-	Huq and Loth (1992)	0.06
	Zhao et al. (2000)	Iterative solution required (the numerical solver 'vpasolve' of MATLAB R2015a was used in this work); Values $\alpha_G > 1$ possible	Zhao et al. (2000)	0.14
Kanizawa and Ribatski (2016)	-	Kanizawa and Ribatski (2016)	0.09	

Homogenous flow models (HFM, or $k-\alpha_G$ models, Equation 2.42) - 9 correlations	Armand (1946)	-	Woldesemayat and Ghajar (2007)	0.06
	Armand and Treschev (1946), sometimes also referred to as Armand-Massina correlation	-	Armand and Treschev (1946)	0.06
	Bankoff (1960)	Pressure correction term calculated as proposed in Woldesemayat and Ghajar (2007)	Bankoff (1960), Woldesemayat and Ghajar (2007)	0.05
	Hughmark (1962)	Iterative solution required (the numerical solver 'vpasolve' of MATLAB R2015a was used in this work)	Hughmark (1962)	0.10
	Guzhov, A.L., Mamayev, V.A., Odishariya (1967)	-	Woldesemayat and Ghajar (2007)	0.13
	Löscher (1973)	Values $\alpha_G > 1$ possible	Woldesemayat and Ghajar (2007)	0.15
	Chisholm (1983)	-	Woldesemayat and Ghajar (2007)	0.06
	Czop et al. (1994)	Values $\alpha_G > 1$ possible	Czop et al. (1994)	0.12
	Sowinski et al. (2009)	Validated in microchannels only	Sowinski et al. (2009)	0.06
Drift-flux models (DFM, Equation 2.46) - 19 correlations	Hughmark (1962)	$u_D = 0$ for horizontal flows	Woldesemayat and Ghajar (2007)	0.06
	Zuber and Findlay (1965)	Equation 2.46	Zuber and Findlay (1965)	0.11
	Rouhani and Axelsson (1970)	Validity limits of intermediate terms are taken from Godbole et al. (2011); Iterative solution required (the numerical solver 'vpasolve' of MATLAB R2015a was used in this work)	Rouhani and Axelsson (1970)	0.12
	Bonnecaze et al. (1971)	-	Bonnecaze et al. (1971)	0.12
	Filimonov, A.I., Przhizhalovski, M.M., Dik, E.P., Petrova (1957)	-	Woldesemayat and Ghajar (2007)	0.15
	Ishii (1977)	$u_D = 0$ for horizontal flows	Ishii (1977)	0.06
	Sun, K.H., Duffey, R.B., Peng (1980)	-	Woldesemayat and Ghajar (2007)	0.11
	Isao and Mamoru (1987)	Obtained from diabatic experiments	Isao and Mamoru (1987)	0.11
	Kokal and Stanislav (1989)	-	Woldesemayat and Ghajar (2007)	0.11
	Sonnenburg (1989)	Iterative solution required (the numerical solver 'vpasolve' of MATLAB R2015a was used in this work); For annular flows C_0 depends on the fraction of entrained droplets (neglected for simplicity); Multiple solutions are obtained from the correlation.	Coddington and Macian (2002)	0.14
	Bestion (1990)	-	Bestion (1990)	0.13

	Chexal et al. (1992)	Iterative solution required (the numerical solver 'vpasolve' of MATLAB R2015a was used in this work)	Chexal et al. (1992)	0.09
	Hibiki and Ishii (2001)	$u_D = 0$ for horizontal flows; Correlation for bubbly flow was used; Iterative solution required (the numerical solver 'vpasolve' of MATLAB R2015a was used in this work)	Hibiki and Ishii (2001)	0.06
	Gomez et al. (2000b)	$u_D = 0$ for horizontal flows	Gomez et al. (2000b)	0.06
	Woldesemayat and Ghajar (2007)	-	Godbole et al. (2011)	0.13
	Choi et al. (2012)	Horizontal flows are accounted for by the inclination angle	Choi et al. (2012)	0.08
	Bhagwat and Ghajar (2014)	Iterative solution required (the numerical solver 'vpasolve' of MATLAB R2015a was used in this work)	Bhagwat and Ghajar (2014)	0.07
	Rassame and Hibiki (2018)	$u_D = 0$ for horizontal flows; Values $\alpha_G > 1$ possible	Rassame and Hibiki (2018)	0.06
	Eghorieta et al. (2018)	-	Eghorieta et al. (2018)	0.12
Models based on the Lockhart-Martinelli parameter (LMP, Equation 2.48) - 8 correlations	Chisholm, D. (1958)	Iterative solution required (the numerical solver 'vpasolve' of MATLAB R2015a was used in this work); Values $\alpha_G > 1$ possible	Chisholm, D. (1958)	0.05
	Wallis (1969)	-	Wallis (1969)	0.05
	Butterworth (1975)	-	Butterworth (1975)	0.08
	Domanski et al. (1983)	Values $\alpha_G > 1$ possible	Domanski et al. (1983)	0.07
	Tandon et al. (1985)	Validated for annular flows only; Values $\alpha_G > 1$ possible	Tandon et al. (1985)	0.16
	Abdul-Majeed (1996)	Distinguishes between laminar flows and turbulent flows (used in this work); Values $\alpha_G > 1$ possible	Abdul-Majeed (1996)	0.14
	Yashar et al. (2001)	-	Yashar et al. (2001)	0.12
	Nino, V.G.; Hrnjak, P.S.; Newell (2002)	-	Pietrzak and Płaczek (2019)	0.06
Empirical models (EMP) - 12 correlations	Sterman (1956)	Values $\alpha_G > 1$ possible	Woldesemayat and Ghajar (2007)	0.13
	Hoogendoorn (1959)	Factor $A = 0.6$; Iterative solution required (the numerical solver 'vpasolve' of MATLAB R2015a was used in this work)	Hoogendoorn (1959)	0.14
	Flanigan (1958)	-	Woldesemayat and Ghajar (2007)	0.15
	Dimentiev et al. (1959)	-	Isao and Mamoru (1987)	0.10
	Beggs (1972)	The model additionally predicts the flow morphology; Values $\alpha_G > 1$ possible	Beggs (1972)	0.20
	Mukherjee and Brill (1983)	Values $\alpha_G > 1$ possible	Mukherjee and Brill (1983)	0.08

Minami and Brill (1987)	Definitions for the dimensionless groups are taken from Woldesemayat and Ghajar (2007)	Minami and Brill (1987), Woldesemayat and Ghajar (2007)	0.10
Hart et al. (1989)	The correlation predicts the void fraction and not the liquid phase fraction as stated in the publication; Iterative solution required (the numerical solver ' <i>vpasolve</i> ' of MATLAB R2015a was used in this work)	Hart et al. (1989)	0.23
Spedding et al. (1990)	The paper of Spedding et al. (1990) refers to another paper Spedding and Spence (1989) that provides a different equation and was used in this work; Iterative solution required (the numerical solver ' <i>vpasolve</i> ' of MATLAB R2015a was used in this work)	Spedding and Spence (1989)	0.08
Gomez et al. (2000a)	Values $\alpha_G > 1$ possible	Gomez et al. (2000a)	0.14
Cioncolini and Thome (2012)	Limited to $\alpha_G < 0.7$ and certain density ratios which were incompatible with the present study	Cioncolini and Thome (2012)	n.a.
Pietrzak (2014)	α_G for an U-bend is obtained from the values of a straight pipe (correlation of Stomma (1979)); Values $\alpha_G > 1$ possible	Pietrzak (2014), Stomma (1979)	0.10

A.14 Empirical void fraction correlations

Models based on the Lockhart-Martinelli parameter

Geometry	Correlation	Boundaries
$D = 50$ mm, location REF, straight pipe	$\alpha_{G,1} = (1 + X^{10.4})^{-0.050}$ $\alpha_{G,2} = (1 + X^{0.70})^{-0.324}$	$X > X_2, X_2 = 10^2$ $X < X_1, X_1 = 1.8$
$D = 50$ mm, location INL, straight pipe	$\alpha_{G,1} = (1 + X^{0.32})^{-1.490}$ $\alpha_{G,2} = (1 + X^{0.92})^{-0.305}$	$X > X_2, X_2 = 10^2$ $X < X_1, X_1 = 10^0$
$D = 50$ mm, location OUT + $L/D = 10$, 90° horizontal bend	$\alpha_{G,1} = (1 + X^{2.87})^{-0.187}$ $\alpha_{G,2} = (1 + X^{0.92})^{-0.344}$	$X > X_2, X_2 = 10^2$ $X < X_1, X_1 = 1.7$
All geometries ($D = 50$ mm)	$\alpha_{G,3} = W \cdot \alpha_{G,1} + (1 - W) \cdot \alpha_{G,2}$	$W = \frac{X - X_1}{X_2 - X_1}$
$D = 200$ mm, location INL, straight pipe	$\alpha_G = (1 + X^{0.3})^{-0.050}$	n.a.
$D = 200$ mm, location OUT + $L/D = 10$, 90° horizontal bend	$\alpha_G = (1 + X^{0.55})^{-0.246}$	n.a.

Drift-flux model (DFM)

Geometry	Correlation	Boundaries
$D = 50$ mm, location REF, straight pipe	$\alpha_G = u_{s,G}(1.16 \cdot u_h + 0 \text{ m s}^{-1})^{-1}$ $\alpha_G = u_{s,G}(1.19 \cdot u_h - 0.84 \text{ m s}^{-1})^{-1}$ $\alpha_G = u_{s,G}(0.99 \cdot u_h + 2.66 \text{ m s}^{-1})^{-1}$	$u_h < 4 \text{ m s}^{-1}$ $4 \text{ m s}^{-1} < u_h < 20 \text{ m s}^{-1}$ $20 \text{ m s}^{-1} > u_h$
$D = 50$ mm, location INL, straight pipe	$\alpha_G = u_{s,G}(1.16 \cdot u_h + 0 \text{ m s}^{-1})^{-1}$ $\alpha_G = u_{s,G}(1.18 \cdot u_h - 0.85 \text{ m s}^{-1})^{-1}$ $\alpha_G = u_{s,G}(1.00 \cdot u_h + 1.89 \text{ m s}^{-1})^{-1}$	$u_h < 4 \text{ m s}^{-1}$ $4 \text{ m s}^{-1} < u_h < 20 \text{ m s}^{-1}$ $20 \text{ m s}^{-1} > u_h$
$D = 50$ mm, location OUT + $L/D = 10$, 90° horizontal bend	$\alpha_G = u_{s,G}(1.95 \cdot u_h + 0 \text{ m s}^{-1})^{-1}$ $\alpha_G = u_{s,G}(1.08 \cdot u_h + 0 \text{ m s}^{-1})^{-1}$ $\alpha_G = u_{s,G}(0.98 \cdot u_h + 2.06 \text{ m s}^{-1})^{-1}$	$u_h < 1.3 \text{ m s}^{-1}$ $1.3 \text{ m s}^{-1} < u_h < 20 \text{ m s}^{-1}$ $20 \text{ m s}^{-1} > u_h$
$D = 200$ mm, location INL, straight pipe	$\alpha_G = u_{s,G}(1.07 \cdot u_h + 0 \text{ m s}^{-1})^{-1}$ $\alpha_G = u_{s,G}(1.16 \cdot u_h - 0.23 \text{ m s}^{-1})^{-1}$	$u_h < 5 \text{ m s}^{-1}$ $5 \text{ m s}^{-1} > u_h$
$D = 200$ mm, location OUT + $L/D = 10$, 90° horizontal bend	$\alpha_G = u_{s,G}(0.77 \cdot u_h + 0 \text{ m s}^{-1})^{-1}$ $\alpha_G = u_{s,G}(1.02 \cdot u_h + 0.66 \text{ m s}^{-1})^{-1}$	$u_h < 0.6 \text{ m s}^{-1}$ $0.6 \text{ m s}^{-1} > u_h$

A.15 Derivation of the modified correlation for ILG

Differentiation of Equation 6.3 gives:

$$\frac{dp}{dz} \Big|_{L,i} = \frac{dP}{dz} \Big|_{G,i} - \sigma \frac{d^3 \bar{h}_L}{dz^3}. \quad \text{A.9}$$

Combining Equation 2.25 for each phase with Equation A.9 and resolving it for the pressure drop yields the combined momentum equation (Barnea and Taitel, 1994a) according to:

$$\begin{aligned} \frac{\tau_L S_L}{A_L} + \frac{\tau_i S_i}{A_L} - \rho_L g \frac{d\bar{h}_L}{dz} - \rho_L \frac{du_L}{dt} - \frac{\gamma}{2} u_L \rho_L \frac{du_L}{dz} \\ = -\frac{\tau_G S_G}{A_G} - \frac{\tau_i S_i}{A_G} - \rho_G g \frac{d\bar{h}_L}{dz} - \rho_G \frac{du_G}{dt} - \frac{\gamma}{2} u_G \rho_G \frac{du_G}{dz} - \sigma \frac{d^3 \bar{h}_L}{dz^3}. \end{aligned} \quad \text{A.10}$$

Re-arranging Equation A.10 and assuming stationary flow gives:

$$g \frac{d\bar{h}_L}{dz} + u_L \frac{\gamma}{2} \frac{du_L}{dz} = F + \frac{\rho_G}{\rho_L} \left(g \frac{d\bar{h}_L}{dz} + \frac{\gamma}{2} u_G \frac{du_G}{dz} \right) + \frac{\sigma}{\rho_L} \frac{d^3 \bar{h}_L}{dz^3} \quad \text{A.11}$$

with

$$F = -\frac{\tau_L S_L}{\rho_L A_L} + \frac{\tau_i S_i}{\rho_L} \left(\frac{1}{A_L} + \frac{1}{A_G} \right) + \frac{\tau_G S_G}{\rho_L A_G}. \quad \text{A.12}$$

Expressing the derivative of u_k according to

$$\frac{du_k}{dz} = \left(-u_k \cdot \frac{A'_L}{A_k} \right) \frac{d\bar{h}_L}{dz} \quad \text{A.13}$$

and combining Equations A.11, A.12 and A.13 yields

$$\rho_L F = \frac{d\bar{h}_L}{dz} \left[g(\rho_L - \rho_G) - \frac{\gamma A'_L}{2} (\rho_G u_G^2 A_G^{-1} + \rho_L u_L^2 A_L^{-1}) - \sigma \frac{d^2 \bar{h}_L}{dz^2} \right]. \quad \text{A.14}$$

Ultimately, Equation A.14 can be re-arranged to obtain Equation 6.4.

Scientific publications and contributions

During the preparation of this thesis, the following scientific contributions were made.

Peer-reviewed publications

Döß, A., Schubert, M., Wiedemann, P., Junge, P., Hampel, U., Schleicher, E., Mehringer, C. and Geipel, C. (2021). Flow Morphologies in Straight and Bent Horizontal Pipes. *ACS Engineering Au* **1**, 39–49.

Döß, A., Schubert, M., Wiezorek, M., Hampel, U., Flegiel, F., Windmeier, C., Schleicher, E. and Schunk, C. (2021). Morphology of Flashing Feeds at Critical Fluid Properties in Larger Pipes. *Chemie Ingenieur Technik* **93**, 1126–1133.

Döß, A., Schubert, M., Hampel, U., Mehringer, C., Geipel, C. and Schleicher, E. (2021). Two-Phase Flow Morphology and Phase Fractions in Larger Feed Line Sections. *Chemie Ingenieur Technik* **93**, 1134–1141.

Döß, A., Schubert, M., Bieberle, A. and Hampel, U. (2017). Non-invasive determination of gas phase dispersion coefficients in bubble columns using periodic gas flow modulation. *Chemical Engineering Science* **171**.

Windmeier, C., Flegiel, F., Döß, A., Franz, R., Schleicher, E., Wiezorek, M., Schubert, M. and Hampel, U. (2021). A New Research Infrastructure for Investigating Flow Hydraulics and Process Equipment at Critical Fluid Properties. *Chemie Ingenieur Technik* **93**, 1119–1125.

Flegiel, F., Windmeier, C., Wiezorek, M., Döß, A., Schubert, M., Hampel, U. and Schleicher, E. (2021). Capacity and Sizing of Wire Mesh Mist Eliminators at Critical Fluid Properties. *Chemie Ingenieur Technik* **93**, 1166–1177.

Xiao, J., Yan, H., Schubert, M., Liu, L., Döß, A., Schleicher, E. and Hampel, U. (2021). Effect of Nozzle Geometry on Centerline Gas Holdup in Submerged Gas Injection. *Metallurgical and Materials Transactions B*.

Hampel, U.; Schubert, M.; Döß, A.; Sohr, J.; Vishwakarma, V.; Repke, J.-U.; Gerke, S. J.; Leuner, H.; Rädle, M.; Kapoustina, V.; Schmitt, L.; Grünewald, M.; Brinkmann, J. H.; Plate, D.; Kenig, E. Y.; Lutters, N.; Bolenz, L.; Buckmann, F.; Toye, D.; Arlt, W.; Linder, T.; Hoffmann, R.; Klein, H.; Rehfeldt, S.; Winkler, T.; Bart, H.-J.; Wirz, D.; Schulz, J.; Scholl, S.; Augustin, W.; Jasch, K.; Schlüter, F.; Schwerdtfeger, N.; Jahnke, S.; Jupke, A.; Kabatnik, C.; Braeuer, A. S.; D'Auria, M.; Runowski, T.; Casal, M. F.; Becker, K.; David, A.-L.; Górak, A.; Skiborowski, M.; Groß, K.; Qammar, H. (2020). Recent Advances in Experimental Techniques for Flow and Mass Transfer Analyses in Thermal Separation Systems. *Chemie Ingenieur Technik* **92**, 926–948.

Wiedemann, P., Döß, A., Schleicher, E. and Hampel, U. (2019). Fuzzy flow pattern identification in horizontal air-water two-phase flow based on wire-mesh sensor data. *International Journal of Multiphase Flow*. Pergamon **117**, 153–162.

Oral presentations

Döß, A., Schubert, M., Wiezorek, M., Hampel, U., Flegiel, F., Windmeier, C., Schleicher, E. (2021). Charakterisierung zweiphasiger Feeds in Trennapparaten mit kritischen Stoffwerten. *Jahrestreffen Fluidverfahrenstechnik und Wärme- und Stoffübertragung 2021*. 24.-26.02.2021. Online conference.

Döß, A., Schubert, M., Wiezorek, M., Hampel, U., Flegiel, F., Windmeier, C., Schleicher, E. (2020). *Strömungsmorphologie flashender Feeds bei kritischen Stoffwerten. Jahrestreffen der ProcessNet-Fachgruppen Fluidverfahrenstechnik, Adsorption und Extraktion 2020*. 25.-28.02.2020. Berchtesgaden, Germany.

Döß, A., Schubert, M., Hampel, U., Mehringer, C., Geipel, C. (2019). Einfluss der Rohrleitungsführung auf die Strömungsmorphologie in Feedleitungen von Destillationskolonnen. *Jahrestreffen der ProcessNet-Fachgruppen Fluidverfahrenstechnik und Membrantechnik 2019*. 27.-29.03.2019. Potsdam, Germany.

Döß, A., Schubert, M., Hampel, U., Schleicher, E., Geipel, C., Mehringer, C., Flegiel, F. (2018). Flow morphology in feed pipes: theoretical analysis and experimental investigation. *ACHEMA 2018, Session: TERESA – Droplet entrainment and droplet reduction in mass transfer devices*. 11.-15.06.2018. Frankfurt am Main, Germany.

Marchini, S., Döß, A., Bieberle, A., Schubert, M., Hampel, U. (2021). Investigations on axial gas dispersion coefficients in bubble columns using gas flow modulation. *European Chemical Engineering Conference*, 20.-24.09.2021. Berlin. Germany.

Posters and other conference contributions

Döß, A., Schubert, M., Schleicher, E., Flegiel, F., Hampel, U. (2022). Flashing Feed and Mist Eliminator performance at Critical Fluid Properties. *The 12th international conference Distillation & Absorption 2022*, 18.-21.09.2022. Toulouse, France.

Döß, A., Schubert, M., Hampel, U. (2018). Experimental Analysis of the effect of column feed pipe configurations on the flow morphology. *ProcessNet-Jahrestagung und 33. DECHEMA-Jahrestagung der Biotechnologen 2018*, 10.-13.09.2018. Aachen, Germany.

Döß, A., Hampel, U. (2017). Experimental investigation of adiabatic two-phase flow in horizontal feed pipes. *HZDR PhD Seminar*, 16.-18.10.2017. Seiffen, Germany.

Döß, A., Schubert, M., Hampel, U. (2018). Analysis of the effect of column feed pipe configurations on the flow morphology. *HZDR PhD Seminar*, 5.-7.11.2018. Ustí nad labem, Czech Republic.

Reports

Döß, A., Schubert, M. (2022). Experimentelle Studie zur Gewinnung von hydrodynamischen Basisdaten für das Stoffsystem Stickstoff / n-Pentan. Dresden, Germany.

Bart, H-J., Beierkuhnlein, K., Borchardt, D., Darvishsefat, N., Döß, A., Falk, H., Fasel, H., Flegiel, F., Franz, R., Geipel, C., Geipel, W., Grünewald, M., Hampel, U., Jasch, K., Kronert, D., Mackowiak, J., Mehringer, C., Merkel, F. S., Michelsen, B., Paschetag, M., Riese, J., Schleicher, E., Scholl, S., Schubert, M., Schultes, M., Schulz, J., Schunk, C., Wandres, P., Wiezorek, M., Windmeier, C. (2021). Schlussbericht BMWi Verbundprojekt "Tropfenentstehung und -reduzierung in Stoffaustauschapparaten". Germany.

Data sets

Döß, A., Schubert, M. (2022). GUI Flow data. <https://doi.org/10.14278/rodare.1531>.

Döß, A., Schubert, M., Wiedemann, P., Schleicher, E., Hampel, U. (2021). Dataset for: Flow morphologies in straight and bent horizontal pipes. <https://doi.org/10.14278/rodare.784>.

Döß, A., Schubert, M., Wiedemann, P., Schleicher, E., Hampel, U. (2021). Dataset for: Flow morphologies in straight and bent horizontal pipes (uncalibrated measurement files). <https://doi.org/10.14278/rodare.786>.

Döß, A., Schubert, M., Wiedemann, P., Schleicher, E., Hampel, U. (2020). Dataset for: Morphology of flashing feeds at critical fluid properties in larger pipes. <https://doi.org/10.14278/rodare.419>.

Supervised student works

Junge, P. (2019). Charakterisierung von Zweiphasenströmungen in komplexen Rohrgeometrien. *Diploma thesis*. Technische Universität Dresden.

Abdlgwad, A. (2019). Numerical simulation of adiabatic two-phase flow in horizontal elbow bends. Internship. Grenoble-INP Ense3 Engineering School.

Eidesstattliche Erklärung

Hiermit versichere ich, dass die vorliegende Arbeit ohne unzulässige Hilfe Dritter und ohne Benutzung anderer als der angegebenen Hilfsmittel angefertigt wurde. Die aus fremden Quellen direkt oder indirekt übernommenen Gedanken sind als solche kenntlich gemacht.

Bei der Auswahl und Auswertung des Materials sowie bei der Erstellung des Manuskripts habe ich Unterstützungsleistungen von folgenden Personen erhalten:

Prof. Dr.-Ing. Markus Schubert

Prof. Dr.-Ing. Dr. h.c. habil. Uwe Hampel

Weitere Personen waren an der geistigen Herstellung der vorliegenden Arbeit nicht beteiligt. Insbesondere habe ich nicht die Hilfe eines kommerziellen Promotionsberaters in Anspruch genommen. Dritte haben von mir keine geldwerten Leistungen für die Arbeiten erhalten, die in Zusammenhang mit dem Inhalt der vorliegenden Dissertationsschrift stehen.

Die Arbeit wurde bisher weder im Inland noch im Ausland in gleicher oder ähnlicher Form einer anderen Prüfungsbehörde vorgelegt und sie ist auch nicht veröffentlicht worden.

Die Promotionsordnung wird anerkannt.

Dresden, den 16.12.2022

Dipl.-Ing. Alexander Döß